2022

Unit Circle Roots Based Sensor Array Signal Processing

Jared P. Smith
Wright State University

UNIT CIRCLE ROOTS BASED SENSOR ARRAY SIGNAL PROCESSING

A dissertation submitted in partial fulfillment
of the requirements for the degree of
Doctor of Philosophy

by

JARED P. SMITH
B.S.E.E., Wright State University, 2015
B.S., Wright State University, 2015
M.S.E.E., Wright State University, 2017

2022
Wright State University

Wright State University
GRADUATE SCHOOL

April 27, 2022

I HEREBY RECOMMEND THAT THE DISSERTATION PREPARED UNDER MY SUPERVISION BY Jared P. Smith ENTITLED Unit Circle Roots Based Sensor Array Signal Processing BE ACCEPTED IN PARTIAL FULFILLMENT OF THE REQUIREMENTS FOR THE DEGREE OF Doctor of Philosophy.

Arnab K. Shaw, Ph.D.
Dissertation Director

Josh N. Ash, Ph.D.
Director, Ph.D. in Electrical Engineering Program

Barry Milligan, Ph.D.
Vice Provost for Academic Affairs
Dean of the Graduate School

Committee on
Final Examination

Arnab K. Shaw, Ph.D.

Aboulnasr Hassanien, Ph.D.

Michael A. Saville, Ph.D., P.E.

Josh N. Ash, Ph.D.

Fred D. Garber, Ph.D.

ABSTRACT

Smith, Jared P. Ph.D., Department of Electrical Engineering, Wright State University, 2022. *Unit Circle Roots Based Sensor Array Signal Processing*.

As technology continues to rapidly evolve, the presence of sensor arrays and the algorithms processing the data they generate take an ever-increasing role in modern human life. From remote sensing to wireless communications, the importance of sensor signal processing cannot be understated. Capon's pioneering work on minimum variance distortionless response (MVDR) beamforming forms the basis of many modern sensor array signal processing (SASP) algorithms. In 2004, Steinhardt and Guerci proved that the roots of the polynomial corresponding to the optimal MVDR beamformer must lie on the unit circle, but this result was limited to only the MVDR. This dissertation contains a new proof of the unit circle roots property which generalizes to other SASP algorithms. Motivated by this result, a unit circle roots constrained (UCRC) framework for SASP is established and includes MVDR as well as single-input single-output (SISO) and distributed multiple-input multiple-output (MIMO) radar moving target detection. Through extensive simulation examples, it will be shown that the UCRC-based SASP algorithms achieve higher output gains and detection probabilities than their non-UCRC counterparts. Additional robustness to signal contamination and limited secondary data will be shown for the UCRC-based beamforming and target detection applications, respectively.

Contents

List of Figures

List of Tables

Acknowledgment

I would like to take this opportunity to extend my thanks to my committee and to my advisor Dr. Arnab Shaw. Without your support and encouragement during this process I would have never come as far as I have.

Thank you to Dr. Aboulnasr Hassanien, your support and encouragement during the early stages of this work were instrumental to my success.

Thank you to Dr. Harvey Schumann and Dr. Dan Thomas of SRC Inc. Your input and our discussions provided helpful insight while conducting this research.

Thank you to Dr. Brian Rigling and the Center for Surveillance Research for their support of this research over the last two years.

Finally, I would like to thank my family, especially my Mom, for their support and encouragement throughout this process.

Introduction

With the advent of modern technology, sensors are ubiquitous in human daily life in diverse applications including home appliances, buildings, smart phones, transportation etc. Sensor arrays are utilized in many scientific and engineering fields that use some form of wave propagation such as, radar, sonar, communication, astronomy, navigation, medical diagnosis, and seismic exploration, etc. The main purpose of processing signals received by an array of sensors is to extract important source signal or target information by analyzing the received signal to perform various useful tasks such as, source localization and target recognition in radar, sonar, communication, astronomy, and seismology.

The seminal work on Minimum-Variance Distortionless Response (MVDR) by Capon [13] largely forms the fundamental basis for much of the theoretical and practical development in Sensor Array Signal Processing (SASP) over the past five decades. MVDR and related extensions remain the backbone of Beamforming, STAP, adaptive target detection, MIMO, and many other SASP algorithms.

A key theoretical property of the MVDR beamformer proven by Steinhardt and Guerci [97] states that the roots of the MVDR array polynomial for a uniform linear array (ULA) ideally fall on the unit circle. An important contribution of this work is to extend and generalize the Steinhardt-Guerci unit-circle theorem for MVDR to prove that the unit circle roots property is also valid for ideal Adaptive Matched Filters (AMF) and a broad class of other important statistical adaptive detectors with vast practical applications. Previously reported proofs for MVDR utilized the Wiener-Khinchin theorem to transform the MVDR optimization problem to the frequency-domain. In this work, Carathèodory's theorem on positive definite, Toeplitz matrices and Vandermonde steering vectors are leveraged to derive a new spatial-domain proof of this fundamental property. However, to the best of our knowledge, existing MVDR or adaptive detection algorithms fail to enforce this theoretically fundamental unit circle roots property during array design, detector optimization or in their practical implementations. Hence, existing SASP algorithms as currently implemented are at best suboptimal, and fail to attain their true underlying potential when the requisite mathematical structure exists to justify unit circle root enforcement.

The analytical expressions of the theoretically optimal MVDR beamformer and AMF weights depend on the ideal covariance matrix of the underlying noise, interference and clutter. The data collected by the sensors almost always include some level of noise, clutter, interference, multipath, or jamming signals and it may also be contaminated by the signal-of-interest (SOI) that exist in the theater of operation. For wide sense stationary signals, the covariance matrix ideally has a Toeplitz structure. However, in practice, the true covariance matrices are never available, and the sample covariance matrix (SCM) estimated using the observed sensor array data is used instead. The SCM does not possess the desired Toeplitz structure, and it typically differs significantly from the true covariance matrix, especially when the data set used to compute the SCM is as small as the dimension of the SOI. Consequently, the array or detector polynomials estimated with the noisy SCM do not possess unit circle roots, *i.e.* zeros on the unit-circle. It is well-recognized that zeros on the unit circle cause deep nulls and lower sidelobes in the frequency spectrum of a filter, enabling suppression or nullification of noise, interference, multipath and jamming, if present. However, lack of unit-circle roots of the designed filter the associated noise suppression and nulling ability is lost, partly explaining the relatively poor performance of almost all existing SCM-based SASP algorithms.

This work will leverage polynomial theory in mathematical literature to enforce unit circle roots [65, 89] on filter polynomials for sensor array design for adaptive beamforming and for adaptive target detection. Specifically, two constraints must be satisfied for a polynomial to have unit circle roots [65],

- $\mathbf{C}1$: The polynomial coefficients have conjugate symmetry and

- $\mathbf{C}2$: The roots of the derivative polynomial lie on or inside the unit circle.

The first condition $\mathbf{C}1$ is relatively easy to satisfy and has been used by many researchers in different fields of SASP [46], [109], [115]. However, imposing $\mathbf{C}1$ on a polynomial will not guarantee UC roots and it typically produces one or more pairs of reciprocal roots. Furthermore, imposing $\mathbf{C}2$ requires non-linear optimization that may be impractical [89, 54, 55].

Interestingly, for a 1st-order polynomial, conjugate symmetry ($\mathbf{C}1$) is sufficient to guarantee a UC root because the derivative required in $\mathbf{C}2$ is a scalar. The key idea behind the proposed novel concept is that the optimization criterion for MVDR and detectors will be reformulated to optimize each root separately by splitting the N-dimensional problems into multiple 1-D optimization problems [89]. This approach effectively utilizes the condition-$\mathbf{C}1$ repeatedly to achieve unit circle root for each first-order factor. Conjugate symmetry will be imposed on each 1st-order factor to guarantee UC root in each case. Since the algorithm works with first-order factors only, condition-$\mathbf{C}2$ becomes inconsequential. The proposed method initializes each 1-D root optimization step with the sample matrix inversion (SMI) roots. The proposed UC roots constrained approach is non-iterative and has a closed-form solution. The approach also works well with limited number of snapshots.

Regarding past work on exploiting unit circle roots in SASP, it is noted that inspired by Steinhardt et. al's [97] unit circle roots theorem for the ideal MVDR beamformer polynomial, Tuladhar et. al [101, 102] had proposed UC-MVDR where the SMI-based roots were radially projected onto the unit circle in an ad-hoc manner. Even with this relatively simple modification, some beamforming performance improvement were achieved in their work. However, no attempt was made to optimize the underlying MVDR criterion while updating the original SMI-based roots, and in that sense, UC-MVDR may be considered suboptimal. Furthermore, their work was limited to MVDR only, and no consideration was given to broadening the scope of the unit-circle roots property by extending it to the moving target detection problem and other areas considered in this work. To the best of our knowledge, no other published work has explicitly studied the efficacy of unit circle roots in beamformer and detector polynomials although there have been some notable indirect connections as discussed next.

In the context of array pattern synthesis, due to the seminal work on linear arrays by Schelkunoff in the early 1940's [83] it has been known for sometime that array null positions can be controlled by placing the array polynomial roots on the unit circle [26]. Indeed, the well-known conventional beamformer (CBF) which is essentially an ideal spatial lowpass filter (or bandpass, in case of steered arrays) with all its roots on the unit circle producing deep nulls in the sidelobe regions while passing the SOI in the mainbeam direction. However, these methods are deterministic and lack adaptivity to the presence of interference. Capon's MVDR was developed to bring adaptivity to array patterns for the purpose of nullifying the effects of directional interference and jamming. Steinhardt et al's unit circle theorem [97] is important because it proved that ideally even Capon's MVDR should also possess unit circle roots. The new unit circle proof in Chapter 2 further broadens the scope of this key property to a larger class of SASP problems, and the rest of the chapters algorithmically enforce this important property to radar moving target detection for SISO and MIMO scenarios in homogeneous and heterogeneous clutter.

Capon's method and traditional statistical detectors rely on the covariance matrix which must be estimated in practice from observed array data or radar pulses using the SCM, and the resulting array polynomials lack the unit circle zeros. Recognizing the inferior covariance estimates provided by the SCM, especially for low sample support, many researchers have proposed a variety of strategies to improve the quality of covariance estimates. These include the use of forward-backward SCM (FB-SCM) covariance estimate that effectively doubles the size of the data. In case of MVDR, it has been shown in literature that the performance of the forward-backward SMI (FB-SMI) is superior to that of the SMI-based solution, and FB-SMI based array coefficients possess conjugate-symmetry property [109], [46],[115], satisfying condition-$\mathbf{C}1$ for UC roots. However, the FB-SMI based polynomial does not guarantee UC roots as it does not satisfy condition $\mathbf{C}2$, and it typically produces one or more pairs of reciprocal roots. Other researchers have recognized certain properties of the ideal covariance matrices, such as persymmetry and the Toeplitz property and these important underlying structures have been enforced during MVDR and detector designs to achieve improved results [30, 28]. Similar to the use of FB-SCM, in order to overcome the need for large amount of secondary data, the persymmetry property has been used for both MVDR beamforming [63] and Adaptive Matched Filtering (PS-AMF) for moving target detection [69] to achieve improved beamforming and detection performance, respectively. Interestingly, it has been shown recently that FB-SMI and persymmetry are essentially equivalent properties via a unitary transformation and their performances are exactly identical in practice [92].

Structured covariance matrix estimation has been a very active research field where the eigen-decomposition properties or Vandermonde decomposition structures of the covariance matrices are utilized for improved covariance estimates [112, 111, 90]. Some of these algorithms have been used for robust beamforming and/or detection [35, 30, 28] to improve performance.

MVDR and detector polynomials estimated using forward-backward or persymmeteric covariance matrices possess conjugate symmetry property that satisfy UC condition-$\mathbf{C}1$. Accordingly, most of the roots produced by those methods do fall on the unit circle although some roots appear in reciprocals pairs as well because the condition-$\mathbf{C}2$ is not satisfied. Furthermore, according to the general unit circle theorem proven in this dissertation (see also [93]) all roots of any MVDR or detector polynomial estimated using Toeplitz rectified covariance matrix will lie on the unit circle. However, to the best of our knowledge, this important connection between FB (or persymmetric) and Toeplitz matrices to unit circle roots has not been recognized in the literature, except for the work reported in [97, 102] with limited scope in MVDR. The unit circle roots constrained approach developed for a comprehensive set of SASP algorithms in this dissertation demonstrate that enforcing unit-circle roots in designing beamformer and detector polynomials can be a powerful tool to achieve improved performance than the current state of the art in the respective fields. This work further shows that although the unit-circle proofs in [97] and Chapter 2 require the Hermitian Toeplitz property of the ideal covariance matrix, the proposed algorithmic framework presented in this work achieves the desired unit-circle roots and associated benefits using the sample covariance matrix (SCM) algorithmically even though SCM does not possess Toeplitz structure.

The primary objective of this research is to enforce the theoretically necessary unit circle roots property to theoretically reformulate a broad class of advanced SASP algorithms to guarantee unit-circle roots during theoretical design and practical implementations. The overall objective is to attain significant performance improvement at relatively low additional computational cost from existing state-of-the-art SASP algorithms by addressing a significant gap that appears to have remained in the SASP field.

This dissertation develops a novel Unit Circle Roots Constrained (UCRC) SASP Framework that will leverage polynomial theory in mathematical [65] and signal processing [89] literature to enforce unit-circle roots on sensor array polynomials that appear in beamforming using uniform linear arrays (ULA), adaptive detection in Gaussian and compound Gaussian clutter in single-input single output (SISO) and multiple-input multiple output (MIMO) problems. In all cases, the proposed novel concept is to reformulate the underlying SASP optimization criteria by splitting the respective multidimensional problems into multiple 1-D optimization problems to optimize each root separately. It will be shown with comprehensive simulation studies that the proposed algorithms consistently outperform conventional methods at relatively low additional computational cost. In addition, a new Toeplitz reconstruction method is also presented that utilizes the unit circle roots estimates in combination with Carathèodory's theorem on full-rank Toeplitz matrices.

In Chapter 3, we propose the unit circle roots constrained MVDR algorithm (UCRC-MVDR). Coupling the unit circle roots constraint into the MVDR optimization problem by exploiting polynomial conjugate symmetry, the resulting root updates can be found in closed form, and it is further shown that UCRC-MVDR has a computational complexity proportional to the sample matrix inversion (SMI) technique. Through extensive simulation examples, it is shown that the UCRC-MVDR drastically outperforms conventional techniques, including a recently proposed UC-MVDR approach [102].

In Chapter 4, the unit circle roots constraint is applied to the radar moving target detection problem using symmetrically spaced pulse trains. It is shown that the derivation of the AMF is similar to the MVDR and thus, the unit circle roots constraint can be applied in the same way. The UCRC-AMF is shown to outperform the SMI-based AMF for limited secondary data. A modified version of the UCRC-AMF based on the forward-backward covariance estimate is also proposed, called the M-UCRC-AMF, which displays drastically improved performance over the UCRC-AMF and persymmetric AMF (PS-AMF).

In Chapter 5 radar moving target detection in low rank clutter is considered, and the unit circle approach is extended to accommodate this scenario. Specifically, analyzing the roots of the classical eigenvector-based adaptive filter shows that many of the roots occur near their Clairvoyant counterparts on the unit circle. Hence, we enforce the unit circle constraint by radially projecting the roots of the eigenvector-based adaptive filter onto the unit circle. The unit circle generalized likelihood ratio test is derived by combining the primary and secondary data under the null and alternative hypotheses, and offers dramatically improved performance over the GLRT based soley on the eigenvectors.

Capitalizing on the proof the unit circle property and the connection to Carathèodory's Vandermonde matrix decomposition, a Toeplitz-structured covariance matrix estimate can be obtained from the roots at the output of the UCRC algorithm. Unlike the approach in Chapters 3, 4, and 5, enforcing Hermitian Toeplitz structure naturally provides unit circle roots, instead of imposing them directly upon the filter design. The improved performance of detectors using this new estimate will be demonstrated in Chapters 6 and 7.

1.1 Main Contributions

1.1.1 New Proof of the Unit Circle Roots Property

As mentioned above, the new proof of the unit circle roots property broadens the scope of the unit circle enforcement to other SASP applications. The new proof is the foundation of the proposed UCRC framework, and differs from previous proofs of this claim available in the literature which only pertain to the MVDR problem.

1.1.2 The Unit Circle Roots Constrained MVDR Algorithm (UCRC-MVDR)

The UCRC-MVDR algorithm drastically enhances the performance and robustness of the conventional sample matrix inversion based MVDR by enforcing the unit circle roots constraint. Additionally, the UCRC-MVDR outperforms the recently proposed UC-MVDR [102], providing higher output gain at lower input signal to noise ratio and for smaller aperture sizes.

1.1.3 The Unit Circle Roots Constrained AMF Algorithm (UCRC-AMF)

The UCRC-AMF and its modified version the M-UCRC-AMF outperform the SMI-based and persymmetric versions of the AMF, respectively. The UCRC-AMF and M-UCRC-AMF also demonstrate improved performance in the case of unknown target Doppler frequency when compared against the AMF and persymmetric AMF. It will be shown in Chapter 4 that both algorithms have approximate constant false alarm rate with respect to the unknown covariance matrix.

1.1.4 Unit Circle Roots Generalized Likelihood Ratio Test

The unit circle generalized likelihood ratio test (UC-GLRT) enhances the performance of principle components inverse (PCI)-based adaptive techniques by radially projecting the roots of the eigenvector-based filter onto the unit circle. Unlike radial projection for the SMI roots, the roots of the PCI-based filter are much closer to the unit circle, meaning their radial projection is much closer to their clairvoyant counterpart. The UC-GLRT outperforms the eigenvector-based detector and displays improved robustness in the case of unknown Doppler frequency and clutter rank.

1.1.5 Unit Circle Roots Based Toeplitz Rectification

The new UCRC-based Toeplitz rectified estimate enforces the unit circle constraint upon adaptive detector design implicitly instead of directly as is the case in Chapters 4 and 5. Unlike conventional Toeplitz rectification approaches [35, 28], this new estimate explicitly makes use of the theoretical necessity of unit circle roots and drastically improves the performance of robust detectors in compound-Gaussian clutter.

1.2 List of Publications

In the process of conducting this research, we have published several conference papers and one journal article:

1. A. Shaw, J. Smith and A. Hassanien, ”MVDR Beamformer Design by Imposing Unit Circle Roots Constraints for Uniform Linear Arrays,” in IEEE Transactions on Signal Processing, vol. 69, pp. 6116-6130, 2021.

2. J. Smith, A. Shaw and A. Hassanien, ”A New Approach to Moving Target Detection using Unit Circle Roots Constrained Adaptive Matched Filter,” 2021 55th Asilomar Conference on Signals, Systems, and Computers, pp. 1091-1097, 2021.

3. J. Smith and A. Shaw, ”Unit Circle Roots Property for Sensor Array Signal Processing,” NAECON 2021 - IEEE National Aerospace and Electronics Conference, pp. 210-216, 2021.

4. A. Shaw, J. Smith and A. Hassanien, ”Unit Circle Roots Constrained MVDR Beamformer,” 2021 55th Asilomar Conference on Signals, Systems, and Computers, pp. 192-198, 2021.

5. J. Smith and A. Shaw ”Improved Moving Target Detection by Modified Unit Circle Roots Constrained Adaptive Matched Filter,” 2022 IEEE Radar Conference (RadarConf22), pp. 01-06, 2022.

6. A. Shaw and J. Smith, ”Spatial Domain Proof of Unit Circle Roots Property of MVDR and Improved Performance Results,” 2022 IEEE Radar Conference (RadarConf22), pp. 1-6, 2022.

7. J. P. Smith and A. Shaw, ”Moving Target Detection using Distributed MIMO Radar in Non-Homogeneous Clutter with Limited Training Data,” 2020 54th Asilomar Conference on Signals, Systems, and Computers, pp. 617-622, 2020.

1.3 Organization of Dissertation

This document is organized in the following way. In Chapter 2, the proof of the unit circle roots property is derived and the connection to general sensor signal processing applications is established. The proof is central to the work contained in this document, and is the foundation of the unit circle roots constrained approach. In Chapter 3, we develop the unit circle roots constrained MVDR algorithm for minimum variance beamforming with uniform linear arrays. In Chapter 4, the unit circle roots constrained adaptive matched filter and modified unit circle roots constrained AMF are proposed and analyzed using extensive simulation examples for moving target detection in homogeneous Gaussian clutter. In Chapter 5, we extend the unit circle approach to moving target detection in low-rank Gaussian clutter, where we apply the unit circle roots constraint to the principle components inverse (PCI) technique to develop the unit circle GLRT. In Chapter 6, we depart from the assumption of homogeneous Gaussian clutter and consider moving target detection in compound-Gaussian clutter using unit circle roots based Toeplitz rectification. Chapter 7 examines the extension of the Toeplitz rectification based detector to moving target detection in compound-Gaussian clutter using an active distributed multiple-input-multiple-output (MIMO) radar network. Finally, Chapter 8 offers concluding remarks and potential directions for future work.

A New Proof of the Unit Circle Roots Property

2.1 Introduction

In this chapter, the theoretical basis for imposing the unit circle roots constraint is established and extended for more general sensor array signal processing applications. The specific goal is to unite different SASP applications under one specific criteria: the unit circle roots property. It will be demonstrated that the mathematical structures which are common-place for applications such as beamforming with uniform linear arrays (ULAs) and moving target detection with symmetrically spaced pulse trains both share this practically impactful property.

From a practical perspective, unit circle roots are desirable in finite impulse response (FIR) filters due to their associated impact upon the filter's frequency response. Unit circle zeros cause deep nulls in the frequency response which can enhance interference suppression, and for adaptive filtering applications; more unit circle zeros implies improved suppression of unwanted signals.

Historically, in a 2004 conference paper Steinhardt and Guerci established the theoretical necessity of unit circle roots for the minimum variance distortionless response (MVDR) beamformer [97] for ULAs. Despite this theoretical development, the Steinhardt's proof was coupled to the MVDR optimization problem, and no attempt was made to generalize this proof to other SASP applications.

In this chapter, we provide a new proof of a critical property pertaining to both the MVDR beamformer [13] and adaptive matched filter [76]: the roots of the filter polynomial computed using the true covariance matrix ideally fall on the unit circle when the data are uniformly sampled (*i.e.,* via uniform linear array (ULA) or symmetrically spaced pulse train).

The proof in this chapter is based on the covariance matrix and steering vector structure, does not make use of either the Weiner-Khinchin or implicit function theorems used in [97], and generalizes to other sensor array signal processing approaches. Our proof leverages Carathèodory's theorem on positive definite, Toeplitz matrices, a well-known theorem in spectrum estimation [14].

2.2 General Linearly Constrained SASP Optimization

The solution of linearly constrained quadratic minimization problems feature prominently in the signal processing community. Specifically, in the context of beamforming with uniform linear arrays and pulsed radar using symmetrically spaced pulse trains, the solution to the following general SASP minimization

$$\min_{\mathbf{w}} \mathbf{w}^H \boldsymbol{\Sigma} \mathbf{w} \;\; \text{s.t. } \mathbf{w}^H \mathbf{g}\left(f_0\right) = c \tag{2.1}$$

is the optimal filter

$$\mathbf{w}_{\text{opt}} = c \frac{\boldsymbol{\Sigma}^{-1} \mathbf{g}(f_0)}{\mathbf{g}^H(f_0) \boldsymbol{\Sigma}^{-1} \mathbf{g}(f_0)}, \tag{2.2}$$

where $\mathbf{g}(f_0)$ is referred to as the steering vector:

$$\mathbf{g}(f_0) \triangleq \left[1, e^{j2\pi f_0}, \ldots, e^{j2\pi(J-1)f_0}\right]^T. \tag{2.3}$$

The optimal filter has different interpretations depending upon the intended application. For example, in array processing, the $\mathbf{w}$ is the minimum variance distortionless response (MVDR) beamformer [13] when $c = 1$. For radar target detection, $\mathbf{w}$ is the adaptive matched filter (AMF) [76] when $c = \sqrt{\mathbf{g}^H(f_0)\,\mathbf{\Sigma}^{-1}\mathbf{g}(f_0)}$.

2.3 Proof of Unit Circle Roots

A few key assumptions are that the covariance matrix $\mathbf{\Sigma}$ is Hermitian positive definite, c is a real scalar, and $\mathbf{g}(f_0)$ is a steering vector corresponding to the frequency f_0, which can be interpreted as either a spatial or temporal frequency. Additionally, we assume that the matrix and steering vector have Toeplitz and and Vandermonde structure, respectively.

The filter $\mathbf{w}$ can be interpreted as a $(J-1)$-degree polynomial in the complex z-domain after applying the forward z-transform,

$$W(z) = w(0) + w(1)z^{-1} + \ldots + w(J-1)z^{-(J-1)} \tag{2.4}$$

where $w(i)$ represents the i-th element of the filter $\mathbf{w}$. The matrix $\mathbf{\Sigma}$ is assumed to be positive definite with Hermitian Toeplitz structure. Due to the definiteness of the matrix, the optimization in (2.1) has a unique optimum given in (2.2).

Theorem 1. *$W(z)$ has $J-1$ unit circle roots.*

Proof. Caratheòdory's theorem states that if $\mathbf{\Sigma}$ is a positive semi-definite, Toeplitz matrix, with rank $r < J$ then there exists a unique decomposition for $\mathbf{\Sigma}$ consisting of a matrix

$\mathbf{G} \in \mathbb{C}^{J\times r}$ and a diagonal matrix $\mathbf{D} \in \mathbb{C}^{r\times r}$ such that [14],

$$\mathbf{\Sigma} = \mathbf{G}\mathbf{D}\mathbf{G}^H = \sum_{i=1}^{r} d_i \mathbf{g}\left(f_i\right)\mathbf{g}^H\left(f_i\right). \tag{2.5}$$

$\mathbf{G} = \left[\mathbf{g}\left(f_1\right), \ldots, \mathbf{g}\left(f_r\right)\right]$ is a Vandermonde matrix with columns consisting of r Vandermonde vectors. The $f_i \in (-0.5, 0.5)$ are distinct for $i = 1, \ldots, r,\ f_i \neq f_j,\ i \neq j$ while $\mathbf{D} = \operatorname{diag}\{d_0, d_1, \ldots, d_r\}$ is a diagonal matrix with $d_i > 0, \forall i$.

If the matrix $\mathbf{\Sigma}$ is full rank the decomposition in (2.5) exists but is no longer unique [112]. We now proceed by assuming that $\mathbf{\Sigma}$ is full rank in (2.5). Due to the non-uniqueness of the decomposition in (2.5) we are free to include the steering vector $\mathbf{g}\left(f_0\right)$ among the columns of $\mathbf{G}$ as long as f_0 is distinct from the other f_i for $i = 1, \ldots, J$. The updated matrices are $\mathbf{G} = \left[\mathbf{g}\left(f_0\right), \ldots, \mathbf{g}\left(f_{J-1}\right)\right]$, $\mathbf{D} = \operatorname{diag}\{d_0, d_1, \ldots, d_{J-1}\}$, and the decomposition now becomes

$$\mathbf{\Sigma} = \sum_{i=0}^{J-1} d_i \mathbf{g}\left(f_i\right)\mathbf{g}^H\left(f_i\right). \tag{2.6}$$

Since it is assumed that each of the f_i is distinct, the columns of the $\mathbf{G}$ are linearly independent and span the J-dimensional column space.

Left multiplying (2.2) by (2.6) yields,

$$\mathbf{\Sigma}\mathbf{w}_{\text{opt}} = d_0 \mathbf{g}\left(f_0\right)\left(\mathbf{g}^H\left(f_0\right)\mathbf{w}_{\text{opt}}\right) + \sum_{i=1}^{J-1} d_i \mathbf{g}\left(f_i\right)\left(\mathbf{g}^H\left(f_i\right)\mathbf{w}_{\text{opt}}\right) = c\frac{\mathbf{g}\left(f_0\right)}{\mathbf{g}^H\left(f_0\right)\mathbf{\Sigma}^{-1}\mathbf{g}\left(f_0\right)}. \tag{2.7}$$

Using the linear constraint in (2.1) and aggregating like terms produces,

$$c\Big(d_0 \quad - \quad \frac{1}{\mathbf{g}^H\left(f_0\right)\boldsymbol{\Sigma}^{-1}\mathbf{g}\left(f_0\right)}\Big)\mathbf{g}\left(f_0\right) \quad + \quad \sum_{i=1}^{J-1} d_i \mathbf{g}\left(f_i\right)\left(\mathbf{g}^H\left(f_i\right)\mathbf{w}_{\text{opt}}\right) \quad = \quad \mathbf{0} \tag{2.8}$$

where $\mathbf{0}$ is the $J \times 1$ zero vector and the parenthetical terms on the left-hand side of (2.8) are constants. Let $\boldsymbol{\beta}$ be a $J \times 1$ vector with

$$\boldsymbol{\beta}(0) = c\left(d_0 - \frac{1}{\mathbf{g}^H\left(f_0\right)\boldsymbol{\Sigma}^{-1}\mathbf{g}\left(f_0\right)}\right) \tag{2.9}$$

as the first element and $\boldsymbol{\beta}(i) = d_i \mathbf{g}^H\left(f_i\right)\mathbf{w}_{\text{opt}}$ for $i = 1, \ldots, J-1$ as the remaining elements. Equation (2.8) can now be written compactly as,

$$\mathbf{G}\boldsymbol{\beta} = \mathbf{0}. \tag{2.10}$$

Since the columns of $\mathbf{G}$ are linearly independent and $\mathbf{G}$ is full-rank, $\operatorname{null}\left(\mathbf{G}\right) = \varnothing$ and therefore, $\boldsymbol{\beta} = \mathbf{0}$,

$$d_0 = \frac{1}{\mathbf{g}^H\left(f_0\right)\boldsymbol{\Sigma}^{-1}\mathbf{g}\left(f_0\right)}, \tag{2.11}$$

and $\mathbf{g}^H\left(f_i\right)\mathbf{w}_{\text{opt}} = 0$ for all $i = 1, \ldots, J-1$.

The quantity $\mathbf{g}^H\left(f_i\right)\mathbf{w}_{\text{opt}}$ is equivalent to evaluating (2.4) on the unit circle at $z = e^{j2\pi f_i}$ and therefore, $z^{-1} = e^{-j2\pi f_i}$, $i = 1, \ldots, J-1$ are the $J-1$ unit circle roots of $W(z)$. □

As a consequence of Theorem 1, we may also prove the following claim.

Corollary 1. $d_j = \left(\mathbf{g}^H\left(f_j\right)\boldsymbol{\Sigma}^{-1}\mathbf{g}\left(f_j\right)\right)^{-1}$ *for* $j = 0, 1, \ldots, J-1$.

Proof. The case for d_0 has already been shown, so without loss of generality, we will consider the case for d_j, $j = 1, \ldots, J-1$. Left multiplying the matrix-vector product $\mathbf{\Sigma}^{-1}\mathbf{g}(f_j)$ by $\mathbf{\Sigma}$ and using (2.6) to expand

$$\mathbf{\Sigma}\Big(\mathbf{\Sigma}^{-1}\mathbf{g}(f_j)\Big) = \sum_{i=0}^{J-1} d_i \mathbf{g}(f_i)\left(\mathbf{g}^H(f_i)\,\mathbf{\Sigma}^{-1}\mathbf{g}(f_j)\right) = \mathbf{g}(f_j)\,. \tag{2.12}$$

By the same linear independence argument from the proof of Theorem 1, it must be the case that every parenthetical $i \neq j$ term within the summation must be identically zero. Hence, we are left with the following equality,

$$d_j(\mathbf{g}^H(f_j)\,\mathbf{\Sigma}^{-1}\mathbf{g}(f_j)) = 1 \tag{2.13}$$

which leads to

$$d_j = \frac{1}{\mathbf{g}^H(f_j)\,\mathbf{\Sigma}^{-1}\mathbf{g}(f_j)} \tag{2.14}$$

for $j = 1, \ldots, J-1$. □

2.4 Conclusion

Theorem 1 establishes the theoretical necessity of unit circle roots for any filter of the form of (2.2), assuming that $\mathbf{\Sigma}$ and $\mathbf{g}(f_0)$ have Toeplitz and Vandermonde structure, respectively. Such structures typically arise when the data are uniformly sampled such as for beamforming with uniform linear arrays [85, 86] or using symmetrically spaced pulse trains for moving target detection [94].

However, Theorem 1 does not provide a means to enforce the unit circle roots property, and in the proceeding chapters we develop the unit circle roots constrained (UCRC) algorithm to bridge this gap between theory and implementation. By exploiting polynomial symmetry, it will be shown that unit circle roots can be imposed in a practical way by manipulating the optimization in (2.1).

Possible applications beyond the AMF and beamforming include bi-static or distributed multiple-input multiple-output (MIMO) radar networks [106, 95]. Additionally, detectors such as the normalized adaptive matched filter (NAMF) [19] (or ACE [81]) are proportional to the AMF, and can benefit from imposing unit circle roots on the respective filter polynomials. Joint domain applications, such as space-time adaptive processing (STAP) [66], may also benefit by exploiting the unit circle roots property in either the spatial or temporal domains.

Unit Circle Roots Constrained MVDR Beamformer Design for Uniform Linear Arrays

3.1 Introduction

Beamforming is ubiquitous in the field of coherent signal processing with specific applications in the fields of radar [113], sonar[96], space-time adaptive processing (STAP) [97, 66], audio signal processing [4], and radio astronomy [57]. Beamforming is applied in the context of array signal processing to exploit the structure of the received signals (*e.g.* narrowband sources) and geometry of the array (*e.g.* uniform linear array) to achieve a coherent processing gain greater than that achievable when using a single receiver. The purpose of beamforming is to isolate a signal of interest (SOI) from a known direction of arrival (DOA) while simultaneously suppressing interference and noise due to other mechanisms (*i.e.* jamming or environmental effects).

The beamformer can be designed using a variety of criterion, and the seminal work on Minimum-Variance Distortionless Response (MVDR) by Capon [13] in the late 1960's largely forms the basis for much of the theoretical and practical development in sensor array signal processing (SASP) over the past five decades. As such, MVDR and related extensions remain the backbone of many SASP algorithms and applications.

Although it has received scant attention in the field, an important theoretical property on the roots of the classical Capon-MVDR beamformer was developed relatively recently in a brief note by Steinhardt et al [97]. For the case of a uniform linear array (ULA) receiving narrowband planewave sources, it was proven that the roots of the MVDR array polynomial computed using the true covariance matrix ideally fall on the unit circle. The interested reader is referred to the appendices of [97] and [102] for detailed derivation of the proof of this claim. To the best of our knowledge, except for an ad-hoc approach [102] in a specific sonar application, no other existing SASP technique has exploited Steinhardt's important and theoretically fundamental contribution to the theory of array polynomials that occur throughout the SASP field. Algorithmic enforcement of this key property for ideal ULAs by optimizing the MVDR criterion forms the basis for the work presented in this chapter. Although Steinhardt's unit-circle proof uses Weiner-Khinchin theorem which requires the Hermitian Toeplitz property of the ideal covariance matrix, the proposed algorithm achieves the desired unit-circle roots using the sample covariance matrix (SCM) even though SCM does not possess Toeplitz structure.

The MVDR requires knowledge of the interference plus noise covariance matrix which is not known in practice and must be estimated from secondary observations. The conventional approach is to use the sample covariance matrix (SCM) which results in the well-known sample matrix inversion [74] (SMI) MVDR beamformer. While simple to compute, the SMI has several undesirable properties - most notably poor performance when the number of secondary snapshots used to estimate the SCM is low. Furthermore, array polynomials estimated with the noisy SCM do not possess unit circle roots, *i.e.* zeros on the unit-circle.

A recent unit circle MVDR (UC-MVDR) approach [102] radially moved the SMI roots to the unit circle. In addition, any SMI root located inside the mainbeam was moved to the edges of the mainbeam in order to avoid mainbeam source attenuation. The combined effect of these two modifications was shown to attain improved output signal-to-interference-plus-noise ratio (SINR) and lower sidelobes over the conventional SMI beamformer. In [78], UC-MVDR was further extended in the snapshot deficient case using diagonal loading (DL). Despite these desirable attributes, the radial projection approach used in [102, 78, 101] may be considered ad-hoc or sub-optimal because it does not strictly adhere to the minimum variance criterion specified by Capon [13].

There has been extensive research on roots of polynomials in the mathematical literature, and the necessary and sufficient conditions to guarantee unit-circle roots have been developed in [65]. Specifically, two constraints must be satisfied for a polynomial to have unit circle roots: the polynomial coefficients must exhibit conjugate symmetry and the roots of the derivative polynomial must lie on or inside the unit circle. The conjugate symmetry constraint was utilized in [89, 54, 11, 87, 55] for maximum-likelihood estimation (MLE) of frequencies and Directions of Arrival (DOA) of narrowband sources to produce UC roots. However, reciprocal roots occurred at low signal-to-noise ratio (SNR) as the second condition was not enforced [89].

It was observed in [89] that for a first-order polynomial, conjugate symmetry is sufficient to guarantee a UC root because the derivative is a scalar. Based on this fact, a UC constrained MLE solution was presented in [89] that uses polynomial factorization in the z-domain. Specifically, *if* the initial MLE optimization produced any non-UC roots, then the MLE was further optimized *w.r.t.* individual first-order factors to algorithmically place each root on the unit circle. This resulted in resolving closely spaced frequencies or DOAs that produced merged roots at low SNR. A similar factorization of the MVDR polynomial into 1st-order factors with conjugate-symmetric coefficients will be used in this work to constrain *all the MVDR polynomial roots* to the unit circle. It should be noted here that the MLE approach reported in [89] and the proposed MVDR solution address distinct optimization problems with entirely different objectives. Specifically, the MLE in [89] does not offer any mechanism to minimize the variance of the signal at the output of a beamformer. Also, unlike MVDR, the MLE cannot control the array look angle as it does not impose a linearity constraint within its optimization. Accordingly, the MLE is not used for estimating interference and noise components in this work as it is not appropriate in the MVDR optimization context. The proposed approach adaptively estimates the unknown interference angles, and the corresponding zeros of the MVDR polynomial are typically placed on the unit-circle very close to the interference angles helping suppress or attenuate the interference. The other unit-circle zeros are also adaptively determined by optimizing the MVDR criterion to attenuate noise at non-interference regions, improving the overall output SINR.

The primary motivation of this work is to reformulate MVDR to guarantee UC roots during theoretical development and in practical implementations. The overall objective is to attain performance improvement by addressing a significant gap that appears to have remained in MVDR-based algorithm development. The focus of this chapter is designing beamformers that satisfy MVDR criteria while simultaneously enforcing UC roots constraint on the array polynomial, satisfying the theoretical property established in [97]. This work will leverage the concept presented in [89] to update any SMI-based root that is not on the unit-circle, while minimizing the variance. Unlike the work in [89], MVDR's linearity constraint on the weight vector will also need to be imposed at every step of optimization. Accordingly, a new derivation of unit-circle constrained Capon beamformer is presented. The mainbeam protection approach of [102] will be incorporated to ensure the corrected roots do not appear within the mainbeam region.

To the best of our knowledge, there has not been any systematic attempt to incorporate UC roots constraints during optimization of the MVDR-beamformer polynomial coefficients to take full advantage of the theoretically fundamental and practically impactful property derived in [97]. Notably, the ad-hoc approach of [102], [78] and [101] enforces UC roots without minimizing the output variance, as required by MVDR. Therefore, the proposed UCRC-MVDR approach constitutes a novel contribution to the field of array signal processing that may be beneficial in potentially vast applications where Capon's MVDR beamformer is routinely used in practice.

From a historical perspective, the proposed algorithm that splits the multi-parameter MVDR optimization problem into multiple independent first-order problems, belongs to a class of algorithms where individual parameters are estimated independently while complying with the underlying optimization criterion. Such algorithms have appeared in the past in astronomy for aperture synthesis [43], high-resolution frequency and DOA estimation [89], [88], [117], [34], [59], and chirp parameter estimation using Compressive Sensing [44], among many others.

This work essentially treats the ULA based MVDR beamformer weights as a special class of FIR filters with all its roots, i.e., zeros located on the unit-circle. A key feature of the proposed MVDR approach is that it has the in-built capability to adaptively estimate the interference angles and place zeros on the unit-circle near the interference angles in an attempt to suppress the interference without requiring any additional zero-forcing mechanism. The unknown zero locations on the unit-circle are adaptively and algorithmically determined by minimizing the output variance at every step via constrained optimization. The proposed MVDR beamformer with unit circle roots are shown to exhibit lower sidelobes and deeper nulls than traditional SMI-based MVDR weights which typically do not possess any unit circle roots. Since the resulting MVDR FIR filters are conjugate-symmetric by design, they possess certain desirable properties such as linear phase with constant group-delay.

The superior performance of the proposed UC-roots based approach is demonstrated using a variety of simulation experiments. Specifically, the performance of the proposed beamformer is compared against the ad-hoc unit circle method of [102] as well as several existing techniques. It is shown that the proposed approach produces UC roots that exhibit lower sidelobes than the beamformer of [102]. The output SINR versus input SNR will be used to demonstrate the improved gain and robust performance of the proposed method when SOI is present in the snapshots used to estimate the covariance matrix. Additional simulations examples demonstrate the robust performance of the proposed approach in the presence of coherent as well as spatially distributed interference sources. Simulation studies further show that the proposed approach results in lower output variance as each root is corrected, resulting in a higher output SINR over the beamformer of [102]. Furthermore, the proposed beamformer exhibits improved performance in the snapshot limited scenario when diagonal loading is used to regularize the covariance matrix to avoid numerical difficulties when inverting the SCM. Distribution analysis will show that the proposed approach performs closer to the optimum than existing methods, including the unit circle approach of [102]. Finally, it will be demonstrated that the proposed beamformer has the same order of computational complexity as SMI, and it achieves superior performance at a smaller aperture size than that attainable by the method of [102], or the conventional approaches.

The remainder of this chapter is organized as follows. In Section 3.2, the MVDR beamforming problem is stated, and conventional SMI approach is discussed. In Section 3.3, the proposed UCRC-MVDR beamformer is derived. Section 3.4 contains simulation results and related discussion. Finally, Section 3.5 summarizes conclusions and possible future work.

3.2 The MVDR Beamformer

Consider a uniform linear array (ULA) of $N_s = N + 1$ sensors, where N is the number of array polynomial roots, each separated by a distance d. The vector of narrowband data at the array input can be expressed as,

$$\mathbf{x} = \underbrace{\beta_0 \mathbf{v}\left(\theta_0\right)}_{\text{SOI}} + \underbrace{\sum_{i=1}^{M} \beta_i \mathbf{v}\left(\theta_i\right) + \mathbf{n}}_{\text{Interference + noise}} \in \mathbb{C}^{N_s \times 1} \tag{3.1}$$

where β_0 is the unknown amplitude of the SOI with variance σ_0^2, θ_0 is the DOA of the SOI, θ_i and $\beta_i,\ i = 1, \ldots, M$ denote the unknown DOAs and coefficients, respectively, of the i-th interference signals, $\mathbf{n} \sim \mathbb{C}N(\mathbf{0}, \sigma_n^2\mathbf{I})$ is spatially white Gaussian noise with zero mean and variance σ_n^2, and $\mathbf{v}\left(\theta_0\right)$ and $\mathbf{v}\left(\theta_i\right)$ are the steering vectors of the SOI and the i-th interference, respectively. The coefficients $\beta_i,\ i = 1, \ldots, M$ are assumed to be zero-mean complex-Gaussian scalars with variances $\sigma_i^2,\ i = 1, \ldots, M$.

In equation (3.1), The steering vector associated with an arbitrary direction θ is defined as [1]:

$$\mathbf{v}(\theta) = \left[1 \;\; e^{j\frac{2\pi d}{\lambda}\sin(\theta)} \;\; \ldots \;\; e^{j\frac{2\pi d}{\lambda}\sin(\theta)(N)}\right]^T \in \mathbb{C}^{N_s \times 1} \tag{3.2}$$

where $(\cdot)^T$ represents the transpose operation and λ is the operating wavelength of the array.

From equation (3.1), the interference pulse noise term is expressed as

$$\mathbf{x}_{i+n} = \sum_{i=1}^{M} \beta_i \mathbf{v}\left(\theta_i\right) + \mathbf{n} \in \mathbb{C}^{N_s \times 1}, \tag{3.3}$$

and the corresponding interference plus noise covariance matrix is given by

$$\begin{aligned} \mathbf{\Sigma} &= E\left\{\mathbf{x}_{i+n}\mathbf{x}_{i+n}^H\right\} \in \mathbb{C}^{N_s \times N_s} \\ &= \sum_{m=1}^{M} \sigma_i^2 \mathbf{v}\left(\theta_m\right)\mathbf{v}^H\left(\theta_m\right) + \sigma_n^2\mathbf{I}, \end{aligned} \tag{3.4}$$

where $E\{\,\cdot\,\}$ is the expectation operation.

The purpose of beamforming is to design a filter $\mathbf{w}$, to extract the desired SOI from angle θ_0 while maximally suppressing interference and noise. The beamformer output is

$$y = \mathbf{w}^H \mathbf{x} \tag{3.5}$$

where $(\cdot)^H$ represents conjugate-transpose. It is typical to design the beamformer weight vector $\mathbf{w}$ to minimize the distortion in the direction of the SOI while minimizing the variance at the beamformer output. This is the well-known minimum-variance distortionless response beamforming problem [13],

$$\min_{\mathbf{w}} \ \mathbf{w}^H \boldsymbol{\Sigma} \mathbf{w} \quad \text{s.t. } \mathbf{w}^H \mathbf{v}(\theta_0) = 1. \tag{3.6}$$

The solution to equation (3.6) is the well-known MVDR beamformer and can be expressed in closed form, that is

$$\mathbf{w}_{\text{opt}} = \frac{\boldsymbol{\Sigma}^{-1}\mathbf{v}(\theta_0)}{\mathbf{v}^H(\theta_0)\boldsymbol{\Sigma}^{-1}\mathbf{v}(\theta_0)} \in \mathbb{C}^{N_s \times 1}. \tag{3.7}$$

Equation (3.7) will hereafter be referred to as the clairvoyant, or optimal, beamformer as it assumes perfect knowledge of the data covariance matrix.

The non-adaptive counterpart of the clairvoyant beamformer in equation (3.7) can be found by assuming the interference and noise are spatially white resulting in the conventional beamformer (CBF) [51],

$$\mathbf{w}_{\text{CBF}} = \frac{\mathbf{v}\left(\theta_0\right)}{N_s} \in \mathbb{C}^{N_s \times 1}. \tag{3.8}$$

Figure 3.1 shows the magnitude response of the CBF and clairvoyant beamformers for array size $N_s = 11$ in the presence of one interference at angle $\theta_1 = 16^\circ \approx \sin^{-1}(3/N_s)$ (*i.e.*, the location of the first sidelobe maximum) with $\text{INR} = 40$ dB. A deep null in the clairvoyant response illustrates the advantage of the adaptive approach to suppress interference if prior knowledge about noise and interference is available. Furthermore, Figure 3.1 illustrates that when strong interference is present near the first sidelobe maximum of the CBF, the optimal adaptive beamformer places a null near this direction to reduce the overall interference and noise power at the expense of increasing the sidelobe level in other locations.

In practice however, the covariance matrix $\mathbf{\Sigma}$ is unknown and is replaced by the sample covariance matrix (SCM) which is computed from a set of secondary snapshots,

$$\hat{\mathbf{\Sigma}} = \frac{1}{L} \sum_{j=1}^{L} \mathbf{x}_j \mathbf{x}_j^H \tag{3.9}$$

where $\mathbf{x}_j$ is the j-th secondary snapshot, and L is the number of secondary snapshots available. The resulting weight vector which satisfies equation (3.6) is known as the sample matrix inversion (SMI) beamformer,

$$\mathbf{w}_{\mathrm{SMI}} = \frac{\hat{\mathbf{\Sigma}}^{-1} \mathbf{v}(\theta_0)}{\mathbf{v}^H(\theta_0) \hat{\mathbf{\Sigma}}^{-1} \mathbf{v}(\theta_0)} \in \mathbb{C}^{N_s \times 1}. \tag{3.10}$$

While the beamformer in equation (3.10) is functional, it is limited by the fidelity of the covariance matrix estimate which is known to be poor when the secondary data are limited [74]. Additionally, the polynomial induced by the beamformer weights in equation (3.10) rarely satisfies the unit circle constraint [97, 102, 101] discussed in the next section, and thus, additional structure is needed to design a beamformer which both satisfies the optimization in equation (3.6) and also has unit circle roots.

3.2.1 Conditions for Unit Circle Roots

The weights of the beamformer $\mathbf{w}$ can be interpreted as the coefficients of a polynomial in the complex z-domain [83],

$$W(z) = w(0) + \ldots + w(N) z^{-N} = \mathcal{Z}\{w\} \tag{3.11}$$

where $w(i)$ is the i-th element of the beamformer weight vector $\mathbf{w}$ and $\mathcal{Z}\{\cdot\}$ represents the z-transform operation.

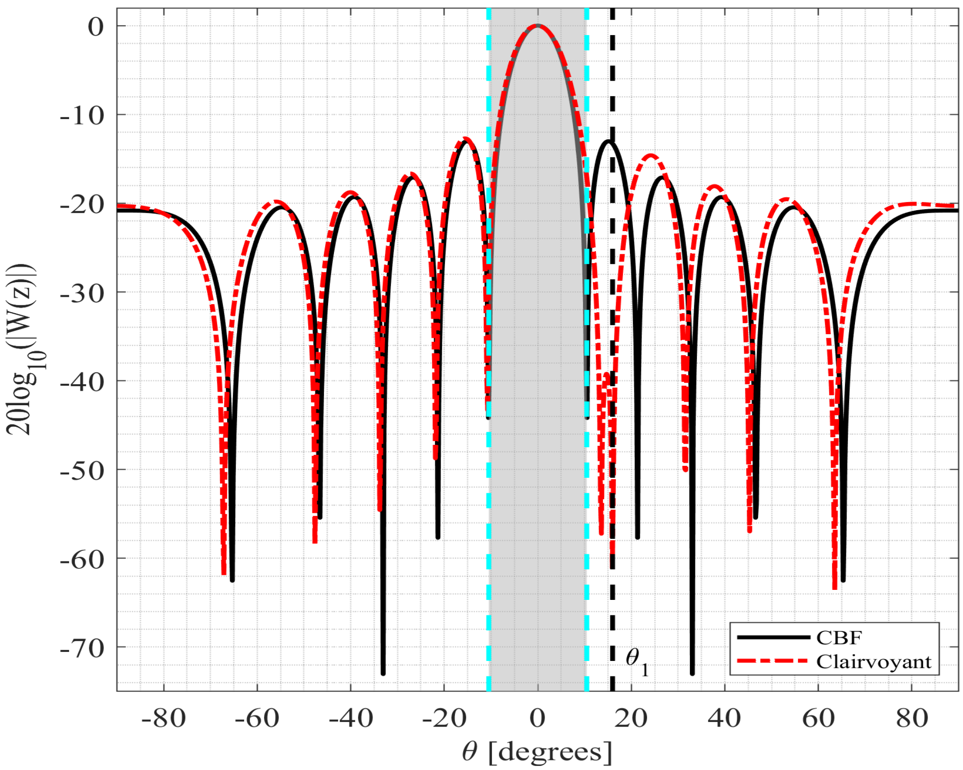

Figure 3.1: Magnitude response of the CBF and clairvoyant beamformers.

It is important to emphasize here that it has been proven theoretically in [97] that if $W(z)$ is formed using the true $\mathbf{w}$-vector computed using known $\mathbf{\Sigma}$ matrix in equation (3.7) then its roots lie upon the unit circle. However, in practice, $W(z)$ is formed using $\mathbf{w}_{\mathrm{SMI}}$ in equation (3.10) and the UC-roots property is lost, causing the conventional MVDR to perform poorly. The overall objective of this work is to derive optimal $\mathbf{w}_{\mathrm{UCRC-MVDR}}$ that minimizes variance while constraining the roots of $W(z)$ to be on the unit circle, satisfying the fundamental property proven in [97].

The two conditions that must be satisfied for a polynomial to have UC roots were developed in the mathematical literature [65], and were later invoked for maximum-likelihood estimation of frequencies and DOAs in [89, 54, 55]:

C1: The coefficients exhibit conjugate symmetry

$$w(k) = w^*(N-k) \ \text{ for } k = 0, \ldots, N \tag{3.12}$$

and

$\mathbf{C}2$: For $N > 1$, the derivative of $W(z)$, the polynomial with coefficients $\mathbf{w}$, must have roots either on or inside the unit circle.

As stated in [89, 54, 55], imposing $\mathbf{C}2$ requires non-linear optimization that may be impractical. It was argued in [89] that if $N = 1$, *i.e.*, the derivative in $\mathbf{C}2$ is a scalar, $\mathbf{C}2$ is inconsequential. Therefore, satisfying $\mathbf{C}1$ is sufficient to guarantee a unit circle root if the polynomial is order one. Accordingly, in [89] the MLE optimization problem was reformulated and split into multiple 1st-order MLE optimization problems to ensure unit circle roots in each case. An equivalent tactic will be used for the MVDR optimization problem to guarantee unit-circle roots, as described next.

3.3 Unit Circle Roots Constrained MVDR Beamformer

In designing the Unit Circle Roots Constrained MVDR (UCRC-MVDR) beamformer, the N-th order MVDR polynomial is factored into N 1st-order factors to split the MVDR criterion into multiple 1-st order optimization problems. Conjugate-symmetry is incorporated in defining the MVDR polynomial and the individual 1-st order factors to satisfy $\mathbf{C}1$ in equation (3.12). The reformulated MVDR criterion is then optimized to determine the coefficients of individual complex-conjugate 1st-order factors, yielding UC roots. The SMI-based MVDR solution in equation (3.10) is used as the starting point and individual 1st-order factors with UC roots are optimized independently under MVDR.

3.3.1 UCRC-MVDR Design with Conjugate Symmetry

Applying the conjugate symmetry conditions of equation (3.12) to the array polynomial in equation (3.11),

$$W(z) = w(0) + w(1)z^{-1} + \ldots + w^*(1)z^{-(N-1)} + w^*(0)z^{-N}. \tag{3.13}$$

In this form, the roots of $W(z)$ are either on the unit circle or they appear in reciprocal pairs. However, equation (3.13) can be further rewritten in factored conjugate-symmetric form as,

$$\begin{aligned} W(z) &= (w_1 - w_1^* z^{-1})(w_2 - w_2^* z^{-1}) \ldots (w_N - w_N^* z^{-1}) \\ &= \prod_{i=1}^{N} (w_i - w_i^* z^{-1}) = w(0) \prod_{i=1}^{N} (1 - \zeta_i z^{-1}), \end{aligned} \tag{3.14}$$

where $\zeta_i = \frac{w_i^*}{w_i}$ are the roots of $W(z)$ and $w(0) = \prod_{i=1}^{N} w_i$. Several interesting observations regarding the factored form of $W(z)$ in equation (3.14) are in order. Firstly, the product of conjugate-symmetric 1st-order factors is also conjugate symmetric, satisfying the necessary condition $\mathbf{C}1$ stipulated in equation (3.12). Secondly, the roots of each 1st-order conjugate-symmetric factor are located on the unit circle. Therefore, estimating the coefficients of the individual 1st-order conjugate symmetric factors, $(w_i - w_i^* z^{-1})$ for $1 \leq i \leq N$, while minimizing the output variance under the linear constraint in equation (3.6) will yield the desired unit circle roots of $W(z)$ under MVDR, as called for in [97].

3.3.2 Splitting the Multidimensional MVDR Problem into Multiple 1-D MVDR Optimization Problems

In order to impose the conjugate symmetry constraints on the first order factors, the proposed approach splits the N-th order MVDR problem stated in equation (3.6) into N independent 1st-order MVDR problems. The derivation for optimizing the MVDR criterion w.r.t. individual 1st-order factors is described next.

Rewriting $W(z)$ in equation (3.11) in factored form [89],

$$W_{(i)}(z) = W_{N-(i)}(z)w_i(z);\ 1 \leq i \leq N \tag{3.15}$$

where $w_i(z) = w_i - w_i^* z^{-1}$ and $W_{N-(i)}(z)$ is a $(N-1)$-th order polynomial formed with $N-1$ roots excluding the i-th root. $w_i(z)$ represents the i-th first-order factor whose root needs to be placed on the unit-circle. The factored weight vector corresponding to $W_{(i)}(z)$ in equation (3.15) can be written as a convolution matrix-vector product [89],

$$\mathbf{w}_{(i)} = \mathbf{W}_{N-(i)}\mathbf{w}_i; \quad 1 \leq i \leq N \tag{3.16}$$

where $\mathbf{w}_i = [w_i \quad w_i^*]^T \in \mathbb{C}^{2\times1}$.

The columns of the convolution matrix,

$$\mathbf{W}_{N-(i)} = \begin{bmatrix} w_{N-(i)}(0) & 0 \\ w_{N-(i)}(1) & w_{N-(i)}(0) \\ w_{N-(i)}(2) & w_{N-(i)}(1) \\ \dots & \dots \\ w_{N-(i)}(N-1) & w_{N-(i)}(N-2) \\ 0 & w_{N-(i)}(N-1) \end{bmatrix} \in \mathbb{C}^{N_s\times2} \tag{3.17}$$

consist of the coefficients of $W_{N-(i)}(z)$. Using this factorization in equation (3.16), the reformulated 1st-order MVDR optimization problems can be re-written as,

$$\begin{aligned} \min_{\mathbf{w}_i} \ & \mathbf{w}_i^H \mathbf{W}_{N-(i)}^H \boldsymbol{\Sigma} \mathbf{W}_{N-(i)} \mathbf{w}_i \\ & \text{s.t. } \mathbf{w}_i^H \mathbf{W}_{N-(i)}^H \mathbf{v}\left(\theta_0\right) \ = 1; \quad 1 \leq i \leq N. \end{aligned} \tag{3.18}$$

Equation (3.18) theoretically splits the N-dimensional MVDR problem in equation (3.6) into N 1-dimensional problems. In practice, the true $\boldsymbol{\Sigma}$'s and $\mathbf{W}_{N-(i)}$'s are not known and are replaced by corresponding SMI-based estimates using equation (3.10) to yield,

$$\begin{aligned} \min_{\mathbf{w}_i} \ & \mathbf{w}_i^H \hat{\mathbf{W}}_{N-(i)}^H \hat{\boldsymbol{\Sigma}} \hat{\mathbf{W}}_{N-(i)} \mathbf{w}_i \\ & \text{s.t. } \mathbf{w}_i^H \hat{\mathbf{W}}_{N-(i)}^H \mathbf{v}\left(\theta_0\right) \ = 1; \quad 1 \leq i \leq N \end{aligned} \tag{3.19}$$

where this optimization is performed N times to place individual SMI-based MVDR roots onto the unit circle.

Optimizing equation (3.19) with conjugate symmetric $\mathbf{w}_i$'s will guarantee unit-circle root in each case, satisfying the theoretical MVDR property proven in [97]. The key advantage of estimating the complex-conjugate coefficients of individual factors is that the derivative of a first order polynomial is a constant, bypassing the need for imposing the derivative constraint in $\mathbf{C}2$.

Splitting a multi-dimensional optimization problem into multiple independent first-order problems have appeared in literature before. See [89], [43], [88], [117], [34], [59] and [44], among many others.

Algorithm 1: UCRC-MVDR

INPUT: $\mathbf{x}_1, \ldots, \mathbf{x}_L$, $\mathbf{v}(\theta_0)$, $u_0 = \sin(\theta_0)$

<u>*start*</u>: $\mathbf{w}_{\text{SMI}} = \frac{\hat{\boldsymbol{\Sigma}}^{-1}\mathbf{v}(\theta_0)}{\mathbf{v}^H(\theta_0)\hat{\boldsymbol{\Sigma}}^{-1}\mathbf{v}(\theta_0)}, \quad \hat{\boldsymbol{\Sigma}} = \frac{1}{L}\sum_{i=1}^{L}\mathbf{x}_i\mathbf{x}_i^H$

$\boldsymbol{\zeta}^{\text{SMI}} \leftarrow \text{roots}\{\mathcal{Z}\{\mathbf{w}_{\text{SMI}}\}\}$ ▷ I

$i = 1$ **up to** $i = N$

  $W_{N-(i)}^{\text{SMI}}(z) = \prod_{j \neq i}(1 - \zeta_j^{\text{SMI}} z^{-1})$

  $\boldsymbol{\Sigma}_i^C = \mathbf{C}^H \mathbf{W}_{N-(i)}^H \hat{\boldsymbol{\Sigma}} \mathbf{W}_{N-(i)} \mathbf{C}$ ▷ II

  $\tilde{\mathbf{v}}_i(\theta_0) = \mathbf{C}^H \mathbf{W}_{N-(i)}^H \mathbf{v}(\theta_0)$ ▷ III

  $\hat{\mathbf{w}}_i = \frac{\mathbf{C}\text{Re}\left(\boldsymbol{\Sigma}_i^C\right)^{-1}\tilde{\mathbf{v}}_i(\theta_0)}{\tilde{\mathbf{v}}_i^T(\theta_0)\text{Re}\left(\boldsymbol{\Sigma}_i^C\right)^{-1}\tilde{\mathbf{v}}_i(\theta_0)}$ ▷ IV

  $\hat{\zeta}_i = \frac{\hat{w}_i^*}{\hat{w}_i}$

  if $|\hat{\omega}_i - \pi u_0| < 2\pi/(N_s)$ **then**

    $\hat{\zeta}_i = e^{j(\pi u_0 + \text{sgn}\{\hat{\omega}_i - \pi u_0\}(2\pi/(N_s)))}$ ▷ $= e^{j\hat{\omega}_i}$

    $\hat{w}_i = e^{-j\hat{\omega}_i/2}$

    $(\hat{w}_i - \hat{w}_i^* z^{-1}) = \frac{(\hat{w}_i - \hat{w}_i^* z^{-1})}{(\hat{w}_i - \hat{w}_i^* e^{-j\theta_0})}$

  end

end

OUTPUT:

$$\hat{W}_{\text{UCRC-MVDR}}(z) = \prod_{i=1}^{N}(\hat{w}_i - \hat{w}_i^* z^{-1}) \rightarrow \hat{\mathbf{w}}_{\text{UCRC-MVDR}}$$

3.3.3 Imposing Complex Conjugate Constraints on 1-D MVDR Optimization Problems

The conjugate symmetry of $\mathbf{w}_i$ is ensured by rewriting $\mathbf{w}_i$ mathematically as a matrix-vector product [89],

$$\mathbf{w}_i = \begin{bmatrix} 1 & j \\ 1 & -j \end{bmatrix} \begin{bmatrix} \text{Real}[w_i] \\ \text{Imag}[w_i] \end{bmatrix} \triangleq \mathbf{C}\mathbf{w}_i^r; \quad 1 \leq i \leq N \tag{3.20}$$

where $\mathbf{C} \in \mathbb{C}^{2\times 2}$ is a constant matrix and $\mathbf{w}_i^r \in \mathbb{R}^{2\times 1}$ is a real vector. Using equation (3.20) in equation (3.19) results in,

$$\min_{\mathbf{w}_i^r} \; \mathbf{w}_i^{rT} \boldsymbol{\Sigma}_i^C \mathbf{w}_i^r \quad \text{s.t. } \mathbf{w}_i^{rT} \tilde{\mathbf{v}}_i(\theta_0) = 1; \quad 1 \le i \le N \tag{3.21}$$

where $\boldsymbol{\Sigma}_i^C = \mathbf{C}^H \hat{\mathbf{W}}_{N-(i)}^H \hat{\boldsymbol{\Sigma}} \hat{\mathbf{W}}_{N-(i)} \mathbf{C} \in \mathbb{C}^{2\times 2}$ and $\tilde{\mathbf{v}}_i(\theta_0) = \mathbf{C}^H \hat{\mathbf{W}}_{N-(i)}^H \mathbf{v}(\theta_0) \in \mathbb{C}^{2\times 1}$ are the transformed covariance matrix and look direction vector, respectively. The solution to this structured optimization can be found using Lagrange multipliers where,

$$\mathcal{L}(\mathbf{w}_i^r) = \mathbf{w}_i^{rT} \boldsymbol{\Sigma}_i^C \mathbf{w}_i^r + \lambda_i \left(\mathbf{w}_i^{rT} \tilde{\mathbf{v}}_i(\theta_0) - 1 \right); \quad 1 \le i \le N \tag{3.22}$$

is the Lagrangian and λ_i is the associated multiplier. Taking the derivative of equation (3.22) and making use of the Hermitian property of $\boldsymbol{\Sigma}_i^C$ produces,

$$\frac{\partial \mathcal{L}(\mathbf{w}_i^r)}{\partial \mathbf{w}_i^r} = 2 \operatorname{Re}\left(\boldsymbol{\Sigma}_i^C \right) \mathbf{w}_i^{rT} + \lambda_i \tilde{\mathbf{v}}_i(\theta_0) = 0; \quad 1 \le i \le N. \tag{3.23}$$

Solving for $\mathbf{w}_i^{rT}$ yields,

$$\mathbf{w}_i^r = -2\lambda_i \operatorname{Re}\left(\boldsymbol{\Sigma}_i^C \right)^{-1} \tilde{\mathbf{v}}_i(\theta_0) \in \mathbb{R}^{2\times 1}; \quad 1 \le i \le N \tag{3.24}$$

where $\operatorname{Re}(\cdot)$ represents the real part of a complex quantity. Substituting equation (3.24) into the linear constraint of equation (3.21) and solving for λ_i results in,

$$\lambda_i = \frac{-1/2}{\tilde{\mathbf{v}}_i^T(\theta_0) \operatorname{Re}\left(\boldsymbol{\Sigma}_i^C \right)^{-1} \tilde{\mathbf{v}}_i(\theta_0)}; \quad 1 \le i \le N \tag{3.25}$$

which, upon re-substituting into equation (3.24) and left multiplying by $\mathbf{C}$, yields a closed-form expression for the conjugate symmetric beamformer factors,

$$\hat{\mathbf{w}}_i = \frac{\mathbf{C}\,\mathrm{Re}\left(\mathbf{\Sigma}_i^C\right)^{-1}\tilde{\mathbf{v}}_i\left(\theta_0\right)}{\tilde{\mathbf{v}}_i^T\left(\theta_0\right)\mathrm{Re}\left(\mathbf{\Sigma}_i^C\right)^{-1}\tilde{\mathbf{v}}_i\left(\theta_0\right)} \in \mathbb{C}^{2\times 1}; \quad 1 \leq i \leq N. \tag{3.26}$$

An alternate version of this algorithm that utilizes a persymmetric version of the covariance matrix to yield a conjugate-symmetric polynomial [46], and gives equivalent results [94].

3.3.4 Preserving the Mainbeam and Linear Constraint

The unit-circle roots of the array polynomial cause nulls in the array response $|W(z)|^2$. The approach of Section 3.3.3 may produce some roots in the CBF mainbeam (*i.e.* $|\hat{\omega}_i - \pi u_0| < 2\pi/(N_s)$, where $\hat{\omega}_i = \arg\{\hat{\zeta}_i\}$ and $u_0 = \sin\left(\theta_0\right)$ is the look direction sine; see Figure 3.1). These mainbeam roots may cause beam distortion and SOI attenuation [20]. Any UC root within the mainbeam that are not part of any specific design requirements, such as 3 dB or noise bandwidth, etc., must be moved to avoid performance degradation in the resulting beamformer. Following [102], the proposed approach maintains mainbeam integrity by moving mainbeam roots to the nearest CBF mainbeam null (*i.e.* $\arg\{\hat{\zeta}_i\} = \pi u_0 + \mathrm{sgn}\{\hat{\omega}_i - \pi u_0\}(2\pi/(N_s))$, where $\mathrm{sgn}\{\cdot\}$ and $\arg\{\cdot\}$ are the sign and complex argument operations). The conjugate-symmetric weights at the CBF nulls can be found as, $\hat{w}_i(0) = e^{-j\hat{\omega}_i/2} = \hat{w}_i^*(1)$. Next, the linear constraint specified in equation (3.19) will be satisfied by normalizing the corresponding array factor as,

$$(\hat{w}_i - \hat{w}_i^* z^{-1}) = \frac{(\hat{w}_i(0) - \hat{w}_i(1)z^{-1})}{(\hat{w}_i(0) - \hat{w}_i(1)e^{-j\theta_0})} \tag{3.27}$$

where θ_0 is the look angle. Note that for a given N, the polynomial factors at the two CBF nulls can be pre-computed and stored in memory, and retrieved as needed, if any undesired root does fall within the mainbeam.

The final step of the proposed approach constructs the beamformer polynomial using the estimated 1st-order factors found using equation (3.26) and equation (3.27),

$$\hat{W}_{\mathrm{UCRC-MVDR}}(z) = \prod_{i=1}^{N} \left(\hat{w}_i - \hat{w}_i^* z^{-1}\right) \tag{3.28}$$

Finally, $\hat{\mathbf{w}}_{\mathrm{UCRC-MVDR}} = \mathcal{Z}^{-1}\{\hat{W}_{\mathrm{UCRC-MVDR}}(z)\}$ where $\mathcal{Z}^{-1}\{\cdot\}$ represents the inverse z-transform.

3.3.5 Spatial Prefiltering Interpretation of the Proposed Algorithm

Assuming ideal scenario with perfectly known $\mathbf{\Sigma}$, the MVDR optimization of equation (3.6) can be re-written using the factorization in equation (3.16) as,

$$\begin{aligned} \min_{\mathbf{w}_i} \ & \mathbf{w}_i^H \mathbf{W}_{N-(i)}^H \mathbf{\Sigma} \mathbf{W}_{N-(i)} \mathbf{w}_i \\ & \text{s.t. } \mathbf{w}_i^H \mathbf{W}_{N-(i)}^H \mathbf{v}\left(\theta_0\right) = 1; \quad 1 \leq i \leq N \end{aligned} \tag{3.29}$$

For large L, replacing $\mathbf{\Sigma}$ by equation (3.9),

$$\begin{aligned} &\mathbf{w}_i^H \mathbf{W}_{N-(i)}^H \mathbf{\Sigma} \mathbf{W}_{N-(i)} \mathbf{w}_i \\ &\qquad = \mathbf{w}_i^H \left(\frac{1}{L} \sum_{j=1}^{L} \mathbf{W}_{N-(i)}^H \mathbf{x}_j \mathbf{x}_j^H \mathbf{W}_{N-(i)} \right) \mathbf{w}_i \\ &\qquad = \mathbf{w}_i^H \left(\frac{1}{L} \sum_{j=1}^{L} \mathbf{x}_{(j)} \mathbf{x}_{(j)}^H \right) \mathbf{w}_i = \mathbf{w}_i^H \mathbf{\Sigma}_i \mathbf{w}_i; \quad 1 \leq i \leq N \end{aligned} \tag{3.30}$$

where, $\mathbf{x}_{(j)} = \mathbf{W}_{N-(i)}^H \mathbf{x}_j \in \mathbb{C}^{2\times 1}$ can be interpreted as *spatially pre-filtered* array snapshots. Assuming $\mathbf{W}_{N-(i)}$ is formed with $N-1$ known true (clairvoyant) roots, only one unknown root needs to be estimated from the pre-filtered array data $\mathbf{x}_{(j)}$ and corresponding $\mathbf{\Sigma}_i$. Equation (3.30) theoretically splits the original N-dimensional MVDR problem in equation (3.6) into N 1-dimensional problems. The key advantage of optimizing equation (3.30) is that imposing conjugate symmetry on the $\mathbf{w}_i$'s guarantees unit-circle root in each case.

In practice, however, the true roots are not known, L is finite and the observed array data is not noise-free. In that case, the $\mathbf{\Sigma}$'s and $\mathbf{x}_{(j)}$'s are replaced by their corresponding estimates. Consequently, initial roots were estimated from the traditional SCM-based MVDR roots in Algorithm 1.

3.3.6 Choice of Initial Estimates

It is recommended that the SMI beamformer in equation (3.10) be used to provide the estimated roots to initiate the proposed method, *i.e.,* in forming $\mathbf{W}_{N-(i)}$, the weight matrices in equation (3.17). It has been shown in literature that the performance of the forward-backward SMI (FB-SMI) is superior to that of the SMI-based solution, and FB-SMI based array coefficients possess conjugate-symmetry [46], [109], [115], satisfying condition $\mathbf{C}1$ for UC roots in equation (3.12). However, FB-SMI based polynomial does not guarantee UC roots and it typically produces one or more pairs of reciprocal roots, as can be observed in Figure 3.2. Accordingly, the angular locations of the FB-SMI based roots on the unit-circle may not be close to the true or optimal roots, and may cause incorrect deep nulls and higher sidelobes (See corresponding magnitude response in Figure 3.4a). On the other hand, although the SMI-based roots are not on the unit-circle they are usually more spread out around the unit-circle and their angles are closer to the clairvoyant roots, providing better initial estimates for the proposed method than FB-SMI would.

3.3.7 Implementation and Computational Complexity Issues

The individual root-updates in equation (3.26) are non-iterative, closed-form, and require 2×2 matrix inverses, the computation cost of which is relatively trivial. Also, since the coefficients in each $\hat{\mathbf{w}}_i$ are complex-conjugate of each other by design, the roots of the individual 1st-order polynomials, $\hat{w}_i(z) = \hat{w}_i - \hat{w}_i^* z^{-1}$ are guaranteed to lie on the unit circle. Then the N-th order conjugate-symmetric $\hat{W}_{\mathrm{UCRC-MVDR}}(z)$ in equation (3.28) will also have the desired UC roots that are obtained by minimizing the MVDR criterion at every step. More importantly, the UC roots property of [97] is achieved without resorting to complex iterative optimization procedure or special-purpose optimization software as would be needed if the derivative constraint in $\mathbf{C}2$ were to be optimized for the N-th order polynomial instead.

The proposed method leverages the SMI solution as its starting point, and the algorithmic steps to constrain each i-th root to lie on the unit-circle rely only on the SMI roots. The SMI roots are placed onto the unit circle in the order they are computed, and no ordering is applied when initializing Algorithm 1.

The SMI beamformer has a computational complexity on the order of $O(N_s^3)$ due to the inversion of the SCM [74]. Since the proposed approach requires computing the SMI beamformer, the same $\mathrm{O}(N_s^3)$ cost will be incurred. To constrain all of the roots to lie on the unit-circle requires an additional N matrix inversions (see step-IV and step-V in Algorithm 1, respectively). However, these matrices are of size 2×2 hence, the operations required to correct all roots is on the order of $\mathrm{O}(N)$, or linear in the number of roots. Therefore, it can be concluded that the UCRC-MVDR beamformer possesses a computational complexity on the order of the SMI at $\mathrm{O}(N_s^3)$.

Finally, in a multicore hardware-based or software-based implementation, all roots in Algorithm-1 can be rectified during concurrent clock cycles. Therefore, parallel implementation is feasible.

The Effect of Repeated Iterations

In this section, we address the effect of repeated iterations of the UCRC algorithm. For the following discussion, consider only the unit circle enforcement in Algorithm 1, and that no mainbeam preservation is enacted or signal contamination is present.

For the 0-th iteration, we apply the UCRC algorithm using the roots of the SMI beamformer, and use the unit circle roots at the output to reconstruct the covariance matrix using (2.6) from Chapter 2,

$$\tilde{\boldsymbol{\Sigma}} = \sum_{i=0}^{N_s-1} \hat{d}_i \mathbf{v}\left(\tilde{f}_i\right) \mathbf{v}^H\left(\tilde{f}_i\right), \tag{3.31}$$

where $\tilde{\boldsymbol{\Sigma}}$ is the reconstructed matrix and the $\tilde{f}_i$ are the spatial frequencies corresponding to each of the UC roots and the look direction spatial frequency. The $\hat{d}_i$ values are estimated using (2.14),

$$\hat{d}_i = \frac{1}{\mathbf{v}^H\left(\tilde{f}_i\right) \hat{\boldsymbol{\Sigma}}^{-1} \mathbf{v}\left(\tilde{f}_i\right)} \tag{3.32}$$

with the SCM in place of the true covariance matrix. Once the covariance has been reconstructed using the obtained roots, the spatial filter is created in the same way described earlier in this chapter. At the t-th iteration, the UCRC algorithm is repeated using roots from the previous iteration and the matrix is again reconstructed from these roots.

The preceding steps were followed for, $N_s = 16$ elements and $L = 17$ secondary data. Without loss of generality, we selected the true interference plus noise covariance matrix as $\boldsymbol{\Sigma} = \mathbf{I}$ and the look direction $\theta_0 = 0°$. Computing the Euclidean distances between the filter at the t-th and the filter at the $t-1$-th iteration for $t = 20$ iterations, the distance between each filter was less than 10^{-5}. Since the distance between subsequent filters is near zero, it follows that the filter at iteration t is roughly equal to the filter at iteration $t-1$ for $t > 0$. Hence, repeated iterations of Algorithm 1 are not useful, and the UCRC-MVDR approach should only be applied once to compute the beamformer.

3.4 Simulation Results

In this section, the results of several simulation experiments are given to demonstrate the properties and performance of the proposed approach. All experiments in this section are conducted using simulated uniform linear array data where $\lambda = 0.3$ m and $d = \lambda/2$ are the center wavelength and inter-element spacing of the array, respectively. Unless mentioned otherwise, most experiments included here are for the low-sample case, where the number of secondary snapshots used to compute the SCM is $L = N_s + 1$.

3.4.1 Experiment 1- Array Polynomial Roots and Magnitude Response

This experiment examines the array polynomial root locations for various beamforming approaches and the associated array magnitude responses. For Figure 3.2, the array consists of $N_s = 11$ elements with $L = 12$ secondary snapshots to compute the SCM. The array is steered toward broadside look direction, $\theta_0 = 0°$ in the presence of a single interferer at angle $\theta_1 = 16°$ with an interference to noise ratio (INR) of 10 dB, corresponding to an angle $u_1 = \pi \sin(\theta_1)$ in the complex plane. No SOI is present in this case. The array polynomial roots of the SMI and FB-SMI [46], [109], [115], respectively, are shown in Figure 3.2. The roots for the clairvoyant case of equation (3.7) are also plotted for reference. The interferer location is denoted by a black dashed line while the mainbeam is shown as a shaded area. Figure 3.3 shows the roots for $N_s = 21$ elements and $L = 22$ snapshots with similar signal, interference and noise configuration.

Figures 3.2 and 3.3 show that all roots for the clairvoyant case fall on the unit circle, as postulated in [97], whereas none of the SMI roots are on the unit circle, which may explain its poor performance and justify the need for imposing the unit-circle roots constraint. Most roots of FB-SMI, a commonly used method [46], [109], [115], fall on the unit-circle, explaining its superior performance compared to SMI. However, FB-SMI satisfies C1 only, and it does not guarantee unit-circle roots that require satisfying C2 as well. For the FB-SMI, an isolated root at approximately $50°$ and a reciprocal pair of roots at around $-75°$ are angularly apart from the clairvoyant roots. Figures 3.2 and 3.3 further show that none of the clairvoyant roots lie inside the mainbeam, justifying the need for mainbeam protection.

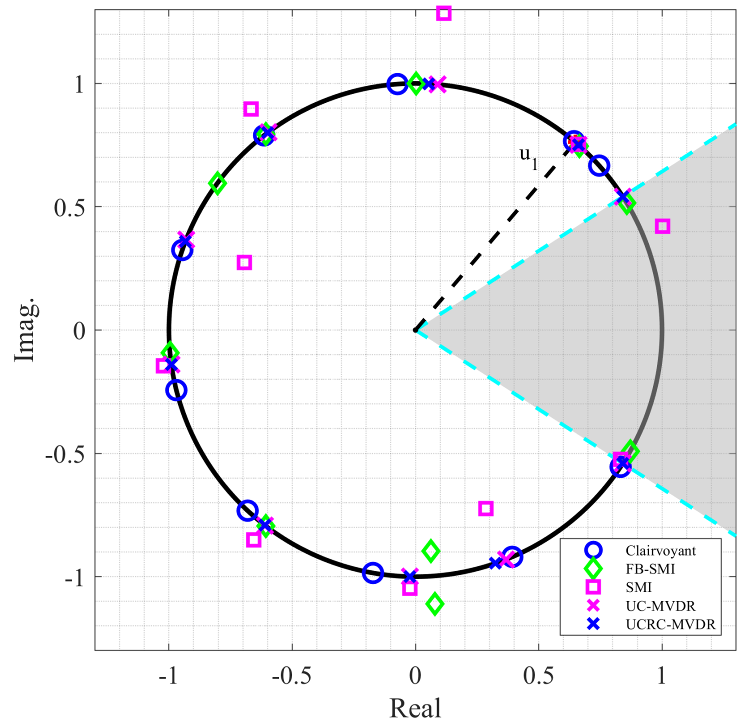

Figure 3.2: Array polynomial roots for clairvoyant, conventional and unit-circle beamformers with (a) $N_s = 11$.

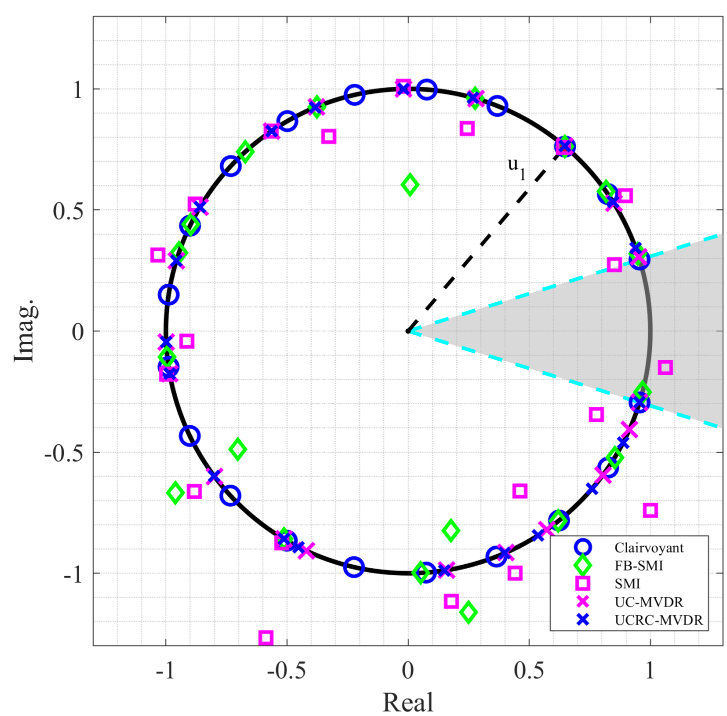

Figure 3.3: Array polynomial roots for clairvoyant, conventional and unit-circle beamformers with $N_s = 21$ elements.

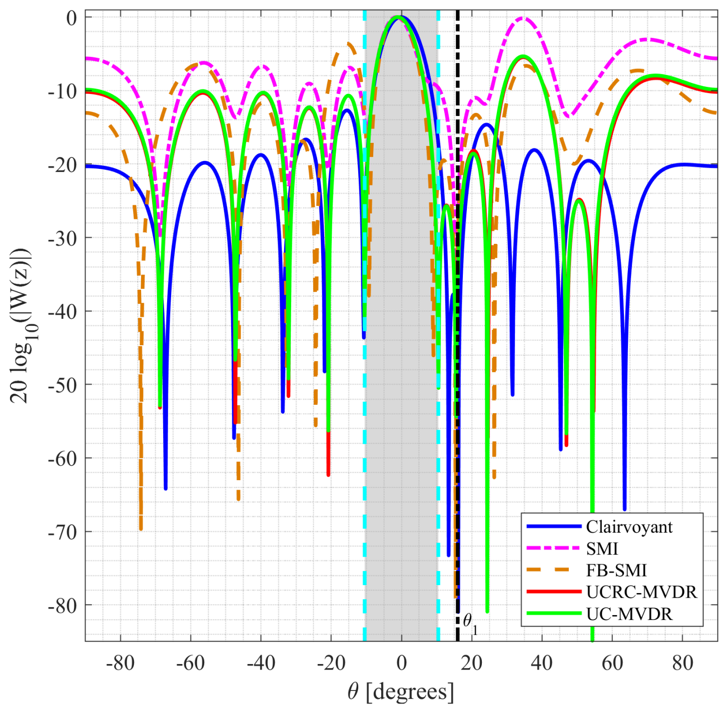

(a) $N_s = 11$ elements.

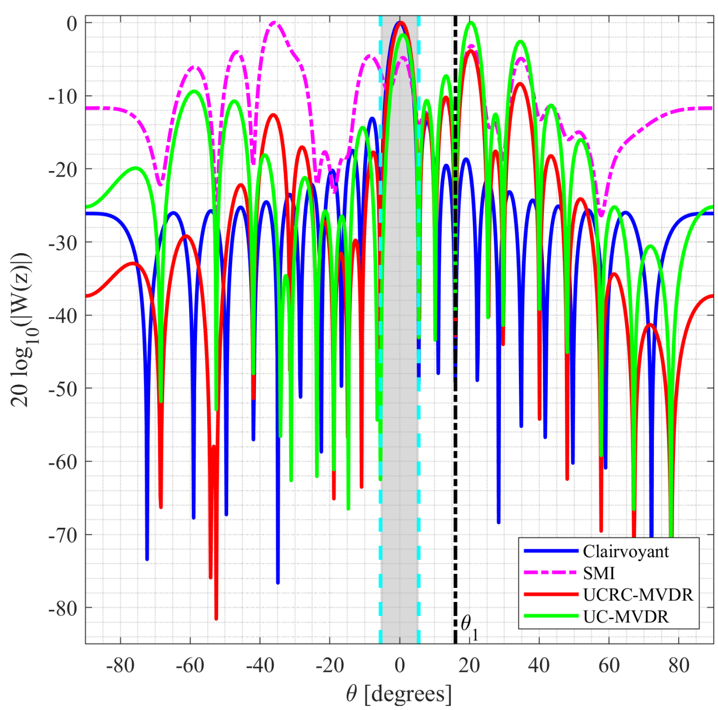

(b) $N_s = 21$ elements.

Figure 3.4: Array magnitude response for proposed, method of [102], and SMI with (a) $N_s = 11$ elements and (b) $N_s = 21$ elements.

The array polynomial roots for the proposed method and the method of [102] after protecting the mainbeam are also included in Figures 3.2 and 3.3 for the same data. All roots in both cases lie on the unit-circle, as designed. The UC roots of the method in [102] were obtained by radially moving the SMI roots to the unit circle, whereas the proposed conjugate symmetric beamformer method estimates the UC roots by optimizing the MVDR criterion in equation (3.26).

Figure 3.4a illustrates the magnitude responses corresponding to all the cases in Figure 3.2 for the same data. All approaches place a null at the interference location. Most of the nulls of FB-SMI are close to those of the unit-circle based methods explaining its effectiveness compared to SMI. It can be seen that for the $N_s = 11$ case, FB-SMI also shows nulls at around $-75°$ and $50°$ that are away from the clairvoyant nulls, and it also shows higher sidelobes in some regions.

Figure 3.4b illustrates the magnitude response of the array versus angle for $N_s = 21$ elements. Lower side-lobe performance of the proposed method over that of [102] is evident, especially in the $N_s = 21$ case of Figure 3.4b.

3.4.2 Experiment 2- Robustness to SOI: Output SINR vs. SNR

This experiment highlights the robustness of the UCRC-MVDR when the SOI contaminates the snapshots used to compute the SCM by comparing the performance of various beamformers in terms of the output SINR versus SNR. In all cases, the performance of the proposed approach is compared against the traditional SMI, FB-SMI [46], [109], [115], the unit-circle based method of [102], as well as the shrinkage [37], [25], and Toeplitz rectification [28] methods. The simpler case with no contamination is also considered.

The output SINR is given by [66],

$$\mathrm{SINR} = \frac{\sigma_0^2 |\mathbf{w}^H \mathbf{v}(\theta_0)|^2}{\mathbf{w}^H \boldsymbol{\Sigma} \mathbf{w}} \tag{3.33}$$

where σ_0^2 represents power of the SOI, respectively. The presence of the SOI in the snapshots used to compute the SCM results in a contaminated covariance estimate [9],

$$\hat{\mathbf{\Sigma}}_X = \sigma_0^2 \mathbf{v}\left(\theta_0\right) \mathbf{v}^H\left(\theta_0\right) + \hat{\mathbf{\Sigma}}. \tag{3.34}$$

For this experiment, this contaminated SCM is used to determine the beamformer weights $\mathbf{w}$ for all approaches, where $\mathrm{SNR} = \sigma_0^2/\sigma_n^2$ is varied while keeping $\mathrm{INR} = \sigma_1^2/\sigma_n^2$ fixed.

Figures 3.5a and 3.5b compare the performance of the proposed approach with those of the existing methods for a single interferer at angle $\theta_1 = 16°$ with $\mathrm{INR} = 10$ dB, and $N_s = 11$, and 21 elements, respectively.

Figure 3.5 demonstrates the performance of the proposed approach when no SOI is present in the secondary snapshots. The figure compares the SINR vs. SNR performance of all beamformers for $N_s = 21$ elements using the same interference parameters used to generate figures 3.5a and 3.5b. While this represents an idealized scenario, the UCRC-MVDR beamformer demonstrates superior performance over the SMI, FB-SMI, and Toeplitz rectification methods, and follows the performance of the shrinkage-based beamformer.

Overall, the UCRC-MVDR beamformer outperforms the UC-MVDR beamformer in [102] as well as the conventional SMI, FB-SMI, and the Toeplitz rectification approach, showing consistent performance across all input SNR values. The UCRC-MVDR follows the performance of the shrinkage-based beamformer at low SNR, but the performance of shrinkage degrades after roughly $\mathrm{SNR} = -8$ dB and $\mathrm{SNR} = -14$ dB for the $N_s = 11$ and $N_s = 21$ element cases, respectively, suffering from self-cancellation in the SOI-contaminated case.

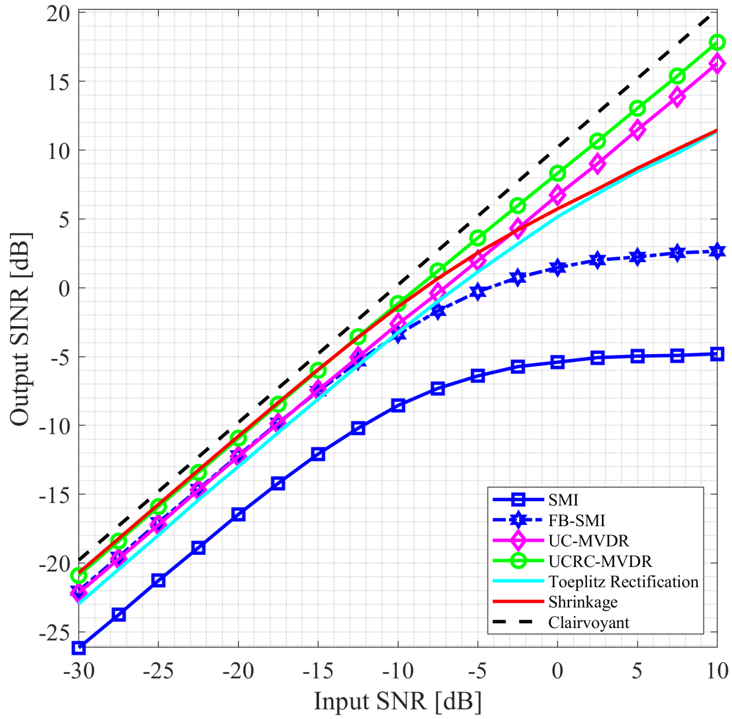

(a) SINR vs. SNR for $N_s = 11$ elements.

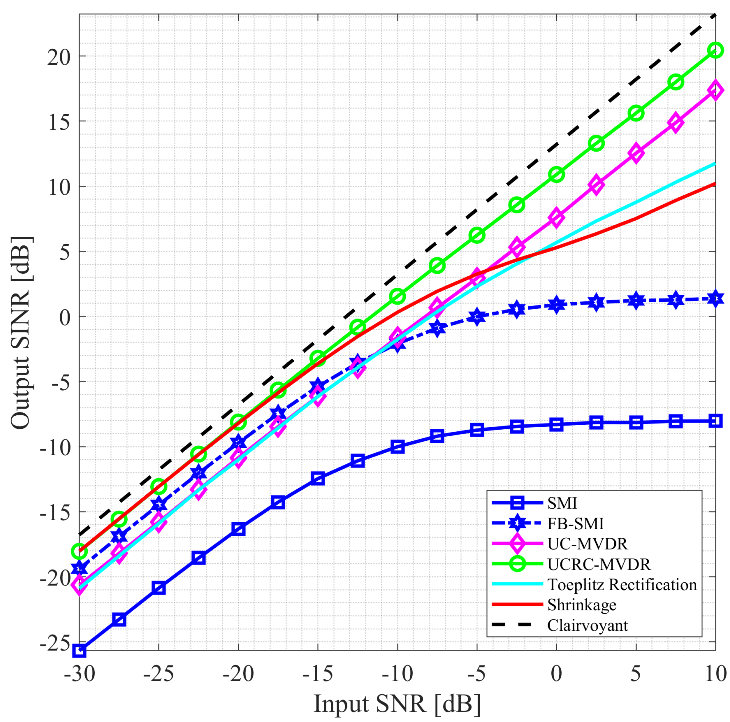

(b) SINR vs. SNR for $N_s = 21$ elements.

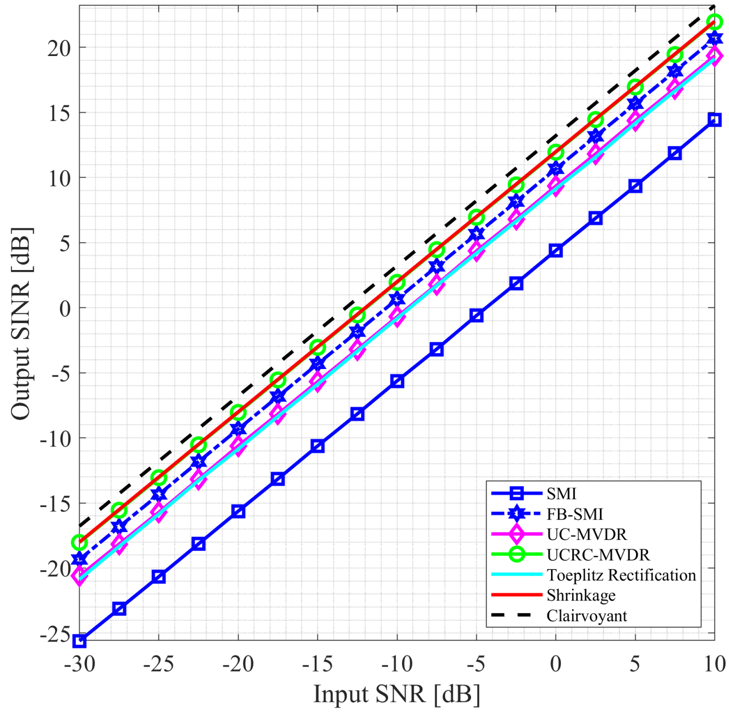

Figure 3.5: SINR vs. SNR for $N_s = 21$ elements without SOI contamination.

3.4.3 Experiment 3-Robustness to Correlated Interference

In many practical scenarios, *e.g.*, multipath propagation, the interference in equation (3.3) may be correlated with the SOI. The conventional MVDR performs poorly in the presence of correlated signals, resulting in spatial distortion and signal cancellation [2]. For this experiment, the performance of the UCRC-MVDR is examined and compared with the existing methods in the presence of both correlated and uncorrelated interference.

For this experiment, the array size is $N_s = 21$ elements with $L = 22$ secondary snapshots used to compute the SCM. $M = 3$ discrete interferers are present at angles $\theta_1 = 16°$, $\theta_2 = 30°$, and $\theta_3 = -43°$ at $\mathrm{INR} = 45$, 30, and 20 dB, respectively. The interferer at angle θ_1 is perfectly correlated with the SOI while the remaining two are uncorrelated with respect to both each other and the SOI. SOI contamination is assumed while generating Figure 3.6a while no SOI contamination is present for figures 3.6b and 3.7.

Comparing figures 3.5b and 3.6a, it is evident that the presence of additional and correlated interference has a deleterious effect upon the performance of all beamformers.

The UCRC-MVDR beamformer again outperforms the SMI, FB-SMI, Toeplitz rectification, and UC-MVDR beamformers, but is marginally outperformed by the shrinkage-based method at low SNR. However, as the input SNR increases, past roughly -20 dB, the UCRC-MVDR outperforms all the other beamformers. Self-cancellation is evident for all beamformers at higher SNR values, but the UCRC-MVDR displays the most robust performance.

Figures 3.6b and 3.7 show the root locations and corresponding magnitude response for the clairvoyant, SMI, and UCRC-MVDR beamformers using the same parameters used to generate Figure 3.6a. The dashed lines in both Figures 3.6b and 3.7 show the locations of the interference sources, where the red and black colorations correspond to correlated and uncorrelated sources, respectively, and $u_i = \pi \sin(\theta_i)$ for $i = 1, \ldots, M$. By examining Figures 3.6b and 3.7 it is clear that all three beamformers place roots at or very close to the roots corresponding to the interference location, resulting in deep nulls in the respective magnitude responses.

3.4.4 Experiment 4-Robustness to Spatially Distributed Interference

For spatially distributed interference, the interference spectrum is continuous over an angular extent and the adaptive beamformer must judiciously use the available degrees of freedom to suppress the interference. From this perspective, it is illuminating to examine the performance and root locations of both the proposed and clairvoyant beamformers.

Spatially distributed interference is modeled using equation (3.3) assuming $M \gg N_s$ sources present at uniformly spaced angles $\theta_i \in [\theta_{\mathrm{L}}, \theta_{\mathrm{H}}]$ for $i = 1, \ldots, M$. For this experiment, $M = 100$ sources are present at uniformly spaced angles between $\theta_{\mathrm{L}} = 15°$ and $\theta_{\mathrm{H}} = 30°$ and scaled to ensure a total per element $\mathrm{INR} = 40$ dB. The array size is $N_s = 21$ elements with $L = 22$ secondary snapshots. No SOI contamination is assumed while generating Figures 3.9 and 3.8b while SOI contamination is used to generate Figure 3.8a.

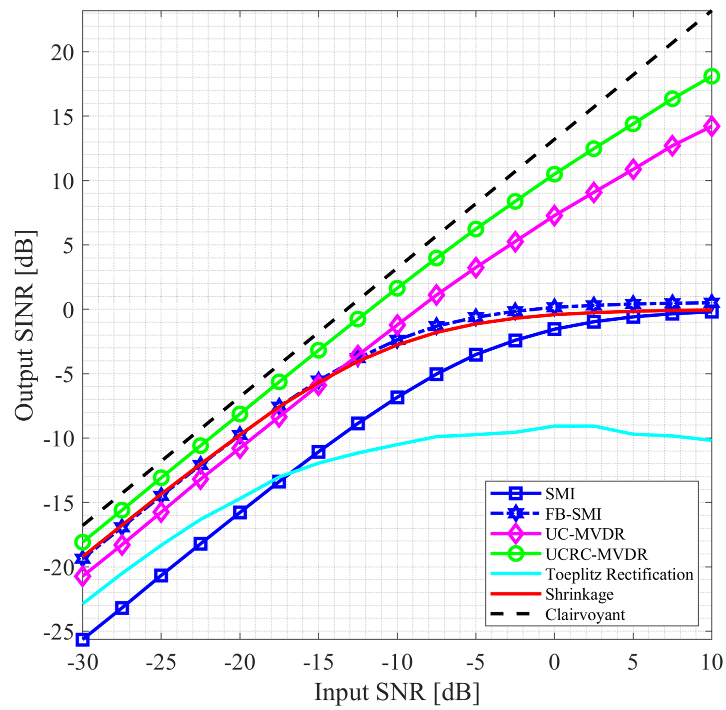

(a) SINR vs. SNR with coherent interference.

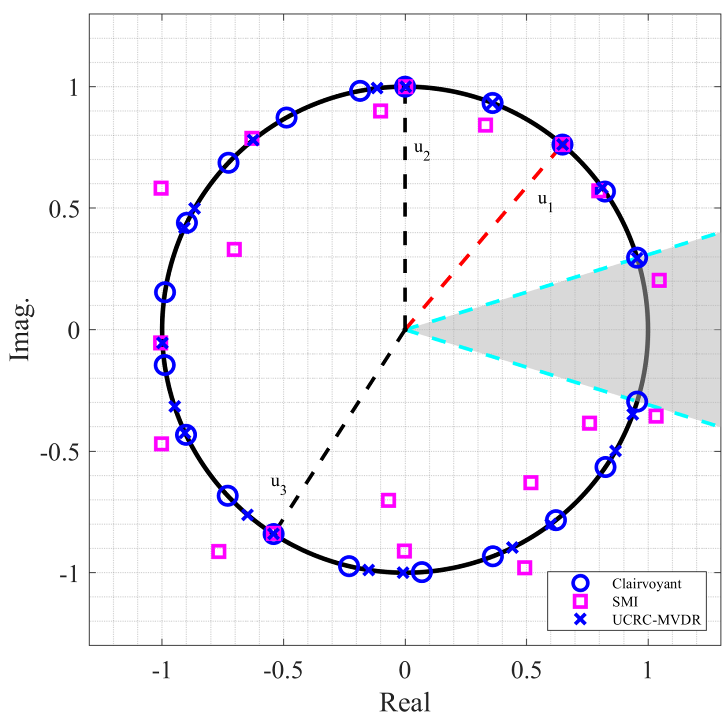

(b) Beamformer roots with coherent interference.

Figure 3.6: (a) SINR vs. SNR and (b) root locations with coherent interference and $N_s = 21$ elements.

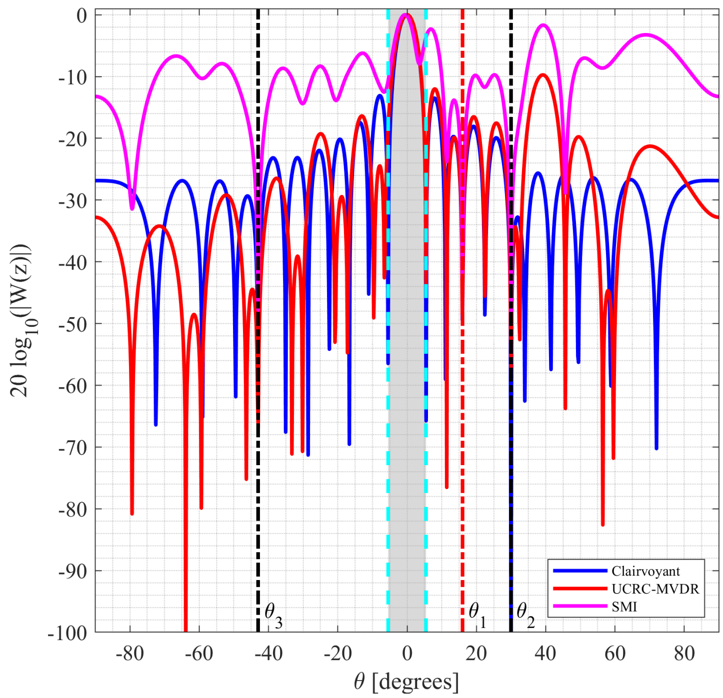

Figure 3.7: Magnitude response with coherent interference and $N_s = 21$ elements.

Figures 3.8b and 3.9 show the root locations and associated magnitude responses of the clairvoyant, SMI, and UCRC-MVDR beamformers. Figure 3.8b illustrates that despite the number of interference sources being greater than the number of degrees of freedom, all of the clairvoyant roots appear on the unit circle, satisfying the theoretical property. The clairvoyant and UCRC-MVDR beamformers allocate six and five roots, respectively, to the interference sector of the unit circle, resulting in a deep notch in their respective magnitude responses.

Figure 3.8a illustrates the SINR vs. SNR performance of all beamformers, where it is immediately clear that the UCRC-MVDR beamformer outperforms all other approaches. Close examination of Figure 3.8a shows that the UCRC-MVDR provides a roughly 4 dB increase in performance over the UC-MVDR approach and nearly 10 dB improvement over the shrinkage beamformer below $\mathrm{SNR} = 0$ dB.

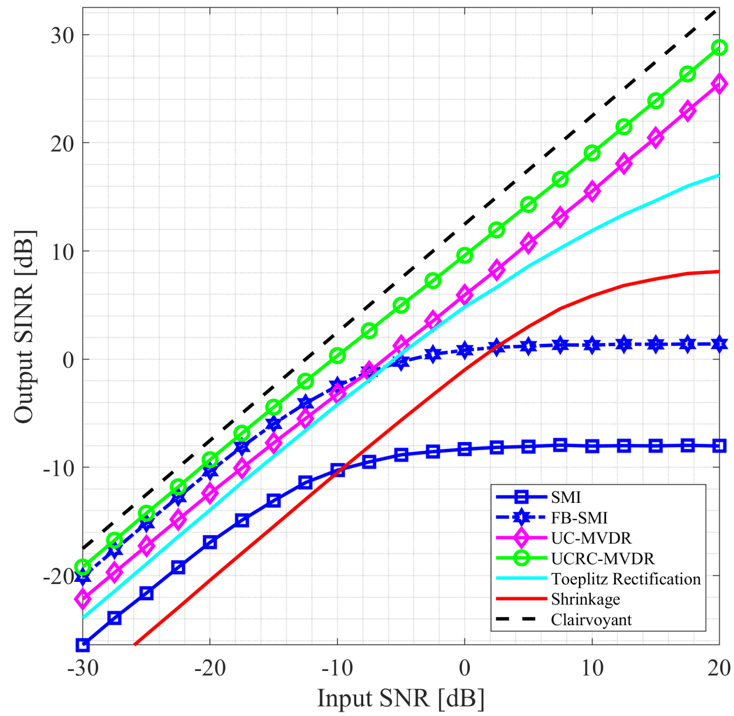

(a) SINR vs. SNR performance.

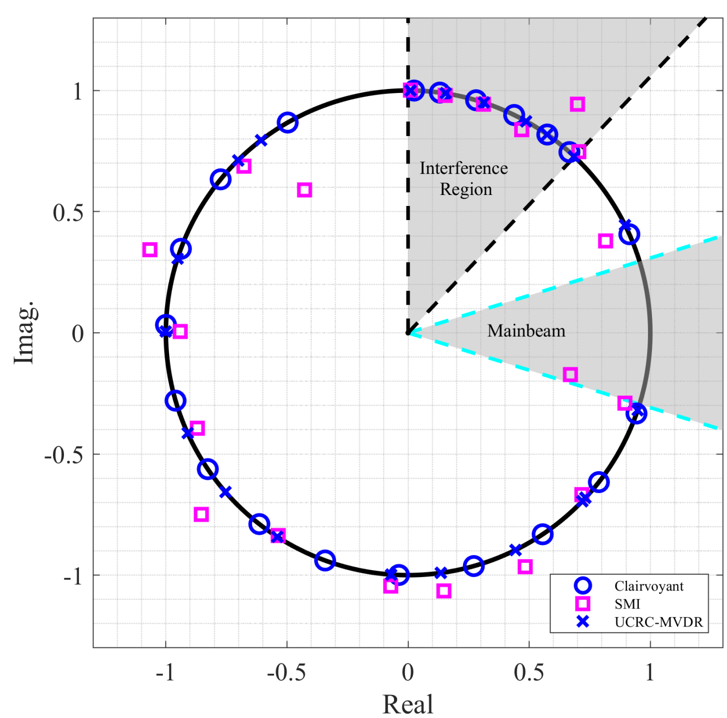

(b) Beamformer root locations.

Figure 3.8: (a) SINR vs. SNR and (b) root locations for distributed interference.

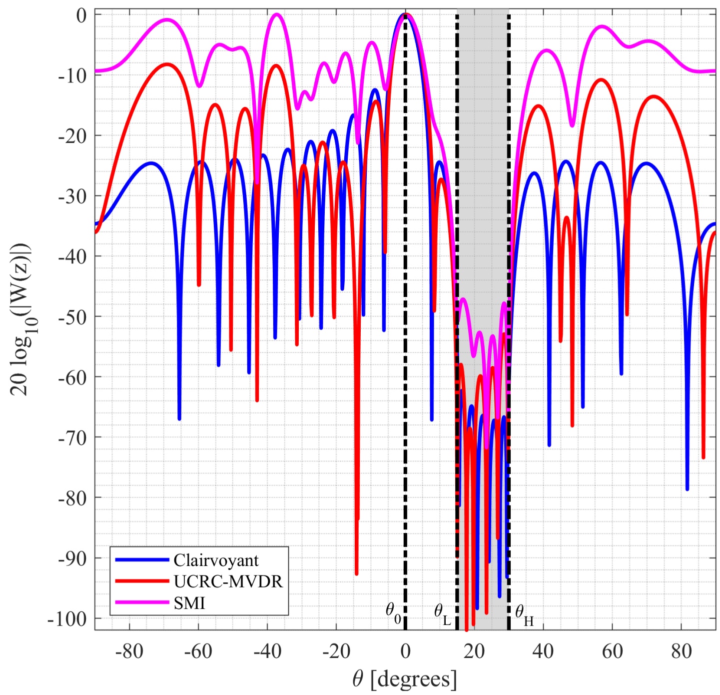

Figure 3.9: Normalized filter and distributed interference magnitude responses.

3.4.5 Experiment 5-Robustness to Limited Snapshots using Diagonal Loading

This experiment examines the robustness of the UCRC-MVDR beamformer in the extreme snapshot-limited scenario ($L << N_s$) when the computed SCM is not full-rank. In such cases, regularization via diagonal loading is typically used to ensure that the resulting diagonally loaded SCM (DL-SCM) is invertible. The DL-SCM takes the following form,

$$\hat{\mathbf{\Sigma}}_{\mathrm{DL-SCM}} = \hat{\mathbf{\Sigma}} + \gamma \mathbf{I} \tag{3.35}$$

where γ is the DL factor and $\mathbf{I}$ is an $N_s \times N_s$ identity matrix. Many approaches for choosing the DL factor exist in the literature [21], [68]. For comparing various diagonally loaded beamforming methods, the empirically optimal [105] $\gamma = 2\sigma_n^2$ is used as the DL factor. The diagonally loaded variants of the SMI, FB-SMI, proposed method, UC-MVDR of [102], and Toeplitz rectification are implemented by replacing the SCM of equation (3.9) with the DL-SCM of equation (3.35). Diagonal loading is not applied for the shrinkage case since shrinkage itself is a form of diagonal loading [37].

For these experiments, the array size is $N_s = 21$ elements with $L = 11$ secondary snapshots. The SOI and a single interferer at $\theta_1 = 16°$ with $\mathrm{INR} = 10$ dB were present in all cases. Each point in Figure 3.10 is the result of averaging over 5000 trials.

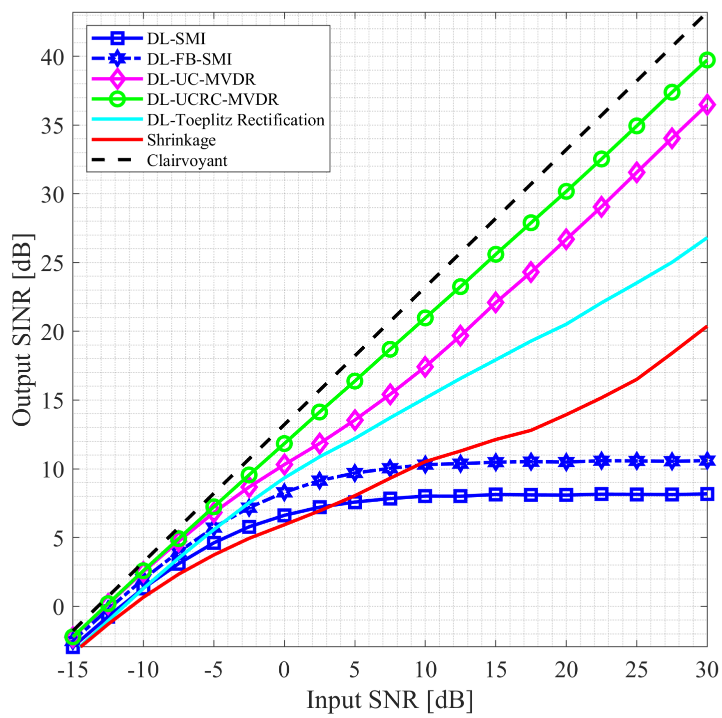

Figure 3.10: Output SINR vs. SNR with DL.

Figure 3.10 illustrates the performance of all the diagonally loaded beamformers including shrinkage. All approaches show consistent performance at lower SNR values, but both the UCRC-MVDR and method of [102] diverge from the others as the SNR increases, indicating robust performance in the presence of strong SOI contamination even with limited snapshots. Furthermore, the proposed approach outperforms all methods and its performance is closer to the clairvoyant case at all SNR levels.

3.4.6 Experiment 6- Output SINR Empirical Cumulative Distribution

Section 3.4.2 highlights the mean output SINR performance of the UCRC-MVDR approach. However, to obtain a better understanding of the overall performance of the proposed technique, the distribution of the output SINR should also be taken into account. For this experiment, one minus the empirical cumulative distribution function (CDF) is used to compute the probability that a particular beamformer exceeds a prescribed output SINR. The array size is $N_s = 21$ elements with $L = 22$ secondary snapshots are used to compute the SCM. A single interference is present at angle $\theta_1 = 16°$ with $\mathrm{INR} = 40$ dB. SOI contamination is also present with $\mathrm{SNR} = 10$ dB at angle $\theta_0 = 0°$. A total of $100,000$ Monte Carlo runs are used to compute the results shown in Figure 3.11.

Figure 3.11 illustrates the performance probabilities for the UCRC-MVDR along with the existing methods, where the output SINR range is the horizontal axis. One minus the theoretical CDF of the clairvoyant beamformer is depicted in black and serves as a performance benchmark. The closer the curves are to the clairvoyant performance, there is a higher probability that method will achieve near optimal performance.

Figure 3.11 quantifies the probability that a particular method exceeds a prescribed output SINR gain. For example, the probabilities that UCRC-MVDR or UC-MVDR exceed an $\mathrm{SINR} = 20$ dB are roughly 0.61 and 0.14, respectively, demonstrating that the UCRC-MVDR beamformer is more likely to outperform the UC-MVDR approach of [102] in this scenario.

3.4.7 Experiment 7- Study of Ensemble Output Variance and Output SINR vs. Number of Corrected Roots

The objective of the MVDR algorithm is to minimize the variance, which consequentially maximizes the output SINR. In an attempt to empirically verify if these goals are achieved

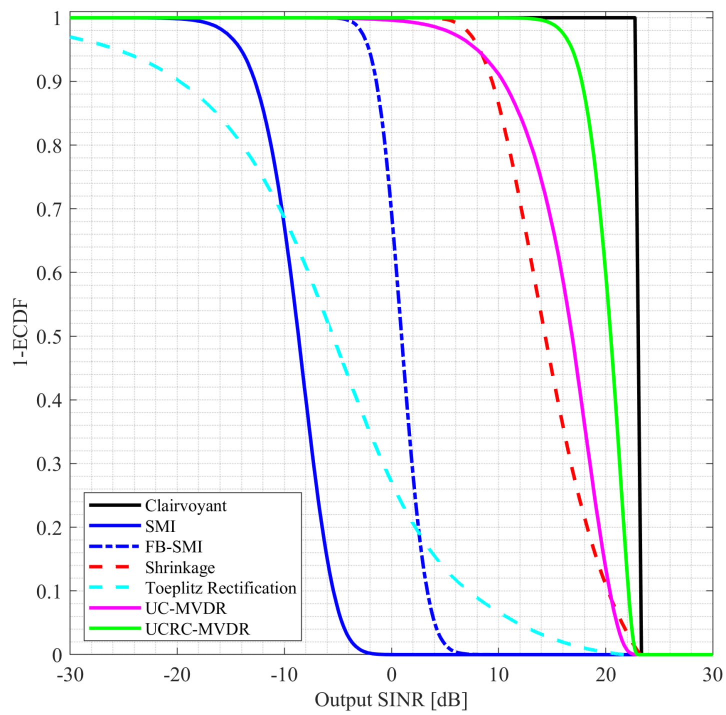

Figure 3.11: One minus the empirical CDF of the output SINR for various approaches

by the algorithm, this experiment studies the effect of placing beamformer polynomial roots on the unit circle on the output variance and SINR by the proposed method. The results are compared with those of [102], as well as the clairvoyant case. The effect of protecting the mainbeam is also analyzed. For generating the plots, $N_s = 11$ sensors are used and the SMI beamformers are constructed using SCMs computed with $L = N_s + 1$ snapshots that included a single interferer with $\mathrm{INR} = 10$ dB. No SOI contamination is present however, for the purposes of calculating the output SINR, an SOI with $\mathrm{SNR} = 0$ dB is assumed. Each point on the plots was generated by averaging the corresponding variance and SINR over 50,000 independent Monte-Carlo trials.

For this experiment, the output variance defined in equation (3.7) and the output SINR defined in equation (3.33) are computed using estimated quantities and the performance in terms of ensemble averages are shown in figures 3.12a and 3.12b, respectively. To generate the plots, the 1-st through k-th root are placed onto the unit circle for $k = 1, \ldots, N$, using either the proposed approach or the method of [102], while leaving the remaining $N - k$

(*i.e.* $k+1$ through N-th) roots undisturbed. The theoretical output variance $\mathbf{w}_{\text{opt}}^H \mathbf{\Sigma} \mathbf{w}_{\text{opt}}$ and SINR corresponding to the benchmark clairvoyant beamformer, is depicted in all figures as a horizontal dashed line.

To study the effect of mainbeam protection, if any of the 1 through k corrected UC roots lie within the mainbeam, then they were moved to the nearest CBF null. The proposed beamformer was also implemented without mainbeam protection and the corresponding results are shown by the blue dashed lines in figures 3.12a and 3.12b.

The far-left and far-right points of both figures correspond to the SMI-roots only (*i.e.* no roots have been corrected) and all roots corrected cases, respectively. It can be seen that the left-most points representing SMI-based quantities without any correction are farthest from the benchmarks, whereas the right-most points representing all roots corrected cases are the closest to the corresponding benchmarks, justifying the need for these corrective steps.

It is interesting to note that the ensemble variance without any correction, as shown by the left-most point on Figure 3.12a, is *lower* than the corresponding clairvoyant variance. Likewise, the leftmost output SINR in Figure 3.12b is *higher* than the corresponding benchmark. This may be explained by the fact that unlike the clairvoyant case, the conventional SMI solution is entirely unconstrained with no restrictions on its root locations. The right-most points in Figure 3.12a and 3.12b further show that the proposed approach is unbiased and converges towards the clairvoyant theoretical variance and theoretical output SINR, respectively, in the limit when all roots are corrected and the mainbeam is protected, further justifying the need for the corrections presented in this work.

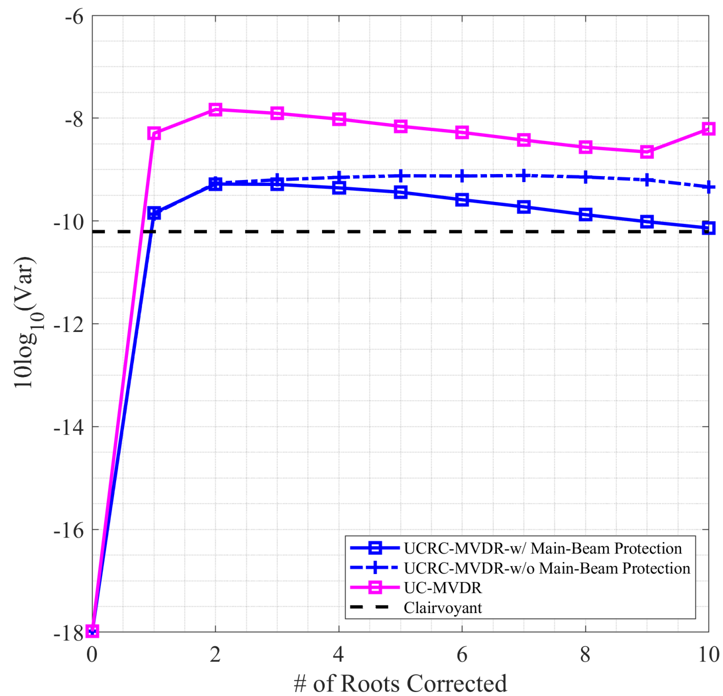

(a) Output variance.

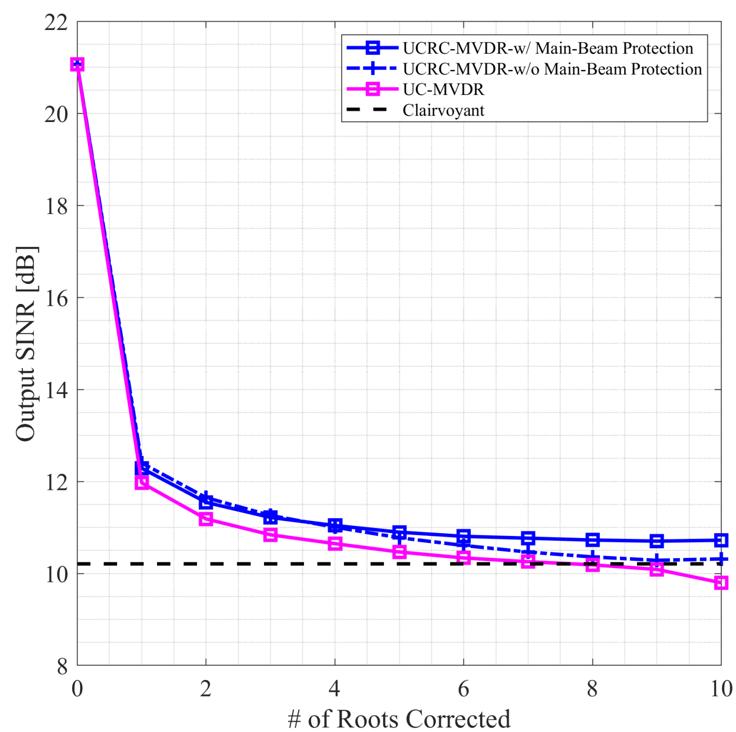

(b) Output SINR.

Figure 3.12: Ensemble output (a) variance and (b) SINR vs. corrected roots.

3.4.8 Experiment 8- Aperture Size Analysis: Output SINR vs. Array Size

This experiment investigates the output SINR versus array size for all beamformers. Figure 3.13 illustrates the performance of the proposed beamformer, that of [102], SMI and FB-SMI, in terms of the output SINR versus the array size where the clairvoyant case is again included as a performance baseline. For this experiment, one interferer is present at $\theta_1 = 16°$ with $\mathrm{INR} = 10$ dB. No signal contamination is present in the $L = N_s + 1$ snapshots used to compute the SCM in this experiment but, $\mathrm{SNR} = 10$ dB is used to calculate the SINR. For each point on the horizontal axis, the performance is averaged over $10,000$ independent trials.

To study the aperture size requirements for various beamformers a black horizontal line is included at constant $\mathrm{SINR} = 19$ dB. The intersections of the horizontal line on the various performance curves represent the array size required to achieve that level of SINR gain. From Figure 3.13, the array sizes required to achieve an output SINR of 19 dB are roughly: $N_s = 11$ elements for the proposed method, $N_s = 13$ for FB-SMI, and $N_s = 19$ elements for the method of [102]. The SMI performs the worst and never achieves this level of output SINR. Aperture size advantage of the proposed method is even starker if higher SINR gain requirement is to be met.

A vertical line at constant array size of $N_s = 21$ elements is also superimposed on the performance curves, and an analogous conclusion follows from examining the intersections of the vertical black line with the various performance curves where it is evident that the proposed beamformer dominates over the other approaches.

When considering the size, weight, and power (SWAP) requirements for deploying an array with limited aperture size, Figure 3.13 demonstrates that considerable performance improvement can be achieved by using the proposed beamformer with lower array size, or higher performance gains can be attained at a fixed array size.

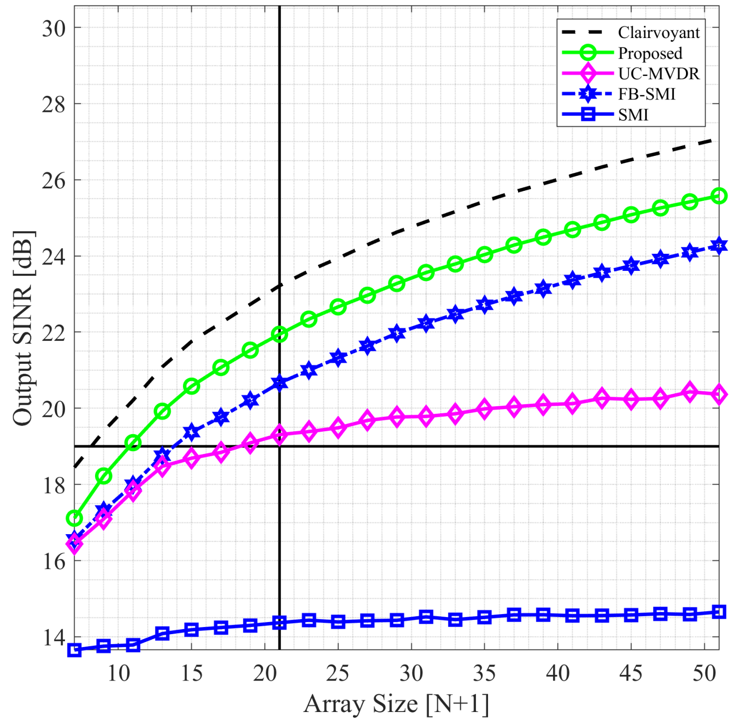

Figure 3.13: Output SINR vs. Array Size.

3.5 Discussions and Conclusions

This chapter proposes a shift in the way MVDR beamformer is designed by reformulating the classical MVDR problem as a unit-circle roots constrained optimization problem. The proposed UCRC-MVDR beamformer is developed by enforcing the theoretically necessary unit-circle roots constraint [97] onto the SMI solution of Capon's MVDR beamformer [13]. Although additional research will be needed to fully establish its general efficacy, based on the extensive results reported in this work, it may be argued that enforcing unit-circle roots on the MVDR polynomial provides a level of robustness and structure to the MVDR solution that may be able to overcome many of the ill effects of the SCM and other beamformer issues requiring robust solutions [105], [31], [32].

The proposed method differs from the ad-hoc radial projection approach of [102], as the unit-circle rectification is performed algorithmically where the N-dimensional MVDR problem is split into N 1-dimensional MVDR problems. Conjugate-symmetry is imposed upon individual first-order factors independently to ensure unit-circle roots. Each of the estimated factors is expressed in closed-form, minimizes the variance, and preserves the linear constraint. The proposed beamformer was shown to have same order of computational complexity as that of the SMI and its implementation is modular and parallelizable as all roots can be updated concurrently.

The superior performance of the proposed unit-circle approach was demonstrated using simulation experiments where the performance of the proposed beamformer was compared against the method of [102] along with existing techniques. It was shown that the proposed approach produces UC roots as well as lower sidelobes than the beamformer of [102] and conventional methods. The output SINR versus SNR demonstrated the improved gain and robust performance of the proposed method in the presence of SOI contamination. Additional simulations examples demonstrated the robust performance of the proposed approach in the presence of coherent as well as spatially distributed interference sources. It was observed that the proposed approach results in lower output variance as each root is corrected resulting in a higher output SINR over the beamformer of [102]. It was shown that the proposed beamformer has improved performance over all of the previously mentioned approaches in the snapshot limited scenario where diagonal loading was used to regularize the estimated covariance matrix. Distribution analysis via the empirical CDF concluded that the proposed approach outperforms the approach of [102] with higher probability in the presence of SOI contamination and strong interference. Finally, the proposed beamformer showed comparable performance at a smaller aperture size than that achieved by other methods at larger array sizes.

The UC root constraint is a fundamental and impactful property of the MVDR beamformer which can be practically imposed to improve spatial filtering performance. Possible avenues where this work can be applied include STAP [66], multiple-input multiple-output (MIMO) radar systems [60], and DOA estimation [13]. Future extensions of this work can include further processing to accommodate coherent sources as well as imposing the unit-circle constraint upon sequential beamforming approaches.

As per general applicability of the proposed unit-circle roots based approach, any existing MVDR-related design for which the roots of the array polynomial are not already on the unit-circle, may benefit from applying the tools developed in this chapter. Specifically, regardless of how the original weight vector was arrived at, any non unit-circle roots can be optimally moved on to the unit-circle by using the proposed algorithm while further minimizing the variance. In addition, the proposed root updates can improve beamformer performance while improving computational efficiency by removing the need to invert the SCM by replacing the SMI-based roots with those of the CBF. This relatively simple update step with little additional computational cost can be expected to produce deeper nulls and lower sidelobes to potentially reduce the effects of noise and interference compared to SMI-based MVDR. Furthermore, if a current design produces a MVDR polynomial with any root inside the mainbeam, then signal fidelity may potentially be improved by moving out the mainbeam roots using the steps given in section 3.3.4 to reduce self-nulling effect. Further investigation is worth pursuing in these directions.

Unit Circle Roots Constrained Adaptive Matched Filter for Improved Moving Target Detection

4.1 Introduction

Target detection in homogeneous clutter with unknown covariance matrix is a well-studied problem in the field of radar signal processing. Conventional approaches such as the generalized likelihood ratio test (GLRT) [48], and adaptive matched filter (AMF) [76] substitute the sample covariance matrix (SCM) estimate in place of the unknown covariance matrix, which requires a set of target-free secondary data. However, SCM-based detectors experience performance degradation unless the secondary data are abundant [75], which is not always a practical assumption [3]. To overcome the need for copious amounts of secondary data, the persymmetric AMF (PS-AMF) [69] has been proposed, which exploits the mathematical structure of the signal and covariance matrix to improve detection performance.

In [97], Steinhardt had proved that the roots of the minimum-variance distortionless response (MVDR) beamformer array polynomial for a uniform linear array (ULA) with plane-wave sources must, theoretically, lie on the unit-circle. Despite establishing the theoretical necessity of unit circle roots, no method of enforcing this property was provided.

Inspired by Steinhardt's proof, we have previously developed a unit circle roots constrained MVDR (UCRC-MVDR) beamformer design approach that has shown significantly improved performance compared to state-of-the-art beamforming methods [85],[86].

It is important to note that the unit-circle roots property proven in [97] is valid for the MVDR optimization problem only. In this chapter, we present a new and general proof that the roots of the filter polynomial corresponding to the AMF must all occur on the unit circle in the known-covariance case. Our proof leverages the Toeplitz structure of the covariance matrix and the Vandermonde structure of the steering vector, decoupling the proof of this property from the optimization required to obtain the optimum filter. The proof does not require the use of either the Weiner-Khinchin or implicit function theorems, as described in both [97] and [102], and includes both the AMF and MVDR solutions as special cases. We use this new proof as the theoretical justification for enforcing unit circle roots upon the conventional AMF.

Intuitively, the proposed UCRC-based approaches treat the AMF detector z-polynomial as an FIR filter polynomial, where unit circle roots are desirable because of their associated effect upon the filter frequency response. It is well known that zeros on the unit circle will produce deep nulls and low sidelobes in the filter frequency response, resulting in improved interference suppression. This observation, coupled with the theoretical necessity of unit circle roots, compels the exploitation of this property for adaptive clutter suppression.

The unit circle roots constrained adaptive matched filter (UCRC-AMF) proposed in this chapter exploits the theoretical necessity of unit circle roots in the known-covariance case to improve detection performance over the conventional AMF when the secondary data are limited. However, the unit circle root estimates of the UCRC-AMF are based on the SCM and thus, will be adversely impacted by limited secondary data. In order to overcome this limitation , in this chapter, we also propose a modified UCRC-AMF (M-UCRC-AMF), which alleviates the aforementioned issue with the UCRC-AMF by judiciously incorporating the forward-backward averaged SCM (FB-SCM) within the UCRC-AMF algorithm, resulting in significant performance improvement over the preliminary results reported in [94].

The UCRC-approaches proposed in this chapter enforce unit circle roots in a manner similar to [89] by breaking the multidimensional optimization specific to the AMF into multiple one-dimensional optimization problems while holding all other parameters fixed. Unit circle roots are guaranteed by enforcing conjugate-symmetry on first-order polynomials and each root estimate is computed in closed form. To the best of our knowledge, no approach for designing the AMF exists which makes use of this fundamental unit-circle roots property.

Simulation examples will be used to demonstrate the improved performance of the UCRC-AMF and M-UCRC-AMF detectors compared to the conventional AMF and PS-AMF. Using the proposed root estimation technique, it will be shown that both the UCRC-AMF and M-UCRC-AMF have roots on the unit circle whereas the AMF does not. Additionally, the improved detection performance of the UCRC-AMF and M-UCRC-AMF will be demonstrated via the receiver operating characteristic (ROC) and probability of detection versus signal-to-interference-plus-noise ratio (SINR) curves. The limited secondary data scenario is the focus of this chapter, and the detection performance will be examined assuming the number of secondary data are slightly greater than the coherent processing interval (CPI) length. The average SINR performance improvement as the number of roots of the AMF are placed onto the unit circle using the proposed algorithm will also be analyzed, where it will be shown that the proposed algorithm results in a monotonic increase in the average output SINR as more roots are placed onto the unit circle. It will be shown that the M-UCRC-AMF and UCRC-AMF consistently achieve higher output SINR with less secondary data than the PS-AMF or AMF. The SINR loss of the M-UCRC-AMF will be examined, where it will be shown that this approach achieves near optimum performance over the non-UC approaches. Finally, evidence that the proposed approach has constant false-alarm rate (CFAR) will also be presented.

The remainder of this chapter is organized as follows. In Section 4.2, a description of the target detection problem, signal, and clutter model are given. In Section 4.3, the conventional AMF is derived. The UCRC-AMF and M-UCRC-AMF are derived and discussed in Section 4.4. Section 4.5 contains simulation results of the proposed detectors. Finally, Section 4.6 provides discussion and concluding remarks.

4.2 Signal Model

Consider a co-located transmitter and receiver mounted on a stationary platform. The transmitter emits K_p periodic, pulses over a coherent processing interval. Pulse-compression is performed at the receiver to isolate the reflected returns originating from a particular range bin. The received slow-time data are stacked into a vector $\mathbf{x} \in \mathbb{C}^{K_p \times 1}$, where each row corresponds to an individual slow-time snapshot.

The received data is modeled as,

$$\mathbf{x} = i\alpha\mathbf{a}(f_0) + \mathbf{c} + \mathbf{n}. \tag{4.1}$$

where $\mathbf{c}$ and $\mathbf{n}$ are the clutter and noise components, respectively, while $\mathbf{a}(f_0)$ is the target temporal steering vector. $\alpha \in \mathbb{C}$ is the complex amplitude of the moving target return and $i = 0, 1$ corresponds to either the presence or absence of the target. α is an unknown scalar determined by the target radar cross section (RCS) and also captures the effects of signal propagation through the environment.

The target steering vector is defined as,

$$\mathbf{a}(f_0) \triangleq [1, e^{-j2\pi f_0}, \dots, e^{-j2\pi f_0 (K_p - 1)}]^T \tag{4.2}$$

where $(\cdot)^T$ is the transpose operator. The normalized Doppler frequency f_0 induced by the motion of the target is,

$$f_0 = \frac{2T_{\text{PRI}}}{\lambda}\Big(v_x \cos(\theta_r) + v_y \sin(\theta_r)\Big) \tag{4.3}$$

where λ is the operating wavelength of the radar, T_{PRI} is the pulse-repetition interval, $\mathbf{v}_t \triangleq [v_x \; v_y]$ is the target velocity vector, and θ_r is the angle with respect to the positive x-axis of the receiver relative to the target. The target-centric geometry with relevant labels is depicted in Fig. 4.1.

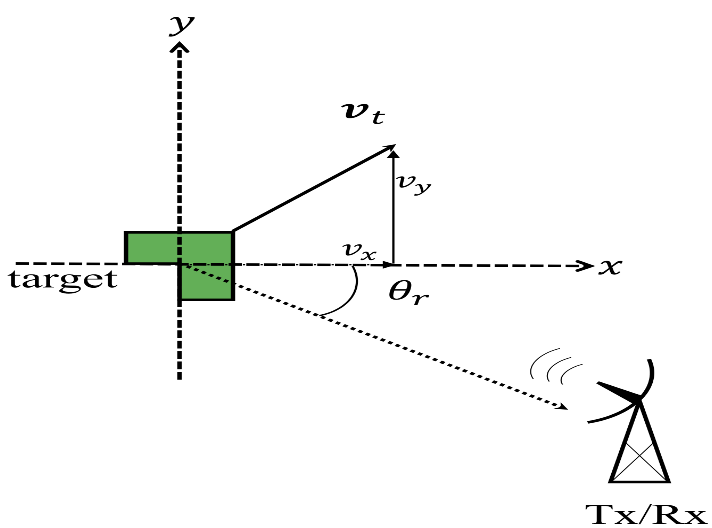

Figure 4.1: Target-centric geometry for moving target detection problem.

4.2.1 Clutter Characterization

The clutter are assumed to be temporally correlated due to the effects of internal clutter motion during the CPI (*i.e.* windblown trees or grasslands) which is described by the clutter power spectral density (PSD). The Gaussian spectral shape has been shown to approximately model measured ground clutter [36] and has been previously used in the moving target detection literature [42],[106] hence, we adopt this approach to model our simulated clutter. Mathematically, the clutter PSD is,

$$P_c(f) = \frac{\sigma_c^2}{2\sqrt{2\pi\delta_v^2}} e^{-\frac{f^2\lambda^2}{8\delta_v^2}} \tag{4.4}$$

where, σ_c^2 is the clutter power, f is the Doppler frequency, and δ_v represents the root mean square (RMS) clutter velocity [42], [106].

Following [42],[106], the clutter covariance matrix is generated by sampling the corresponding clutter autocorrelation function (ACF),

$$\phi(\tau) = \sigma_c^2 e^{-8\pi^2\tau^2\frac{\delta_v^2}{\lambda^2}} \tag{4.5}$$

at times $\tau = kT_{\text{PRI}}$ for $k = 0, \ldots, K_p - 1$. The sampled ACF are arranged to form the clutter covariance matrix,

$$\mathbf{\Sigma}_C = \sigma_c^2 \begin{bmatrix} \rho(0) & \rho(1) & \ldots & \rho(K_p-1) \\ \rho(1) & \rho(0) & \ldots & \vdots \\ \ldots & \ldots & \ddots & \rho(1) \\ \rho(K_p-1) & \ldots & \rho(1) & \rho(0) \end{bmatrix} \tag{4.6}$$

where, $\rho(k) = \phi(kT_{\text{PRI}})$ are the sampled ACF values.

Both the clutter and noise are independent, complex, zero-mean, Gaussian random vectors and are assumed to be the result of environmental factors such as background noise and reflections unrelated to the target of interest. The total clutter-plus-noise covariance matrix is,

$$\mathbf{\Sigma} = \mathbf{\Sigma}_C + \sigma_n^2\mathbf{I} \tag{4.7}$$

where σ_n^2 is the noise variance.

4.2.2 Problem Statement

Moving target detection consists of declaring either the presence or absence of a moving target within the range bin of interest, represented by hypothesises H_1 and H_0, respectively. The hypothesis test can be described mathematically as,

$$H_0 : \ \mathbf{x} = \mathbf{c} + \mathbf{n} \tag{4.8}$$

$$H_1 : \ \mathbf{x} = \alpha \mathbf{a}(f_0) + \mathbf{c} + \mathbf{n} \tag{4.9}$$

The radar output is the filtered slow-time data,

$$y = \mathbf{w}^H \mathbf{x} \tag{4.10}$$

where $\mathbf{w} \in \mathbb{C}^{K_p \times 1}$ is a filter which has been designed, according to some performance metric, to cancel the clutter and noise while retaining the target signal.

The test statistic for the moving target detection problem can be interpreted as the square of the filter output [66],

$$|y|^2 \underset{H_0}{\overset{H_1}{\gtrless}} \gamma \tag{4.11}$$

where γ is a threshold used to satisfy a prescribed probability of false alarm.

The focus of this chapter is to improve moving target detection performance by incorporating the unit circle roots constraint within the design of the filter $\mathbf{w}$.

4.3 The Adaptive Matched Filter

The optimum filter maximizes the signal-to-interference-plus-noise ratio (SINR) [75], [99], [94],

$$\mathrm{SINR} = \frac{\sigma_s^2 |\mathbf{w}^H \mathbf{a}\left(f_0\right)|^2}{\mathbf{w}^H \mathbf{\Sigma} \mathbf{w}} \tag{4.12}$$

where σ_s^2 is the variance or power of the complex target amplitude α. The optimal AMF can be derived in a variety of ways: via Lagrange multipliers [99], or by the Cauchy-Schwarz inequality [66]. Regardless of the means of derivation, the optimal filter takes the form

$$\mathbf{w}_{\text{opt}} \propto \kappa \mathbf{\Sigma}^{-1} \mathbf{a}(f_0) \tag{4.13}$$

where, κ is an arbitrary constant.

In this chapter, the AMF is derived by minimizing the expected output clutter-plus-noise power $\mathbf{w}^H \mathbf{\Sigma} \mathbf{w}$ subject to the linear constraint $\mathbf{w}^H \mathbf{a}\left(f_0\right) = c$, where c is a real constant. Since the SINR is unchanged by scaling the filter $\mathbf{w}$, the specific constant is arbitrary. However, selecting

$$c = \sqrt{\mathbf{a}^H \left(f_0\right) \mathbf{\Sigma}^{-1} \mathbf{a}\left(f_0\right)} \tag{4.14}$$

has been shown to provide CFAR behavior when the covariance matrix is unknown and results in the limiting case of the GLRT for a large number of secondary data [76]. Hence, we use this constant when deriving the AMF and the proposed unit-circle roots constrained AMF detector in the sequel.

In order to motivate the development of the proposed unit circle rectification approach, we first derive the AMF in the same way as the MVDR beamformer [13]. This will help establish the background and terminologies necessary to prove the claim that the AMF with perfectly known covariance matrix must also have unit circle roots. The necessary optimization is

$$\min_{\mathbf{w}} \ \mathbf{w}^H \mathbf{\Sigma} \mathbf{w} \quad \text{s.t. } \mathbf{w}^H \mathbf{a}(f_0) = c. \tag{4.15}$$

This optimization can be solved using Lagrange multipliers where

$$\mathcal{L}(\mathbf{w}) = \mathbf{w}^H \mathbf{\Sigma} \mathbf{w} + \lambda \left(\mathbf{w}^H \mathbf{a}\left(f_0\right) - c\right) \tag{4.16}$$

is the Lagrangian and λ is the associated multiplier. Taking the derivative of (4.16) and equating to zero results in,

$$\frac{\partial \mathcal{L}\left(\mathbf{w}\right)}{\partial \mathbf{w}} = \left(\boldsymbol{\Sigma}\mathbf{w}\right)^{*} + \lambda \mathbf{a}^{*}\left(f_0\right) = 0 \tag{4.17}$$

where $(\cdot)^{*}$ is the conjugation operator. Conjugating and solving for $\mathbf{w}$ yields,

$$\mathbf{w} = -\lambda^{*}\boldsymbol{\Sigma}^{-1}\mathbf{a}\left(f_0\right). \tag{4.18}$$

Substituting (4.18) into the linear constraint in (4.15) produces,

$$\lambda = -\frac{1}{c} \tag{4.19}$$

which, upon substitution back into (4.18), results in,

$$\mathbf{w}_{\mathrm{opt}} = \frac{\boldsymbol{\Sigma}^{-1}\mathbf{a}\left(f_0\right)}{\sqrt{\mathbf{a}^{H}\left(f_0\right)\boldsymbol{\Sigma}^{-1}\mathbf{a}\left(f_0\right)}} \tag{4.20}$$

as the optimum. Since (4.20) assumes perfect knowledge of the clutter-plus-noise covariance matrix, this filter will be referred to as the Clairvoyant, or optimal, for the remainder of this chapter.

Typically, the covariance matrix is unknown and is replaced by the SCM, which is computed from a set of target-free secondary data,

$$\hat{\boldsymbol{\Sigma}}_{\mathrm{SCM}} = \frac{1}{L}\sum_{i=1}^{L}\mathbf{x}_i\mathbf{x}_i^{H} \tag{4.21}$$

where $\mathbf{x}_i$ is the i-th secondary data vector and L is the number of secondary data. The SCM can be improved by incorporating forward-backward averaging resulting in the forward-backward SCM (FB-SCM) [46],

$$\hat{\mathbf{\Sigma}}_{\mathrm{FB-SCM}} = \frac{1}{2}\left(\hat{\mathbf{\Sigma}}_{\mathrm{SCM}} + \mathbf{J}\hat{\mathbf{\Sigma}}^{*}_{\mathrm{SCM}}\mathbf{J}\right) \tag{4.22}$$

where $\mathbf{J} \in \mathbb{R}^{K_p \times K_p}$ is the exchange matrix with ones along the anti-diagonal.

The target Doppler frequency is also unknown in practice and must be estimated. However, it is common in practice to segment the Doppler space into a number of cells and perform detection in each. Therefore, we assume perfect knowledge of f_0.

The conventional AMF replaces the true clutter-plus-noise covariance matrix in (4.20) with the SCM [76],

$$\mathbf{w}_{\mathrm{AMF}} = \frac{\hat{\mathbf{\Sigma}}^{-1}_{\mathrm{SCM}}\mathbf{a}\left(f_0\right)}{\sqrt{\mathbf{a}^{H}\left(f_0\right)\hat{\mathbf{\Sigma}}^{-1}_{\mathrm{SCM}}\mathbf{a}\left(f_0\right)}} \tag{4.23}$$

and will be hereafter referred to as the AMF.

4.4 Unit Circle Roots Constrained AMF

Theorem 1 establishes the theoretical necessity of unit circle roots for the Clairvoyant AMF. However, when the SCM is used to compute the filter, the roots rarely occur on the unit circle.

For a polynomial to have unit circle roots, two conditions must be satisfied [89], [65]:

C1: The coefficients exhibit conjugate-symmetry

$$w(k) = w^{*}(K-k) \;\; \text{for } k = 0, \ldots, K \tag{4.24}$$

and

C2: The derivative of $W(z)$ must have roots either on or inside the unit circle.

C2 requires non-linear optimization to impose [89] and is, therefore, too restrictive

Algorithm 2: UCRC-AMF

INPUT: $\hat{\boldsymbol{\Sigma}}_{\text{SCM}}$, $\mathbf{a}\left(f_0\right)$, c

start: $\mathbf{w}_{\text{AMF}} = \dfrac{\hat{\boldsymbol{\Sigma}}_{\text{SCM}}^{-1}\mathbf{a}(f_0)}{\sqrt{\mathbf{a}^H(f_0)\hat{\boldsymbol{\Sigma}}_{\text{SCM}}^{-1}\mathbf{a}(f_0)}}$

$\boldsymbol{\zeta} \leftarrow \text{roots}\{\mathcal{Z}\{\mathbf{w}_{\text{AMF}}\}\}$ ▷ I

$i = 1$ **up to** $i = K$

$W_{K-(i)}(z) = \prod_{j \neq i}(1 - \zeta_j z^{-1})$

$\boldsymbol{\Sigma}_i^W = \mathbf{W}_{K-(i)}^H \hat{\boldsymbol{\Sigma}}_{\text{SCM}} \mathbf{W}_{K-(i)}$ ▷ II

$\tilde{\boldsymbol{\Sigma}}_i = \frac{1}{2}\left(\boldsymbol{\Sigma}_i^W + \mathbf{J}\boldsymbol{\Sigma}_i^{W*}\mathbf{J}\right)$ ▷ III

$\mathbf{q}_i = \mathbf{W}_{K-(i)}^H \mathbf{a}\left(f_0\right)$ ▷ IV

$\hat{\mathbf{w}}_i = \tilde{\boldsymbol{\Sigma}}_i^{-1}\mathbf{q}_i$ ▷ V

$\zeta_i = \hat{w}_i(1)/\hat{w}_i(0)$ ▷ VI

end

OUTPUT:

$W_{\text{UC}}(z) = \prod_{i=1}^{K}(1 - \zeta_i z^{-1}) \xrightarrow{Z^{-1}} \hat{\mathbf{w}}$

$\mathbf{w}_{\text{UCRC}-\text{AMF}} = c\frac{\hat{\mathbf{w}}}{\mathbf{a}^H(f_0)\hat{\mathbf{w}}}$

for the present application. When $K = 1$, the derivative of $W(z)$ is a scalar rendering $\mathbf{C}2$ negligible and $\mathbf{C}1$ is sufficient to ensure unit circle roots [89]. Hence, we enforce unit circle roots by imposing $\mathbf{C}1$ onto the order-one factors of $W(z)$.

The UCRC-AMF derivation described below closely follows the one for UCRC-MVDR given in Chapter 3, but is included here for completeness' sake. There are some key differences in the implementation steps, as will be pointed out later in this Chapter.

Rewriting $W(z)$ in factored form [89],

$$W_{(i)}(z) = W_{K-(i)}(z)w_i(z);\ 1 \leq i \leq K \tag{4.25}$$

where $w_i(z) = w_i - w_i^* z^{-1}$ and $W_{K-(i)}(z)$ is a $(K-1)$-th order polynomial formed with $K - 1$ known roots excluding the i-th root. $w_i(z)$ represents the i-th first-order factor whose root needs to be placed on the unit-circle. The factored weight vector corresponding to $W_{(i)}(z)$ in (4.25) can be written as a convolution matrix-vector product [89],

$$\mathbf{w}_{(i)} = \mathbf{W}_{K-(i)}\mathbf{w}_i; \quad 1 \leq i \leq K \tag{4.26}$$

where $\mathbf{w}_i = [w_i \quad w_i^*]^T \in \mathbb{C}^{2\times 1}$. Using this factorization, the K_p-dimensional optimization in (4.15) can be split into K 1-dimensional optimization problems. The columns of the convolution matrix,

$$\mathbf{W}_{K-(i)} = \begin{bmatrix} w_{K-(i)}(0) & 0 \\ w_{K-(i)}(1) & w_{K-(i)}(0) \\ \cdots & \cdots \\ 0 & w_{K-(i)}(K-1) \end{bmatrix} \in \mathbb{C}^{K_p\times 2} \tag{4.27}$$

consist of the coefficients of $W_{K-(i)}(z)$. However, unlike in Chapter 3, $W_{K-(i)}(z)$ for UCRC-AMF is a $(K-1)$-th order polynomial formed using the $i-1$ previously estimated unit circle roots and the $K-i$ remaining SMI-based AMF roots while excluding the i-th root that is being updated. The reformulated 1st-order AMF optimization problem becomes,

$$\begin{aligned} \min_{\mathbf{w}_i} \ & \mathbf{w}_i^H \mathbf{W}_{K-(i)}^H \boldsymbol{\Sigma} \mathbf{W}_{K-(i)} \mathbf{w}_i \\ \text{s.t. } & \mathbf{w}_i^H \mathbf{W}_{K-(i)}^H \mathbf{a}\left(f_0\right) = c; \quad 1 \leq i \leq K \end{aligned} \tag{4.28}$$

where this optimization is performed K times to place individual roots onto the unit circle.

Call $\boldsymbol{\Sigma}_i^W = \mathbf{W}_{K-(i)}^H \boldsymbol{\Sigma} \mathbf{W}_{K-(i)} \in \mathbb{C}^{2\times 2}$ and $\mathbf{q}_i = \mathbf{W}_{K-(i)}^H \mathbf{a}\left(f_0\right) \in \mathbb{C}^{2\times 1}$, the weighted covariance matrix and weighted steering vector, respectively. The optimizations in (4.28) can now be written compactly,

$$\min_{\mathbf{w}_i} \ \mathbf{w}_i^H \boldsymbol{\Sigma}_i^W \mathbf{w}_i \quad \text{s.t. } \mathbf{w}_i^H \mathbf{q}_i = c; \quad 1 \leq i \leq K. \tag{4.29}$$

Interestingly, forward-backward averaging the weighted covariance matrix $\boldsymbol{\Sigma}_i^W$ will ensure that the $\mathbf{w}_i$ are conjugate-symmetric [46]. The forward-backward averaged weighted covariance matrix is defined as [46],

$$\tilde{\mathbf{\Sigma}}_i = \frac{1}{2}\left(\mathbf{\Sigma}_i^W + \mathbf{J}\mathbf{\Sigma}_i^{W*}\mathbf{J}\right) \in \mathbb{C}^{2\times 2}; \quad 1 \leq i \leq K \tag{4.30}$$

where, $\mathbf{J} \in \mathbb{R}^{2\times 2}$ is the exchange matrix with ones along the anti-diagonal. Substituting (4.30) into (4.29),

$$\min_{\mathbf{w}_i} \ \mathbf{w}_i^H \tilde{\mathbf{\Sigma}}_i \mathbf{w}_i \quad \text{s.t. } \mathbf{w}_i^H \mathbf{q}_i = c; \quad 1 \leq i \leq K. \tag{4.31}$$

This minimization can be solved by invoking the theory of Lagrange multipliers where the Lagrangian is

$$\mathcal{L}(\mathbf{w}_i) = \mathbf{w}_i^H \tilde{\mathbf{\Sigma}}_i \mathbf{w}_i + \lambda_i(\mathbf{w}_i^H \mathbf{q}_i - c); \quad 1 \leq i \leq K \tag{4.32}$$

and λ_i is the associated multiplier. Taking the derivative with respect to $\mathbf{w}_i$ and equating to zero results in,

$$\frac{\partial \mathcal{L}(\mathbf{w}_i)}{\partial \mathbf{w}_i} = (\tilde{\mathbf{\Sigma}}_i \mathbf{w}_i)^* + \lambda_i \mathbf{q}_i^* = 0; \quad 1 \leq i \leq K. \tag{4.33}$$

The root of the polynomial $w_i(z)$ is unaffected by scaling the coefficients hence, we solve (4.33) for $\mathbf{w}_i$ and disregard the constant λ_i to retain

$$\hat{\mathbf{w}}_i = \tilde{\mathbf{\Sigma}}_i^{-1} \mathbf{q}_i; \quad 1 \leq i \leq K. \tag{4.34}$$

The root estimate is $\zeta_i = \hat{w}_i(1)/\hat{w}_i(0)$. The filter polynomial with unit circle roots is

$$W_{\text{UC}}(z) = \prod_{i=1}^{K}\left(1 - \zeta_i z^{-1}\right). \tag{4.35}$$

To construct the filter vector which satisfies the linear constraint in (4.15), define the auxiliary vector $\hat{\mathbf{w}} = \mathcal{Z}^{-1}\{W_{\mathrm{UC}}(z)\}$, where $\mathcal{Z}^{-1}\{\cdot\}$ is the inverse z-transform. Scaling $\hat{\mathbf{w}}$ produces [101],

$$\mathbf{w}_{\mathrm{UCRC-AMF}} = c\frac{\hat{\mathbf{w}}}{\mathbf{a}^{H}\left(f_0\right)\hat{\mathbf{w}}} \tag{4.36}$$

which satisfies the linear constraint.

In practice, the true covariance matrix is not known and must be estimated. Consequently, $\mathbf{\Sigma}_i^W$, c, and $\mathbf{W}_{K-(i)}$ are replaced with their empirical counterparts based on the SCM and AMF roots, respectively. Each of the $\hat{\mathbf{w}}_i$ can be computed in closed form, and correspond to a unit circle root. Pseudocode of the UCRC-AMF is provided in Algorithm-2.

4.4.1 The Modified UCRC-AMF

The Modified UCRC-AMF (M-UCRC-AMF) is distinct from the UCRC-AMF, where the primary modification is the use of the FB-SCM to compute the constant c in (4.14) and within step-II of Algorithm 2. $\hat{\Sigma}_{\mathrm{FB-SCM}}$ has complex persymmetric structure and in literature, such structure have been extensively used in time-series modelling [103], spectrum estimation [56], MVDR beamforming [46], adaptive matched filtering [69], and many other related fields to achieve improved performance. For the proposed M-UCRC-AMF algorithm, using $\hat{\Sigma}_{\mathrm{FB-SCM}}$ over $\hat{\Sigma}_{\mathrm{SCM}}$ in step-II of Algorithm 2 and in evaluating the constant c drastically improves the estimated unit circle root locations and detection performance without requiring any additional steps or complexity to the UCRC-AMF algorithm. More importantly, M-UCRC-AMF provides improved detection performance and output SINR over the UCRC-AMF, as will be shown in the simulation section. It is worth noting that despite these minor changes between the UCRC-AMF and modified UCRC-AMF, the choice of initial estimates remains the same, as explained in the following subsection.

4.4.2 Differences Between UCRC-MVDR and M-UCRC/UCRC-AMF

Unlike the UCRC-MVDR discussed in Chapter 3, the roots of the UCRC-AMF are updated in series instead of in parallel. In this way, the i-th root, ζ_i, is updated based on the previously estimated roots ζ_{i-1}, ζ_{i-2}, etc, that are already on the unit circle.

Both the M-UCRC/UCRC-AMF and UCRC-MVDR are initialized using the roots of the SMI-based adaptive filter (see step-I in algorithms 1 and 2). However, for M-UCRC/UCRC-AMF the i-th root estimate is computed based on the $i-1$ previously estimated unit circle roots and the remaining $K-i-1$ SMI roots. All roots except the i-th are assumed to be constant, and encapsulated in the matrix (4.27). Furthermore, M-UCRC/UCRC-AMF enforce conjugate symmetry implicitly via forward backward averaging of the weighted covariance matrix, instead of explicitly enforcing this property using the $\mathbf{C}$ matrix described in Chapter 3, although the latter can be used instead and will produce the same results.

The other notable difference between the proposed detectors and the UCRC-MVDR is the constant c used to normalize the output filter. For UCRC-MVDR, $c = 1$ preserves the distortionless response constraint. The normalization of the M-UCRC/UCRC-AMF using $c = \sqrt{\mathbf{a}^H(f_0)\,\boldsymbol{\Sigma}^{-1}\mathbf{a}(f_0)}$ (see (4.14)) results in the same output at the target Doppler frequency for the AMF and FB-AMF, which we hypothesis is the reason why the M-UCRC/UCRC-AMF have approximate CFAR behaviour. It will be shown empirically that the proposed detectors have approximate CFAR later in this chapter.

The final difference between M-UCRC/UCRC-AMF and UCRC-MVDR is the former do not implement the mainbeam protection strategy described in Chapter 3. Mainbeam protection is not applicable for moving target detection since target contamination in the secondary snapshots is not assumed in this chapter. However, the same strategy could be used to accommodate target-contaminated secondary data in the same way as described for the UCRC-MVDR.

4.4.3 Choice of Initial Estimates and Computational Complexity Issues

Proper choice of initializing the UCRC-AMF and M-UCRC-AMF algorithm is important for achieving desirable performance. Using the SCM to compute AMF will be shown to result in roots that are well distributed around the unit circle. Therefore, conventional SCM-based AMF roots serve as a good initial choice for the proposed M-UCRC-AMF and UCRC-AMF algorithms. It may be further noted that using the FB-SCM to compute the AMF results in a conjugate symmetric filter [46] that satisfies condition $\mathbf{C}1$ in (4.24). However, in that case, the roots occur either on the unit circle or in conjugate pairs. This angular redundancy reduces the overall degrees of freedom and makes FB-SCM a poor choice for initiating the proposed algorithms.

Essentially, the SCM provides good initial root estimates in step-I of both UCRC-AMF and M-UCRC-AMF, while the FB-SCM is a superior covariance matrix estimate to use in step-II of M-UCRC-AMF for the subsequent unit circle root estimates.

Equation (4.34) expresses the 2×1 estimated weight vector $\mathbf{w}_i$ in closed-form and requires only a 2×2 matrix inverse, which can be computed algebraically and has a trivial computational cost. Consequentially, each root estimate ζ_i can be obtained with computational ease.

Also, since the coefficients in each $\hat{\mathbf{w}}_i$ are complex-conjugate of each other by design, the roots of the individual 1st-order polynomials, $\hat{w}_i(z) = \hat{w}_i - \hat{w}_i^* z^{-1}$ are guaranteed to lie on the unit circle. Then the K-th order conjugate-symmetric polynomial $W_{\mathrm{UCRC-AMF}}(z)$ corresponding to (4.36) will also have UC roots that are obtained by minimizing the output clutter and noise power at every step. More importantly, the UC roots property of Theorem 1 is achieved without resorting to complex iterative optimization procedure or special-purpose optimization software as would be needed if the derivative constraint in $\mathbf{C}2$ were to be optimized for the K_p-th order polynomial instead.

Both the UCRC-AMF and M-UCRC-AMF leverage the SMI-based AMF as their starting point, where the algorithm places each i-th root on the unit-circle using the AMF roots. Due to the inversion of the SCM, the AMF has a computational complexity on the order of $\mathrm{O}(K_p^3)$ [75]. Since the proposed approach requires computing the conventional AMF, the same $\mathrm{O}(K_p^3)$ cost will be incurred.

Step-II is the most computationally complex after computing the AMF, and requires $2(2K_p - 1)K_p + 4(2K_p - 1)$ flops (*i.e.*, complex multiplications and additions) to compute the Hermitian form. Step-IV requires $2(2K_p - 1)$ flops to compute the transformed steering vector $\mathbf{q}_i$. Steps III, V, and VI are performed using either scalars or 2x2 matrices which are independent of the number of pulses K_p and are therefore omitted from the analysis. In total, to place one root on the unit circle requires $2(2K_p - 1)(K_p + 3)$ flops. This process must be performed $K_p - 1$ times to place all roots there and hence, the total flop count is $2(2K_p - 1)(K_p + 3)(K_p - 1) = 4K_p^3 + 6K_p^2 - 16K_p + 6$ flops or $\mathrm{O}(K_p^3)$.

The UCRC-AMF and M-UCRC-AMF are initialized using the SMI-based AMF, and based on the previous analysis placing all roots onto the unit circle has a proportional complexity. Therefore, it can be concluded that $\mathrm{O}(K_p^3)$ is the asymptotic complexity of both the UCRC-AMF and M-UCRC-AMF.

4.5 Simulation Examples

The efficacy of the UCRC-AMF and M-UCRC-AMF are demonstrated using several simulation examples where the simulation parameters are described as follows. A radar operating frequency of $f_c = 1$ GHz is used with a pulse repetition frequency (PRF) of 500 Hz. A single moving target is moving along a linear trajectory with constant velocity $|\mathbf{v}_t|= 108$ km/h and heading $30°$ with respect to the positive x-axis. The angle of the receiver/-transmitter with respect to the target is $\theta_r = 10°$ (see Fig. 4.1). The normalized target Doppler frequency is $f_0 = 0.3761$. Both the clutter-plus-noise covariance matrix $\mathbf{\Sigma}$ and complex target amplitude α are assumed unknown.

The detection performance is quantified using the receiver operating characteristic (ROC) for fixed clutter-to-noise ratio (CNR) and signal-to-noise ratio (SNR). Probability of detection versus SINR curves are also generated assuming a fixed probability of false alarm.

The CNR,

$$\mathrm{CNR} = K_p \frac{\sigma_c^2}{\sigma_n^2} \tag{4.37}$$

is fixed at 40 dB for all examples, unless stated otherwise. We define the SNR as,

$$\mathrm{SNR} = K_p \frac{\sigma_s^2}{\sigma_n^2} \tag{4.38}$$

where σ_n^2 is the noise variance. Unless noted otherwise, the secondary data are assumed to be limited with $L = K_p + 1$ snapshots, *i.e.,* barely sufficient to invert the SCM.

The thresholds used in (4.11) for the AMF, PS-AMF, M-UCRC-AMF, and UCRC-AMF detectors are computed empirically using the simulation data. Each of the curves in Figs. 4.4, 4.5, 4.6, and 4.7 are computed using Monte-Carlo-based simulations, where P_{FA} and $N_{\mathrm{MC}} = 100/P_{\mathrm{FA}}$ are the minimum probability of false alarm and number of trials, respectively.

4.5.1 Example 1 : AMF Root Locations and Magnitude Response

Fig. 4.2a shows the roots of the AMF, Clairvoyant, UCRC-AMF, and M-UCRC-AMF plotted in the complex plane, where the number of pulses is $K_p = 16$ to ensure that the plot is not too populated. The $\mathrm{CNR} = 40$ dB with an RMS clutter velocity of $\delta_v = 1.5$ m/s. Note that in Fig. 4.2a all roots for the Clairvoyant AMF lie on the unit circle, satisfying Theorem 1. On the other hand, none of roots for conventional AMF fall on the unit circle and only a few of the AMF roots come close to the unit circle near $(1, 0)$. This may explain the relatively poor performance of the AMF for the limited data case. Both the UCRC-AMF and M-UCRC-AMF have unit circle roots, as designed.

Fig. 4.3 depicts the normalized filter magnitude responses corresponding to the roots depicted in Fig. 4.2a, where the normalized clutter power spectral density has also been superimposed. Fig. 4.3 shows that the majority of the clutter energy is concentrated around zero-Doppler. Therefore, it is not surprising that the Clairvoyant, AMF, UCRC-AMF, and M-UCRC-AMF place multiple roots, i.e., zeros, in the zero-Doppler frequency region. However, since both the UCRC-AMF and M-UCRC-AMF enforce the unit circle roots constraint while the AMF does not, deeper nulls in the frequency response of the UCRC-AMF and M-UCRC-AMF can be expected, which will suppress more of the clutter than the AMF. This observation is corroborated by Fig. 4.3, which also shows that strong peaks at the known target Doppler frequency were produced by all the adaptive detectors. It can be observed however that for the traditional AMF case, the peak at the target Doppler is slightly weaker than all other cases, indicating potential signal attenuation, further explaining its poor detection performance for the limited secondary data scenario.

The roots of the PS-AMF [69, 62] are shown in Fig. 4.2b for both the Clairvoyant and estimated versions of this filter. It is clear that the PS-AMF does not produce unit circle roots even in the Clairvoyant case and therefore, enforcing the unit circle roots constraint is impractical for this filter. The roots of the FB-AMF (*i.e.*, the AMF with the FB-SCM used in place of the SCM) are also shown in Fig. 4.2b. Some FB-AMF roots appear on the unit circle however, others appear in conjugate pairs, which is an inefficient usage of the available degrees of freedom. It is hypothesized that this root behaviour is the reason the FB-AMF roots are a poor starting point for the UCRC-AMF and M-UCRC-AMF algorithms.

Fig. 4.3 also plots the magnitude response for PS-AMF, where the magnitude response of the PS-AMF in Fig. 4.3 is the filter output power at the frequency f corresponding to transformed steering vector $\mathbf{s}(f) = \mathbf{Ta}(f)$. Since the PS-AMF is applied to the transformed real data, the filter output is evaluated on an image of the unit circle under the transformation $\mathbf{T}$ which is defined in [69].

4.5.2 Example 2 : Non-Fluctuating Target Detection

In this example, the detection performance of the M-UCRC-AMF and UCRC-AMF are compared to the AMF and PS-AMF for a non-fluctuating target using a CPI length of $K_p = 32$ in clutter with $\delta_v = 1.5$ m/s. $\mathrm{SNR} = 13$ dB is used to generate the receiver operating characteristics shown in Fig. 4.4. We also generate the probability of detection versus SINR shown in Fig. 4.5, where a minimum probability $P_{\mathrm{FA}} = 10^{-3}$ is used to ease the computational burden.

In Figs. 4.4 and 4.5, the AMF performance is unsurprisingly poor due to the lack of substantial secondary data whereas the UCRC-AMF is not as adversely impacted. This observation implies that judicious enforcement of the unit circle constraint can improve the robustness of the AMF to limited secondary data. The M-UCRC-AMF performance is superior to the PS-AMF, showing a roughly 40% improvement in P_D at the lowest $P_{FA} = 10^{-4}$ and approximately 2 dB SINR improvement over the PS-AMF in Fig. 4.5. The M-UCRC-AMF dramatically outperforms the UCRC-AMF, showcasing the utility of the proposed modification, which utilizes FB-SCM as described in Section 4.4.1. The results of Figs. 4.4 and 4.5 demonstrate that the M-UCRC-AMF is the practical choice in limited data circumstances over both the PS-AMF and conventional AMF.

The FB-AMF performance is included in Figures 4.4 and 4.5 to draw comparisons with the PS-AMF. The two detectors have identical performance as shown in the figures, and this is not surprising since the FB-SCM and transformation $\mathbf{T}$ are both designed to exploit the symmetry present in the true covariance matrix. However, examining Figure 4.2b shows that the two detectors have different roots. We speculate that the PS-AMF is the image of the FB-AMF under the unitary transformation $\mathbf{T}$, at least in the Clairvoyant case.

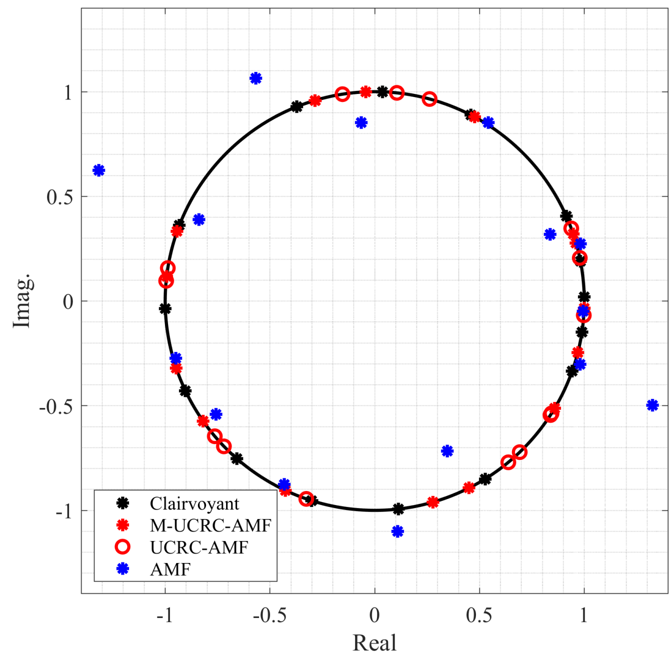

(a) M-UCRC-AMF, UCRC-AMF, and AMF roots.

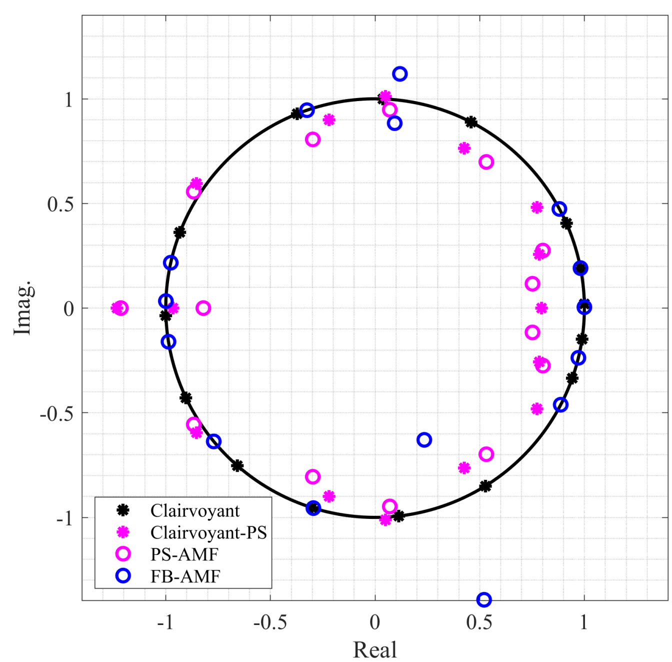

(b) PS-AMF roots.

Figure 4.2: Root locations in the complex plane.

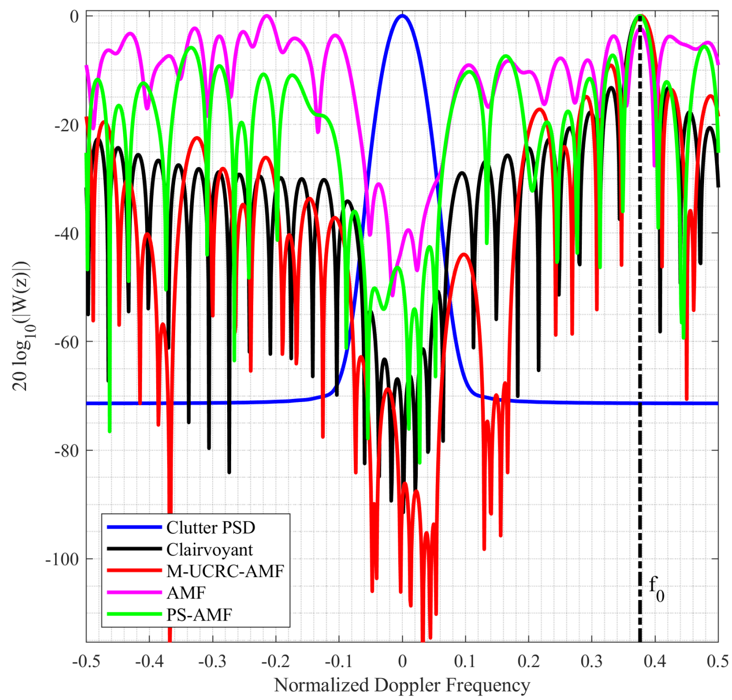

Figure 4.3: Normalized filter responses and clutter PSD

Therefore, it could be that the roots of the PS-AMF are the image of the FB-AMF roots under this same transformation. The FB-AMF performance is excluded from the proceeding figures due to the identical performance with the PS-AMF.

4.5.3 Example 3 : Fluctuating Target Detection

In this example, the performance of the M-UCRC-AMF and UCRC-AMF are examined assuming a fluctuating target amplitude. The target amplitude α is modeled as complex Gaussian with variance σ_s^2 scaled to meet a prescribed SINR or SNR. The parameters for this example are identical to those used in Example 2 with the exception of $\mathrm{SNR} = 10$ dB used to generate Fig. 4.6. Minimum probability $P_{\mathrm{FA}} = 10^{-3}$ is used to generate Fig. 4.7.

Figs. 4.6 and 4.7 demonstrate the performance of the AMF, PS-AMF, M-UCRC-AMF, UCRC-AMF, and Clairvoyant detectors in terms of the probability of detection versus false

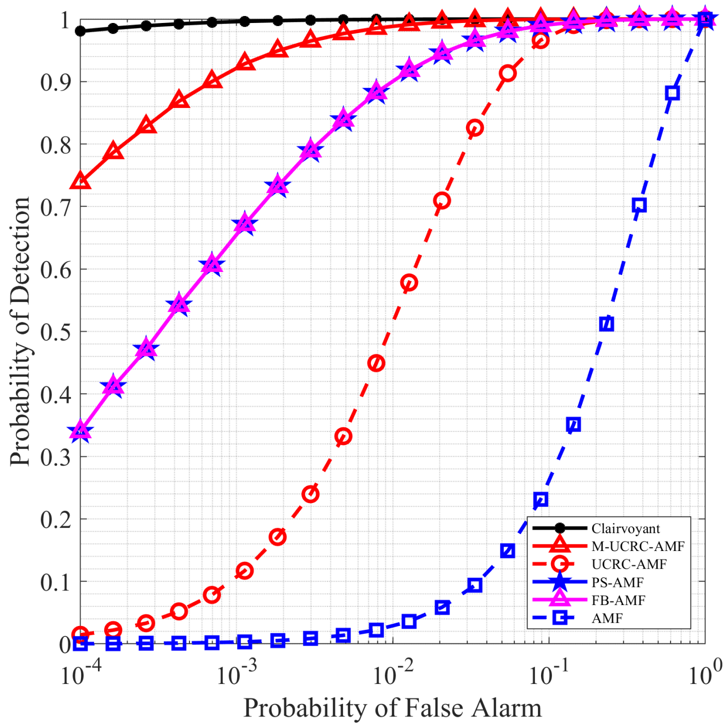

Figure 4.4: ROC with limited secondary data.

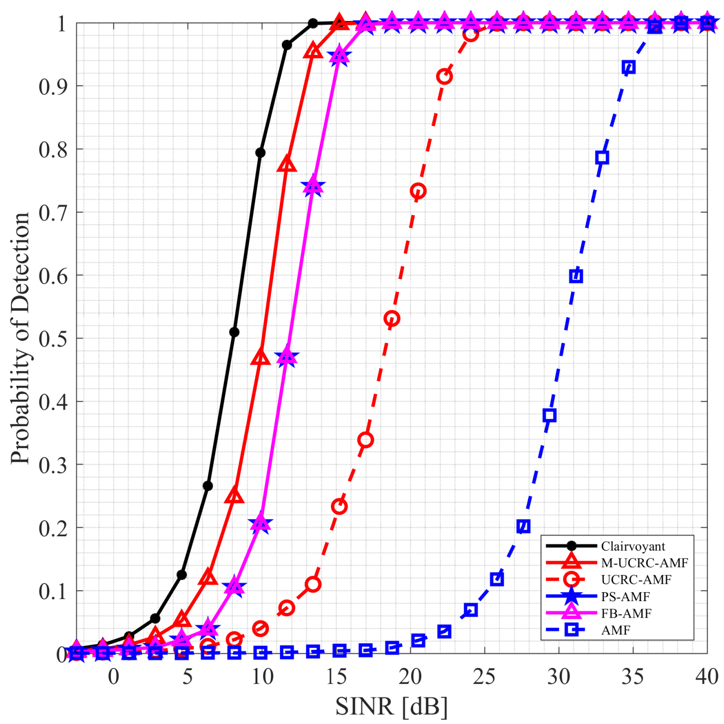

Figure 4.5: Probability of detection vs. SINR with limited secondary data.

alarm rate and SINR, respectively. From both figures it is evident that the random nature of the target amplitude has impacted the performance of all detectors. However, despite the deleterious effects of the fluctuating amplitude and limited secondary data, the M-UCRC-AMF and UCRC-AMF show superior detection performance when compared to the PS-AMF and AMF, respectively. These results further emphasize the utility of the proposed unit circle approach in practical target detection scenarios.

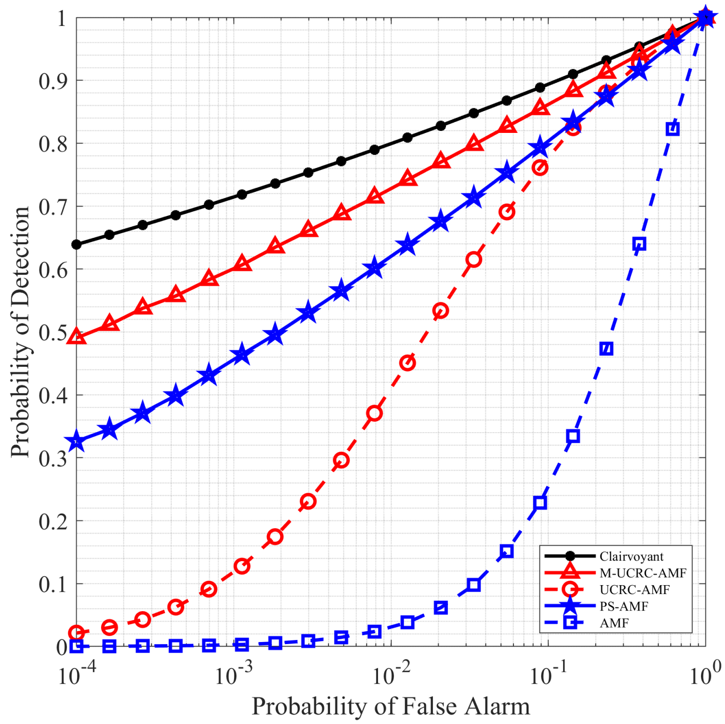

Figure 4.6: ROC for fluctuating target with limited secondary data.

4.5.4 Example 4 : SINR Improvement vs. Number of Corrected Roots

Since the focus of this chapter is the impact of enforcing unit circle roots upon the AMF, it is illustrative to examine the output SINR performance as the subsequent roots are placed onto the unit circle using Algorithm 2 and the proposed modification wherein the SCM is replaced by the FB-SCM.

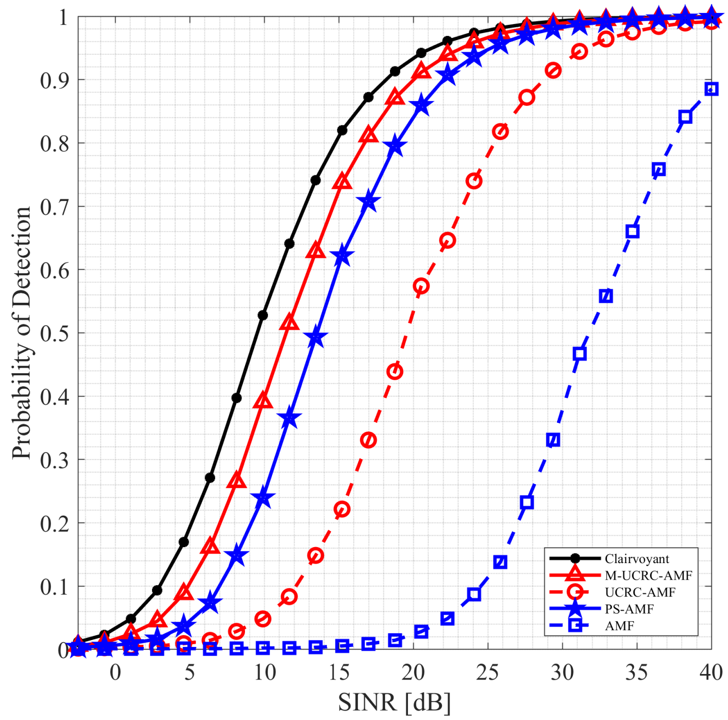

Figure 4.7: Probability of detection vs. SINR for fluctuating target with limited secondary data.

As each of the i roots are corrected, the remaining $K - i$ roots are left as the AMF roots for $i = 0, \ldots K$. For this example, the true covariance matrix is set as $\mathbf{\Sigma} = \mathbf{I}$ so that the Clairvoyant filter is $\mathbf{w}_{\text{opt}} = \mathbf{a}(f_0)/\sqrt{K_p}$ and the optimal SINR is K_p. The CPI length is $K_p = 32$ and a hypothetical target is assumed to be present with $\text{SNR} = 0$ dB for the purposes of computing the SINR.

The horizontal axis of Fig. 4.8 shows the number of roots corrected, where the far left point corresponds to the zero roots corrected case (*i.e.*, the AMF) while the far right point corresponds to the case where all roots have been placed on the unit circle (i.e., UCRC-AMF or M-UCRC-AMF). The Clairvoyant, PS-AMF, and AMF are shown as benchmarks and limiting cases. Finally, for each point in Fig. 4.8, the computed SINR is averaged over 10^4 Monte-Carlo trials and displayed in dB on the vertical axis.

It is evident from Fig. 4.8 that as the number of roots placed onto the unit circle increases, the average SINR also increases, further justifying the imposition of the unit circle constraint. The SINR improvement of the M-UCRC-AMF over the UCRC-AMF as more roots are corrected is evidence of the improved root estimates provided by using the FB-SCM over the SCM. Furthermore, since the SINR is invariant to the filter scaling, it is hypothesized that the increase in SINR performance of the proposed approach is due to the unit circle structure alone.

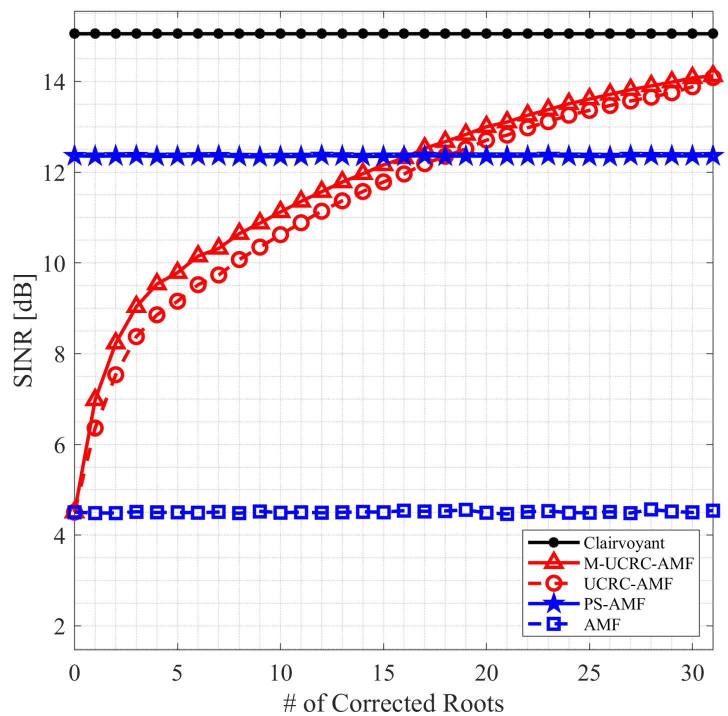

Figure 4.8: Average SINR vs. number of roots placed on the unit circle.

4.5.5 Example 5 : SINR vs. Number of Secondary Data

Fig. 4.9 shows the average output SINR versus the number of secondary data for the M-UCRC-AMF, UCRC-AMF, PS-AMF, and AMF using a CPI length of $K_p = 32$ pulses. The average SINR is computed using (4.12) by averaging over 2000 independent trials. For this example, the clutter plus noise covariance matrix is $\mathbf{\Sigma} = \mathbf{I}$ so that the optimal output SINR is K_p which is shown in black in Fig. 4.9 as a performance benchmark.

The two UCRC-based approaches outperform both the PS-AMF and AMF for limited secondary data, providing nearly 2 dB SINR improvement over the PS-AMF. Additionally, both the M-UCRC-AMF and UCRC-AMF show consistent performance across all secondary dataset sizes.

Because of the dramatic detection performance of the M-UCRC-AMF over the UCRC-AMF, only the M-UCRC-AMF will be considered for the remaining two examples.

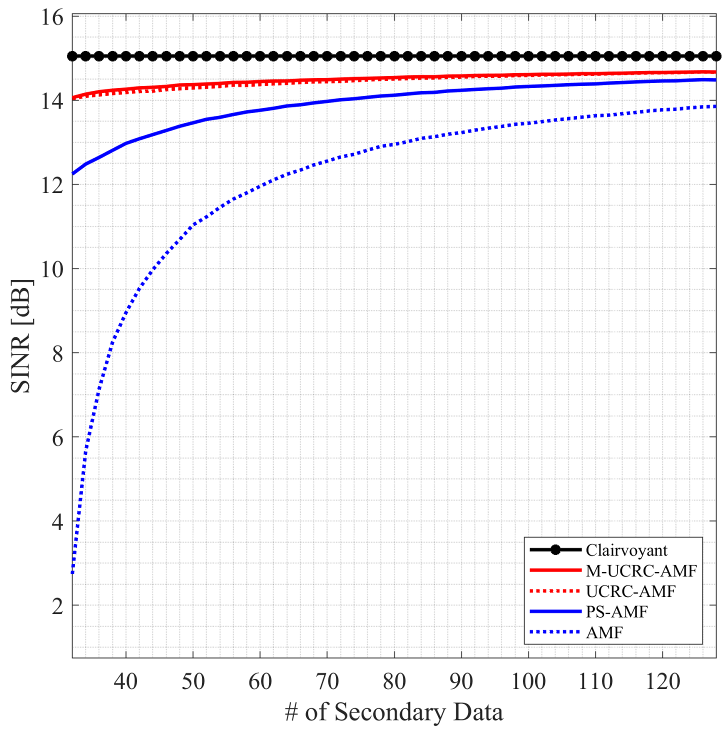

Figure 4.9: Output SINR vs. secondary data.

4.5.6 Example 6 : SINR Loss

The SINR loss is a common metric used to quantify moving target detection performance [66]. Defined as the ratio of the clutter-limited performance with respect to the optimal output SNR, SINR loss characterizes the minimum detection velocity offered by a a moving target detection approach. The optimal output SNR is obtained by substituting (4.20) into

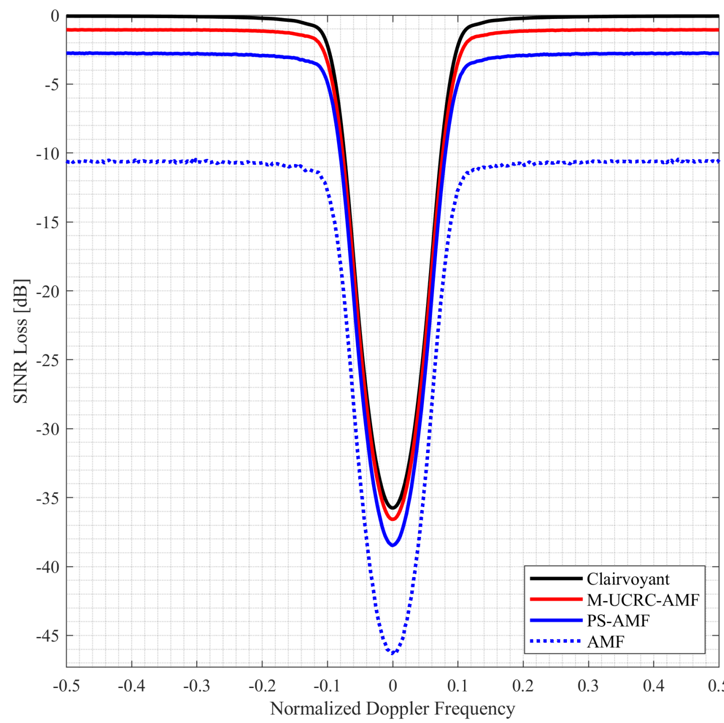

(a) SINR loss for $\delta_v = 1.5$ m/s.

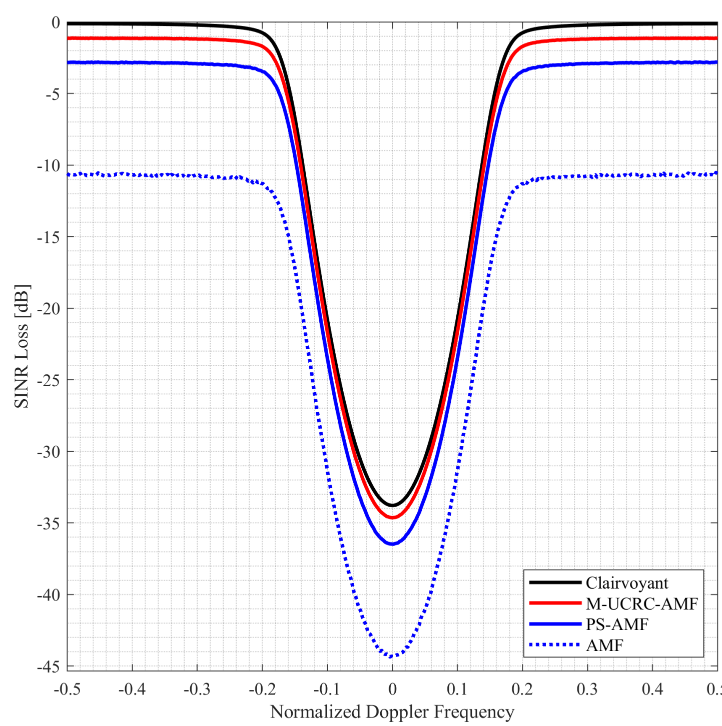

(b) SINR loss for $\delta_v = 3$ m/s.

Figure 4.10: SINR loss for varying RMS clutter velocity.

(4.12) and by replacing $\mathbf{\Sigma}$ with $\mathbf{I}$,

$$\mathrm{SNR}_{\mathrm{opt}} = \frac{\sigma_s^2}{\sigma_n^2} K_P \tag{4.39}$$

where σ_s^2 is the variance or power of the complex target amplitude α. The SINR loss is the ratio of (4.12) and (4.39) [66],[40],

$$\mathrm{SINR}_L(f_d) = \mathrm{SINR} / \Big(\frac{\sigma_s^2}{\sigma_n^2} K_P \Big) \tag{4.40}$$

where f_d is a normalized Doppler frequency.

Figs 4.10a and 4.10b demonstrate the SINR loss of the M-UCRC-AMF, PS-AMF, and AMF for RMS clutter velocities $\delta_v = 1.5$ and $\delta_v = 3$ m/s, respectively. The CPI length is $K_p = 32$ pulses and $L = 33$ secondary snapshots are used to compute the SCM. The Clairvoyant results are included in both figures as performance benchmarks.

In both figures, the M-UCRC-AMF achieves near optimal SINR loss. The PS-AMF also performs well, but it is evident from both figures that the proposed unit circle root constrained approach outperforms the PS-AMF. It is clear that the increased clutter spread provided by $\delta_v = 3$ m/s shown in Fig. 4.10b has little impact upon the M-UCRC-AMF performance, where the AMF performance is impacted by this parameter. The near optimal M-UCRC-AMF SINR loss demonstrates that the proposed detector can detect slower moving targets than the PS-AMF or conventional AMF.

4.5.7 Example 7 : Detection Performance with Unknown Target Doppler Frequency

In practice, the target Doppler frequency is unknown and must be estimated from the primary data. The maximum likelihood estimate of the normalized frequency can be found by maximizing

$$\hat{f}_0 = \max_f \frac{|\mathbf{a}^H(f)\hat{\mathbf{\Sigma}}^{-1}\mathbf{x}|^2}{\mathbf{a}^H(f)\hat{\mathbf{\Sigma}}^{-1}\mathbf{a}(f)}, \tag{4.41}$$

where $\hat{\mathbf{\Sigma}}$ is an estimate of the clutter covariance matrix. This maximization can be performed efficiently by applying a length N_{FT} discrete Fourier transform to the whitened primary data and searching for the peak.

For this example, we consider the detection performance of the M-UCRC and UCRC AMF approaches when the target Doppler frequency is unknown, and we will estimate f_0 using (4.41) and a length $N_{\text{FT}} = 1024$ Fourier transform. We will use $\hat{\mathbf{\Sigma}}_{\text{FB}-\text{SCM}}$ as the covariance estimate in (4.41), in order to provide the most accurate estimate of f_0 given the secondary data. All of the parameters for this example are identical to those used in Section 4.5.2 with the exception of the unknown target frequency.

The performance curves are shown in Figs. 4.11a and 4.11b, where again $P_{\text{FA}} = 10^{-3}$ is used in generating Fig. 4.11b to ease the computational burden. The known f_0 performances are included in both figures as a benchmark. The most dramatic performance impact is depicted in Fig. 4.11a, where the unknown frequency results in a roughly 35 percent reduction in the probability of detection of the M-UCRC-AMF versus when f_0 is known at $P_{\text{FA}} = 10^{-4}$. Despite the performance degradation of the M-UCRC-AMF, this detector consistently outperforms in the UCRC-AMF at all false alarm rates. Additionally, closely examining Fig. 4.11b shows a roughly 2.5 dB performance loss between the two M-UCRC-AMF curves and roughly 4 dB performance loss for the UCRC-AMF around the $P_{\text{D}} = 0.5$ level.

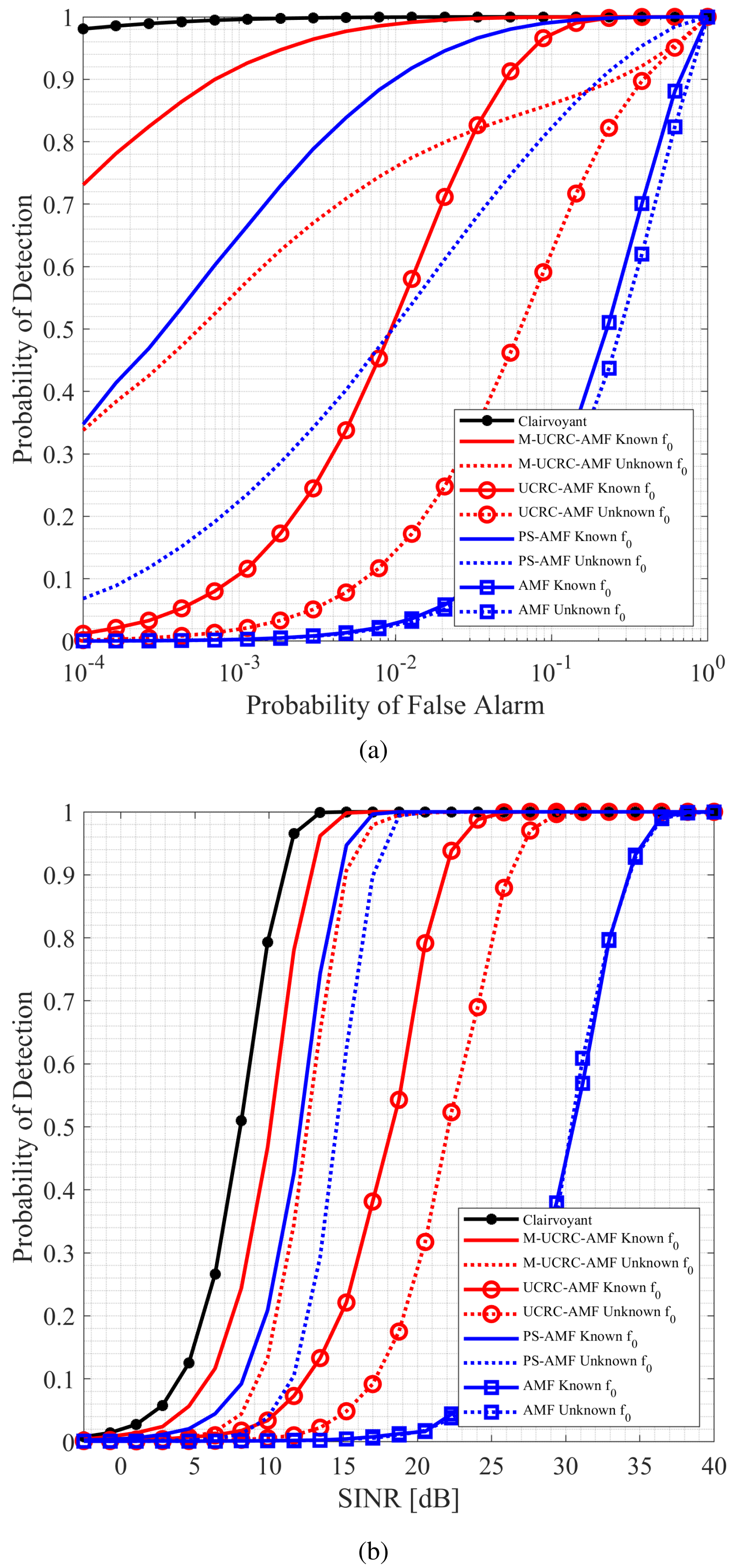

Figure 4.11: Detection performance with unknown f_0 (a) ROC curves (b) P_{D} vs. SINR

4.5.8 Example 8 : Numerical Evidence of Approximate CFAR Performance

A detector is said to have constant false-alarm rate with respect to a particular parameter if the probability density function of the test statistic is invariant to changes in that parameter. Classical detectors such as the AMF and GLRT allow for algebraic manipulations of the test statistics to show that the detectors are CFAR with respect to the unknown covariance matrix. However, the M-UCRC and UCRC approaches are algorithmic and hence, algebraic manipulations such as those described in [48] and [76] will be of little use. Instead, we provide numerical evidence of this property for the UCRC-AMF and M-UCRC-AMF.

In this example, we analyze the CFAR behavior by estimating the probability of false alarm using a fixed threshold for the M-UCRC-AMF and UCRC-AMF while varying the covariance matrix structure. Specifically, we employ the exponentially shaped covariance matrix model, where the (i, j)-th element is defined as [15],

$$\mathbf{\Sigma}_{(i,j)} = \rho^{|i-j|} \tag{4.42}$$

and ρ is the first lag correlation coefficient. We vary the correlation coefficient $0 \leq \rho < 1$ and estimate the probability of false alarm using 10^5 independent trails for each value of ρ. The exponentially shaped covariance matrix replaces the clutter plus noise covariance matrix used in the previous examples, and we set $K_p = 16$ pulses with $L = 17$ for the CPI and secondary data, respectively.

Figure 4.5.8 illustrates the estimated probability of false alarm versus the covariance structure parameter ρ. The constant thresholds for the M-UCRC-AMF and UCRC-AMF were computed numerically using a fixed value of ρ for a $P_{\text{FA}} = 10^{-2}$ and held constant for each trial as ρ was varied. Remarkably, the false alarm rate for M-UCRC-AMF and UCRC-AMF remains approximately fixed as the covariance structure is varied, demonstrating that the proposed detectors have approximate CFAR with respect to the unknown covariance matrix.

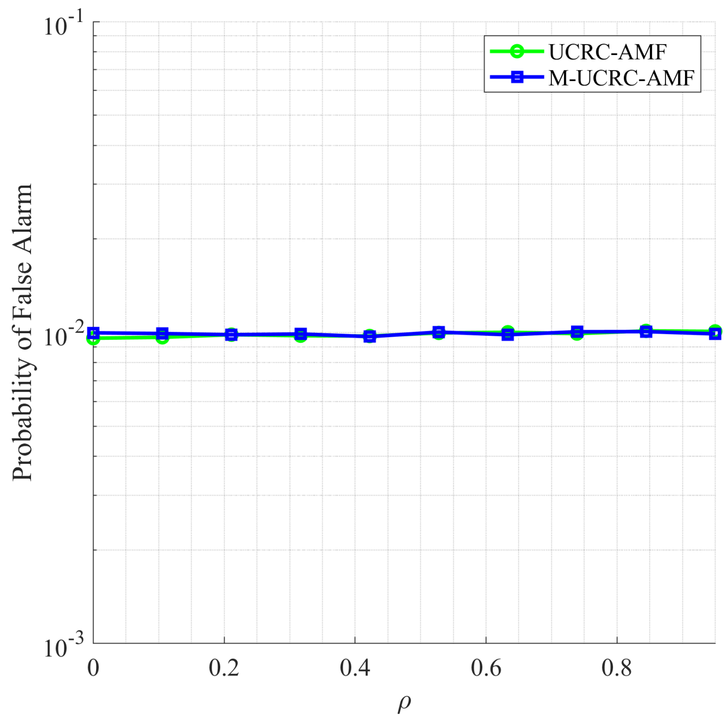

Figure 4.12: P_{FA} vs. ρ showing approximate CFAR behavior

4.5.9 Example 9 : Detection Performance with Mismatched Covariance Structure

For this example, we deviate the Hermitian Toeplitz covariance structure necessary for unit circle roots per Theorem 1, and investigate the impact upon the M-UCRC-AMF and UCRC-AMF performance, using a CPI length of $K_p = 32$ pulses. We will examine two cases in detail: one where the true covariance matrix (CM) $\mathbf{\Sigma}$ is exponentially shaped as in (4.42) with $\rho = 0.9$, and in the other we set the true covariance matrix as a random draw from a Wishart distribution with an exponentially shaped mean with $\rho = 0.9$ and $2K_p$ degrees of freedom. The latter case ensures that the true covariance does not have

Hermitian Toeplitz structure and hence, unit circle roots are not theoretically necessary. The purpose of this example is to show the practical utility of UC root enforcement in more adverse scenarios where the required covariance structure may not exist.

The roots of the Clairvoyant filter computed using the two matrices are depicted in Fig. 4.5.9. We see that when the Hermitian Toeplitz matrix is used, Theorem 1 applies, and the roots must all occur on the unit circle. However, when the random covariance matrix is used instead the Clairvoyant filter roots occur randomly around but not exactly on the unit circle boundary. Hence, the M-UCRC and UCRC-AMF performance is expected to suffer in this case compared to when the Toeplitz matrix is used.

Figures 4.14a and 4.14b show the performance of all detectors for the Hermitian Toeplitz structured matrix and the mismatched case, where we set $\mathrm{SINR} = 13$ dB in Fig. 4.14a to scale the non-fluctuating target amplitude.

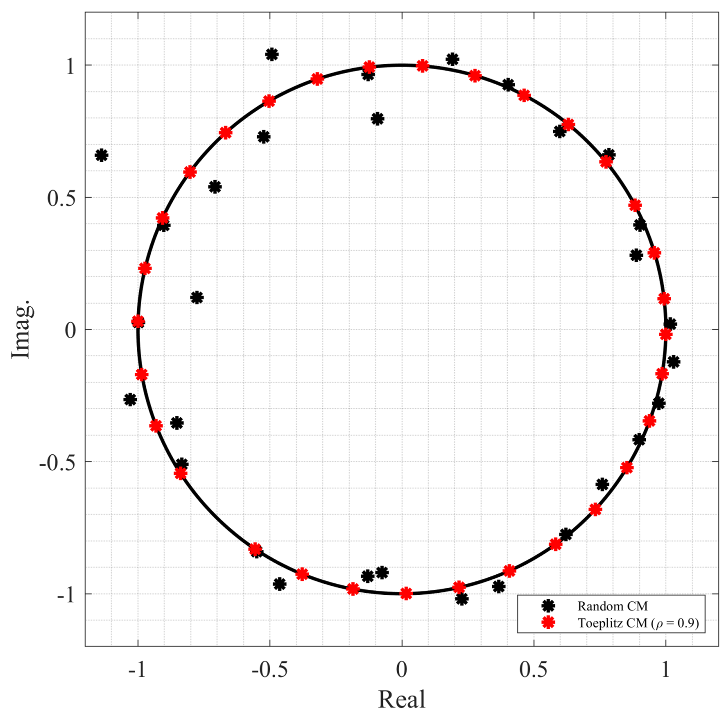

Figure 4.13: Clairvoyant filter root locations for Toeplitz and random covariance matrix models.

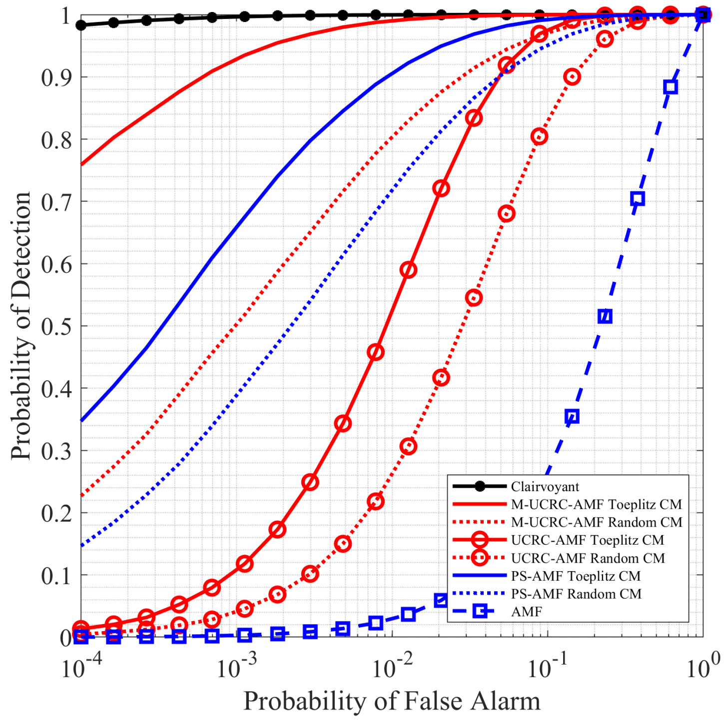

(a)

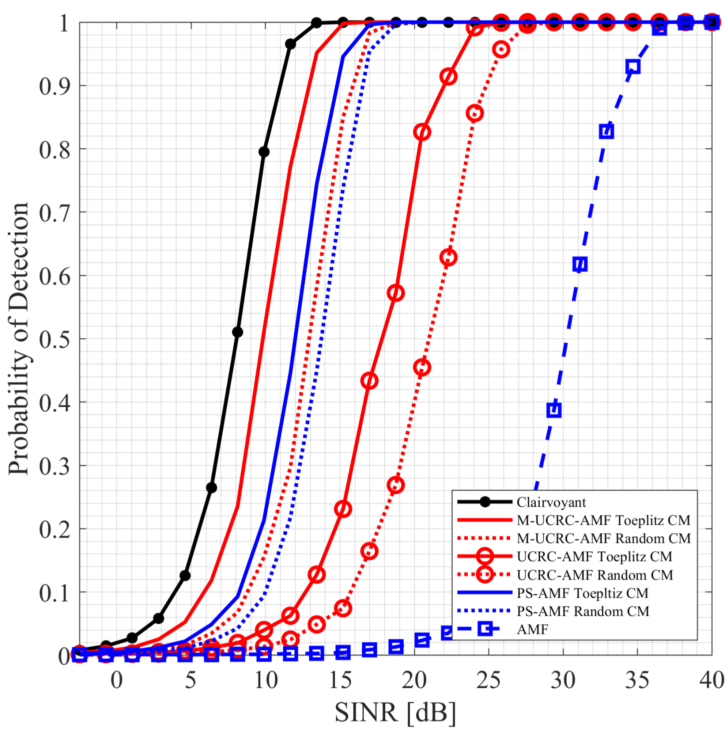

(b)

Figure 4.14: Detection performance with covariance mismatch (a) ROC (b) P_{D} vs. SINR

4.6 Conclusion

This chapter proposes the M-UCRC-AMF and UCRC-AMF for adaptive radar moving target detection in homogeneous clutter with limited secondary data. This work utilizes the new proof given in Chapter 2 that the AMF z-polynomial ideally possesses unit circle roots when the underlying covariance matrix is known. Motivated by this new proof, we proposed a potentially transformative means of designing the adaptive matched filter by enforcing the theoretically necessary unit circle roots constraints. Two versions of unit circle roots constrained AMF algorithm are presented: UCRC-AMF uses the conventional SCM to initialize the algorithm as well as to impose unit circle property on each AMF root by optimizing the output clutter-plus-noise power. The M-UCRC-AMF is initialized in the same manner using the conventional AMF, but the FB-SCM is used in the second stage for enforcing the unit circle property. Both UCRC-AMF and M-UCRC-AMF approaches estimate each root in closed-form by enforcing conjugate-symmetry upon the first-order polynomial factors. The M-UCRC-AMF enhances the performance of the UCRC-AMF significantly with negligible additional computational overhead by incorporating the FB-SCM within the proposed root estimation scheme.

Through extensive simulation examples it was shown that judicious enforcement of the unit circle roots property can result in drastically improved moving target detection performance. Specifically, the M-UCRC-AMF and UCRC-AMF show improved probability of detection at lower false alarm rates and output SINR. When the number of secondary data are limited, the UCRC-AMF outperformed the conventional AMF and the M-UCRC-AMF outperformed the PS-AMF, achieving higher probability of detection at lower output SINR and false alarm rate, demonstrating the superiority of the proposed unit circle approach. It was further shown that the M-UCRC-AMF and UCRC-AMF consistently achieve higher output SINR with less secondary data than what is attainable using the PS-AMF or AMF. We showed that rectifying the individual roots using the UCRC algorithm consistently provides higher average output SINR as more roots are placed on the unit circle. The near optimal SINR loss of the M-UCRC-AMF ensures a lower minimum detectable velocity for moving target detection applications. Finally, the approximate CFAR performance of the M-UCRC-AMF and UCRC-AMF with respect to the unknown clutter covariance matrix was shown numerically.

In the following chapters, extensions of unit-circle enforcement for moving target detection will be considered; including for low-rank homogeneous clutter, compound-Gaussian clutter, and distributed MIMO radar in compound-Gaussian clutter. Regarding potential future extensions of the proposed unit-circle enforcement framework, it has been noted in Chapter 2 that constrained optimization under similar mathematical structures arise in many other sensor array signal processing applications beyond the AMF and beamforming. These include bi-static or distributed MIMO radar networks [106, 95], statistical detectors such as the NAMF for non-homogeneous clutter [19], and STAP [66]. Based on the demonstrated success of the unit-circle based approach thus far, it is fair to postulate that these methods may also benefit from unit circle roots enforcement at the design stage and attain significant performance gains over the current state of the art in the respective fields.

Exploiting Unit Circle Roots for Moving Target Detection in Low-Rank Clutter

5.1 Introduction

Adaptive target detection is an integral component in the field of remote sensing, whether using radar/sonar [66, 81], or hyperspectral [99]. For radar in particular, adaptive moving target detection is of significant interest, and has a rich history within the radar literature. Since the seminal work of Reed, Mallat, and Brennan [75] in the later half of the twentieth century, followed by the classical generalized likelihood ratio test (GLRT) of Kelly [48] and the adaptive matched filter (AMF) [76], moving target detection continues to garner significant research interest.

The radar attempts to detect a target embedded in clutter and noise the statistics of which are unknown at the receiver, and must be estimated. The standard estimation technique is the sample covariance matrix (SCM) which is computed from a set of homogeneous, target-free secondary data, resulting in the sample matrix inversion (SMI) based detector [75]. However, it is well known that to achieve satisfactory performance from the SMI detector the number of secondary data must be at least twice the dimension of the signal of interest [75]. This constraint can be overly restrictive for practical radar systems, especially in space-time adaptive processing applications (STAP) [66]. Additionally, detection performance can be further impacted when the secondary data are not homogeneous, as is the case when observing sea-clutter using high-resolution radar [79]

Recently, it was theoretically proven that the polynomial corresponding to the known-covariance, or Clairvoyant, AMF must have unit circle roots [93] for radar using symmetrically spaced pulse trains. The unit-circle roots property was previously proven for minimum variance distortionless response (MVDR) beamforming with uniform linear arrays (ULA) [97]. MVDR beamformer design for ULAs with unit circle roots have also been developed in [102],[85]. The equivalent mathematical structure resulting from the use of symmetrically spaced pulse trains and uniform linear arrays has been noted before in the literature [23],[15]. However, barring a few recent exceptions [94] [92], to the best of our knowledge, no other technique explicitly enforces the unit circle roots property for practical adaptive filter design for moving target detection.

In [94] and [92] two algorithms to enforce the unit circle roots constraint were provided: the unit circle roots constrained AMF (UCRC-AMF) and the modified UCRC-AMF (M-UCRC-AMF). However, both the UCRC-AMF and M-UCRC-AMF are algorithmic and lacked an algebraic closed-form expression for the test statistic. Despite demonstrating the efficacy of enforcing unit circle roots via simulations, no discussion of the statistical properties of detectors with unit circle roots was provided. Additionally, the work in [94] did not address low rank clutter, which is the primary focus of this work. This chapter presents an alternative moving target detector with unit circle roots that exploits the low-rank characteristics of typical clutter. The proposed design provides a closed-form test statistic that is conducive to statistical performance analysis, as developed in this work.

In practice, and especially in the context of (STAP), the clutter often occupy a low-dimensional subspace relative to the signal dimension [108],[10]. This low-rank structure can be advantageous for reducing the required number of secondary data [49]. Based on this low-rank assumption, we derive the generalized likelihood ratio test (GLRT) by first assuming that the clutter subspace is known. The GLRT derivation closely follows that presented in [106] for distributed multiple input multiple ouput (MIMO) radar, where only the primary data was utilized and the clutter subspace were modeled as Vandermonde vectors. In this work, the dominant eigenvectors of the clutter subspace are used to model homogeneous clutter and we use both primary and secondary data when deriving the GLRT for monostatic radar, although straight-forward extension to MIMO radar is feasible.

In order to analyze the limiting performance of the proposed algorithm, we derive the known clutter subspace GLRT under the assumption that the roots of the Clairvoyant filter polynomial are known. The purpose is to show the limiting performance of a detector which explicitly enforces the unit circle roots property when the roots can be estimated to an arbitrary degree of accuracy. Through distribution analysis and simulation studies it will be shown that the known-roots GLRT has CFAR, but is outperformed by the known clutter subspace GLRT. A possible explanation may be attributed to eigen-subspaces incorporating more complete information on the underlying clutter phenomenon than what could be modeled by a finite number of unit circle roots. Because of this performance disparity, we propose a modification to the known-roots GLRT: estimating the white noise power based on the known subspace instead of based on the known roots. The modified GLRT will also be shown to have CFAR with respect to the clutter and noise parameters. It may be noted here that incorporating clutter eigen-subspaces within the GLRT itself is not sufficient, because this approach does not guarantee unit circle roots as required by the theorem derived in [93]. Additional performance improvement of the proposed UC-GLRT is achieved when the roots generated by eigen-subspace GLRT are moved onto the unit circle in simulations, satisfying the unit circle theorem [93].

For practical implementation of the subspace GLRT, we estimate the unknown clutter subspace using the dominant eigenvectors of the sample covariance matrix, amounting to a scaled variation of the principle components inverse (PCI) based adaptive filter [100]. Eigenvector-based techniques are commonly used to address low-rank clutter (see [72, 73] among others) and are commonly used within the signal processing community as a whole

[38],[116]. For practically imposing unit circle roots, we start with the roots of the filter corresponding the subspace GLRT described earlier and radially project those roots onto the unit circle. This unit circle approach, hereafter referred to as the unit circle GLRT (UC-GLRT), uses the properties of orthogonal projection matrices to enforce the unit circle roots constraint, resulting in an algebraic expression for the test statistic, something which was not present in other unit circle roots based detectors such as the UCRC-AMF [94] and M-UCRC-AMF [92].

Simulation examples will be used to demonstrate the superiority of the proposed UC-GLRT over several existing methods, as well as the eigenvector-based GLRT. It will be shown that the UC-GLRT has unit circle roots, as designed, while the other practical detectors do not. The UC-GLRT will be shown to achieve higher probability of detection at lower false alarm rates in low-rank clutter than the eigenvector-based approach, which does not guarantee unit circle roots. We will also consider the impact of rank mismatch upon the UC-GLRT, and compare its effectiveness with several methods for same data set. The rapid convergence of the UC-GLRT in terms of the normalized signal-to-interference plus noise ratio (NSINR) will also be demonstrated. All simulations are conducted using limited secondary data, when the number of secondary data is barely sufficient to invert the SCM.

This Chapter is organized as follows: In Section 5.2, the signal and clutter model are defined and the standard hypothesis testing framework for both primary and secondary data are stated. In Section 5.4, the Clairvoyant GLRT for Known Subspace (eigen) and Known roots cases, and the motivation behind combining primary and secondary data are presented. Section 5.5 derives the distributions for the Known Subspace and Known Roots GLRTs. In Section 5.6, we derive the unit circle GLRT. Section 5.7 contains simulation examples and discussion related to the performance of the UC-GLRT under various operating conditions. Section 5.8 provides concluding remarks and potential future applications.

5.2 Signal Model

Consider a co-located transmitter and receiver mounted on a stationary platform. The transmitter emits K_p periodic, pulses over a coherent processing interval. Pulse-compression is performed at the receiver to isolate the reflected returns originating from a particular range bin. The received slow-time data are stacked into a vector $\mathbf{x} \in \mathbb{C}^{K_p \times 1}$, where each row corresponds to an individual slow-time snapshot.

The received data are modeled as,

$$\mathbf{x} = \alpha \mathbf{a}(f_0) + \mathbf{c} + \mathbf{n} \tag{5.1}$$

where $\mathbf{c}$ and $\mathbf{n}$ are the clutter and noise vectors, respectively. The vector

$$\mathbf{a}(f_0) \triangleq [1, e^{-j2\pi f_0}, \ldots, e^{-j2\pi f_0 (K_p - 1)}]^T \tag{5.2}$$

is the target temporal steering vector corresponding to a normalized Doppler frequency,

$$f_0 = \frac{2T_{\mathrm{PRI}}}{\lambda} \mathbf{k}_r^T \mathbf{v}_t \tag{5.3}$$

where $\mathbf{k}_r \triangleq [\cos(\theta_r) \;\; \sin(\theta_r)]$ is the unit vector in the direction of the receiver relative to the target, θ_r is the angle of the receiver relative to the target, $\mathbf{v}_t \triangleq [v_x \; v_y]$ is the target velocity vector, λ is the wavelength of the radar, and T_{PRI} is the pulse-repetition interval. $\alpha \in \mathbb{C}$ is the unknown complex amplitude of the moving target return determined by the target radar cross section (RCS) and also captures the effects of signal propagation through the environment.

5.2.1 Subspace Clutter Model

In many practical scenarios, the clutter can be appropriately modeled using a low-rank subspace [108]. In [106], a linear model for the clutter was proposed, which received great attention within the research community (see [39],[41],[40],[114], and [58] among others). We adopt the same approach in this chapter, and the clutter vectors are modeled as,

$$\mathbf{c} = \mathbf{H}\boldsymbol{\beta} \tag{5.4}$$

where $\mathbf{H} = [\mathbf{h}_1, \ldots, \mathbf{h}_r] \in \mathbb{C}^{K_p \times r}$, $r \ll K_p$ is a matrix of clutter basis vectors and $\boldsymbol{\beta} \in \mathbb{C}^{r\times 1}$ are the clutter coefficients. The clutter coefficients are modeled as $\boldsymbol{\beta} \sim \mathcal{CN}\left(\mathbf{0}, \sigma_c^2\mathbf{I}\right)$, where σ_c^2 is the variance of the clutter coefficients.

5.2.2 Problem Statement

Moving target detection consists of declaring either the presence or absence of a moving target within the range bin of interest, represented by hypothesises H_1 and H_0, respectively. The hypothesis test can be described mathematically as,

$$H_0 : \begin{cases} \mathbf{x}_0 & = \mathbf{c} + \mathbf{n} \\ \mathbf{x}_\ell & = \mathbf{c}_\ell + \mathbf{n}_\ell \;\; \ell = 1\ldots, L \end{cases} \tag{5.5}$$

$$H_1 : \begin{cases} \mathbf{x}_0 & = \alpha\mathbf{a}(f_0) + \mathbf{c} + \mathbf{n} \\ \mathbf{x}_\ell & = \mathbf{c}_\ell + \mathbf{n}_\ell \;\; \ell = 1\ldots, L \end{cases} \tag{5.6}$$

where $\mathbf{x}_0$ and $\mathbf{x}_\ell$'s represent the primary and secondary data under each hypothesis.

The radar output is the filtered slow-time data,

$$y = \mathbf{w}^H\mathbf{x} \tag{5.7}$$

where $\mathbf{w} \in \mathbb{C}^{K_p \times 1}$ is a filter which has been designed, according to some performance metric, to cancel the clutter and noise while retaining the target signal.

The test statistic is the square of the filter output [66],

$$|y|^2 \underset{H_0}{\overset{H_1}{\gtrless}} \tau \tag{5.8}$$

where τ is a threshold used to satisfy a prescribed probability of false alarm.

5.3 The Clairvoyant Filter

For this chapter, we compare the performance of the proposed approach against the known-covariance adaptive matched filter test statistic,

$$\frac{\left|\mathbf{a}^H (f_0) \mathbf{\Sigma}^{-1} \mathbf{x}_0\right|^2}{\mathbf{a}^H (f_0) \mathbf{\Sigma}^{-1} \mathbf{a} (f_0)} \underset{H_0}{\overset{H_1}{\gtrless}} \tau_{\text{opt}} \tag{5.9}$$

where $\mathbf{\Sigma} = E\left[(\mathbf{c} + \mathbf{n})(\mathbf{c} + \mathbf{n})^H\right]$ is the clutter plus noise covariance matrix, τ_{opt} is the threshold, and $\mathbf{x}_0$ the testing data for the range cell under test. To express (5.9) in the same form as (5.8), define the filter

$$\mathbf{w}_{\text{opt}} = \frac{\mathbf{\Sigma}^{-1} \mathbf{a}^H (f_0)}{\sqrt{\mathbf{a}^H (f_0) \mathbf{\Sigma}^{-1} \mathbf{a} (f_0)}} \tag{5.10}$$

which we refer to as the Clairvoyant or optimal filter for the remainder of this chapter.

In practice, the covariance matrix is unknown, and must be estimated using the sample covariance matrix (SCM), which is computed from a set of L target-free secondary data,

$$\hat{\mathbf{\Sigma}} = \sum_{\ell=1}^{L} \mathbf{x}_\ell \mathbf{x}_\ell^H. \tag{5.11}$$

It is well known that when the $L < 2K_p$ the SCM is a poor estimate and can adversely impact detection performance [75]. Therefore, other approaches are necessary which make use of mathematical structure in the clutter and noise to enhance detection performance when the secondary data are limited.

In general, any filter $\mathbf{w}$ can be interpreted as a $(K_p - 1)$-degree polynomial in the complex z-domain after applying the forward z-transform,

$$W(z) = w(0) + w(1)z^{-1} + \ldots + w(K_p - 1)z^{-(K_p-1)} \tag{5.12}$$

where $w(i)$ represents the i-th element of the filter $\mathbf{w}$. It was proven in [93] that when the coefficients of (5.12) correspond to the elements of the filter $\mathbf{w}_{\text{opt}}$, then $W(z)$ must have exactly $K_p - 1$ unit circle roots. In the following sections, we explain how the unit circle roots property can be exploited to improve the performance of the GLRT.

5.4 The GLRT

The derivation of the GLRT proceeds using the joint PDF of the primary and secondary data.

This section is divided into two subsections: the GLRT derivation supposing a known clutter basis' $\mathbf{H}$, and the GLRT derivation assuming the unit circle roots of the Clairvoyant filter are known. The latter represents the limiting case if the Clairvoyant filter roots can be estimated to an arbitrary degree of accuracy, while the former is the limiting case when the clutter subspace is known.

5.4.1 Known Subspace GLRT

For mathematical expediency, we define

$$J\left(\mathbf{X}, \mathbf{B} | H_0\right) = ||\mathbf{x}_0 - \mathbf{H}\boldsymbol{\beta}_0||_2^2 + \sum_{\ell=1}^{L} ||\mathbf{x}_\ell - \mathbf{H}\boldsymbol{\beta}_\ell||_2^2 \tag{5.13}$$

for H_0 and

$$J\left(\mathbf{X}, \alpha, \mathbf{B} | H_1\right) = ||\mathbf{x}_0 - \alpha \mathbf{a}\left(f_0\right) - \mathbf{H}\boldsymbol{\beta}_0||_2^2 + \sum_{\ell=1}^{L} ||\mathbf{x}_\ell - \mathbf{H}\boldsymbol{\beta}_\ell||_2^2 \tag{5.14}$$

for H_1. $\mathbf{X} = \{\mathbf{x}_\ell\}_{\ell=0}^{L}$ is the combined set of primary ($\ell = 0$) and secondary ($\ell = 1, \ldots, L$) data vectors and $\mathbf{B} = \{\boldsymbol{\beta}_\ell\}_{\ell=0}^{L}$ is the combined set of clutter coefficients for the primary, $\ell = 0$, and secondary, $\ell = 1, \ldots, L$, data.

The joint likelihood of the primary and secondary data may now be expressed as

$$p\left(\mathbf{X}; \sigma, \mathbf{B} | \, H_0\right) = \left(\pi\sigma^2\right)^{-K(L+1)} \exp\left[-\frac{J\left(\mathbf{X}, \mathbf{B}, H_0\right)}{\sigma^2}\right] \tag{5.15}$$

under H_0, and

$$p\left(\mathbf{X}; \alpha, \sigma, \mathbf{B} | H_1\right) = \left(\pi\sigma^2\right)^{-K(L+1)} \exp\left[-\frac{J\left(\mathbf{X}, \alpha, \mathbf{B}, H_1\right)}{\sigma^2}\right] \tag{5.16}$$

under H_1. The parameters α, $\mathbf{B}$, f_0, and σ are unknown hence, we form the generalized likelihood ratio (GLR) by maximizing over these unknown parameters under H_0 and H_1, respectively,

$$\mathrm{GLR} = \frac{\max_{\alpha, \mathbf{B}, f_0, \sigma} p\left(\mathbf{X}; \alpha, \sigma, \mathbf{B} | H_1\right)}{\max_{\alpha, \mathbf{B}, f_0, \sigma} p\left(\mathbf{X}; \sigma, \mathbf{B} | \, H_0\right)}. \tag{5.17}$$

The MLEs of the unknown parameters are listed here, but the necessary derivations are omitted from this section and can be found in Appendix 5.9.

Under H_1:

$$\hat{f}_0 = \max_f \frac{\left|\mathbf{a}^H(f)\,\mathbf{P}_{\mathbf{H}}^{\perp}\mathbf{x}_0\right|^2}{\mathbf{a}^H(f)\,\mathbf{P}_{\mathbf{H}}^{\perp}\mathbf{a}(f)} \tag{5.18}$$

$$\hat{\alpha} = \frac{\left|\mathbf{a}^H(f_0)\,\mathbf{P}_{\mathbf{H}}^{\perp}\mathbf{x}_0\right|^2}{\mathbf{a}^H(f_0)\,\mathbf{P}_{\mathbf{H}}^{\perp}\mathbf{a}(f_0)}, \tag{5.19}$$

$$\hat{\boldsymbol{\beta}}_0 = (\mathbf{HH})^{-1}\,\mathbf{H}^H(\mathbf{x}_0 - \hat{\alpha}\mathbf{a}(f_0)) \tag{5.20}$$

$$\hat{\boldsymbol{\beta}}_\ell = (\mathbf{HH})^{-1}\,\mathbf{H}^H\mathbf{x}_0;\ \ell = 1,\ldots,L, \tag{5.21}$$

and

$$\hat{\sigma}_1^2 = \frac{1}{K(L+1)}\left[-\hat{\alpha} + \sum_{\ell=0}^{L}\mathbf{x}_\ell^H\mathbf{P}_{\mathbf{H}}^{\perp}\mathbf{x}_\ell\right] \tag{5.22}$$

while under H_0:

$$\hat{\boldsymbol{\beta}}_\ell = (\mathbf{HH})^{-1}\,\mathbf{H}^H\mathbf{x}_0;\ \ell = 0,\ldots,L, \tag{5.23}$$

and

$$\hat{\sigma}_0^2 = \frac{1}{K(L+1)}\sum_{\ell=0}^{L}\mathbf{x}_\ell^H\mathbf{P}_{\mathbf{H}}^{\perp}\mathbf{x}_\ell \tag{5.24}$$

Let $\mathbf{P}_{\mathbf{H}} = \mathbf{H}(\mathbf{HH})^{-1}\mathbf{H}^H$, then the matrix

$$\mathbf{P}_{\mathbf{H}}^{\perp} = \mathbf{I} - \mathbf{P}_{\mathbf{H}} \tag{5.25}$$

is the projection onto the subspace orthogonal to the column space of $\mathbf{H}$.

After substitution of the maximum likelihood estimates, it is straightforward to show that the generalized likelihood ratio becomes,

$$\mathrm{GLR} = \left(\frac{\hat{\sigma}_0^2}{\hat{\sigma}_1^2}\right)^{K(L+1)} \tag{5.26}$$

which, after neglecting the $K(L+1)$ exponent and using the monotone property of the function $1/(1-x)$ becomes,

$$\mathrm{T}_{\mathrm{GLR}} = \frac{\left|\mathbf{a}^H\left(f_0\right)\mathbf{P}_{\mathbf{H}}^{\perp}\mathbf{x}_0\right|^2}{\left(\mathbf{a}^H\left(f_0\right)\mathbf{P}_{\mathbf{H}}^{\perp}\mathbf{a}\left(f_0\right)\right)\left(\sum_{\ell=0}^{L}\mathbf{x}_\ell^H\mathbf{P}_{\mathbf{H}}^{\perp}\mathbf{x}_\ell\right)}. \tag{5.27}$$

Similar to (5.8), the known subspace GLRT can be expressed as the squared output of a filter $\mathbf{w}_t$ and the test data $\mathbf{x}_0$,

$$\left|\mathbf{w}_t^H\mathbf{x}_0\right|^2 \underset{H_0}{\overset{H_1}{\gtrless}} \tau_t \tag{5.28}$$

where

$$\mathbf{w}_t = \frac{\mathbf{P}_{\mathbf{H}}^{\perp}\mathbf{a}\left(f_0\right)}{\sqrt{\left(\mathbf{a}^H\left(f_0\right)\mathbf{P}_{\mathbf{H}}^{\perp}\mathbf{a}\left(f_0\right)\right)\left(\sum_{\ell=0}^{L}\mathbf{x}_\ell^H\mathbf{P}_{\mathbf{H}}^{\perp}\mathbf{x}_\ell\right)}} \tag{5.29}$$

and τ_t is the threshold.

5.4.2 Known Roots GLRT

Assuming that the roots of the Clairvoyant filter polynomial are known or can be estimated to an arbitrary degree of accuracy, the GLRT can be derived similar to Section 5.4.1.

Let $\{z_k = e^{j2\pi f_k}\}_{k=1}^{K_p-1}$ denote the roots of the Clairvoyant filter polynomial. Note that these roots must appear on the unit circle [93]. Hence, let $\{f_i\}_{k=1}^{K_p-1}$ be the set of distinct frequencies $f_k \in (-0.5, 0.5),\ k = 1, \ldots, K_p - 1$ corresponding to each of the $K_p - 1$ roots.

Construct a matrix

$$\mathbf{A} = \left[\mathbf{a}\left(f_1\right), \ldots, \mathbf{a}\left(f_{K_p-1}\right)\right] \in \mathbb{C}^{K_p\times(K_p-1)}, \tag{5.30}$$

where each column is a Vandermonde vector in the form of (5.2) and define $\mathbf{P}_{\mathbf{A}} = \mathbf{A}\left(\mathbf{A}^H\mathbf{A}\right)^{-1}\mathbf{A}^H$

as the projection onto the column space of $\mathbf{A}$. Consequently,

$$\mathbf{P}_{\mathbf{A}}^{\perp} = \mathbf{I} - \mathbf{P}_{\mathbf{A}} \tag{5.31}$$

is the rank-1 projection onto the complementary subspace. Let $\mathcal{A}$ and $\mathcal{A}^{\perp}$ denote the column space of $\mathbf{A}$ and the orthogonal complement of $\mathcal{A}$, respectively.

The estimates in (5.18)-(5.24) and (5.21)-(5.22) can be modified to reflect knowledge of the Clairvoyant roots by replacing $\mathbf{H}$ and $\mathbf{P}_{\mathbf{H}}^{\perp}$ with $\mathbf{A}$ and $\mathbf{P}_{\mathbf{A}}^{\perp}$, respectively.

After substituting the estimates and following the steps for the GLRT in Section 5.4.1, generalized likelihood ratio becomes

$$\mathrm{S}_{\mathrm{GLR}} = \frac{\left|\mathbf{a}^{H}\left(f_0\right)\mathbf{P}_{\mathbf{A}}^{\perp}\mathbf{x}_0\right|^2}{\left(\mathbf{a}^{H}\left(f_0\right)\mathbf{P}_{\mathbf{A}}^{\perp}\mathbf{a}\left(f_0\right)\right)\left(\sum_{\ell=0}^{L}\mathbf{x}_{\ell}^{H}\mathbf{P}_{\mathbf{A}}^{\perp}\mathbf{x}_{\ell}\right)}. \tag{5.32}$$

The known roots GLRT may also be expressed as the squared output of a filter and test data,

$$\left|\mathbf{w}_s^{H}\mathbf{x}_0\right|^2 \underset{H_0}{\overset{H_1}{\gtrless}} \tau_s \tag{5.33}$$

where

$$\mathbf{w}_s = \frac{\mathbf{P}_{\mathbf{A}}^{\perp}\mathbf{a}\left(f_0\right)}{\sqrt{\left(\mathbf{a}^{H}\left(f_0\right)\mathbf{P}_{\mathbf{A}}^{\perp}\mathbf{a}\left(f_0\right)\right)\left(\sum_{\ell=0}^{L}\mathbf{x}_{\ell}^{H}\mathbf{P}_{\mathbf{A}}^{\perp}\mathbf{x}_{\ell}\right)}} \tag{5.34}$$

and τ_s is the threshold.

We can now prove the following claim regarding the roots of filter polynomial corresponding to (5.34).

Theorem 2. *The polynomial $W_s(z)$ whose coefficients are the elements of the vector $\mathbf{w}_s$ has $K_p - 1$ unit circle roots.*

Proof. The proof of this property follows directly from the fact that the columns of $\mathbf{A} =$

$\{\mathbf{a}(f_k)\}_{k=1}^{K_p-1} \in \mathcal{A}$, and it must be that

$$\mathbf{a}^H(f_k)\,\mathbf{w} = 0; \quad k = 1, \ldots, K_p - 1. \tag{5.35}$$

Since the above equation is equivalent to evaluating the polynomial $W_s(z)$ at $z = e^{j2\pi f_k}$, it follows that the $z_k = e^{j2\pi f_k}$ are the $K_p - 1$ unit circle roots of $W_s(z)$. □

5.4.3 Motivation for Combining Primary and Secondary Data

Equations (5.27) and (5.32) incorporate the primary data and secondary data into the final test statistic, and there are two reasons why we have adopted this approach. The first is to improve the estimation accuracy of the unknown white noise power. From both clutter models described Section 5.4, the white noise power is identical between the secondary data vectors as well as the primary data. Hence, we may exploit this statistical homogeneity to improve the detection performance of the GLRT.

The second reason is to avoid mathematical difficulties when enforcing unit circle roots using a rank-1 projection matrix. Specifically, we have that

$$\frac{|\mathbf{a}^H(f_0)\,\mathbf{P}_{\mathbf{A}}^{\perp}\mathbf{x}_0|^2}{\mathbf{a}^H(f_0)\,\mathbf{P}_{\mathbf{A}}^{\perp}\mathbf{a}(f_0)} = \mathbf{x}_0^H\mathbf{P}_{\mathbf{A}}^{\perp}\mathbf{x}_0. \tag{5.36}$$

To see why this is the case, let the eigenvalue decomposition of $\mathbf{P}$ be

$$\mathbf{P}_{\mathbf{A}}^{\perp} = \mathbf{E}\boldsymbol{\Lambda}\mathbf{E}^H = \sum_{k=1}^{K_p} \lambda_k \mathbf{e}_k \mathbf{e}_k^H \tag{5.37}$$

where $\mathbf{E} = \left[\mathbf{e}_1, \ldots, \mathbf{e}_{K_p}\right]$ is the matrix of eigenvectors, and $\boldsymbol{\Lambda} = \mathrm{diag}\{\lambda_1, \ldots, \lambda_K\}$ is the matrix of eigenvalues. Now $\lambda_1 = 1$ and $\lambda_k = 0$ for $k = 2, \ldots, K_p$ because we assume $\mathbf{P}$ is a rank-1 projection. Let $\mathbf{e}_1 = \frac{\mathbf{P}\mathbf{a}(f_0)}{\sqrt{\mathbf{a}^H(f_0)\mathbf{P}\mathbf{a}(f_0)}}$ be the eigenvector corresponding to λ_1.

The remaining eigenvectors are arbitrary so long as they are mutually orthogonal to one another.

From the left hand side of (5.36), it is straightforward to show that

$$\frac{\left|\mathbf{a}^H\left(f_0\right)\mathbf{P}\mathbf{x}_0\right|^2}{\mathbf{a}^H\left(f_0\right)\mathbf{P}\mathbf{a}\left(f_0\right)} = \mathbf{x}_0^H\mathbf{e}_1\mathbf{e}_1^H\mathbf{x}_0. \tag{5.38}$$

To show the equivalence, rewrite the right hand side of (5.36) using the EVD of $\mathbf{P}$

$$\mathbf{x}_0^H\mathbf{P}_{\mathbf{A}}^{\perp}\mathbf{x}_0 = \sum_{k=1}^{K_p}\lambda_k\mathbf{x}_0^H\mathbf{e}_k\mathbf{e}_k^H\mathbf{x}_0 = \mathbf{x}_0^H\mathbf{e}_1\mathbf{e}_1^H\mathbf{x}_0. \tag{5.39}$$

The above derivations show that using the primary data alone (*i.e.*, $\mathbf{x}_0^H\mathbf{P}_{\mathbf{A}}^{\perp}\mathbf{x}_0$) in the denominator of (5.32) would result in $S_{\mathrm{GLR}} = 1$, and no useful test statistic can be obtained. Therefore, in order to obtain a useful test statistic we must use the primary and secondary data within the denominator of S_{GLR}.

5.5 Performance Analysis

The theoretical performance of each detector is determined by the probability density under the null and alternative hypotheses.

Theorem 3. *The distributions of* (5.27) *are:*

$$T_{\mathrm{GLR}} \sim \begin{cases} \beta_{1,(L+1)(K_p-r)-1} & \text{under } H_0 \\ \beta'_{1,(L+1)(K_p-r)-1}(\gamma_t) & \text{under } H_1 \end{cases} \tag{5.40}$$

where $\beta_{1,(L+1)(K_p-r)-1}$ and $\beta_{1,(L+1)(K_p-r)-1}(\gamma_t)$ are the central and noncentral beta distributions, respectively, with parameters 1 and $(L+1)(K_p-r)-1$, and noncentrality parameter

[106].

$$\gamma_t = \frac{2}{\sigma^2}|\alpha|^2\left(\mathbf{a}^H(f_0)\,\mathbf{P}_{\mathbf{H}}^{\perp}\mathbf{a}(f_0)\right) \tag{5.41}$$

Theorem 4. *The distributions of* (5.32) *are:*

$$S_{\mathrm{GLR}} \sim \begin{cases} \beta_{1,L} & \text{under } H_0 \\ \beta'_{1,L}(\gamma_s) & \text{under } H_1 \end{cases} \tag{5.42}$$

where the noncentrality parameter is,

$$\gamma_s = \frac{2}{\sigma^2}|\alpha|^2\left(\mathbf{a}^H(f_0)\,\mathbf{P}_{\mathbf{A}}^{\perp}\mathbf{a}(f_0)\right). \tag{5.43}$$

The proofs of Theorems 3 and 4 can be found in Appendices 5.10 and 5.11, respectively. The two proofs are similar to those derived in [106], where the focus is upon distributed MIMO radar and only the testing data are utilized. For our proofs, we include both the training and testing data and focus on monostatic radar case.

5.5.1 Performance Differences between the Two Cases

The distributions for (5.27) and (5.32) are both independent of the clutter and noise parameters and are therefore CFAR detectors. However, the detection performance can be expected to be different based on the difference in rank between the two projection matrices $\mathbf{P}_{\mathbf{H}}^{\perp}$ and $\mathbf{P}_{\mathbf{A}}^{\perp}$. Hence, we propose the following modification to (5.32).

Replacing the white noise power estimate using $\mathbf{P}_{\mathbf{A}}^{\perp}$ with the estimate based on $\mathbf{P}_{\mathbf{H}}^{\perp}$

from (5.24), the known-roots GLR in (5.32) can be modified such that,

$$\mathrm{G_{GLR}} = \frac{\left|\mathbf{a}^H\left(f_0\right)\mathbf{P}_{\mathbf{A}}^{\perp}\mathbf{x}_0\right|^2}{\left(\mathbf{a}^H\left(f_0\right)\mathbf{P}_{\mathbf{A}}^{\perp}\mathbf{a}\left(f_0\right)\right)\left(\sum_{\ell=0}^{L}\mathbf{x}_\ell^H\mathbf{P}_{\mathbf{H}}^{\perp}\mathbf{x}_\ell\right)}. \tag{5.44}$$

The following partial claim can be made about the performance of (5.44):

Theorem 5. *The distribution of* (5.44) *is*

$$G_{\mathrm{GLR}} \sim \beta_{1,(L+1)(K_p-r)-1} \text{ under } H_0 \tag{5.45}$$

Under H_1, the distribution of (5.44) is complicated by the different noncentrality parameters present in the numerator and the denominator. Hence, we only analyze the distribution of G_{GLR} under H_0, which is enough to prove CFAR in the case when the Clairvoyant roots and $\mathbf{P}_{\mathbf{H}}^{\perp}$ are known. The proof of Theorem 5 can be found in Appendix 5.12.

Figure 5.1 illustrates the simulated and analytical performance of (5.27) and (5.32), where $K_p = 32$ pulses, $L = 32$ secondary data, and with clutter rank $r = 11$, $\mathrm{CNR} = 30$ dB, and $\mathrm{SNR} = 10$ dB. The performance is computed using Monte Carlo simulations where $300/P_{\mathrm{FA}}$ trials were used for minimum probability of false alarm $P_{\mathrm{FA}} = 10^{-4}$. From this figure, it can be seen that the simulated performances of (5.27),(5.32), and (5.44) closely match the theoretical performances predicted using Theorems 3,4, and 5, respectively. However, the performance of (5.32) is worse than that for (5.27) due to the aforementioned rank difference.

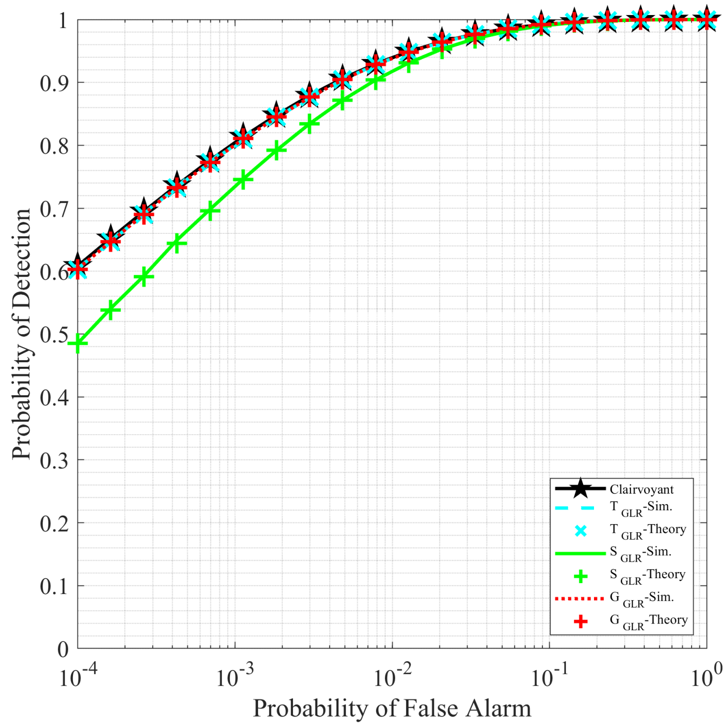

Figure 5.1: Simulated and Theoretical performance of the GLRT's and Clairvoyant Detector

---

Algorithm 3: UC-GLRT

INPUT: $\hat{\mathbf{P}}^{\perp}$, $\mathbf{a}\left(f_0\right), \{\mathbf{x}_\ell\}_{\ell=0}^{L}$

start: $\mathbf{w} = \hat{\mathbf{P}}^{\perp}\mathbf{a}\left(f_0\right)$

$\{\xi\}_{i=1}^{K_p-1} \leftarrow \text{roots}\{\mathcal{Z}\{\mathbf{w}\}\}$ ▷ I

$i = 1$ **up to** $i = K_p - 1$

  $\hat{f}_i = \arg\{\xi_i\}/2\pi$ ▷ II

  $\mathbf{g}_i = \left[1, e^{-j2\pi\hat{f}_i}, \ldots, e^{-j2\pi\hat{f}_i(K_p-1)}\right]^T$

end

$\mathbf{G} = \left[\mathbf{g}_1, \ldots, \mathbf{g}_{K_p-1}\right]$ ▷ III

$\mathbf{P}_{\mathbf{G}}^{\perp} = \mathbf{I} - \mathbf{G}\left(\mathbf{G}^H\mathbf{G}\right)^{-1}\mathbf{G}^H$ ▷ IV

OUTPUT:

$$\mathbf{w}_g = \frac{\mathbf{P}_{\mathbf{G}}^{\perp}\mathbf{a}(f_0)}{\sqrt{\left(\mathbf{a}^H(f_0)\mathbf{P}_{\mathbf{G}}^{\perp}\mathbf{a}(f_0)\right)\left(\sum_{\ell=0}^{L}\mathbf{x}_\ell^H\hat{\mathbf{P}}^{\perp}\mathbf{x}_\ell\right)}}$$

5.6 Unit Circle GLRT

At high CNR, the inverse covariance is well approximated using r dominant eigenvectors of the covariance matrix [50],[73],

$$\mathbf{\Sigma}^{-1} \approx \frac{1}{\sigma^2}\left(\mathbf{I}-\mathbf{P}\right) \tag{5.46}$$

where $\mathbf{P} = \sum_{i=1}^{r} \mathbf{u}_i\mathbf{u}_i^H$ is the rank-r projection onto the clutter subspace and $\{\mathbf{u}_i\}_{i=1}^{r}$ are the r dominant eigenvectors.

In the absence of the true covariance matrix, detectors such as the low-rank normalized adaptive matched filter (LR-NAMF) [72, 73] substitute the r dominant eigenvectors of the SCM to compute,

$$\hat{\mathbf{P}} = \sum_{i=1}^{r} \hat{\mathbf{u}}_i\hat{\mathbf{u}}_i^H \tag{5.47}$$

where the $\hat{\mathbf{u}}_i$ are the r dominant eigenvectors of the SCM. Let $\hat{\mathbf{P}}^{\perp} = \mathbf{I} - \hat{\mathbf{P}}$ be the complementary projection. In this way, the filter in (5.29) may be estimated as,

$$\hat{\mathbf{w}}_t = \frac{\hat{\mathbf{P}}^{\perp}\mathbf{a}\left(f_0\right)}{\sqrt{\left(\mathbf{a}^H\left(f_0\right)\hat{\mathbf{P}}^{\perp}\mathbf{a}\left(f_0\right)\right)\left(\sum_{\ell=0}^{L}\mathbf{x}_\ell^H\hat{\mathbf{P}}^{\perp}\mathbf{x}_\ell\right)}} \tag{5.48}$$

when the clutter subspace is unknown. The corresponding GLRT is,

$$\left|\hat{\mathbf{w}}_t^H\mathbf{x}_0\right|^2 \underset{H_0}{\overset{H_1}{\gtrless}} \tau_t. \tag{5.49}$$

This filter $\mathbf{w}_t$ is analogous to the LR-NAMF [73] with the exception that the secondary data have been incorporated into the denominator of (5.48).

Despite the accuracy of the approximation in (5.46), the filter in (5.48) is not guaranteed to have unit circle roots. However, for high CNR, we can assume that the approximation in (5.46) will be better than sample matrix inversion [75]. Hence, we suppose that the roots of any filter $\mathbf{w} \propto \hat{\mathbf{P}}^{\perp}\mathbf{a}\left(f_0\right)$ will be near the unit circle and therefore, close to their Clairvoyant counterparts.

For the proposed approach, we radially project the roots of eigenvector-based filter in (5.48) onto the unit circle to enforce the theoretically necessary property [93].

Let $\{\zeta\}_{i=1}^{K_p-1}$ be the roots of the filter polynomial corresponding to a filter $\mathbf{w} = \hat{\mathbf{P}}^{\perp}\mathbf{a}\left(f_0\right)$ (see step-I in Algorithm 3). For each of the i roots, we estimate the normalized frequencies as $\hat{f}_i = \arg\{\zeta_i\}/2\pi$. Next, construct the Vandermonde-structured column vectors $\mathbf{g}_i$ from the discrete frequencies and assemble the matrix $\mathbf{G} = [\mathbf{g}_1, \ldots, \mathbf{g}_{K_p-1}] \in \mathbb{C}^{K_p \times (K_p-1)}$ (see steps II and III in Algorithm 3). Next, compute the projection onto the orthogonal complement of the columns space of $\mathbf{G}$. Finally, construct the filter,

$$\mathbf{w}_g = \frac{\mathbf{P}_{\mathbf{G}}^{\perp}\mathbf{a}\left(f_0\right)}{\sqrt{\left(\mathbf{a}^H\left(f_0\right)\mathbf{P}_{\mathbf{G}}^{\perp}\mathbf{a}\left(f_0\right)\right)\left(\sum_{\ell=0}^{L}\mathbf{x}_\ell^H\hat{\mathbf{P}}^{\perp}\mathbf{x}_\ell\right)}}, \tag{5.50}$$

and the GLRT becomes,

$$\left|\mathbf{w}_g^H\mathbf{x}_0\right|^2 \underset{H_0}{\overset{H_1}{\gtrless}} \tau_g. \tag{5.51}$$

From Theorem 2, the polynomial corresponding to (5.50) clearly has K_p-1 unit circle roots located at angles $2\pi\hat{f}_i$. Note that the projection $\hat{\mathbf{P}}^{\perp}$ is used in the normalization of (5.50) instead of $\mathbf{P}_{\mathbf{G}}^{\perp}$. This done to avoid model mismatch, when estimating the white noise power σ^2. The purpose of $\mathbf{P}_{\mathbf{G}}^{\perp}$ in the numerator of (5.50) is to enforce unit circle roots, which are invariant to scaling of the filter vector.

Pseudocode of the UC-GLRT algorithm is provided in Algorithm 3.

5.7 Simulation Results

Consider a single moving target with a linear trajectory in the x, y-plane and heading $\theta_t = 10°$ with velocity $|v_t| = 108$ km/h. The radar uses a $\mathrm{PRF} = 500$ Hz and center frequency $f_c = 1$ GHz for detection. The direction of the receiver relative to the target is $\theta_r = 30°$. Using these parameters results in a target normalized Doppler frequency of $f_0 = 0.376$. Unless stated otherwise, it is assumed that the number of secondary data is limited with $L = K_p$.

The target signal is assumed to be nonfluctuating for each example in this section, specifically we set $|\alpha|^2 = 1.125$ when computing the probability of detection versus probability of false alarm plots. We define the CNR and SNR as,

$$\mathrm{CNR} = \frac{K_p}{\sigma^2} E\left[\boldsymbol{\beta}^H \boldsymbol{\beta}\right], \tag{5.52}$$

and

$$\mathrm{SNR} = K_p \frac{|\alpha|^2}{\sigma^2} \tag{5.53}$$

where $E[\cdot]$ is the expectation operator. The output SINR is [66],

$$\mathrm{SINR} = \frac{|\alpha|^2 |\mathbf{w}^H \mathbf{a}(f_0)|^2}{\mathbf{w}^H \boldsymbol{\Sigma}^{-1} \mathbf{w}}. \tag{5.54}$$

where the output SINR is computed with respect to the Clairvoyant filter $\mathbf{w}_{\mathrm{opt}}$ to allow for scaling to a particular SINR level.

For computing the detection performances we use Monte-Carlo simulations with $100/P_{\mathrm{FA}}$ trials, where P_{FA} is the minimum probability of false alarm. The detection thresholds for the considered detectors are computed numerically using the simulation data.

Two clutter models will be considered in this section: continuous clutter with an exponential (PSD) and low-rank clutter generated using (5.4). In the latter case, the columns of $\mathbf{H}$ in (5.4) are selected as the top r eigenvectors of the exponential Toeplitz covariance matrix model [15],

$$\mathbf{\Sigma}_{\mathrm{C}}\left(i,j\right)=\rho^{|i-j|} \tag{5.55}$$

where $0\leq\rho<1$ is the correlation coefficient which also controls the clutter bandwidth.

We will consider two mismatched cases: where the assumed clutter rank r' is different from the true clutter rank r and when full rank clutter are used instead of low-rank.

5.7.1 Example 1: Root Locations in the Complex Plane

Figure 5.2a shows the roots of the Clairvoyant, (5.50), and (5.48) filters in the complex plane. In each case, $\mathrm{CNR}=30$ dB and $K_p=16$ pulses with $L=16$ secondary data. The clutter rank is $r=6$ and the assumed rank is $r'=r$.

In Fig. 5.2a, the columns of the clutter matrix $\mathbf{H}$ are the top $r=6$ eigenvectors of the AR(1) covariance matrix. The clutter in this case cannot be appropriately modeled as discrete frequencies, but the Clairvoyant filter roots must still occur on the unit circle. The roots of (5.48) occur near but not entirely on the unit circle, especially near $(1,0)$ where the clutter energy is most concentrated.

Figure 5.2b shows the magnitude responses for the UC-GLRT filter, along with the responses for the other detectors. The clutter spectrum, computed using Capon's method, is also included in this figure, where it can be seen that the majority of the clutter energy resides near zero-Doppler with a total bandwidth of approximately 200 Hz. The target Doppler frequency is assumed to be known in this case, and $r=11$ is the true clutter rank with an assumed clutter rank of $r'=11$. The clutter basis' are the top r eigenvectors of the AR(1) matrix with $\rho=0.8$. $\mathrm{CNR}=30$ dB and all filters were generated under H_0, without the target present. Depicted on the right hand side of Fig. 5.2b, is the peak in the spectra corresponding to the target Doppler frequency.

Closely examining Fig. 5.2b shows that the greatest agreement between the eigenvector-

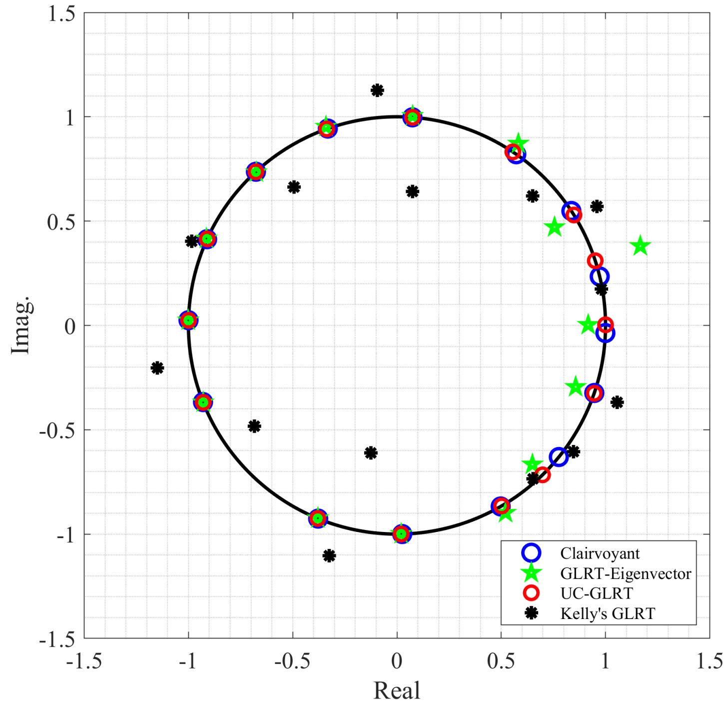

(a) Root locations with rank $r = 6$ AR(1) clutter

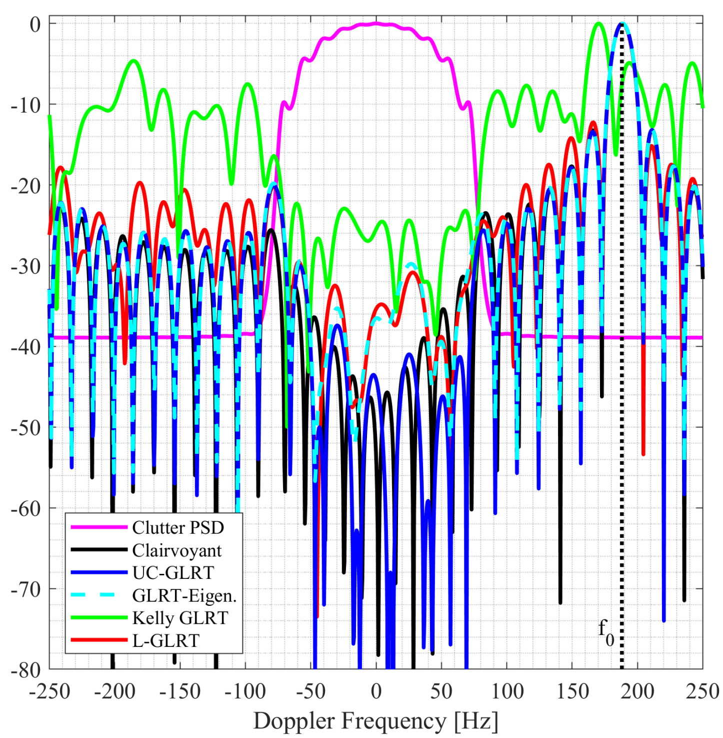

(b) Magnitude response figure with $r = 11$ and $r' = 11$

Figure 5.2: (a) Root locations and (b) Filter magnitude responses

based filter and the UC-based filter responses occurs at the outer edges of the spectrum, mirroring the behaviour shown by the roots in Fig. 5.2a. Closer to zero-Doppler the greatest differences between the eigenvector-based filter and the UC-GLRT can be seen since the UC-GLRT enforces unit circle roots in this location while the eigenvector-based GLRT does not. Intuitively, one can expect greater performance from a filter that enforces unit circle zeros over one that does not. Since unit circle zeros cause deep nulls in the filter magnitude response, it is expected that by enforcing the unit circle root constraint we may achieve better clutter cancellation and hence, improved detection performance.

5.7.2 Example 2: Detection Performance in Low-Rank Clutter

Figures 5.3a and 5.3b illustrate the detection performance of the considered approaches in low-rank clutter for the cases where the clutter rank is assumed known and unknown, respectively. In both cases the clutter rank is $r = 11$, $\mathrm{CNR} = 30$ dB, and $\mathrm{SNR} = 10$ dB. Each discrete clutter component is assumed to have identical clutter power σ_c^2.

In Fig. 5.3a, the clutter rank is assumed to be perfectly known to gauge the performance of the UC-GLRT. From this figure it is evident that the proposed approach outperforms all others, achieving a higher probability of false alarm than the other considered approaches. Here, we also see that the performance of the eigenvector-based GLRT (5.49), diagonally loaded GLRT (L-GLRT) [5], and M-UCRC-AMF display similar performance. For the L-GLRT, the diagonal loading factor is 7, roughly the average of the clutter and white noise variances.

In practice, the clutter rank cannot be known a priori, and mismatch between the true clutter rank r and assumed clutter rank r' may occur. In that case, the performance of the proposed approach will suffer, as it is dependent upon the clutter rank. This is the case depicted in Fig. 5.3b where the assumed clutter rank is $r' = 14$ and the true rank is $r = 11$. As expected the performance of the UC-GLRT is impacted by this rank mismatch compared

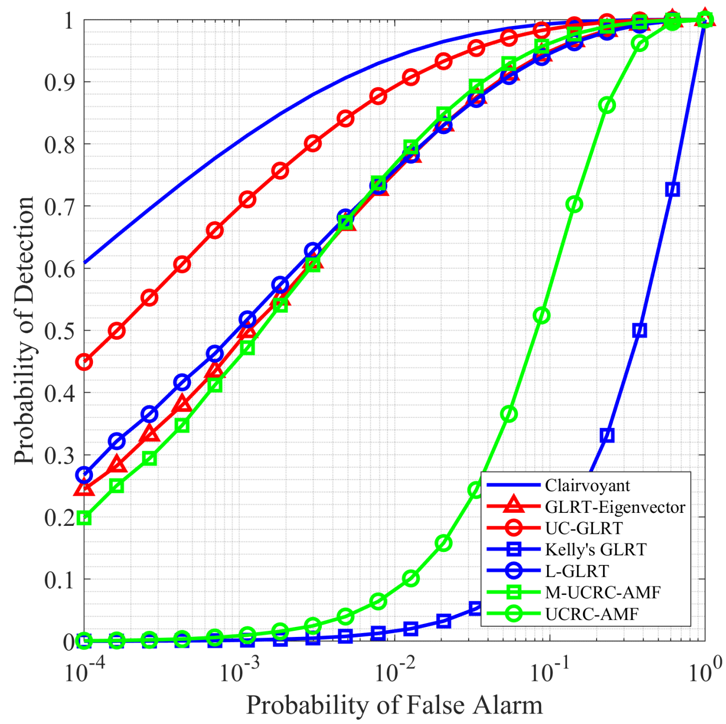

(a) ROC with low rank clutter, known rank $r' = 11$, and known f_0.

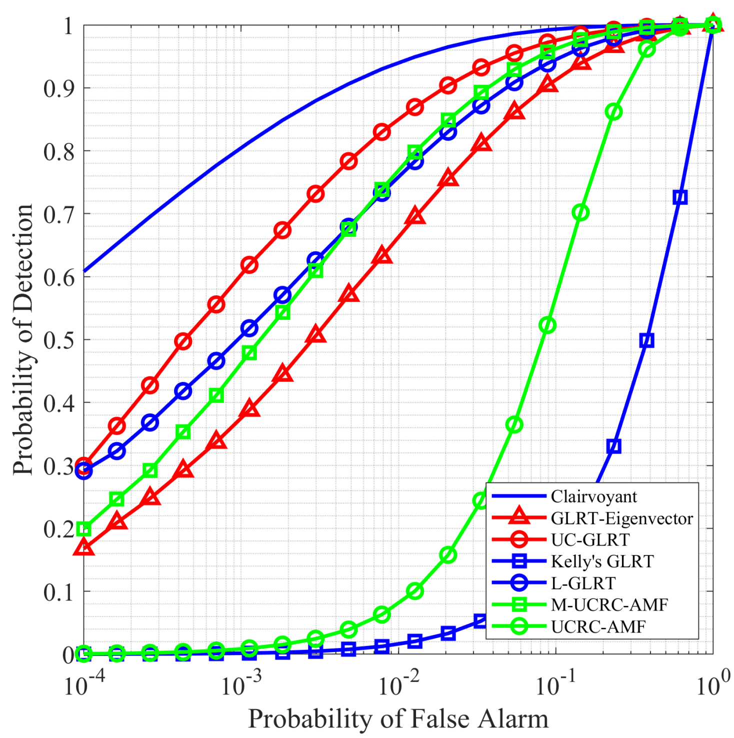

(b) ROC with low rank clutter, mismatched rank $r' = 14$, and known f_0.

Figure 5.3: Detection performance with low-rank clutter (a) $r' = 11$ (b) $r' = 14$

to the ideal case shown in Fig. 5.3a. Overestimating the rank will result in modeling noise eigenvectors as interference eigenvectors. In the context of root positioning, modeling noise eigenvectors as clutter eigenvectors will negatively affect the corresponding root position in the complex plane (see Fig. 5.2a).

5.7.3 Example 3: Detection Performance in Continuous Clutter

In this example, we consider the case where the clutter is full-rank, which is a mismatch from the low-rank assumption used to derive the UC-GLRT and eigenvector-based GLRT. The clutter covariance matrix is the exponential model described in (5.55) with $\rho = 0.95$. When choosing the assumed rank, we preserve the top r' of eigenvectors such that the ratio of the sum of the r' eigenvalues to the total eigenvalue sum equal to 0.95 [40]. For $\rho = 0.95$, the number of necessary eigenvectors is $r' = 7$.

Figure 5.4a shows the detection performance for $K_p = 32$, $\mathrm{SNR} = 13$ dB, and $\mathrm{CNR} = 30$ dB with an assumed clutter rank of $r' = 7$. The UC-GLRT exhibits the best detection performance, followed by the eigenvector-based GLRT, M-UCRC-AMF, and L-GLRT, respectively. The L-GLRT was implemented with $\alpha = 1.63$ in this example, roughly the midpoint between the minimum eigenvector of the clutter covariance matrix and the white noise power.

Figure 5.4b shows the detection performance under the same parameters used to generate Fig. 5.4a with the exception that now the assumed clutter rank is $r' = 11$. The detection performances of the UC-GLRT and eigenvector-based GLRT have been perceptively impacted by the increased rank, while the L-GLRT and M-UCRC-AMF remain unaltered.

Clearly, the UC-GLRT is sensitive to overestimation of the clutter rank, and similar results were seen in Section 5.7.2. While retaining $r' = 7$ eigenvectors captures roughly 95 percent of the clutter energy for $\rho = 0.95$, increasing to $r' = 11$ only increases the ratio of captured clutter energy to roughly 97 percent. Hence, there exists a point of diminishing

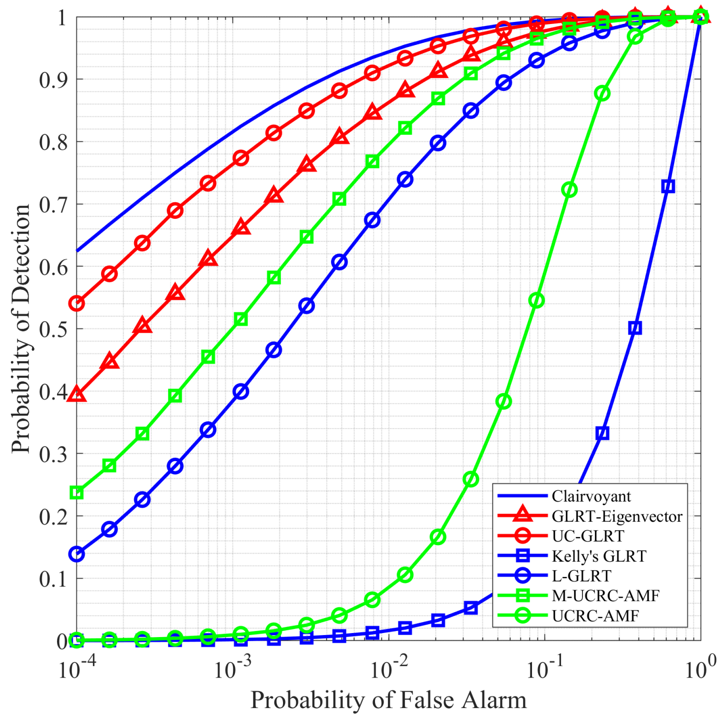

(a) ROC for full rank clutter with $r' = 7$ and known f_0.

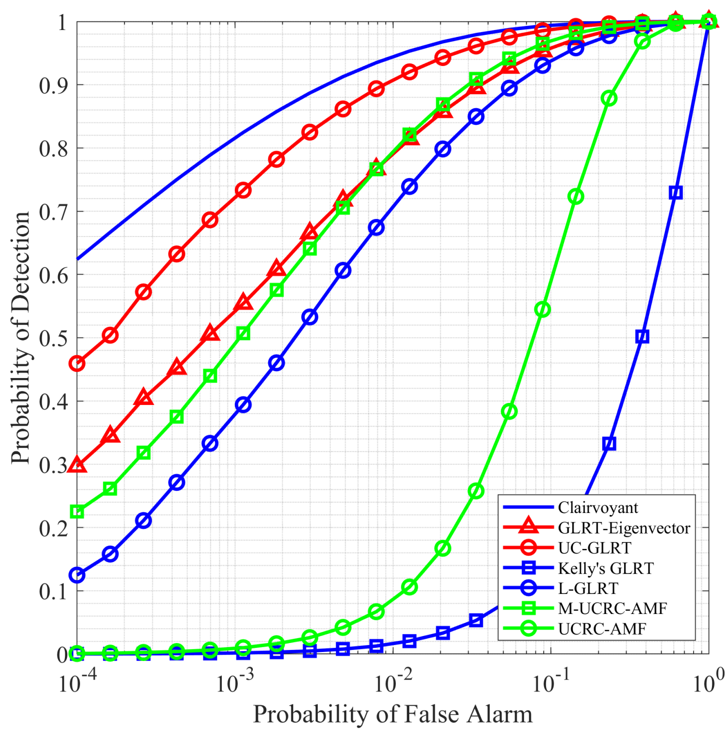

(b) ROC for full rank clutter with $r' = 11$ and known f_0.

Figure 5.4: Full rank clutter detection performance (a) $r' = 7$ (b) $r' = 11$

returns when increasing the assumed rank to try and cancel more clutter. We hypothesize that increasing the clutter rank results in modeling noise eigenvectors as clutter eigenvectors, resulting in roots that may occur far from its proper location on the unit circle (see Fig. 5.2a). This will adversely impact radial root placement after applying the UC-GLRT algorithm.

5.7.4 Example 4: Detection Performance with Unknown Target Doppler Frequency

Algorithm 3 requires an estimate of the target Doppler frequency to initialize the UC approach. However, in practice it is not representative to assume that f_0 is known, and this quantity must be estimated before the UC-GLRT can be applied.

A means for estimating the target Doppler frequency is outside of the scope of this chapter. However, the UC-GLRT does require an eigendecomposition of the sample covariance matrix to initialize the algorithm. Hence, we are free to use $\hat{\mathbf{P}}^{\perp}$ in the following way to compute the maximum likelihood estimate of the target Doppler,

$$\hat{f}_0 = \max_f \frac{|\mathbf{a}^H(f)\,\hat{\mathbf{P}}^{\perp}\mathbf{x}_0|^2}{\mathbf{a}^H(f)\,\hat{\mathbf{P}}^{\perp}\mathbf{a}(f)} \tag{5.56}$$

where the maximization takes place over the set of normalized Doppler frequencies $f \in (-0.5, 0.5)$. In practice, we implement this estimate by pre-whitening the test data $\mathbf{x}_0$ using $\hat{\mathbf{P}}^{\perp}$, taking a length N_{FT} discrete Fourier transform and searching for the maximum.

Figure 5.5a shows the performance of the UC-GLRT (5.51) and eigenvector-based GLRT (5.49) when the target Doppler frequency is unknown. The unknown frequency is estimated using (5.56) with a length $N_{\mathrm{FT}} = 1024$ Fourier transform. The known frequency curves are included as a benchmark. As expected, the performance of the two detectors suffers when the target Doppler is unknown however, the UC-GLRT exhibits superior detection performance over the eigenvector approach, providing consistent performance for $P_{\text{FA}} < 10^{-1}$.

Figure 5.5b shows the probability of detection versus SINR when the Doppler frequency is unknown, where the known frequency cases are included again as benchmarks. From this figure, it is clear that the UC-GLRT outperforms the eigenvector-based approach, attaining a 2 dB performance improvement over the latter around the $P_{\text{D}} = .45$ level.

5.7.5 Example 5: Normalized SINR versus Secondary Data

In this section, we examine the convergence properties of the UC-GLRT for difference CPI lengths. We assess the convergence of the proposed approach using the normalized SINR as a function of the number of available i.i.d. secondary data. The normalized SINR (NSINR) is [48],

$$\text{NSINR} = \frac{|\hat{\mathbf{w}}^H \mathbf{a}\left(f_0\right)|^2}{\left(\mathbf{a}^H\left(f_0\right)\boldsymbol{\Sigma}^{-1}\mathbf{a}\left(f_0\right)\right)\left(\hat{\mathbf{w}}^H\boldsymbol{\Sigma}\hat{\mathbf{w}}\right)} \tag{5.57}$$

where $\hat{\mathbf{w}}$ is an arbitrary filter. For the purposes of this example, we define acceptable performance as the point where $\text{NSINR} = 3$ dB.

In this example, $r = 11$ is used throughout with $\text{CNR} = 30$ dB and there is no mismatch between the assumed target steering vector and the true steering vector. The number of secondary data ranges from 8 up to $3r$. For each point on the horizontal axes of Figs. 5.6a and 5.6b, the average NSINR is computed using 5000 Monte-Carlo trials.

Figure 5.6a illustrates the performance of the UC-GLRT filter (5.50), the eigenvector-based filter (5.48), and the L-GLRT for $K_p = 32$ pulses. The point on the horizontal axis where the performance curves intersect the black line shows the number of secondary data required to achieve a 3 dB performance relative to the Clairvoyant filter. The eigenvector approach achieves this this performance at roughly 21 secondary data, which is approximately what is predicted for eigenvector-based techniques [66]. The UC-GLRT displays the fastest convergence out of all of the other approaches, achieving roughly 2 dB performance

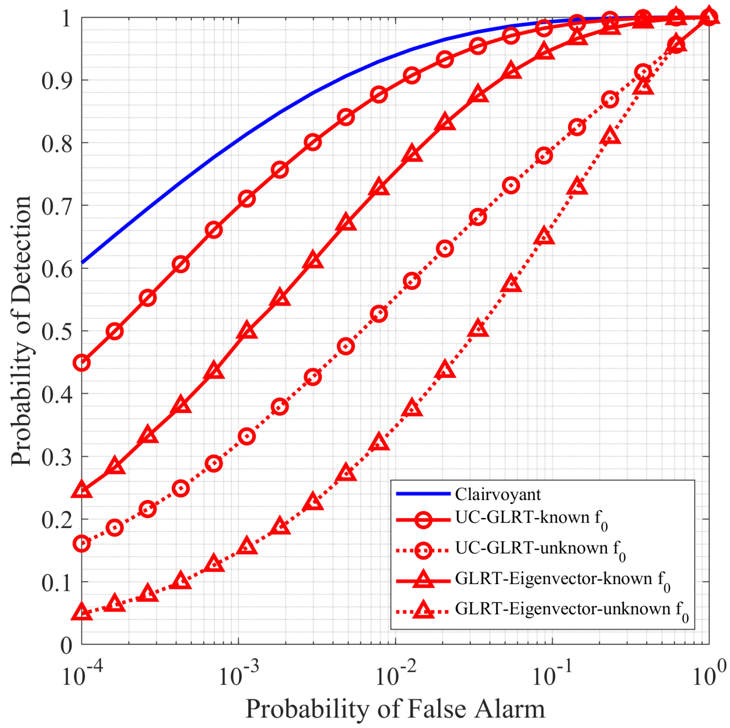

(a) ROC

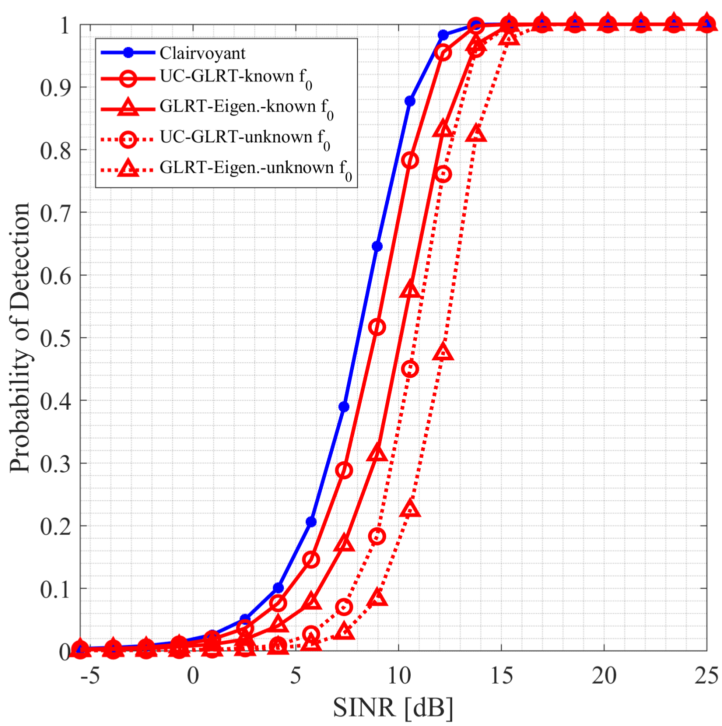

(b) P_{D} vs. SINR

Figure 5.5: Low rank clutter detection performance with known clutter rank $r' = 11$ and unknown f_0 (a) ROC curve (b) P_{D} vs. SINR.

improvement over the eigenvector approach at $2r$ secondary data. The same observations persist for the $K_p = 64$ pulses case shown in Fig. 5.6b. The UC-GLRT approach again displays rapid convergence compared to the other three approaches.

Extrapolating the results shown in Figs. 5.6a and 5.6b, we can assert that enforcing the unit circle roots constraint using Algorithm 3 decreases the amount of secondary data necessary to achieve 3 dB performance by more than half of that required when using a PCI-based technique. Furthermore, since the NSINR is invariant to scaling of the filter, we hypothesis that the NSINR gains of the proposed approach are due only to enforcement of the unit circle roots constraint.

5.7.6 Example 6: Detection Performance with Extremely Limited Secondary Data

In this example, we consider the impact of extremely limited sample support upon the proposed detectors. The same clutter model that was used in Section 5.7.2 is used here, where the $\rho = 0.8$ is used for the covariance matrix and $r = 11$ dominant eigenvectors are retained to generate the low-rank clutter. We assume that the clutter rank and Doppler frequency are known in this example. The number of secondary data is $L = 22 = 2r < K_p$ and hence, we only examine the performance of the UC-GLRT, eigenvector-GLRT, and L-GLRT. The loading factor for the L-GLRT is $\alpha = 7$, which is the same from Section 5.7.2. The number of pulses per CPI is $K_p = 32$.

Figures 5.7a and 5.7b show the receiver operating characteristics and probability of detection P_{D} versus SINR curves. For Fig. 5.7a, we set $\mathrm{SNR} = 10$ dB and $\mathrm{CNR} = 30$ dB. To ease the computational burden, we set the probability of false alarm to $P_{\mathrm{FA}} = 10^{-3}$ in Fig. 5.7b.

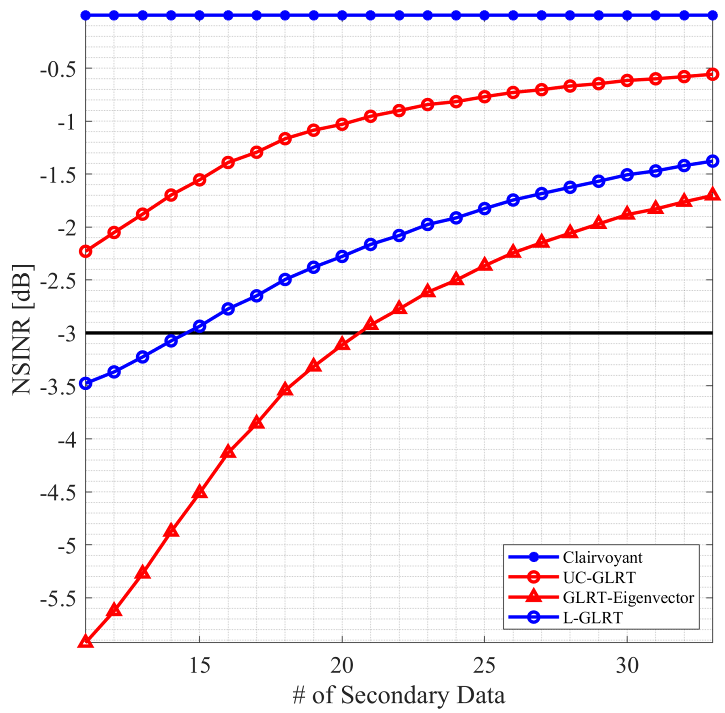

(a) NSINR $K_p = 32$ pulses.

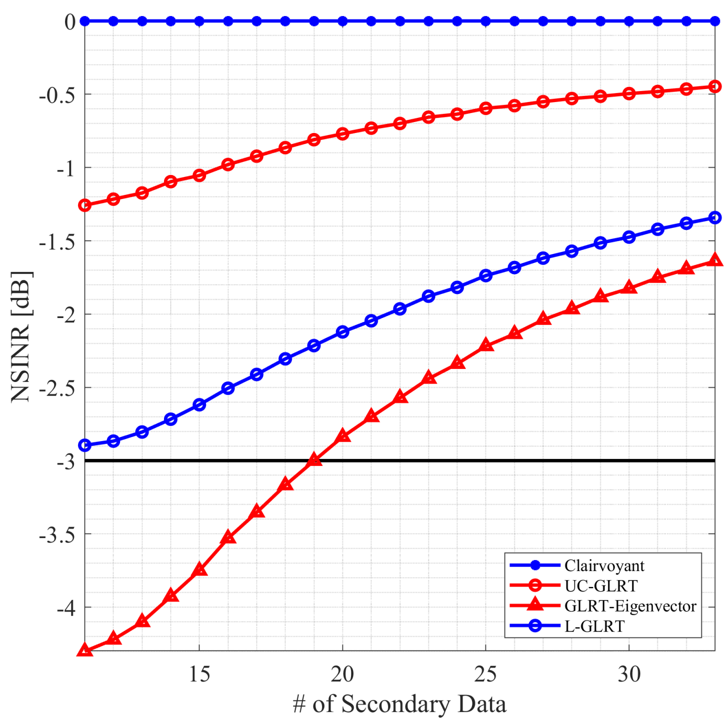

(b) NSINR $K_p = 64$ pulses.

Figure 5.6: NSINR performance (a) $K_p = 32$ pulses (b) $K_p = 64$ pulses

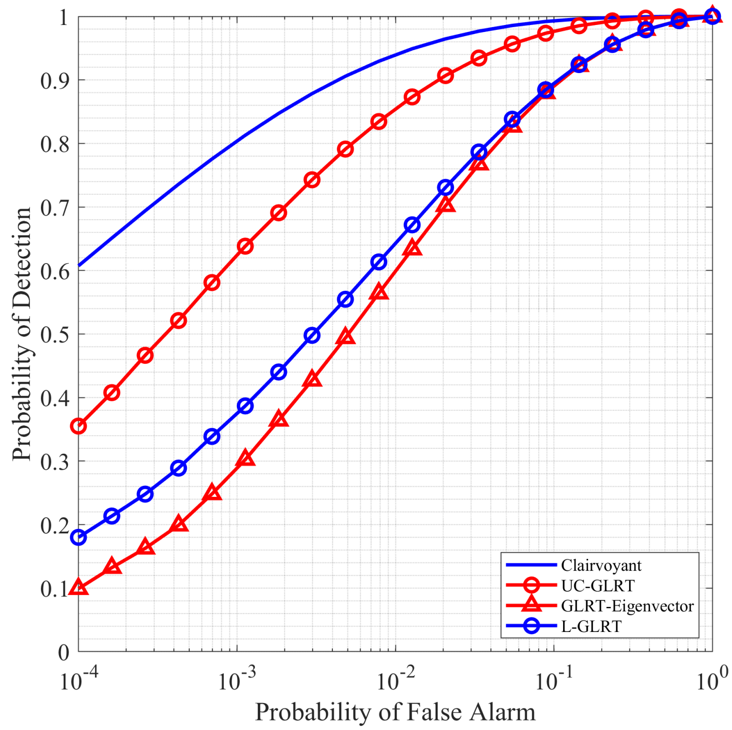

(a) ROC with known r and known f_0.

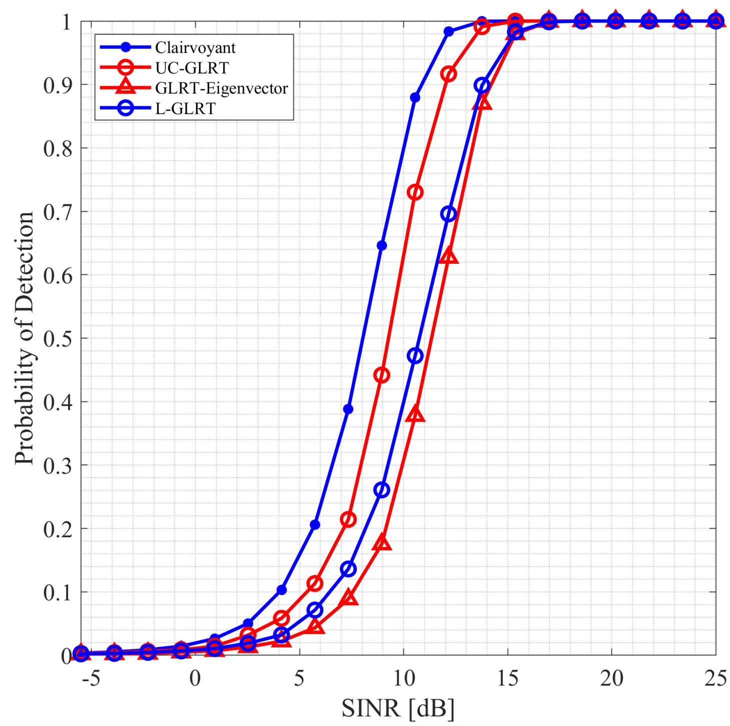

(b) P_{D} vs. SINR with known r and known f_0.

Figure 5.7: Low sample support detection performance in low rank clutter (a) ROC curve (b) P_{D} vs. SINR

5.8 Conclusion

In this chapter, the UC-GLRT was proposed for moving target detection in low rank Gaussian clutter. Under the assumption that the clutter occupy a fixed low-rank subspace, a GLRT based on explicitly enforcing unit circle roots was proposed and its asymptotic detection performance was derived. It was shown that although the unit circle roots based detector has CFAR with respect to the clutter coefficients and noise power, its performance is inferior to the GLRT derived under the assumption that the true clutter subspace is known. To rectify this performance disparity, it was proposed to modify the known roots GLRT by incorporating knowledge of the true clutter subspace within the detector structure. Finally, we showed that after this modification, the GLRT retains CFAR with respect to the clutter coefficients and noise power.

In the absence of either the true clutter subspace or the roots of the Clairvoyant filter, we estimated the clutter subspace using the dominant eigenvectors of the SCM. To obtain a set of unit circle roots, we radially projected the roots of the eigenvector-based detector onto the unit circle.

Through simulation examples, it was shown that the UC-GLRT achieves a higher probability of detection at lower false alarm rates with limited secondary data than the L-GLRT or eigenvector-based GLRT. The rapid convergence of the UC-GLRT in terms of the normalized signal-to-interference plus noise ratio was demonstrated, where we showed empirically that the proposed UC roots approach converges in performance with less than half of the data necessary for the eigenvector-based detector.

5.9 Appendix-I: MLE Derivations

In this appendix, the maximum likelihood estimates (5.18)-(5.24) are derived under H_1 and H_0, respectively.

5.9.1 Parameter Estimation under H_1 :

Under H_1, the MLEs of f_0, α, $\boldsymbol{\beta}_0$, $\boldsymbol{\beta}_\ell$, and σ are required. The MLE of the clutter coefficients for the primary data can be found by minimizing (5.14) with respect to $\boldsymbol{\beta}_0$. Expanding (5.14), taking the derivative, conjugating, and equating to zero yields,

$$\frac{\partial J}{\partial \boldsymbol{\beta}_0} = \left(\mathbf{H}^H \mathbf{H}\right) \boldsymbol{\beta}_0 + \alpha \mathbf{H}^H \mathbf{a}\left(f_0\right) - \mathbf{H}^H \mathbf{x}_0 = 0. \tag{5.58}$$

After solving for $\boldsymbol{\beta}_0$ we arrive at

$$\hat{\boldsymbol{\beta}}_0 = \left(\mathbf{H}^H \mathbf{H}\right)^{-1} \mathbf{H}^H \left(\mathbf{x}_0 - \alpha \mathbf{a}\left(f_0\right)\right), \tag{5.59}$$

The MLEs for $\boldsymbol{\beta}_\ell$, $\ell = 1, \ldots, L$ can also be found by minimizing (5.14). After expanding, differentiating, conjugating, and equating to zero we have

$$\frac{\partial J}{\partial \boldsymbol{\beta}_\ell} = \left(\mathbf{H}^H \mathbf{H}\right) \boldsymbol{\beta}_\ell - \mathbf{H}^H \mathbf{x}_0 = 0. \tag{5.60}$$

Solving for $\boldsymbol{\beta}_\ell$ produces,

$$\hat{\boldsymbol{\beta}}_\ell = \left(\mathbf{H}^H \mathbf{H}\right)^{-1} \mathbf{H}^H \mathbf{x}_\ell; \;\; \ell = 1, \ldots, L. \tag{5.61}$$

Note that we may eliminate the clutter coefficients from (5.14) by substituting the MLEs. Consequently, (5.14) may be expressed as

$$J\left(\mathbf{X}, \alpha, \hat{\mathbf{B}} | H_1\right) = \left(\mathbf{x}_0 - \alpha \mathbf{a}\left(f_0\right)\right)^H \mathbf{P}_{\mathbf{H}}^{\perp} \left(\mathbf{x}_0 - \alpha \mathbf{a}\left(f_0\right)\right) + \sum_{\ell=1}^{L} \mathbf{x}_\ell^H \mathbf{P}_{\mathbf{H}}^{\perp} \mathbf{x}_\ell \tag{5.62}$$

where $\mathbf{P}_{\mathbf{H}}^{\perp}$ is the orthogonal projection from (5.25).

The MLE of α can found by minimizing (5.62). Expanding, taking the derivative with respect to α, conjugating, and equating to zero we have

$$\frac{\partial J}{\partial \alpha} = \alpha \left(\mathbf{a}^H(f_0) \mathbf{P}_{\mathbf{H}}^{\perp} \mathbf{a}(f_0) \right) - \mathbf{a}^H(f_0) \mathbf{P}_{\mathbf{H}}^{\perp} \mathbf{x}_0 = 0, \tag{5.63}$$

which leads to

$$\hat{\alpha} = \frac{\left| \mathbf{a}^H(f_0) \mathbf{P}_{\mathbf{H}}^{\perp} \mathbf{x}_0 \right|^2}{\mathbf{a}^H(f_0) \mathbf{P}_{\mathbf{H}}^{\perp} \mathbf{a}(f_0)}. \tag{5.64}$$

We may now further rewrite (5.62) as,

$$J\left(\mathbf{X}, \hat{\alpha}, \hat{\mathbf{B}} | H_1\right) = -\frac{\left| \mathbf{a}^H(f_0) \mathbf{P}_{\mathbf{H}}^{\perp} \mathbf{x}_0 \right|^2}{\mathbf{a}^H(f_0) \mathbf{P}_{\mathbf{H}}^{\perp} \mathbf{a}^H(f_0)} + \sum_{\ell=1}^{L} \mathbf{x}_\ell^H \mathbf{P}_{\mathbf{H}}^{\perp} \mathbf{x}_\ell. \tag{5.65}$$

The MLE of the target Doppler frequency can be found by maximizing (5.65) and dropping the extraneous terms,

$$\hat{f}_0 = \max_f \frac{\left| \mathbf{a}^H(f) \mathbf{P}_{\mathbf{H}}^{\perp} \mathbf{x}_0 \right|^2}{\mathbf{a}^H(f) \mathbf{P}_{\mathbf{H}}^{\perp} \mathbf{a}(f)}. \tag{5.66}$$

To find the MLE of σ, form the log-likelihood function

$$\mathcal{L}\left(\mathbf{X}; \hat{\alpha}, \sigma, \hat{\mathbf{B}} | H_1\right) = -K(L+1)\log(\pi\sigma^2) - \frac{1}{\sigma^2}\left(-\hat{\alpha} + \sum_{\ell=0}^{L} \mathbf{x}_\ell^H \mathbf{P}_{\mathbf{H}}^{\perp} \mathbf{x}_\ell \right), \tag{5.67}$$

Taking the derivative with respect to σ produces

$$\frac{\partial \mathcal{L}}{\partial \sigma} = -\frac{2K(L+1)}{\sigma^2} + \frac{2}{\sigma^3}\left[-\hat{\alpha} + \sum_{\ell=0}^{L} \mathbf{x}_\ell^H \mathbf{P}_{\mathbf{H}}^{\perp} \mathbf{x}_\ell \right] = 0. \tag{5.68}$$

Solving the above equation gives the MLE of the white noise variance under H_1:

$$\hat{\sigma}_1^2 = \frac{1}{K(L+1)}\left[-\hat{\alpha} + \sum_{\ell=0}^{L} \mathbf{x}_\ell^H \mathbf{P}_{\mathbf{H}}^{\perp} \mathbf{x}_\ell \right]. \tag{5.69}$$

5.9.2 Parameter Estimation under H_0 :

The only necessary estimates under H_1 are the clutter coefficients of the primary and secondary data $\boldsymbol{\beta}_\ell;\ \ \ell = 0, \ldots, L$ and the white noise power σ.

The MLEs for $\boldsymbol{\beta}_\ell,\ \ell = 0, \ldots, L$ can also be found by minimizing (5.13). After expanding, differentiating, conjugating, and equating to zero we have

$$\frac{\partial J}{\partial \boldsymbol{\beta}_\ell} = \left(\mathbf{H}^H\mathbf{H}\right)\boldsymbol{\beta}_\ell - \mathbf{H}^H\mathbf{x}_0 = 0. \tag{5.70}$$

Solving for $\boldsymbol{\beta}_\ell$ produces,

$$\hat{\boldsymbol{\beta}}_\ell = \left(\mathbf{H}^H\mathbf{H}\right)^{-1}\mathbf{H}^H\mathbf{x}_\ell;\ \ \ell = 0, \ldots, L. \tag{5.71}$$

Again, we may eliminate the clutter coefficients from (5.13) by substituting the MLEs. Consequently, (5.13) may be expressed as

$$J\left(\mathbf{X}, \alpha, \hat{\mathbf{B}}|H_0\right) = \sum_{\ell=0}^{L}\mathbf{x}_\ell^H\mathbf{P}_{\mathbf{H}}^{\perp}\mathbf{x}_\ell. \tag{5.72}$$

All that remains is to find the MLE of σ. Under H_0, the log-likelihood function is

$$\mathcal{L}\left(\mathbf{X}; \sigma, \hat{\mathbf{B}}|H_0\right) = -K(L+1)\log(\pi\sigma^2) - \frac{1}{\sigma^2}\sum_{\ell=0}^{L}\mathbf{x}_\ell^H\mathbf{P}_{\mathbf{H}}^{\perp}\mathbf{x}_\ell. \tag{5.73}$$

Taking the derivative of (5.73) with respect to σ produces

$$\frac{\partial \mathcal{L}}{\partial \sigma} = -\frac{2K(L+1)}{\sigma^2} + \frac{2}{\sigma^3}\sum_{\ell=0}^{L}\mathbf{x}_\ell^H\mathbf{P}_{\mathbf{H}}^{\perp}\mathbf{x}_\ell = 0. \tag{5.74}$$

Solving the above equation gives the MLE of the white noise variance under H_0:

$$\hat{\sigma}_0^2 = \frac{1}{K(L+1)} \sum_{\ell=0}^{L} \mathbf{x}_\ell^H \mathbf{P}_{\mathbf{H}}^{\perp} \mathbf{x}_\ell. \tag{5.75}$$

5.10 Appendix II: Proof of Theorem 2

In this section, the performance of the known clutter subspace GLRT (5.27) is derived. To facilitate the proof, define

$$t_{\mathrm{N}} = \frac{\left|\mathbf{a}\left(f_0\right) \mathbf{P}_{\mathbf{H}}^{\perp} \mathbf{x}_0\right|^2}{\mathbf{a}^H\left(f_0\right) \mathbf{P}_{\mathbf{H}}^{\perp} \mathbf{a}\left(f_0\right)}, \tag{5.76}$$

and

$$t_{\mathrm{D}} = \sum_{\ell=0}^{L} \mathbf{x}_\ell^H \mathbf{P}_{\mathbf{H}}^{\perp} \mathbf{x}_\ell \tag{5.77}$$

as the numerator and denominator of (5.27), respectively. The statistical properties of the (5.27) can now be analysed by examining the distributions of (5.76) and (5.77) separately, under H_0 and H_1.

5.10.1 Performance Under H_0

Lemma 1. $\frac{2}{\sigma^2} t_{\mathrm{N}} \sim \chi_2^2$

Proof. Note that

$$\mathbf{P}_{\mathbf{H}}^{\perp} \mathbf{x}_0 = \mathbf{P}_{\mathbf{H}}^{\perp} \mathbf{n}_0, \tag{5.78}$$

so we may rewrite (5.76) as,

$$t_{\mathrm{N}} = \frac{\left|\mathbf{a}\left(f_0\right) \mathbf{P}_{\mathbf{H}}^{\perp} \mathbf{n}_0\right|^2}{\mathbf{a}^H\left(f_0\right) \mathbf{P}_{H}^{\perp} \mathbf{a}\left(f_0\right)}. \tag{5.79}$$

Define the unit vector

$$\mathbf{e} = \frac{\mathbf{P}_{\mathbf{H}}^{\perp}\mathbf{a}\left(f_0\right)}{\sqrt{\left(\mathbf{a}^H\left(f_0\right)\mathbf{P}_{\mathbf{H}}^{\perp}\mathbf{a}\left(f_0\right)\right)}}, \tag{5.80}$$

and simplifying further produces

$$t_{\mathrm{N}} = \mathbf{n}_0^H \mathbf{e}\mathbf{e}^H \mathbf{n}_0. \tag{5.81}$$

The matrix $\mathbf{e}\mathbf{e}^H$ is a rank-1 projection onto the subspace spanned by the vector $\mathbf{e}$. Define the eigenvalue decomposition of this matrix as,

$$\mathbf{e}\mathbf{e}^H = \mathbf{Q}\mathrm{diag}\{1, 0, \ldots, 0\}\mathbf{Q}^H \tag{5.82}$$

where $\mathbf{Q} = \left[\mathbf{q}_1, \ldots, \mathbf{q}_{K_p}\right]$ is the matrix of eigenvectors. For convenience, let $\mathbf{q}_1 = \mathbf{e}$. Substituting (5.82) into (5.81) we obtain

$$t_{\mathrm{N}} = \boldsymbol{\eta}_0^H \mathrm{diag}\{1, 0, \ldots, 0\}\boldsymbol{\eta}_0 = |\eta_{0,1}|^2 \tag{5.83}$$

where $\boldsymbol{\eta}_0 = \mathbf{Q}^H\mathbf{n}_0$ is the transformed noise vector, and $\eta_{0,1}$ is the first element of the this vector. Since $\mathbf{n} \sim \mathcal{CN}\left(\mathbf{0}, \sigma^2\mathbf{I}\right)$ it follows that $\boldsymbol{\eta}_0 \sim \mathcal{CN}\left(\mathbf{0}, \sigma^2\mathbf{I}\right)$ under the orthogonal transformation. Therefore, $\frac{2}{\sigma^2}|\eta_{0,1}|^2 = \frac{2}{\sigma^2}t_N \sim \chi_2^2$ after scaling for the noise variance. □

Lemma 2. $\frac{2}{\sigma^2}t_{\mathrm{D}} \sim \chi^2_{2(L+1)(K_p-r)}$

Proof. From (5.78), we may rewrite

$$\mathbf{x}_\ell^H \mathbf{P}_{\mathbf{H}}^{\perp} \mathbf{x}_\ell = \mathbf{n}_\ell^H \mathbf{P}_{\mathbf{H}}^{\perp} \mathbf{n}_\ell. \tag{5.84}$$

Let the eigenvalue decomposition of $\mathbf{P}_{\mathbf{H}}^{\perp}$ be,

$$\mathbf{P}_{\mathbf{H}}^{\perp} = \mathbf{U}\mathrm{diag}\{\underbrace{1,\ldots,1}_{K_p-r},\underbrace{0,\ldots,0}_{r}\}\mathbf{U}^{H}, \tag{5.85}$$

where $\mathbf{U} = [\mathbf{u}_1,\ldots,\mathbf{u}_{K_p}]$ is the matrix of eigenvectors. Following the logic in [106], we conveniently choose $\mathbf{u}_1 = \mathbf{q}_1$, $\mathbf{u}_k \in \mathcal{H}^{\perp}$ for $k = 1,\ldots,K_p - r$, and $\mathbf{u}_k \in \mathcal{H}$ for $k = K_p - r + 1,\ldots,K_p$, where $\mathcal{H}$ and $\mathcal{H}^{\perp}$ represent the column space of $\mathbf{H}$ and its orthogonal complement, respectively.

Let $\boldsymbol{\eta}_\ell = \mathbf{U}^H\mathbf{n}_\ell$ be the ℓ-th transformed noise vector, and further rewrite (5.84) as

$$\mathbf{n}_\ell^H\mathbf{P}_{\mathbf{H}}^{\perp}\mathbf{n}_\ell = \sum_{k=1}^{K_p-r}|\eta_{\ell,k}|^2 \tag{5.86}$$

where $\eta_{\ell,k}$ is the k-th element of the ℓ-th transformed data vector.

Equation (5.77) can now be rewritten as,

$$t_{\mathrm{D}} = \sum_{\ell=0}^{L}\sum_{k=1}^{K_p-r}|\eta_{\ell,k}|^2. \tag{5.87}$$

Since $\mathbf{n}_\ell \sim \mathcal{CN}\left(\mathbf{0},\sigma^2\mathbf{I}\right)$, it follows that $\boldsymbol{\eta}_\ell \sim \mathcal{CN}\left(\mathbf{0},\sigma^2\mathbf{I}\right)$ due to invariance under the orthogonal transformations. Hence, the independent scalars $\eta_{\ell,k} \sim \mathcal{CN}\left(0,\sigma^2\right)$, and $\frac{2}{\sigma^2}|\eta_{\ell,k}|^2 \sim \chi_2^2$ after accounting for scaling by the noise variance. It follows that the interior summation in (5.87) must also be a scaled chi square random variable with $K_p - r$ degrees of freedom.

Since each of the $\mathbf{x}_\ell$ are drawn i.i.d., their orthogonal transformations are also independent and therefore, the exterior summation in (5.87) is sum of independent $L+1$ scaled chi squared random variables. Hence, $\frac{2}{\sigma^2}t_{\mathrm{D}} \sim \chi^2_{2(L+1)(K_p-r)}$ and the proof is complete. $\square$

Note that (5.87) can be rewritten as,

$$t_{\mathrm{D}} = |\eta_{0,1}|^2 + \sum_{k=2}^{K_p-r} |\eta_{0,k}|^2 + \sum_{\ell=1}^{L} \sum_{k=2}^{K_p-r} |\eta_{\ell,k}|^2 = t_{\mathrm{N}} + \sum_{k=2}^{K_p-r} |\eta_{\ell,k}|^2 + \sum_{\ell=1}^{L} \sum_{k=1}^{K_p-r} |\eta_{\ell,k}|^2 \tag{5.88}$$

without affecting the final distribution. Consequently, T_{GLR} may also be rewritten as

$$T_{\mathrm{GLR}} = \frac{t_{\mathrm{N}}}{t_{\mathrm{N}} + \sum_{k=2}^{K_p-r} |\eta_{0,k}|^2 + \sum_{\ell=1}^{L} \sum_{k=1}^{K_p-r} |\eta_{\ell,k}|^2} = \frac{1}{1+t_0}, \tag{5.89}$$

where

$$t_0 \triangleq \frac{\sum_{k=2}^{K_p-r} |\eta_{0,k}|^2 + \sum_{\ell=1}^{L} \sum_{k=2}^{K_p-r} |\eta_{\ell,k}|^2}{t_{\mathrm{N}}}. \tag{5.90}$$

Since t_0 is the ratio of two central chi squared random variables, t_0 follows a central F distribution and therefore, T_{GLR} has a central Beta distribution with parameters 1 and $(L+1)(K_p-r)-1$, respectively [106].

5.10.2 Performance Under H_1

Lemma 3. $\frac{2}{\sigma^2}t_{\mathrm{N}} \sim \chi^2_2(\gamma_t)$

Proof. From (5.78), under H_1 we have that

$$\mathbf{P}^{\perp}_{\mathbf{H}}\mathbf{x}_0 = \mathbf{P}^{\perp}_{\mathbf{H}}(\alpha\mathbf{a}(f_0) + \mathbf{c} + \mathbf{n}) = \mathbf{P}^{\perp}_{\mathbf{H}}(\alpha\mathbf{a}(f_0) + \mathbf{n}) = \mathbf{P}^{\perp}_{\mathbf{H}}\mathbf{z}_0, \tag{5.91}$$

where $\mathbf{z}_0 = \alpha\mathbf{a}(f_0) + \mathbf{n}$. Since $\mathbf{n} \sim \mathcal{CN}(\mathbf{0}, \sigma^2\mathbf{I})$, it follows that $\mathbf{z}_0 \sim \mathcal{CN}(\alpha\mathbf{a}(f_0), \sigma^2\mathbf{I})$.

From (5.81), we may express t_{N} in the following way

$$t_{\mathrm{N}} = \mathbf{z}_0^H \mathbf{e}\mathbf{e}^H \mathbf{z}_0 = |\mathbf{e}^H \mathbf{z}_0|^2. \tag{5.92}$$

By the properties of linear transformations of a complex Gaussian random variable and the definition of $\mathbf{e}$, it follows that the quantity $\mathbf{e}^H \mathbf{z}_0$ is also Gaussian with mean

$$E\left[\mathbf{e}^H \mathbf{z}_0\right] = \alpha \left(\mathbf{a}^H (f_0) \mathbf{P}_{\mathbf{H}}^{\perp} \mathbf{a}(f_0)\right), \tag{5.93}$$

and variance σ^2. Therefore, t_{N} can be expressed as the magnitude squared of a complex Gaussian random variable and hence, $\frac{2}{\sigma^2} t_{\mathrm{N}} \sim \chi_2^2(\gamma_t)$ after scaling by the variance. The noncentrality parameter is

$$\gamma_t = 2\frac{|\alpha|^2}{\sigma^2} \left(\mathbf{a}^H (f_0) \mathbf{P}_{\mathbf{H}}^{\perp} \mathbf{a}(f_0)\right). \tag{5.94}$$

□

Lemma 4. $\frac{2}{\sigma^2} t_{\mathrm{D}} \sim \chi^2_{2(K_p - r)(L+1)}(\gamma_t)$

Proof. We begin the proof by separating the t_{D} into its primary and secondary components,

$$t_{\mathrm{D}} = \sum_{\ell=0}^{L} \mathbf{x}_\ell^H \mathbf{P}_{\mathbf{H}}^{\perp} \mathbf{x}_\ell = \mathbf{z}_0^H \mathbf{P}_{\mathbf{H}}^{\perp} \mathbf{z}_0 + \sum_{\ell=1}^{L} \mathbf{x}_\ell^H \mathbf{P}_{\mathbf{H}}^{\perp} \mathbf{x}_\ell, \tag{5.95}$$

where we have made use of the definition of $\mathbf{z}_0$ from the proof of Lemma 3. Noting that $\mathbf{x}_\ell$

contain no target for $\ell = 1, \ldots, L$ we may further write

$$t_{\mathrm{D}} = \mathbf{z}_0^H \mathbf{P}_{\mathbf{H}}^{\perp} \mathbf{z}_0 + \sum_{\ell=1}^{L} \mathbf{n}_{\ell}^H \mathbf{P}_{\mathbf{H}}^{\perp} \mathbf{n}_{\ell}. \tag{5.96}$$

From (5.86), we can expand the sum term in (5.96)

$$t_{\mathrm{D}} = \mathbf{z}_0^H \mathbf{P}_{\mathbf{H}}^{\perp} \mathbf{z}_0 + \sum_{\ell=1}^{L} \sum_{k=1}^{K_p - r} |\eta_{\ell,k}|^2, \tag{5.97}$$

where the $\eta_{\ell,k}$ are the same as in the proof of Lemma 2. From the proof of Lemma 2, it follows that the summation in (5.97) is a scaled central chi squared random variable with $L\,(K_p - r)$ degrees of freedom.

The proof now proceeds by analyzing the quantity

$$\mathbf{z}_0^H \mathbf{P}_{\mathbf{H}}^{\perp} \mathbf{z}_0. \tag{5.98}$$

Substituting the EVD of $\mathbf{P}_{\mathbf{H}}^{\perp}$ from (5.85) into (5.98) produces,

$$\mathbf{z}_0^H \mathbf{P}_{\mathbf{H}}^{\perp} \mathbf{z}_0 = \sum_{k=1}^{K_p - r} \mathbf{z}_0^H \mathbf{u}_k \mathbf{u}_k^H \mathbf{z}_0 = \sum_{k=1}^{K_p - r} |\mathbf{u}_k^H \mathbf{z}_0|^2, \tag{5.99}$$

where $\mathbf{u}_k$ are the eigenvectors of $\mathbf{P}_{\mathbf{H}}^{\perp}$. Since $\mathbf{z}_0 \sim \mathcal{CN}\left(\alpha \mathbf{a}\left(f_0\right), \sigma^2 \mathbf{I}\right)$, it follows that the quantities $\mathbf{u}_k^H \mathbf{z}_0$ are also complex Gaussian with mean

$$E\left[\mathbf{u}_k^H \mathbf{z}_0\right] = \alpha \mathbf{u}_k^H \mathbf{a}\left(f_0\right);\ k = 1, \ldots, K_p - r \tag{5.100}$$

each with variance σ^2. Equation (5.98) can now be seen as a scaled noncentral chi squared random variable with noncentrality parameter

$$2\frac{|\alpha|^2}{\sigma^2}\sum_{k=1}^{K_p-r}\left(\mathbf{a}^H\left(f_0\right)\mathbf{u}_k\mathbf{u}_k^H\mathbf{a}\left(f_0\right)\right). \tag{5.101}$$

However, in the proof of Lemma 2 we assumed that $\mathbf{u}_1 = \mathbf{e} = \frac{\mathbf{P}_{\mathbf{H}}^{\perp}\mathbf{a}(f_0)}{\mathbf{a}^H(f_0)\mathbf{P}_{\mathbf{H}}^{\perp}\mathbf{a}(f_0)}$ and that $\mathbf{u}_k \in \mathcal{H}^{\perp};\ k = 2, \ldots, K_p - r$ so that $\mathbf{u}_k = \mathbf{P}_{\mathbf{H}}^{\perp}\mathbf{u}_k$. Therefore, by the orthogonality of the eigenvectors, $\mathbf{a}^H\left(f_0\right)\mathbf{u}_k = \mathbf{a}^H\left(f_0\right)\mathbf{P}_{\mathbf{H}}^{\perp}\mathbf{u}_k = 0$ and $\mathbf{a}^H\left(f_0\right)\mathbf{u}_1 = \mathbf{a}^H\left(f_0\right)\mathbf{P}_{\mathbf{H}}^{\perp}\mathbf{a}\left(f_0\right)$. Equation (5.101) now reduces to γ_t.

We may now assert that (5.98) is a scaled noncentral chi squared random variable with $K_p - r$ degrees of freedom and noncentrality parameter γ_t. Finally, t_{D} can be seen as the summation of a scaled noncentral and scaled central chi squared random variables and hence, $\frac{2}{\sigma^2}t_{\mathrm{D}} \sim \chi^2_{2(L+1)(K_p-r)}$. □

Our previous observations can be used to expand (5.99):

$$\mathbf{z}_0^H\mathbf{P}_{\mathbf{H}}^{\perp}\mathbf{z}_0 = |\mathbf{e}^H\mathbf{z}_0|^2 + \sum_{k=2}^{K_p-r}|\eta_{0,k}|^2, \tag{5.102}$$

where we have made use off $\mathbf{u}_1 = \mathbf{e}$ and the orthogonality $\mathbf{u}_k^H\mathbf{a}\left(f_0\right) = 0$. Substituting back into (5.95)

$$t_{\mathrm{D}} = |\mathbf{e}^H\mathbf{z}_0|^2 + \sum_{k=2}^{K_p-r}|\eta_{0,k}|^2 + \sum_{\ell=1}^{L}|\eta_{\ell,k}|^2 = t_{\mathrm{N}} + \sum_{k=2}^{K_p-r}|\eta_{0,k}|^2 + \sum_{\ell=1}^{L}\sum_{k=1}^{K_p-r}|\eta_{\ell,k}|^2. \tag{5.103}$$

Now, T_{GLR} can be expressed as

$$T_{\mathrm{GLR}} = \frac{t_{\mathrm{N}}}{t_{\mathrm{N}} + \sum_{k=2}^{K_p-r} |\eta_{0,k}|^2 + \sum_{\ell=1}^{L} \sum_{k=1}^{K_p-r} |\eta_{\ell,k}|^2} = \frac{t_1}{t_1+1}, \tag{5.104}$$

where

$$t_1 \triangleq \frac{t_{\mathrm{N}}}{\sum_{k=2}^{K_p-r} |\eta_{0,k}|^2 + \sum_{\ell=1}^{L} \sum_{k=1}^{K_p-r} |\eta_{\ell,k}|^2}. \tag{5.105}$$

Equation 5.105 is the ratio of a noncentral chi squared with 2 degrees of freedom to a central chi squared random variable with $2\left(\left(L+1\right)\left(K_p-r\right)-1\right)$. Hence, t_1 follows a noncentral F distribution and T_{GLR} follows a noncentral Beta distribution with parameters 1 and $\left(L+1\right)\left(K_p-r\right)-1$ [106].

5.11 Appendix III: Proof of Theorem 3

Following Appendix 5.10, we define

$$s_{\mathrm{N}} = \frac{\left|\mathbf{a}\left(f_0\right)\mathbf{P}_{\mathbf{A}}^{\perp}\mathbf{x}_0\right|^2}{\mathbf{a}^H\left(f_0\right)\mathbf{P}_{\mathbf{A}}^{\perp}\mathbf{a}\left(f_0\right)}, \tag{5.106}$$

and

$$s_{\mathrm{D}} = \sum_{\ell=0}^{L} \mathbf{x}_\ell^H \mathbf{P}_{\mathbf{A}}^{\perp}\mathbf{x}_\ell \tag{5.107}$$

to be the numerator and denominator of (5.32), respectively.

We must note that in the known roots case, $\mathbf{P}_{\mathbf{A}}^{\perp}\mathbf{x}_\ell \neq \mathbf{P}_{\mathbf{A}}^{\perp}\mathbf{n}_\ell;\ \ell = 1,\ldots,L$ due to the imperfect clutter cancellation caused by subspace mismatch between $\mathbf{A}$ and $\mathbf{H}$. However, we assert that reasonable clutter cancellation is achieved and thus we approximate

$$\mathbf{P}_{\mathbf{A}}^{\perp}\mathbf{x}_\ell \approx \mathbf{P}_{\mathbf{A}}^{\perp}\mathbf{n}_\ell;\ \ell = 1,\ldots,L \tag{5.108}$$

for the purposes of determining the statistical performance.

5.11.1 Performance Under H_0

Lemma 5. $\frac{2}{\sigma^2} s_{\mathrm{N}} \sim \chi_2^2$

Proof. Using (5.108), we may write s_{N} as

$$s_{\mathrm{N}} = \frac{\left|\mathbf{a}\left(f_0\right)\mathbf{P}_{\mathbf{A}}^{\perp}\mathbf{n}_0\right|^2}{\mathbf{a}^H\left(f_0\right)\mathbf{P}_{\mathbf{A}}^{\perp}\mathbf{a}\left(f_0\right)}. \tag{5.109}$$

We will use the eigenvalue decomposition of $\mathbf{P}_{\mathbf{A}}^{\perp}$ given in Section 5.4.3, which is repeated here for clarity

$$\mathbf{P}_{\mathbf{A}}^{\perp} = \mathbf{E}\boldsymbol{\Lambda}\mathbf{E}^H = \sum_{k=1}^{K_p} \lambda_k \mathbf{e}_k \mathbf{e}_k^H \tag{5.110}$$

where $\lambda_1 = 1$, $\lambda_k = 0$ for $k = 2, \ldots, K_p$, and $\mathbf{e}_1 = \frac{\mathbf{P}_{\mathbf{A}}^{\perp}\mathbf{a}(f_0)}{\sqrt{\mathbf{a}^H(f_0)\mathbf{P}_{\mathbf{A}}^{\perp}\mathbf{a}(f_0)}}$. As shown in Section 5.4.3, we may write s_{N} in terms of $\mathbf{e}_1$ and thus,

$$s_{\mathrm{N}} = \mathbf{n}_0^H \mathbf{e}_1 \mathbf{e}_1^H \mathbf{n}_0 = \mathbf{n}_0^H \mathbf{E}\boldsymbol{\Lambda}\mathbf{E}^H \mathbf{n}_0, \tag{5.111}$$

from the EVD of $\mathbf{P}_{\mathbf{A}}^{\perp}$. Let $\boldsymbol{\xi}_0 = \mathbf{E}^H\mathbf{n}_0 = \mathbf{e}_1^H\mathbf{n}_0$ be the transformed noise vector. Then, (5.111) can be rewritten as,

$$s_{\mathrm{N}} = \boldsymbol{\xi}_0^H \boldsymbol{\Lambda} \boldsymbol{\xi}_0 = \left|\xi_{0,1}\right|^2, \tag{5.112}$$

where $\xi_{0,1}$ is the first element of the vector $\boldsymbol{\xi}_0$. Since $\mathbf{n}_0 \sim \mathcal{CN}\left(\mathbf{0}, \sigma^2\mathbf{I}\right)$, it follows that $\boldsymbol{\xi}_0 \sim \mathcal{CN}\left(\mathbf{0}, \sigma^2\mathbf{I}\right)$ under the orthogonal transformation. Therefore, $\xi_{0,1}$ is zero-mean complex Gaussian with variance σ^2, and from this it follows that $\frac{2}{\sigma^2} s_{\mathrm{N}} \sim \chi_2^2$. $\square$

Lemma 6. $\frac{2}{\sigma^2} s_{\mathrm{D}} \sim \chi^2_{2(L+1)}$

Proof. Using the approximation in (5.108), rewrite (5.107) as

$$s_{\mathrm{D}} = \sum_{\ell=0}^{L} \mathbf{n}_\ell^H \mathbf{P}_{\mathbf{A}}^{\perp} \mathbf{n}_\ell. \tag{5.113}$$

Substituting the eigenvalue decomposition (5.110) into (5.113), we may further rewrite (5.113) as

$$s_{\mathrm{D}} = \sum_{\ell=0}^{L} \mathbf{n}_\ell^H \mathbf{E} \boldsymbol{\Lambda} \mathbf{E}^H \mathbf{n}_\ell = \sum_{\ell=0}^{L} \boldsymbol{\xi}_\ell^H \boldsymbol{\Lambda} \boldsymbol{\xi}_\ell \tag{5.114}$$

where $\boldsymbol{\xi}_\ell = \mathbf{E}^H \mathbf{n}_\ell$ is the ℓ-th transformed noise vector.

Equation (5.114) can now be expressed as

$$s_{\mathrm{D}} = \sum_{\ell=0}^{L} |\xi_{\ell,1}|^2, \tag{5.115}$$

where $\xi_{\ell,1}$ is the first element of the vector $\boldsymbol{\xi}_\ell$.

Since it is assumed that the $\mathbf{n}_\ell$ are independent and $\mathbf{n}_\ell \sim \mathcal{CN}\left(\mathbf{0}, \sigma^2 \mathbf{I}\right)$, it follows that the $\boldsymbol{\xi}_\ell$ are also independent with $\boldsymbol{\xi}_\ell \sim \mathcal{CN}\left(\mathbf{0}, \sigma^2 \mathbf{I}\right)$ under the orthogonal transformation. Hence, $\xi_{\ell,1} \sim \mathcal{CN}\left(0, \sigma^2\right)$, and (5.115) is the sum of independent scaled chi squared random variables. Finally, $\frac{2}{\sigma^2} s_{\mathrm{D}} \sim \chi^2_{2(L+1)}$. $\square$

As was the case in Appendix 5.10, it is possible to write

$$s_{\mathrm{D}} = |\xi_{0,1}|^2 + \sum_{\ell=1}^{L} |\xi_{\ell,1}|^2 = s_{\mathrm{N}} + \sum_{\ell=1}^{L} |\xi_{\ell,1}|^2. \tag{5.116}$$

Hence, the GLR of (5.32) may be expressed as

$$S_{\text{GLR}} = \frac{s_{\text{N}}}{s_{\text{N}} + \sum_{\ell=1}^{L} |\xi_{\ell,1}|^2} = \frac{1}{1 + s_0}, \tag{5.117}$$

where

$$s_0 \triangleq \frac{\sum_{\ell=1}^{L} |\xi_{\ell,k}|^2}{s_{\text{N}}}. \tag{5.118}$$

Equation (5.118) must also follow a central F distribution and hence, S_{GLR} is central Beta distributed with parameters 1 and L [106].

5.11.2 Performance Under H_1

Lemma 7. $\frac{2}{\sigma^2} s_{\text{N}} \sim \chi_2^2(\gamma_s)$

Proof. Using (5.108), we note that under H_1 we have

$$\mathbf{P}_{\mathbf{A}}^{\perp} \mathbf{x}_0 = \mathbf{P}_{\mathbf{A}}^{\perp} \left(\alpha \mathbf{a} \left(f_0 \right) + \mathbf{c} + \mathbf{n} \right) = \mathbf{P}_{\mathbf{A}}^{\perp} \left(\alpha \mathbf{a} \left(f_0 \right) + \mathbf{n} \right) = \mathbf{P}_{\mathbf{A}}^{\perp} \mathbf{y}_0, \tag{5.119}$$

where $\mathbf{y}_0 = \alpha \mathbf{a} \left(f_0 \right) + \mathbf{n}$. Since $\mathbf{n} \sim \mathcal{CN} \left(\mathbf{0}, \sigma^2 \mathbf{I} \right)$, we must have that $\mathbf{y}_0 \sim \mathcal{CN} \left(\alpha \mathbf{a} \left(f_0 \right), \sigma^2 \mathbf{I} \right)$.

We will again make use of the eigenvalue decomposition of $\mathbf{P}_{\mathbf{A}}^{\perp}$ given in (5.37) specifically the unit vector $\mathbf{e}_1 = \frac{\mathbf{P}_{\mathbf{A}}^{\perp} \mathbf{a}(f_0)}{\sqrt{\mathbf{a}^H(f_0) \mathbf{P}_{\mathbf{A}}^{\perp} \mathbf{a}(f_0)}}$. In Section 5.4.3, it was shown s_{N} may be expressed in the following way

$$s_{\text{N}} = \mathbf{y}_0^H \mathbf{e}_1 \mathbf{e}_1^H \mathbf{y}_0 = |\mathbf{e}_1^H \mathbf{y}_0|^2. \tag{5.120}$$

If follows from the properties of linear transformations of a complex Gaussian random vector that $\mathbf{e}_1^H \mathbf{y}_0$ is also complex Gaussian with mean

$$E\left[\mathbf{e}_1^H \mathbf{y}\right] = \alpha \left(\mathbf{a}^H\left(f_0\right) \mathbf{P}_{\mathbf{A}}^{\perp} \mathbf{a}\left(f_0\right)\right) \tag{5.121}$$

and variance σ^2. Hence, the quantity s_{N} is the square of a complex Gaussian with non-zero mean and variance σ^2, and therefore, after scaling the random variable, $\frac{2}{\sigma^2} s_{\mathrm{N}} \sim \chi_2^2\left(\gamma_s\right)$. The non-centrality parameter is

$$\gamma_s = 2\frac{|\alpha|^2}{\sigma^2}\left(\mathbf{a}^H\left(f_0\right) \mathbf{P}_{\mathbf{A}}^{\perp} \mathbf{a}\left(f_0\right)\right) \tag{5.122}$$

□

Lemma 8. $\frac{2}{\sigma^2} s_{\mathrm{D}} \sim \chi_{2(L+1)}^2\left(\gamma_s\right)$

Proof. We start the proof by expanding the quantity

$$s_{\mathrm{D}} = \sum_{\ell=0}^{L} \mathbf{x}_\ell^H \mathbf{P}_{\mathbf{A}}^{\perp} \mathbf{x}_\ell = \mathbf{y}_0^H \mathbf{P}_{\mathbf{A}}^{\perp} \mathbf{y}_0 + \sum_{\ell=1}^{L} \mathbf{x}_\ell^H \mathbf{P}_{\mathbf{A}}^{\perp} \mathbf{x}_\ell \tag{5.123}$$

where we have separated the sum into primary and secondary data components, and used the variable $\mathbf{y}_0$ from the proof of Lemma 5.

We invoke the equality proven in Section 5.4.3 to assert that

$$s_{\mathrm{N}} = \mathbf{y}_0^H \mathbf{P}_{\mathbf{A}}^{\perp} \mathbf{y}_0. \tag{5.124}$$

Noting that the secondary data $\{\mathbf{x}_\ell\}_{\ell=1}^{L}$ contain no target signal and $\mathbf{P}_{\mathbf{A}}^{\perp} \mathbf{x}_\ell \approx \mathbf{P}_{\mathbf{A}}^{\perp} \mathbf{n}_\ell$

we may write (5.123) as,

$$s_{\mathrm{D}} = s_{\mathrm{N}} + \sum_{\ell=1}^{L} \mathbf{n}_{\ell}^{H} \mathbf{P}_{\mathbf{A}}^{\perp} \mathbf{n}_{\ell} = s_{\mathrm{N}} + \sum_{\ell=1}^{L} |\xi_{\ell,1}|^2, \tag{5.125}$$

where we have used the eigenvalue decomposition of $\mathbf{P}_{\mathbf{A}}^{\perp}$ and the transformed noise vector definition from Lemma 4.

In Lemma 4, it was shown that the $\xi_{\ell,1}$ are independent and $\xi_{\ell,1} \sim \mathcal{CN}\left(0, \sigma^2\right)$ and therefore the sum on the last line of (5.125) is a scaled central chi squared random variable with L degrees of freedom. In Lemma 5, it was shown that s_{N} is a scaled non-central chi squared random variable. Since the sum independent chi squared random variables is also chi squared, $\frac{2}{\sigma^2} s_{\mathrm{D}} \sim \chi^2_{2(L+1)}\left(\gamma_s\right)$. □

Using (5.125), it is possible to write

$$S_{\mathrm{GLR}} = \frac{s_{\mathrm{N}}}{s_{\mathrm{N}} + \sum_{\ell=1}^{L} |\xi_{\ell,1}|^2} = \frac{s_1}{s_1 + 1}, \tag{5.126}$$

where

$$s_1 \triangleq \frac{s_{\mathrm{N}}}{\sum_{\ell=1}^{L} |\xi_{\ell,1}|^2}. \tag{5.127}$$

Equation (5.127) is the ratio of a non-central chi squared random variable with 2 degrees of freedom and non-centrality parameter γ_s to a central chi squared random variable with $2L$ degrees of freedom. Hence, s_1 follows a non-central F distribution, and S_{GLR} follows a non-central Beta distribution with parameters 1 and L [106].

5.12 Appendix IV: Proof of Theorem 4

As in the previous appendices, let

$$g_{\mathrm{N}} = s_{\mathrm{N}} = \frac{\left|\mathbf{a}\left(f_0\right)\mathbf{P}_{\mathbf{A}}^{\perp}\mathbf{x}_0\right|^2}{\mathbf{a}^H\left(f_0\right)\mathbf{P}_{\mathbf{A}}^{\perp}\mathbf{a}\left(f_0\right)}, \tag{5.128}$$

and

$$g_{\mathrm{D}} = \sum_{\ell=0}^{L}\mathbf{x}_{\ell}^{H}\mathbf{P}_{\mathbf{H}}^{\perp}\mathbf{x}_{\ell} \tag{5.129}$$

be the numerator and denominator of (5.44), respectively. We will now analyze the performance of (5.44) under H_0 by examining the distributions of g_{N} and g_{D} separately.

From Lemma 5, it is clear that $\frac{2}{\sigma^2}g_{\mathrm{N}} \sim \chi_2^2$, and this can be proven in an identical way to Lemma 5. The same statement is also true for g_{D} where $g_{\mathrm{D}} \sim \frac{2}{\sigma^2}g_{\mathrm{D}} \sim \chi^2_{2(L+1)((K_p-r)}$, and this follows directly from Lemma 2. From the proofs of Lemmas 5 and 2 (specifically, equations (5.112) and (5.88)), respectively, we have that

$$g_{\mathrm{N}} = \boldsymbol{\xi}_0^H\boldsymbol{\Lambda}\boldsymbol{\xi}_0 = |\xi_{0,1}|^2, \tag{5.130}$$

and

$$g_{\mathrm{D}} = |\eta_{0,1}|^2 + \sum_{k=2}^{K_p-r}|\eta_{0,k}|^2 + \sum_{\ell=1}^{L}\sum_{k=2}^{K_p-r}|\eta_{\ell,k}|^2. \tag{5.131}$$

Unlike for Theorems 3 and 4 we cannot assert the equivalence $g_{\mathrm{N}} = |\zeta_{0,1}|^2 = |\eta_{0,1}|^2$ and express the ratio $G_{\mathrm{GLR}} = g_{\mathrm{N}}/g_{\mathrm{D}}$ in a convenient way. However, we know that $|\zeta_{0,1}|^2$ and $|\eta_{0,1}|^2$ are scaled chi squared random variables with two degrees of freedom, and if we let

$$g_{\mathrm{D}} = g_{\mathrm{D}1} + g_{\mathrm{D}2} \tag{5.132}$$

where $g_{\mathrm{D1}} = |\eta_{0,1}|^2$ and

$$g_{\mathrm{D2}} = \sum_{k=2}^{K_p-r} |\eta_{0,k}|^2 + \sum_{\ell=1}^{L} \sum_{k=2}^{K_p-r} |\eta_{\ell,k}|^2, \tag{5.133}$$

it is straightforward to show that g_{D2} is a scaled chi squared random variable with $2(L+1)\,(K_p - r) - 2$ degrees of freedom. Hence, we may express

$$G_{\mathrm{GLR}} = \frac{\chi_2^2}{\chi_2^2 + \chi^2_{2((L+1)(K_p-r)-1)}}. \tag{5.134}$$

Therefore, G_{GLR} must follow a central Beta distribution with parameters 1 and $(L+1)\,(K_p - r) - 1$, and the proof is now complete.

Moving Target Detection in K-Distributed Clutter using Unit Circle Toeplitz Rectification with Limited Secondary Data

6.1 Introduction

Moving target detection in heterogeneous clutter is a classic problem in the radar literature, and many detection and estimation strategies have been proposed over the years to address this challenge [17, 19, 45, 82]. The family of distributions known as compound-Gaussian encompasses a wide range of clutter models, which have been used to theoretically represent empirical radar data. Of these clutter models, the K-distribution has been shown to fit observed sea clutter for high resolution radar with low grazing angle [80]. Optimal detectors have been derived for K-distributed clutter, but they are computationally complex, and expressed in terms of modified Bessel functions. In the context of this thesis, these detectors do not admit the unit circle interpretation from Chapter 2. The normalized adaptive matched filter (NAMF) and its persymmetric counterpart the PS-NAMF [16],[69], have also been proposed for compound-Gaussian clutter [19], and have been shown to retain the CFAR property along with scale invariance [53].

Similar to previous chapters, this chapter's theme is moving target detection by exploiting the unit circle property. However, the proposed approach differs from that described in Chapters 4 and 5 namely; the roots are used to design a Hermitian Toeplitz structured covariance estimate which retains the UC roots property instead of directly designing the filter itself. Toeplitz rectification [12, 28, 30, 35, 104] is not new, and has been applied to many signal processing applications; including beamforming and adaptive detection. However, to the best of our knowledge, no current approach exploits the unit circle roots property for Toeplitz rectification.

Simulation examples will be used to investigate the properties of the proposed Toeplitz rectification approach and to demonstrate its superiority when used in conjunction with the normalized adaptive matched filter detector. Specifically, we examine the false alarm rate characteristics of the NAMF utilizing the UCRC Toeplitz estimate. It will be shown that use of the proposed estimate in the normalized adaptive matched filter retains the constant false alarm rate (CFAR) property with respect to the texture's scale parameter, but this property is not preserved with respect to the clutter covariance matrix structure parameter. The detection performance will also be examined for a non-fluctuating target in K-distributed clutter with limited secondary data. It will be shown that the NAMF with the UCRC Toeplitz estimate outperforms the NAMF and PS-NAMF using the fixed point covariance estimator (FPE) [17], and the NAMF using conventional Toeplitz rectification by averaging the diagonals of the FPE.

This chapter is organized in the following way. In Section 6.2, the received signal model, K-distribution clutter model, and detection problem are described in detail. In Section 6.3, the known-covariance detector is derived and its adaptive counterpart are discussed. In Section 6.4, a detailed discussion of the proposed unit circle roots based Toeplitz rectification method is provided. Section 6.5 contains simulation examples, and Section 6.6

provides closing remarks and discussions on future work.

6.2 Signal Model

Consider a co-located transmitter and receiver mounted on a stationary platform. The transmitter emits K_p periodic, pulses over a coherent processing interval. Pulse-compression is performed at the receiver to isolate the reflected returns originating from a particular range bin. The received slow-time data are stacked into a vector $\mathbf{x} \in \mathbb{C}^{K_p \times 1}$, where each row corresponds to an individual slow-time snapshot.

The received data is modeled as,

$$\mathbf{x} = \alpha \mathbf{a}(f_0) + \boldsymbol{\zeta}. \tag{6.1}$$

where $\boldsymbol{\zeta}$ clutter component, and $\mathbf{a}(f_0)$ is the target temporal steering vector. $\alpha \in \mathbb{C}$ is the unknown complex amplitude of the moving target return.

The temporal steering vector is,

$$\mathbf{a}(f_0) \triangleq [1, e^{-j2\pi f_0}, \ldots, e^{-j2\pi f_0 (K_p - 1)}]^T \tag{6.2}$$

where $(\cdot)^T$ is the transpose operator. The normalized Doppler frequency f_0 induced by the motion of the target is,

$$f_0 = \frac{2T_{\text{PRI}}}{\lambda} \Big(v_x \cos(\theta_r) + v_y \sin(\theta_r) \Big) \tag{6.3}$$

where λ is the operating wavelength of the radar, T_{PRI} is the pulse-repetition interval, $\mathbf{v}_t \triangleq [v_x \; v_y]$ is the target velocity vector, and θ_r is the angle with respect to the positive x-axis of the receiver relative to the target.

6.2.1 Clutter Model

The clutter vectors are modeled as SIRV, which can be modeled in product form [110]:

$$\boldsymbol{\zeta} = \sigma \mathbf{g}, \tag{6.4}$$

where σ is the *texture* component, and g is the coherent *speckle* component. The g are modeled as g $\sim \mathcal{CN}\left(\mathbf{0}, \boldsymbol{\Sigma}_{\mathrm{c}}\right)$, while $\sigma \sim p_\sigma\left(\sigma\right)$ is a non-negative random variable [24]. We assume K-distributed clutter in this chapter, where the texture distribution is given by

$$p_\sigma(\sigma) = \frac{2}{\beta^\nu \Gamma(\nu)} \sigma^{2\nu - 1} e^{-\frac{\sigma^2}{\beta}} \tag{6.5}$$

where we use scale parameter ν and shape parameter $\beta = 1/\nu$ to normalize $E\left[\sigma^2\right]{=}1$ [24].

The total clutter probability distribution is,

$$p_{\boldsymbol{\zeta}}\left(\boldsymbol{\zeta}\right) = \frac{1}{\pi^{K_p} |\boldsymbol{\Sigma}|} \int_0^\infty \frac{1}{\sigma^{2K_p}} e^{\frac{1}{\sigma^2 \boldsymbol{\zeta}^H \boldsymbol{\Sigma}^{-1} \boldsymbol{\zeta}}} p_\sigma\left(\sigma\right) d\sigma, \tag{6.6}$$

which is dependent upon the texture pdf. The above integration does not admit a closed form PDF for the clutter distribution when (6.5) is substituted into (6.6). However, it will be shown in a later chapter that another choices of texture pdf will result in a closed form distribution which can then be used in the derivation of the generalized likelihood ratio test when the pdf parameters are known.

The covariance matrix $\boldsymbol{\Sigma}$ is normalized such that $tr\left(\boldsymbol{\Sigma}\right) = K_p$ and controls the slow-time spectral properties of the clutter. We employ the exponentially shaped covariance model for $\boldsymbol{\Sigma}$:

$$\boldsymbol{\Sigma}(i,j) = \rho^{|i-j|}; \quad i \leq K_p, \quad j \leq K_p \tag{6.7}$$

where $0 \leq \rho < 1$ is the correlation coefficient.

6.2.2 Problem Statement

Identical to Chapters 4 and 5, the moving target detection problem consists of declaring either the presence or absence of a moving target within the resolution cell of interest. The binary hypothesis test is,

$$H_0 : \begin{cases} \mathbf{x}_0 & = \boldsymbol{\zeta} \\ \mathbf{x}_\ell & = \boldsymbol{\zeta}_\ell \;\; \ell = 1 \ldots, L \end{cases} \tag{6.8}$$

$$H_1 : \begin{cases} \mathbf{x}_0 & = \alpha \mathbf{a}(f_0) + \boldsymbol{\zeta} \\ \mathbf{x}_\ell & = \boldsymbol{\zeta}_\ell \;\; \ell = 1 \ldots, L \end{cases} \tag{6.9}$$

where H_0 and H_1 correspond to the target absent and target present hypotheses, respectively. The vectors $\mathbf{x}_0$ and $\mathbf{x}_\ell$'s represent the primary and secondary data, respectively, under each hypothesis.

Following the methodology described in Chapter 4, we express the radar output as the inner product,

$$y = \mathbf{w}^H \mathbf{x}_0 \tag{6.10}$$

where $\mathbf{w} \in \mathbb{C}^{K_p \times 1}$ is a filter specific to the detector.

The test statistic is the square of the filter output [66],

$$|y|^2 \underset{H_0}{\overset{H_1}{\gtrless}} \tau \tag{6.11}$$

where τ is a threshold used to satisfy a prescribed probability of false alarm.

6.3 The Normalized Matched Filter

In this section, the normalized matched filter (NMF) is derived in the same way as the generalized likelihood ratio test. Concordantly, the derivation follows a two-step approach, where the covariance matrix is assumed to be known and is then replaced by an estimate once the test statistic is derived. For the remainder of this chapter, it is assumed that the target Doppler frequency is known to gauge the impact of the unknown covariance matrix and heterogeneous clutter power upon the detectors.

Conditioning with respect to the textures and treating σ_0 and σ_1 as deterministic but unknown scalars, the pdf of the primary data is,

$$p\left(\mathbf{x}_0|\sigma_0, H_0\right) = \pi^{-K_p}\sigma_0^{-2K_p}|\mathbf{\Sigma}|^{-1}\exp\left[-\frac{\mathbf{x}_0^H\mathbf{\Sigma}^{-1}\mathbf{x}_0}{\sigma_0^2}\right] \tag{6.12}$$

under H_0, and

$$p\left(\mathbf{x}_0;\alpha|\sigma_1, H_1\right) = \pi^{-K_p}\sigma_1^{-2K_p}|\mathbf{\Sigma}|^{-1}\exp\left[-\frac{\left(\mathbf{x}_0-\alpha\mathbf{a}\left(f_0\right)\right)^H\mathbf{\Sigma}^{-1}\left(\mathbf{x}_0-\alpha\mathbf{a}\left(f_0\right)\right)}{\sigma_1^2}\right] \tag{6.13}$$

under H_1. Taking the logarithm of (6.12) and (6.13) produces the following log-likelihood functions:

$$\mathcal{L}\left(\mathbf{x}_0|\sigma_0, H_0\right) = -\log\left(\pi^{K_p}|\mathbf{\Sigma}|\right) - 2K_p\log\left(\sigma_0\right) - \frac{\mathbf{x}_0^H\mathbf{\Sigma}^{-1}\mathbf{x}_0}{\sigma_0^2}, \tag{6.14}$$

and

$$\mathcal{L}\left(\mathbf{x}_0|\sigma_1, H_1\right) = -\log\left(\pi^{K_p}|\mathbf{\Sigma}|\right) - 2K_p\log\left(\sigma_1\right) - \frac{\left(\mathbf{x}_0-\alpha\mathbf{a}\left(f_0\right)\right)^H\mathbf{\Sigma}^{-1}\left(\mathbf{x}_0-\alpha\mathbf{a}\left(f_0\right)\right)}{\sigma_1^2} \tag{6.15}$$

for H_0 and H_1, respectively.

The generalized likelihood ratio is expressed as

$$\Lambda_{\mathrm{GLR}} = \frac{\max_{\alpha,\sigma_1} p\left(\mathbf{x}_0; \alpha|\sigma_1, H_1\right)}{\max_{\sigma_1} p\left(\mathbf{x}_0|\sigma_0, H_0\right)}, \tag{6.16}$$

and it is now possible to compute the maximum likelihood estimates (MLEs) for α, σ_0, and σ_1 under the two hypotheses to determine the desired test statistic.

6.3.1 Parameter Estimation Under H_0

The only estimate necessary is the MLE of σ_0. Taking the derivative of (6.14) with respect to σ_0 and equating to zero results in,

$$\frac{\partial \mathcal{L}\left(\mathbf{x}_0|\sigma_0, H_0\right)}{\partial \sigma_0} = -2\frac{K_p}{\sigma_0} + 2\frac{\mathbf{x}_0^H \mathbf{\Sigma}^{-1}\mathbf{x}_0}{\sigma_0^3} = 0. \tag{6.17}$$

Solving the above equation produces the MLE of σ_0^2 under H_0:

$$\hat{\sigma}_0^2 = \frac{\mathbf{x}_0^H \mathbf{\Sigma}^{-1}\mathbf{x}_0}{K_p} \tag{6.18}$$

6.3.2 Parameter Estimation Under H_1

Under H_1, the MLEs of α and σ_1 must be found. To find the MLE of α, take the derivative of (6.15) with respect to this term and equate to zero, producing

$$\frac{\partial \mathcal{L}\left(\mathbf{x}_0; \alpha|\sigma_1, H_1\right)}{\partial \alpha} = \alpha^* \left(\mathbf{a}^H\left(f_0\right)\mathbf{\Sigma}^{-1}\mathbf{a}\left(f_0\right)\right) - \mathbf{x}_0^H \mathbf{\Sigma}^{-1}\mathbf{a}\left(f_0\right) = 0. \tag{6.19}$$

Conjugating the above equation and solving for α yields the MLE:

$$\hat{\alpha} = \frac{\mathbf{a}^H (f_0) \boldsymbol{\Sigma}^{-1} \mathbf{x}_0}{\mathbf{a}^H (f_0) \boldsymbol{\Sigma}^{-1} \mathbf{a} (f_0)}. \tag{6.20}$$

To find the MLE of σ_1, take the derivative of (6.15) with respect to this term and equate to zero,

$$\frac{\partial \mathcal{L} (\mathbf{x}_0; \alpha | \sigma_1, H_1)}{\partial \sigma_1} = -2 \frac{K_p}{\sigma_1} + 2 \frac{(\mathbf{x}_0 - \alpha \mathbf{a} (f_0))^H \boldsymbol{\Sigma}^{-1} (\mathbf{x}_0 - \alpha \mathbf{a} (f_0))}{\sigma_1^3} = 0. \tag{6.21}$$

Substituting $\hat{\alpha}$ into the above equation and solving for σ_1 produces the MLE

$$\hat{\sigma}_1^2 = \frac{(\mathbf{x}_0 - \hat{\alpha} \mathbf{a} (f_0))^H \boldsymbol{\Sigma}^{-1} (\mathbf{x}_0 - \hat{\alpha} \mathbf{a} (f_0))}{K_p}. \tag{6.22}$$

Note that $\hat{\sigma}_1^2$ may be expanded to give,

$$\hat{\sigma}_1^2 = \frac{\mathbf{x}_0^H \boldsymbol{\Sigma}^{-1} \mathbf{x}_0}{K_p} - \frac{|\mathbf{a}^H (f_0) \boldsymbol{\Sigma}^{-1} \mathbf{x}_0|^2}{K_p \mathbf{a}^H (f_0) \boldsymbol{\Sigma}^{-1} \mathbf{a} (f_0)}. \tag{6.23}$$

Substituting the MLEs (6.18), (6.20), and (6.22) into (6.16), it is straightforward to show that the likelihood ratio simplifies to,

$$\Lambda_{\mathrm{GLR}} = \left(\frac{\hat{\sigma}_0^2}{\hat{\sigma}_1^2} \right)^{K_p}. \tag{6.24}$$

Noting that $\hat{\sigma}_1^2$ is a function of $\hat{\sigma}_0^2$, the GLR can be expressed as

$$\Lambda_{\mathrm{GLR}} = \left(\frac{1}{1 - T_{\mathrm{GLR}}} \right)^{K_p}, \tag{6.25}$$

where

$$T_{\mathrm{GLR}} = \frac{\left|\mathbf{a}^H(f_0)\,\mathbf{\Sigma}^{-1}\mathbf{x}_0\right|^2}{\left(\mathbf{x}_0^H\mathbf{\Sigma}^{-1}\mathbf{x}_0\right)\left(\mathbf{a}^H(f_0)\,\mathbf{\Sigma}^{-1}\mathbf{a}(f_0)\right)} \tag{6.26}$$

after dividing the numerator and denominator of (6.24) by $\hat{\sigma}_0^2$. After dropping the K_p power in (6.25) and making use of the monotone property of the function $f(x) = 1/(1-x)$, the final test statistic is,

$$\frac{\left|\mathbf{a}^H(f_0)\,\mathbf{\Sigma}^{-1}\mathbf{x}_0\right|^2}{\left(\mathbf{x}_0^H\mathbf{\Sigma}^{-1}\mathbf{x}_0\right)\left(\mathbf{a}^H(f_0)\,\mathbf{\Sigma}^{-1}\mathbf{a}(f_0)\right)} \underset{H_0}{\overset{H_1}{\gtrless}} \tau \tag{6.27}$$

where τ is the detection threshold.

To express (6.27) in the form of (6.10), let

$$\mathbf{w}_{\mathrm{NMF}} = \frac{\mathbf{\Sigma}^{-1}\mathbf{a}(f_0)}{\sqrt{\left(\mathbf{x}_0^H\mathbf{\Sigma}^{-1}\mathbf{x}_0\right)\left(\mathbf{a}^H(f_0)\,\mathbf{\Sigma}^{-1}\mathbf{a}(f_0)\right)}}, \tag{6.28}$$

and the corresponding test statistic will be,

$$\left|\mathbf{w}_{\mathrm{NMF}}^H\mathbf{x}_0\right|^2 \underset{H_0}{\overset{H_1}{\gtrless}} \tau_{\mathrm{NMF}}. \tag{6.29}$$

Equation (6.28) is known as the normalized matched filter (NMF) and is proportional to (2.2). Hence, the unit circle roots constraint applies when $\mathbf{\Sigma}$ and $\mathbf{a}(f_0)$ have the appropriate structure.

In practice, $\mathbf{\Sigma}$ is unknown and must be estimated from the secondary data. Let $\hat{\mathbf{\Sigma}}$ be one such estimate, and substitute into (6.28) to get,

$$\mathbf{w}_{\mathrm{NAMF}} = \frac{\hat{\mathbf{\Sigma}}^{-1}\mathbf{a}(f_0)}{\sqrt{\left(\mathbf{x}_0^H\hat{\mathbf{\Sigma}}^{-1}\mathbf{x}_0\right)\left(\mathbf{a}^H(f_0)\,\hat{\mathbf{\Sigma}}^{-1}\mathbf{a}(f_0)\right)}}, \tag{6.30}$$

which is known as the normalized adaptive matched filter (NAMF) (or GLRT-LQ) [19].

The corresponding test statistic will be,

$$\left|\mathbf{w}_{\mathrm{NAMF}}^{H}\mathbf{x}_{0}\right|^{2}\underset{H_0}{\overset{H_1}{\gtrless}}\tau_{\mathrm{NAMF}}. \tag{6.31}$$

With limited secondary data, the estimation performance of unstructured covariance estimators will be adversely impacted, leading to poor detection performance. To avoid this, we combine the theory in Chapter 2 with the unit circle roots at the output of the UCRC algorithm to develop the UCRC Toeplitz rectification estimate. Aside from imposing crucial structure upon the covariance estimate, using a Toeplitz-structured covariance matrix to compute the adaptive detector in (6.30) will also satisfy the unit circle roots constraint per Theorem 1. In the following sections, different possibilities for the covariance estimate will be introduced, and their impact upon the detection performance will by examined using simulations examples.

6.4 UCRC Toeplitz Rectification

In this section, a new covariance estimate is proposed which preserves the Toeplitz structure of the true covariance matrix and hence, retains the unit circle roots property when substituted into the adaptive detector (6.30).

The new Toeplitz rectified estimate is based on the roots at the output of the UCRC-AMF algorithm described in Chapter 4, which requires an initial covariance estimate. However, unlike in Chapter 4, the secondary data have heterogeneous clutter power, and therefore; the sample covariance matrix is a poor initial estimate. Fortunately, the following estimate has been proposed in the radar literature specifically for SIRP clutter called the fixed point estimator (FPE) [17]:

$$\hat{\mathbf{\Sigma}}_{\mathrm{FPE}}^{(t+1)}=\frac{K_p}{L}\sum_{\ell=0}^{L-1}\frac{\mathbf{x}_{\ell}\mathbf{x}_{\ell}^{H}}{\mathbf{x}_{\ell}^{H}\hat{\mathbf{\Sigma}}_{\mathrm{FPE}}^{-(t)}\mathbf{x}_{\ell}}. \tag{6.32}$$

The FPE is an iterative approximate maximum likelihood estimate in compound-Gaussian clutter, hence we use this matrix instead of the SCM when using the UCRC-AMF algorithm.

Let $\{f_i\}_{i=0}^{K_p-1}$ be the set of normalized frequencies $f_i \in (-0.5, 0.5);\ \ i = 0, \ldots, K_p-1$ corresponding to the unit circle roots returned by the UCRC-AMF algorithm, including the target normalized Doppler frequency f_0. Also, let $\{\mathbf{a}(f_i)\};\ \ i = 0, \ldots, K_p - 1$ be the set of Vandermonde vectors in the form of (6.2) corresponding to these frequencies. From Theorem 1, a Hermitian Toeplitz structured matrix may be constructed from the roots and a set of real constants $\{\hat{d}_i\}_{i=0}^{K_p-1}$,

$$\sum_{i=0}^{K_p-1} \hat{d}_i \mathbf{a}(f_i)\, \mathbf{a}^H(f_i) = d_0 \mathbf{a}(f_0)\, \mathbf{a}^H(f_0) + \mathbf{A}\mathbf{D}\mathbf{A}^H, \tag{6.33}$$

where $\mathbf{A} = \left[\mathbf{a}(f_1), \ldots, \mathbf{a}\left(f_{K_p-1}\right)\right] \in \mathbb{C}^{K_p \times (K_p-1)}$ and $\mathbf{D} = \mathrm{diag}\{\hat{d}_1, \ldots, \hat{d}_{K_p-1}\} \in \mathbb{R}^{(K_p-1)\times(K_p-1)}$. The $\hat{d}_i$ are estimated as,

$$\hat{d}_i = \frac{1}{\mathbf{a}^H(f_i)\, \hat{\mathbf{\Sigma}}_{\mathrm{FPE}}^{-1} \mathbf{a}(f_i)}; \quad i = 0, \ldots, K_p - 1. \tag{6.34}$$

In practice, trying to invert (6.33) directly is numerically unstable, especially when the secondary data are limited. This is because the roots returned by the UCRC algorithm may be in close proximity to one another on the unit circle, resulting in co-linearity between the $\mathbf{a}(f_i)$'s. Therefore, the following ad-hoc regularization is proposed. Let $\kappa \in \mathbb{R}$ be a real scalar and writing the approximation

$$\hat{\mathbf{\Sigma}}_{\mathrm{FPE}} \approx \hat{d}_0 \mathbf{a}(f_0)\, \mathbf{a}^H(f_0) + \mathbf{A}\mathbf{D}\mathbf{A}^H + \kappa \mathbf{I} \tag{6.35}$$

where $\mathbf{I} \in \mathbb{R}^{K_p \times K_p}$ is the identity matrix. When $\hat{\mathbf{\Sigma}}_{\mathrm{FPE}}$ is replaced with the true covariance on the right hand side of (6.35), κ vanishes. Define the rank one projection matrix onto the orthogonal complement of the column space of $\mathbf{A}$,

$$\mathbf{P} = \mathbf{I} - \mathbf{A}\left(\mathbf{A}^H\mathbf{A}\right)^{-1}\mathbf{A}^H, \tag{6.36}$$

and note that due to the aforementioned numerical instability, (6.36) would be computed by first orthonormalizing the columns of $\mathbf{A}$. Left multiplying by $\mathbf{P}$ in (6.35) and applying the trace operator results in

$$\mathrm{tr}\{\mathbf{P}\hat{\boldsymbol{\Sigma}}_{\mathrm{FPE}}\} = \hat{d}_0\mathrm{tr}\{\mathbf{a}^H(f_0)\,\mathbf{P}\mathbf{a}(f_0)\} + \kappa, \tag{6.37}$$

where the cyclic property of the trace operator has been used, $\mathrm{tr}\{\mathbf{P}\} = 1$, and the approximation is replaced with equality to allow solving for $\hat{\kappa}$,

$$\hat{\kappa} = \mathrm{tr}\{\mathbf{P}\hat{\boldsymbol{\Sigma}}_{\mathrm{FPE}}\} - \hat{d}_0\mathrm{tr}\{\mathbf{a}^H(f_0)\,\mathbf{P}\mathbf{a}(f_0)\}. \tag{6.38}$$

The UCRC-based Toeplitz rectified estimate is,

$$\hat{\boldsymbol{\Sigma}}_{\mathrm{UCRC-TR}} = \sum_{i=0}^{K_p-1}\left[\hat{d}_i\mathbf{a}(f_i)\,\mathbf{a}^H(f_i)\right] + \hat{\kappa}\mathbf{I}. \tag{6.39}$$

As the number of secondary data increases, $\hat{\boldsymbol{\Sigma}}_{\mathrm{FPE}}$ becomes more accurate, and κ approaches zero. When the secondary data are limited, κ regularizes the estimate based on the roots and ensures an invertible estimate.

6.5 Simulation Results

Simulation examples are used to show the performance of the UCRC Toeplitz rectification estimate. For consistency, the same radar parameters as described in Chapters 4 and 5 are used in this section, and are repeated for additional clarity. A radar operating frequency of $f_c = 1$ GHz is used with a pulse repetition frequency (PRF) of 500 Hz. A single moving target with a linear trajectory, constant velocity $|\mathbf{v}_t|= 108$ km/h, and heading $30°$ with respect to the positive x-axis. The angle of the receiver/transmitter with respect to the target is $\theta_r = 10°$. The normalized target Doppler frequency is $f_0 = 0.3761$. The clutter covariance matrix $\mathbf{\Sigma}$, texture σ, and target amplitude α are assumed unknown. Unless stated otherwise, a constant $\rho = 0.9$ is used in (6.7) to construct the covariance matrix.

The detection performance is quantified using the receiver operating characteristic (ROC) for fixed signal-to-clutter ratio. Probability of detection versus SCR curves are also generated assuming a fixed false rate $P_{\text{FA}} = 10^{-3}$ to limit the computational burden when conducting the simulations.

We define the signal-to-clutter ratio,

$$\text{SCR} = \frac{|\alpha|^2}{K_p \text{E}\left[\sigma^2\right]} \left(\mathbf{a}^H\left(f_0\right) \mathbf{\Sigma}^{-1} \mathbf{a}\left(f_0\right)\right) \tag{6.40}$$

to allow for scaling the target amplitude $|\alpha|^2$ to meet a prescribed SCR value.

The benchmark detector in this section is this optimal K-distribution detector (OKD) [45, 80]:

$$\Lambda_{\text{OKD}} = \left(\frac{q_0}{q_1}\right)^{(K_p-\nu)/2} \frac{K_{K_p-\nu}\left(2\sqrt{\nu q_1}\right)}{K_{K_p-\nu}\left(2\sqrt{\nu q_0}\right)} \underset{H_0}{\overset{H_1}{\gtrless}} \tau_{\text{OKD}}, \tag{6.41}$$

where

$$q_0 = \mathbf{x}_0^H \mathbf{\Sigma}^{-1} \mathbf{x}_0, \tag{6.42}$$

$$q_1 = \frac{|\mathbf{a}^H(f_0)\mathbf{\Sigma}^{-1}\mathbf{x}_0|^2}{\mathbf{a}^H(f_0)\mathbf{\Sigma}^{-1}\mathbf{a}(f_0)}, \tag{6.43}$$

and $K_{K_p-\nu}(\cdot)$ is the modified Bessel function of the second kind. For all detectors, the performance is computed using Monte-Carlo simulations where the number of independent trials is $100/P_{\mathrm{FA}}$, where P_{FA} is the minimum probability of false alarm. Unless stated otherwise, the scale parameter for the texture distribution is fixed $\nu = 0.5$.

6.5.1 Example 1 :Detection Performance in K-Distributed Clutter with Limited Secondary Data

For this example, the detection performance of the NAMF using the UCRC Toeplitz rectification estimate is demonstrated using the receiver operating characteristics and probability of detection versus the SCR. The coherent processing interval consists of $K_p = 16$ pulses with $L = 17$ secondary data, barely enough to invert the FPE. The detection performance using the proposed estimate is compared against the NAMF and the PS-NAMF using the FPE only and conventional Toeplitz rectification applied to the FPE. The FPE is computed using $t = 8$ iterations.

Figures 6.1a and 6.1b illustrate the performances for the aforementioned detectors. An $\mathrm{SCR} = -5$ dB is used to compute the ROC curves shown in Fig. 6.1a. It is clear from both figures that the NAMF using the proposed estimate outperforms all other detectors while the NAMF in conjunction with conventional Toeplitz rectification [35] applied to the FPE performs the worst. The PS-NAMF with the FPE has the most competitive performance and the NAMF with the FPE comes in nearly second to last in all cases. The performance disparity between the UCRC Toeplitz rectification and the conventional one is interesting since, according to Theorem 1, the former should also correspond to a set of unit circle roots. However, the diagonal loading present in the UCRC Toeplitz rectification could be positively impacting the performance.

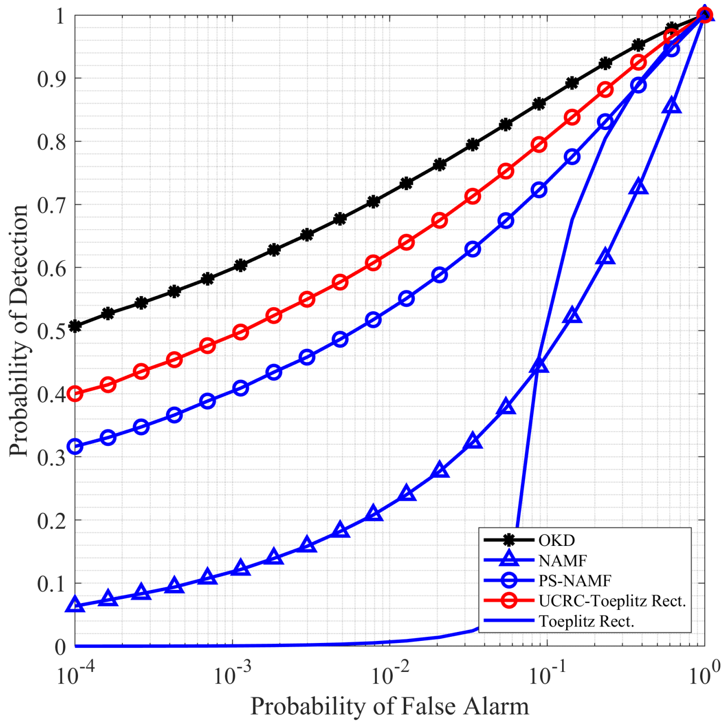

(a) P_{D} vs. P_{FA}

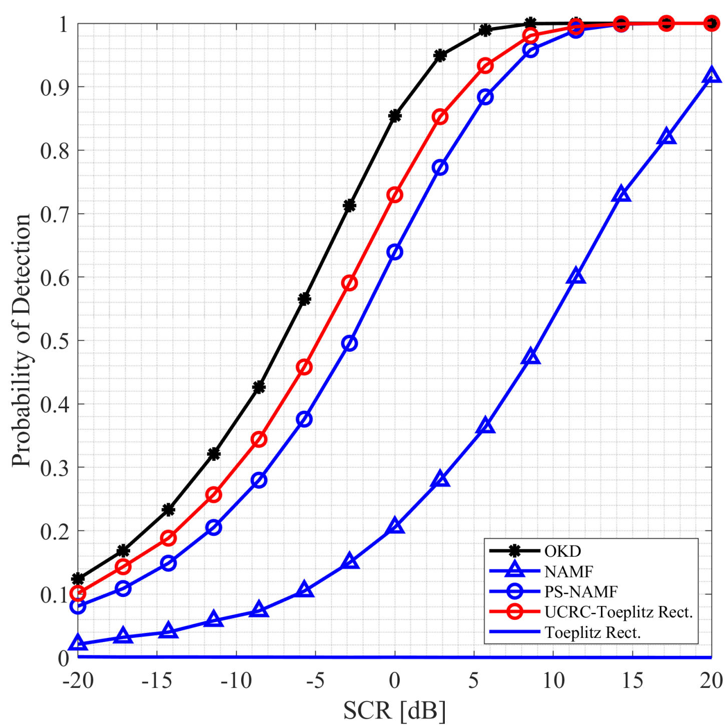

(b) P_{D} vs. SCR

Figure 6.1: Detection performance (a) P_{D} vs. P_{FA} (b) P_{D} vs. SCR

6.5.2 Example 2 : Numerical CFAR Evaluation

In this example, we examine the behavior of the estimated probability of false alarm versus the clutter parameters for a fixed threshold using the UCRC Toeplitz rectification estimate in the NAMF detector. In each case, $K_p = 16$ pulses with $L = 17$ secondary data. The constant thresholds were computed numerically using the simulation data and selected to provide and set $P_{\text{FA}} = 10^{-1}$ to reduce the computational complexity of each simulation. To calculate the false alarm probabilities, $100,000$ trials were conducted for each parameter value.

Fig. 6.2a, shows the estimated probability of false alarm versus the scale parameter of the SIRP texture distribution in (6.5). For this figure, $\rho = 0.9$ is constant while ν varies. The scale parameter controls how "spikey" the clutter power is, and so invariance to this parameter determines how robust the detector will be in the presence of impulsive clutter. The uniform false alarm rate exhibited by the detector as ν is varied demonstrates that NAMF using the proposed estimate has approximate CFAR with respect to the scale parameter.

Fig. 6.2b, shows the estimated probability of false alarm versus the covariance structure parameter in (6.7). For this figure, $\nu = 0.5$ is fixed. The correlation ρ controls the clutter bandwidth about zero Doppler, with lower values indicating a wider bandwidth. The false alarm rate is not uniform as it was in Fig. 6.2a, indicating that using the proposed estimate in the NAMF does not preserve CFAR with respect to the clutter covariance matrix.

6.6 Conclusion

In this chapter, the UCRC Toeplitz rectification approach was developed and applied to moving target detection in K-distributed clutter with limited secondary data. Numerical examples demonstrated the properties of the proposed Toeplitz rectification approach when used in normalized adaptive matched filter detector. It was shown that use of the proposed

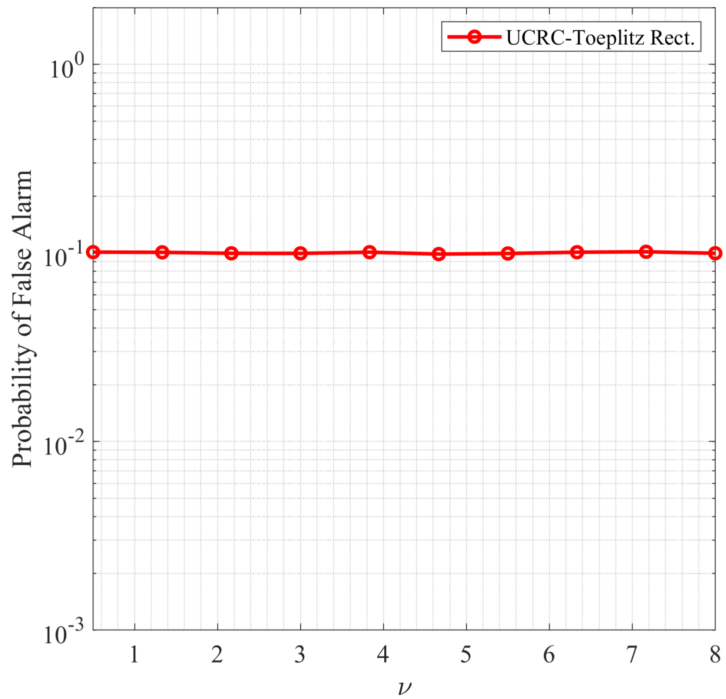

(a) P_{FA} vs. ν

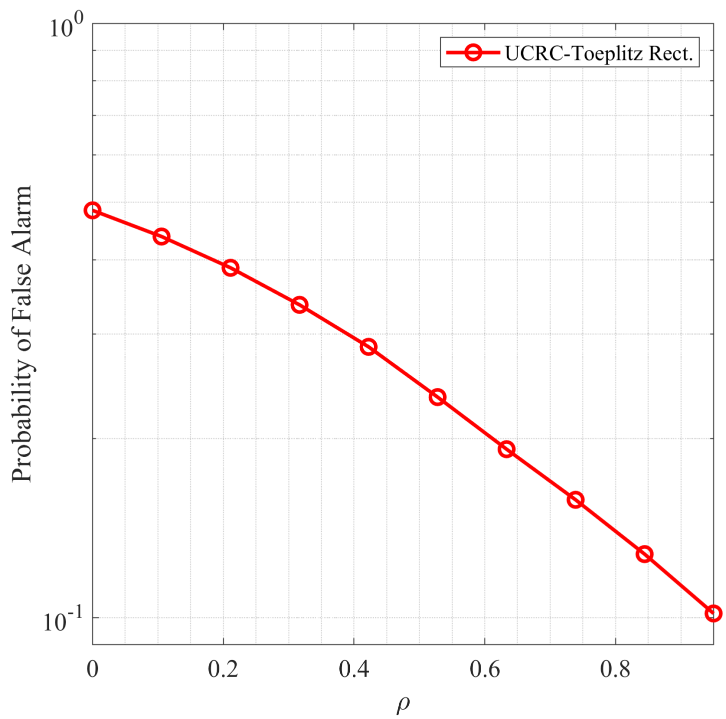

(b) P_{FA} vs. ρ

Figure 6.2: Numerical CFAR evaluation (a) P_{FA} vs. SIRP scale parameter (b) P_{FA} vs. covariance structure parameter ρ.

estimate retains the CFAR property with respect to the clutter scale parameter, but CFAR is not maintained with respect to the clutter covariance matrix. Despite the loss of this property, the UCRC based approach still outperformed the NAMF and PS-NAMF using the FPE alone, and the NAMF when using conventional Toeplitz rectification applied to the FPE.

Clearly, more work is necessary to correct for the loss of CFAR with respect to the clutter covariance matrix in the NAMF when using UCRC Toeplitz rectification. The loss of covariance CFAR severely limits the applicability of the UCRC Toeplitz estimate for adaptive detection. However, the detector still achieved remarkable performance improvement over the other detectors. Therefore, further research is warranted to refine the performance of this estimator.

In the following chapter, UCRC Toeplitz rectification is applied to moving target detection in compound-Gaussian clutter using a distributed active MIMO radar network.

Distributed MIMO Radar Moving Target Detection in Compound-Gaussian Clutter

7.1 Introduction

Multiple-input multiple-output (MIMO) radar utilizing multiple orthogonal waveforms offers numerous advantages over traditional phased array radar including: improved spatial coverage [29] and diversity gain [27]. Two classes of MIMO radar exist in the literature namely, colocated and distributed [107]. The focus of this chapter is strictly upon the latter and is hereafter referred to as MIMO radar.

Adaptive detectors require an estimate of the unknown clutter covariance matrix which is computed from a set of target-free secondary data collected from cells adjacent to the resolution cell of interest [77],[48]. The maximum likelihood estimate (MLE) of the clutter covariance matrix assuming i.i.d complex Gaussian clutter is the well-known sample covariance matrix (SCM) [33], which requires that the number of available secondary data must be at least as large as the dimensionality of the signal of interest or the resulting estimate will be singular. To circumvent the need for extensive amounts of secondary data, estimation techniques such as the rank-constrained maximum likelihood (RCML) [47] and its extension [91] have been developed for use when specific structure can be imposed upon the underlying clutter covariance matrix (*e.g.,* airborne radar [108]).

Certain environments (e.g. sea-clutter) are not well-modeled by Gaussian processes due to the non-stationary nature of the clutter power across resolution cells. Such clutter can be theoretically modeled as a spherically invariant random process (SIRP) [6]. In this chapter, we focus on a sub-class of SIRP clutter with inverse-Gamma distributed power. Inverse gamma texture has been considered before for adaptive detection, and is particularly attractive because the generalized likelihood ratio test (GLRT) can be computed in closed form [84].

In Chapter 6, the UCRC-based Toeplitz rectification was proposed. Making use of Theorem 1 and Corollary 1 from Chapter 2, the improved covariance estimate was applied to the moving target detection in a monostatic radar system in compound-Gaussian clutter. In this chapter, the UCRC Toeplitz rectification approach is applied to moving target detection in a distributed MIMO radar network in compound-Gaussian clutter. We implement two detectors namely; the SIRP-GLRT of [24] and the GLRT derived in the case of Gaussian clutter with unknown level [52, 61] where both detectors are extended for use within a distributed MIMO network. Through simulation examples, we will show that using the aforementioned detectors in conjunction with a covariance matrix estimate based on UCRC Toeplitz rectification yields a performance increase over the same detectors employing the fixed point covariance matrix estimate (FPE) alone in the presence of limited and non-homogeneous secondary data. Finally, the convergence in performance of the GLRT toward the SIRP-GLRT as the number of pulses-per-node increases for the case where each distinct covariance matrix is known. To the best of our knowledge, the effectiveness of exploiting unit circle roots has never been demonstrated before in the distributed MIMO radar literature.

This chapter is organized as follows. The distributed MIMO radar signal model is given in Section 7.2 while the clutter signal characterization is given in Section 7.3. The detectors are presented in Section 7.4. Section 7.6 gives the details of the covariance estimators used to generate simulated results. Section 7.7 gives the simulations results while conclusions are drawn in Section 7.8.

7.2 Signal Model

Consider a MIMO radar network consisting of M widely separated transmit antennas and N receivers mounted upon stationary platforms in a two-dimensional (2D) plane. Each bistatic (m, n) pair in the network interrogates a common scene of interest using a periodic train of K_p consecutive pulses consisting of M orthogonal waveforms to facilitate separation at the receivers. The signal at the output of the n-th receiver due to the m-th transmitter is modeled mathematically as

$$\mathbf{x}_{\mathrm{m,n}} = \alpha_{\mathrm{m,n}} \mathbf{a}\left(f_{\mathrm{m,n}}\right) + \boldsymbol{\zeta}_{\mathrm{m,n}} \tag{7.1}$$

where $\alpha_{\mathrm{m,n}} \in \mathbb{C}$ is the target reflection coefficient, $f_{\mathrm{m,n}}$ is the target Doppler frequency, $\mathbf{a}(f_{\mathrm{m,n}})$ denotes the temporal steering vector associated with the target, and $\boldsymbol{\zeta}_{\mathrm{m,n}} \in \mathbb{C}^{K_p \times 1}$ is the vector of additive disturbance signals accounting for clutter, interference, and noise, which is assumed to be zero-mean Gaussian with covariance matrix $\boldsymbol{\Sigma}_{\mathrm{m,n}}$. The temporal steering vector associated with an arbitrary Doppler frequency f is defined as,

$$\mathbf{a}(f) \triangleq [1, \ldots, \exp\left(j2\pi T_{\mathrm{PRI}}(K_p - 1)f\right)]^T, \tag{7.2}$$

where T_{PRI} denotes the pulse repetition interval (PRI) and $(\cdot)^T$ stands for the transpose operation. It is worth noting that, the target motion will induce a differing Doppler frequency for each transmit-receive pair of the multistatic system. Assume a hypothetical target with velocity vector $\mathbf{v} \triangleq (v_x, v_y)$ is located at the origin of a Cartesian 2D coordinate system.

Let θ_m and ϕ_n denote the angle with respect to the positive x-axis of the m-th transmitter and n-th receiver, respectively. Then, the target Doppler frequency associated with the mn-th transmit-receive pair is defined as [107],

$$f_{\mathrm{m,n}} = \frac{v_x}{\lambda}(\cos(\phi_n) + \cos(\theta_m)) + \frac{v_y}{\lambda}(\sin(\phi_n) + \sin(\theta_m)) \tag{7.3}$$

where, λ is the wavelength of the radar.

7.3 Clutter Characterization

Low resolution radar systems observe the contributions of many clutter scatterers within one resolution cell, motivating the use of the Central Limit Theorem to model the resulting data as Gaussian [71]. At higher resolution, individual clutter scatterers are not as numerous and hence, the Gaussian model is no longer appropriate. In this case, the clutter is modeled as a product of two independent components: a quickly evolving speckle process and a temporally correlated texture component [18]. The clutter component of equation (7.1) may be modeled in product form [110] as,

$$\boldsymbol{\zeta}_{\mathrm{m,n}} = \sigma_{\mathrm{m,n}} \mathbf{g}_{\mathrm{m,n}}, \tag{7.4}$$

where, $\sigma_{\mathrm{m,n}}$ denotes the texture component with distribution $p(\sigma_{\mathrm{m,n}})$, and $\mathbf{g}_{\mathrm{m,n}} \in \mathbb{C}^{K_p \times 1}$ is zero-mean Gaussian with covariance matrix $\boldsymbol{\Sigma}_{\mathrm{m,n}}$ of dimension $K_p \times K_p$. In the following discussion we assume that the texture distribution is the same across the entire network while the covariance matrix is assumed to be distinct for each mn bistatic pair. Specifically, suppose that the square of the texture $\sigma^2_{\mathrm{m,n}}$ follows an inverse-Gamma distribution each with scale and shape parameter $\nu_{\mathrm{m,n}}$ and $\beta_{\mathrm{m,n}}$ [84], where $\nu_{m,n} = \nu$ and $\beta_{\mathrm{m,n}} = \beta$ respectively. After accounting for the random variable transformation the resulting texture distribution is [84]

$$p(\sigma_{\mathrm{m,n}}) = \frac{2/\beta^{\nu}}{\Gamma(\nu)} \sigma_{\mathrm{m,n}}^{-2\nu-1} \exp\left(-\frac{1/\beta}{\sigma_{\mathrm{m,n}}^2}\right). \tag{7.5}$$

where, $\Gamma(\cdot)$ is the continuous gamma function.

7.4 Generalized Likelihood Ratio Tests

We consider deterministic texture components $\sigma_{\mathrm{m,n}}$ to facilitate the derivation of the GLRT. We follow a two-step approach to derive the GLRT, where we first assume that the mn-th clutter covariance matrix is known and then substitute with its estimate after the test statistic is found.

Define the variables $\boldsymbol{\alpha} \in \mathbb{C}^{MN\times 1}$, $\boldsymbol{\sigma} \in \mathbb{R}^{MN\times 1}$, and $\mathbf{X} \in \mathbb{C}^{K_p\times MN}$ as the vector of amplitudes, textures, and measured data, respectively across the network. The generalized likelihood ratio test statistic will be [61],

$$\Lambda_{\mathrm{GLRT}} = \frac{\max_{\boldsymbol{\alpha},\boldsymbol{\sigma}} p(\mathbf{X};\boldsymbol{\alpha},\boldsymbol{\sigma})}{\max_{\boldsymbol{\sigma}} p(\mathbf{X};\boldsymbol{\sigma})}, \tag{7.6}$$

where $p(\mathbf{X};\boldsymbol{\alpha},\boldsymbol{\sigma})$ and $p(\mathbf{X};\boldsymbol{\sigma})$ are the likelihoods of the data $\mathbf{X}$ across the network of MN nodes under H_1 and H_0, respectively.

Focusing on the likelihood under H_1, we assume independence between the primary data vectors $\mathbf{x}_{\mathrm{m,n}}$ to yield

$$p(\mathbf{X};\boldsymbol{\alpha},\boldsymbol{\sigma}) = \prod_{\mathrm{m,n}} p(\mathbf{x}_{\mathrm{m,n}};\alpha_{\mathrm{m,n}},\sigma_{\mathrm{m,n}}) \tag{7.7}$$

under H_1, and

$$p(\mathbf{X};\boldsymbol{\sigma}) = \prod_{\mathrm{m,n}} p(\mathbf{x}_{\mathrm{m,n}};\sigma_{\mathrm{m,n}}). \tag{7.8}$$

under H_0.

In general, each bistatic pair measures complex, zero-mean, Gaussian clutter with distinct texture $\sigma_{\mathrm{m,n}}$ which varies from CPI-to-CPI and covariance matrix $\mathbf{\Sigma}_{\mathrm{m,n}}$ resulting in an individual likelihood from the mn-th bistatic pair,

$$p\left(\mathbf{x}_{\mathrm{m,n}};\sigma_{\mathrm{m,n}}\right)=\left(\pi\sigma_{\mathrm{m,n}}\right)^{-2K_p}\left|\mathbf{\Sigma}_{\mathrm{m,n}}\right|^{-1}\exp\left[-\frac{\mathbf{x}_{\mathrm{m,n}}^H\mathbf{\Sigma}_{\mathrm{m,n}}^{-1}\mathbf{x}_{\mathrm{m,n}}}{\sigma_{\mathrm{m,n}}^2}\right], \tag{7.9}$$

under H_0, and

$$p\left(\mathbf{x}_{\mathrm{m,n}};\alpha_{\mathrm{m,n}},\sigma_{\mathrm{m,n}}\right)=\left(\pi\sigma_{\mathrm{m,n}}\right)^{-2K_p}\left|\mathbf{\Sigma}_{\mathrm{m,n}}\right|^{-1}\exp\left[-\frac{\mathbf{y}_{\mathrm{m,n}}^H\mathbf{\Sigma}_{\mathrm{m,n}}^{-1}\mathbf{y}_{\mathrm{m,n}}}{\sigma_{\mathrm{m,n}}^2}\right], \tag{7.10}$$

under H_1, where we define

$$\mathbf{y}_{\mathrm{m,n}}=\mathbf{x}_{\mathrm{m,n}}-\alpha_{\mathrm{m,n}}\mathbf{a}\left(f_{\mathrm{m,n}}\right) \tag{7.11}$$

for brevity.

7.4.1 Parameter estimation under H_0

The only parameter we must estimate in this case is the individual node textures. Taking the logarithm of (7.8) results in the log-likelihood function

$$\log\left(p(\mathbf{X};\boldsymbol{\sigma})\right)=\sum_{\mathrm{m,n}}\Big[-2K_p\log\left(\pi\sigma_{\mathrm{m,n}}\right)-\log\left(\left|\mathbf{\Sigma}_{\mathrm{m,n}}\right|\right)-\frac{\mathbf{x}_{\mathrm{m,n}}^H\mathbf{\Sigma}_{\mathrm{m,n}}^{-1}\mathbf{x}_{\mathrm{m,n}}}{\sigma_{\mathrm{m,n}}^2}\Big]. \tag{7.12}$$

Taking the derivative with respect to $\sigma_{\mathrm{m,n}}$ produces

$$\frac{\partial\log\left(p(\mathbf{X};\boldsymbol{\sigma})\right)}{\partial\sigma_{\mathrm{m,n}}}=-2\frac{K_p}{\sigma_{\mathrm{m,n}}}+2\frac{\mathbf{x}_{\mathrm{m,n}}^H\mathbf{\Sigma}_{\mathrm{m,n}}^{-1}\mathbf{x}_{\mathrm{m,n}}}{\sigma_{\mathrm{m,n}}^3}. \tag{7.13}$$

Setting the above equation equal to zero and solving yields the MLE of $\sigma^2_{\mathrm{m,n}}$ under H_0,

$$\hat{\sigma}^{2(H_0)}_{\mathrm{m,n}} = \frac{\mathbf{x}^H_{\mathrm{m,n}} \mathbf{\Sigma}^{-1}_{\mathrm{m,n}} \mathbf{x}_{\mathrm{m,n}}}{K_p} \tag{7.14}$$

7.4.2 Parameter Estimation Under H_1

Under H_1, we must estimate the values of $\alpha_{\mathrm{m,n}}$ and $\sigma_{\mathrm{m,n}}$. We begin by estimating $\alpha_{\mathrm{m,n}}$ first and then estimating $\sigma_{\mathrm{m,n}}$. Taking the logarithm of (7.7) produces the log-likelihood function

$$\log\left(p(\mathbf{X};\boldsymbol{\alpha},\boldsymbol{\sigma})\right) = \sum_{\mathrm{m,n}} -2K_p \log\left(\pi\sigma_{\mathrm{m,n}}\right) - \log\left(|\mathbf{\Sigma}_{\mathrm{m,n}}|\right) - \frac{\mathbf{y}^H_{\mathrm{m,n}} \mathbf{\Sigma}^{-1}_{\mathrm{m,n}} \mathbf{y}_{\mathrm{m,n}}}{\sigma^2_{\mathrm{m,n}}}. \tag{7.15}$$

Taking the derivative of the above equation with respect to $\alpha_{\mathrm{m,n}}$ yields,

$$\frac{\partial \log\left(p(\mathbf{X};\boldsymbol{\alpha},\boldsymbol{\sigma})\right)}{\partial \alpha_{\mathrm{m,n}}} = \alpha^*_{\mathrm{m,n}}\left(\mathbf{a}^H\left(f_{\mathrm{m,n}}\right)\mathbf{\Sigma}^{-1}_{\mathrm{m,n}}\mathbf{a}\left(f_{\mathrm{m,n}}\right)\right) - \mathbf{x}_{\mathrm{m,n}}\mathbf{\Sigma}^{-1}_{\mathrm{m,n}}\mathbf{a}\left(f_{\mathrm{m,n}}\right). \tag{7.16}$$

Equating to zero, conjugating, and solving the above equation produces the MLE of $\alpha_{\mathrm{m,n}}$,

$$\hat{\alpha}_{\mathrm{m,n}} = \frac{\mathbf{a}^H(f_{\mathrm{m,n}})\mathbf{\Sigma}^{-1}_{\mathrm{m,n}}\mathbf{x}_{\mathrm{m,n}}}{\mathbf{a}^H(f_{\mathrm{m,n}})\mathbf{\Sigma}^{-1}_{\mathrm{m,n}}\mathbf{a}(f_{\mathrm{m,n}})}. \tag{7.17}$$

To find the MLE of $\sigma_{\mathrm{m,n}}$ under H_1, take the derivative of (7.15) with respect to $\sigma_{\mathrm{m,n}}$,

$$\frac{\partial \log\left(p(\mathbf{X};\boldsymbol{\alpha},\boldsymbol{\sigma})\right)}{\partial \sigma_{\mathrm{m,n}}} = -\frac{2K_p}{\sigma_{\mathrm{m,n}}} + 2\frac{\mathbf{y}^H_{\mathrm{m,n}} \mathbf{\Sigma}^{-1}_{\mathrm{m,n}} \mathbf{y}_{\mathrm{m,n}}}{\sigma^3_{\mathrm{m,n}}}. \tag{7.18}$$

Setting the above equation equal to zero and solving results in the MLE of $\sigma_{\mathrm{m,n}}$ under H_1,

$$\hat{\sigma}^{2(H_1)}_{\mathrm{m,n}} = \frac{\mathbf{y}^H_{\mathrm{m,n}} \mathbf{\Sigma}^{-1}_{\mathrm{m,n}} \mathbf{y}_{\mathrm{m,n}}}{K_p}. \tag{7.19}$$

Substituting the MLEs into (7.6), it is straight forward to show that the generalized likelihood ratio simplifies to

$$\Lambda_{\text{GLR}} = \prod_{\text{m,n}} \left(\frac{\hat{\sigma}^{2(H_0)}_{\text{m,n}}}{\hat{\sigma}^{2(H_1)}_{\text{m,n}}} \right)^{K_p}. \tag{7.20}$$

Notice that $\hat{\sigma}^{2(H_1)}_{\text{m,n}}$ may be written in the following way

$$\hat{\sigma}^{2(H_1)}_{\text{m,n}} = \hat{\sigma}^{2(H_0)}_{\text{m,n}} - \frac{|\mathbf{a}^H(f_{\text{m,n}})\boldsymbol{\Sigma}^{-1}_{\text{m,n}}\mathbf{x}_{\text{m,n}}|^2}{K_p\left(\mathbf{a}^H(f_{\text{m,n}})\boldsymbol{\Sigma}^{-1}_{\text{m,n}}\mathbf{a}(f_{\text{m,n}})\right)}. \tag{7.21}$$

So after substituting the above equation into the expression for the GLR, and dropping the exponent, we achieve the GLRT test statistic

$$\Lambda_{\text{GLRT}} = \prod_{\text{m,n}}^{NM} \left(\frac{1}{1 - T^{(m,n)}_{\text{GLR}}} \right) \underset{H_0}{\overset{H_1}{\gtrless}} \gamma_{\text{GLRT}}, \tag{7.22}$$

where

$$T^{(m,n)}_{\text{GLR}} = \frac{|\mathbf{a}^H(f_{\text{m,n}})\boldsymbol{\Sigma}^{-1}_{\text{m,n}}\mathbf{x}_{\text{m,n}}|^2}{\left(\mathbf{x}^H_{\text{m,n}}\boldsymbol{\Sigma}^{-1}_{\text{m,n}}\mathbf{x}_{\text{m,n}}\right)\left(\mathbf{a}^H(f_{\text{m,n}})\boldsymbol{\Sigma}^{-1}_{\text{m,n}}\mathbf{a}(f_{\text{m,n}})\right)}, \tag{7.23}$$

and γ_{GLRT} is chosen to satisfy a specified probability of false-alarm.

7.5 SIRP-GLRT

In [24], the SIRP-GLRT was developed by expressing the likelihood of the clutter in terms of the texture probability distribution and clutter probability conditioned upon the texture component,

$$p(\mathbf{x}_{\text{m,n}}; i\alpha_{\text{m,n}}|H_i) = \int_0^\infty p(\mathbf{x}_{\text{m,n}}; i\alpha_{\text{m,n}}|\sigma_{\text{m,n}})p(\sigma_{\text{m,n}})d\sigma_{\text{m,n}} \tag{7.24}$$

with $i = 0, 1$ corresponding to H_0 and H_1, respectively. The joint distribution for the entire network can be expressed as,

$$p(\mathbf{X}; i\boldsymbol{\alpha}|H_i) = \prod_{\mathrm{m,n}} \int_0^\infty p(\mathbf{x}_{\mathrm{m,n}}; i\alpha_{\mathrm{m,n}}|\sigma_{\mathrm{m,n}})p(\sigma_{\mathrm{m,n}})d\sigma_{\mathrm{m,n}} \tag{7.25}$$

which is independent of the texture. It is straight forward to show that the integration in (7.24) results in the likelihood,

$$p(\mathbf{x}_{\mathrm{m,n}}; i\alpha_{\mathrm{m,n}}|H_i) = \frac{\beta_{\mathrm{m,n}}^{(H_i)\tilde{\nu}}\Gamma(\tilde{\nu})}{\beta^{\nu}\Gamma(\nu)\pi^K|\boldsymbol{\Sigma}_{\mathrm{m,n}}|}, \tag{7.26}$$

where, $\tilde{\nu} = \nu + K$. Following [84] and our previous notation, we define

$$\beta_{\mathrm{m,n}}^{(H_0)} = \frac{1}{\mathbf{x}_{\mathrm{m,n}}^H \boldsymbol{\Sigma}_{\mathrm{m,n}}^{-1}\mathbf{x}_{\mathrm{m,n}} + 1/\beta}, \tag{7.27}$$

under H_0 and

$$\beta_{\mathrm{m,n}}^{(H_0)} = \frac{1}{\mathbf{y}_{\mathrm{m,n}}^H \boldsymbol{\Sigma}_{\mathrm{m,n}}^{-1}\mathbf{y}_{\mathrm{m,n}} + 1/\beta}, \tag{7.28}$$

under H_1. Substituting (7.26) into equation (7.25) results in the joint distribution

$$p(\mathbf{X}; i\boldsymbol{\alpha}|H_i) = \prod_{\mathrm{m,n}} \frac{\beta_{\mathrm{m,n}}^{(H_i)\tilde{\nu}}\Gamma(\tilde{\nu})}{\beta^{\nu}\Gamma(\nu)\pi^K|\boldsymbol{\Sigma}_{\mathrm{m,n}}|}, \tag{7.29}$$

where the only remaining step is to find the MLE of $\alpha_{\mathrm{m,n}}$. Fortunately, it is simple to show that this MLE is same as the one in (7.17). Noting this, we may write the likelihood ratio as,

$$\Lambda_{\mathrm{SIRP-GLR}} = \prod_{\mathrm{m,n}} \left(\frac{\beta_{\mathrm{m,n}}^{(H_1)}}{\beta_{\mathrm{m,n}}^{(H_0)}} \right)^{\tilde{\nu}} \underset{H_0}{\overset{H_1}{\gtrless}} \gamma_{\mathrm{SIRP-GLRT}} \tag{7.30}$$

where, $\gamma_{\mathrm{SIRP-GLRT}}$ is the detection threshold chosen to satisfy a specified probability of false alarm.

Similar to the GLRT, we may simplify (7.30) by noting that

$$\beta_{\mathrm{m,n}}^{(H_1)} = \left(\mathbf{x}_{\mathrm{m,n}}^H \mathbf{\Sigma}_{\mathrm{m,n}}^{-1} \mathbf{x}_{\mathrm{m,n}} + 1/\beta - \frac{|\mathbf{a}^H(f_{\mathrm{m,n}}) \mathbf{\Sigma}_{\mathrm{m,n}}^{-1} \mathbf{x}_{\mathrm{m,n}}|^2}{K_p \left(\mathbf{a}^H(f_{\mathrm{m,n}}) \mathbf{\Sigma}_{\mathrm{m,n}}^{-1} \mathbf{a}(f_{\mathrm{m,n}}) \right)} \right)^{-1}, \tag{7.31}$$

and therefore, after dropping the exponent, the test statistic in (7.30) can be expressed as

$$\Lambda_{\mathrm{SIRP-GLRT}} = \prod_{\mathrm{m,n}}^{NM} \left(\frac{1}{1 - S_{\mathrm{GLR}}^{(m,n)}} \right) \underset{H_0}{\overset{H_1}{\gtrless}} \gamma_{\mathrm{SIRP-GLRT}} \tag{7.32}$$

where

$$S_{\mathrm{GLR}}^{(m,n)} = \frac{|\mathbf{a}^H(f_{\mathrm{m,n}}) \mathbf{\Sigma}_{\mathrm{m,n}}^{-1} \mathbf{x}_{\mathrm{m,n}}|^2}{\left(\mathbf{x}_{\mathrm{m,n}}^H \mathbf{\Sigma}_{\mathrm{m,n}}^{-1} \mathbf{x}_{\mathrm{m,n}} + 1/\beta \right) \left(\mathbf{a}^H(f_{\mathrm{m,n}}) \mathbf{\Sigma}_{\mathrm{m,n}}^{-1} \mathbf{a}(f_{\mathrm{m,n}}) \right)}, \tag{7.33}$$

7.5.1 Clairvoyant Detector

In evaluating the performance of the above detectors, it will be useful to have a benchmark to compare against. The natural choice for this benchmark is the clairvoyant detector where the covariance matrix assumed to be known at each receiver. In this case we assume that the complex amplitude $\alpha_{\mathrm{m,n}}$ is still unknown for each path and that the texture is also unknown. Hence, we select the GLRT of (7.22) with the true covariance as the clairvoyant detector.

As a final note, unlike previous chapters, the detectors derived here do not take the form of a linear operation applied to the received data (*i.e.,* $\mathbf{w}^H\mathbf{x}$). However, the GLRT (7.22) and SIRP-GLRT (7.32) test statistics are both function of quantities $T_{\mathrm{GLR}}^{(m,n)}$ and $S_{\mathrm{GLR}}^{(m,n)}$, respectively, which have been shown in previous chapters can be written as a linear filter applied to the received data for each node. Therefore, under this interpretation, the GLRT and SIRP-GLRT for inverse gamma texture are both functions of the output of a filter with unit circle roots in the known covariance case. Hence, imposition of the unit circle property is justified in the practical case, and we are free to design filters which enforce the unit circle roots constraint for each node.

7.6 Covariance Matrix Estimation

The covariance matrix of the clutter speckle component is assumed to be unknown and must be estimated to transform the detectors into their adaptive counterparts. Assuming a set of L target-free secondary data are available at each receiver, the sample covariance matrix is a poor estimate due to the heterogeneous SIRP clutter power. Instead, we will use an estimate which is more robust to outliers in the secondary data: the fixed point estimator (FPE) [17]:

$$\hat{\mathbf{\Sigma}}_{\text{FPE}}^{t+1} = \frac{K_p}{L} \sum_{\ell=0}^{L-1} \frac{\mathbf{x}_\ell \mathbf{x}_\ell^H}{\mathbf{x}_\ell^H \hat{\mathbf{\Sigma}}_{\text{FPE}}^{t} \mathbf{x}_\ell}, \tag{7.34}$$

where $\hat{\mathbf{\Sigma}}_{\text{FPE}}^{t}$ is the t-th estimate. The FPE is an approximate maximum likelihood estimate for the covariance structure and is an unbiased estimator [70]. For the initialization, we set $\hat{\mathbf{\Sigma}}_{\text{FPE}}^{0} = \mathbf{I}$.

The FPE minimizes the affect of non-homogeneous clutter power upon the covariance estimates, but does not take into account any additional structure in the true covariance matrix. For the proposed approach, we will will employ the UCRC-based Toeplitz rectification approach described in Chapter 6, substituting each node's rectified covariance estimate in place of the true covariance in (7.22) and (7.32).

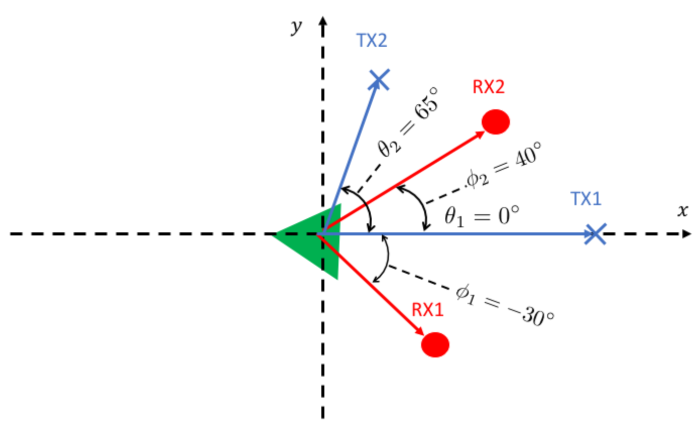

Figure 7.1: Target-centered simulation geometry

7.7 Simulation Setup

In this section, we describe the computer simulation used to evaluate the performance of the above mentioned detectors in compound-Gaussian clutter with inverse gamma distributed texture. A simulated MIMO radar network consisting of $N = M = 2$ transmitters and receivers operates at $f_c = 1$ GHz and pulse-repetition frequency (PRF) of 500 Hz. A target moves linearly with a starting direction $\theta = 30°$ at a radial velocity of $|\mathbf{v}|= 108$ km/h within the plane. The simulation geometry depicted in Fig. 7.1 is centered upon the moving target and the angles of the transmitters and receivers with respect to the positive x-axis are: $\phi_1 = -30°$, $\phi_2 = 40°$ and $\theta_1 = 0°$, $\theta_2 = 65°$. The target Doppler frequencies $f_{\mathrm{m,n}}$ are assumed known at the N receivers. The scale and shape parameters of the texture distribution were chosen such that $E[\sigma^2_{\mathrm{m,n}}] = 1$ which can be achieved using $\nu = 2$ and $\beta = 1$, respectively, and the texture distribution is assumed to be identical for each bistatic pair in the network.

The complex amplitudes $\alpha_{\mathrm{m,n}}$ are assumed to be non-fluctuating, equal constants across all nodes, allowing the signal-to-clutter ratio (SCR) to be scaled across the entire network. Noting this, we define the average SCR across the entire network to be,

$$\mathrm{SCR} = \frac{|\alpha|^2}{K_p MN} \sum_m \sum_n \mathbf{a}^H \left(f_{\mathrm{m,n}}\right) \mathbf{\Sigma}^{-1}_{\mathrm{m,n}} \mathbf{a} \left(f_{\mathrm{m,n}}\right). \tag{7.35}$$

The thresholds corresponding to the GLRT, SIRP-GLRT, and clairvoyant detectors along with the resulting statistics are computed using Monte-Carlo-based numerical integration and simulations, respectively, where $N_{MC} = \frac{100}{P_{FA}}$ and P_{FA} is the minimum probability of false-alarm.

Each clutter covariance matrix $\mathbf{\Sigma}_{\mathrm{m,n}}$ is distinct for each mn-th bistatic pair and defined according to the exponentially tapered matrix model [8] with the (i, j) element defined as,

$$\mathbf{\Sigma}_{\mathrm{m,n}}(i, j) = \rho^{|i-j|}_{\mathrm{m,n}} \tag{7.36}$$

Table 7.1: MIMO Simulation Parameters

(m,n)	(1,1)	(1,2)	(2,1)	(2,2)
$\rho_{\mathrm{m,n}}$	0.9	0.8	0.7	0.85
$f_{\mathrm{m,n}}$	0.2732	0.2638	0.3702	0.3608

where, the exponential parameters $\rho_{\mathrm{m,n}}$ and normalized Doppler frequencies are given in Table 7.1. Finally, $t = 8$ iterations when implementing the FPE.

7.7.1 Example 1 : Distributed MIMO Moving Target Detection

Figures 7.2a and 7.2b illustrate the performance of the SIRP-GLRT and GLRT for $K_p = 12$ pulses per node and $L = 24$ secondary data at each receiver. For Fig. 7.2a, a network $\mathrm{SCR} = -5$ dB is used to compute the performance, and for Fig. 7.2b; the minimum false alarm rate is $P_{\mathrm{FA}} = 10^{-3}$ to ease the computational burden.

Slight performance contrast between the SIRP-GLRT and GLRT is evident in Figs. 7.2a and 7.2b, where the inclusion of prior knowledge about the clutter power distribution results in a slight performance improvement when the UCRC Toeplitz rectification is used. Conventional Topelitz rectification is also included in these results, where the resulting rectified covariance estimate is obtained by averaging along the diagonals [35] and substituted into the GLRT in (7.22). Evidently, this approach suffers severe performance degradation and erratic performance at varying false alarm rates shown in Fig. 7.2a. The GLRT and SIRP-GLRT using only the FPE perform second best, and the performance constrast between the two detectors is not as clear as when the UCRC Toeplitz rectification is used.

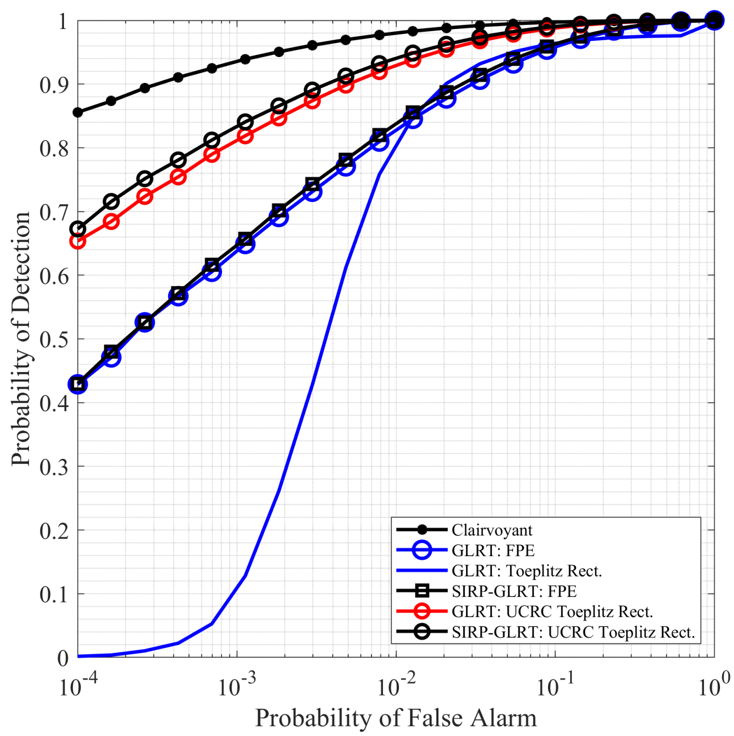

(a) ROC

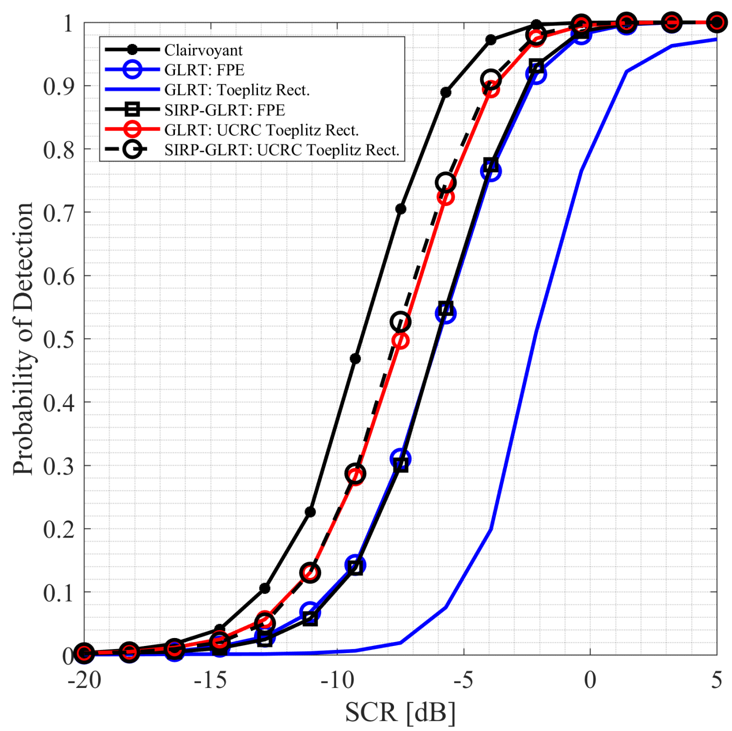

(b) P_{D} vs. SCR

Figure 7.2: Detection performance with $K_p = 12$ and $L = 13$ secondary data (a) ROC (b) P_{D} vs. SCR.

7.7.2 Example 2 : MIMO Moving Target Detection with Limited Secondary Data

In this example, the performance of the distributed MIMO GLRT and SIRP-GLRT are considered where the number of secondary data are limited. Again, the receiver operating characteristics are computed using a constant network $\mathrm{SCR} = -5$ dB and the probability of the detection versus SCR results are computed using $P_{\mathrm{FA}} = 10^{-3}$. $K_p = 12$ pulses per node are used and $L = 13$ secondary data are present at each receiver.

Figures 7.3a and 7.3b illustrate the performance of the SIRP-GLRT and GLRT using the different covariance estimates. Similar to the results shown in Section 7.7.1, there is a performance contrast between the GLRT and SIRP-GLRT when the UCRC Toeplitz rectification approach is used. The performance of the SIRP-GLRT/GLRT are greatly impacted when only the FPE is used, suffering a roughly 9 dB performance loss over the same detectors using the UCRC Toeplitz rectification. Additionally, comparing Figures 7.2b and 7.2a against Figures 7.3b and 7.3a shows that the performance disparity for the SIRP-GLRT and GLRT employing the UCRC Toeplitz rectification estimate is not as drastically impacted by the reduction of the secondary data.

7.7.3 Example 3 : Convergence of the MIMO SIRP-GLRT and GLRT

This final example investigates the convergence of the GLRT towards the SIRP-GLRT when the (m, n)-th covariance matrix is known for each detector. However, the textures and complex amplitudes are assumed unknown and estimated. Figure 7.4 shows the probability of detection versus the network SCR as the number of pulses per node increases. From this result, it is clear that the GLRT converges to SIRP-GLRT performance, illustrating the diminished utility of prior knowledge about the texture distribution as the number of pulses per node increases. This is an extension of the single node result found in [24] to the case of

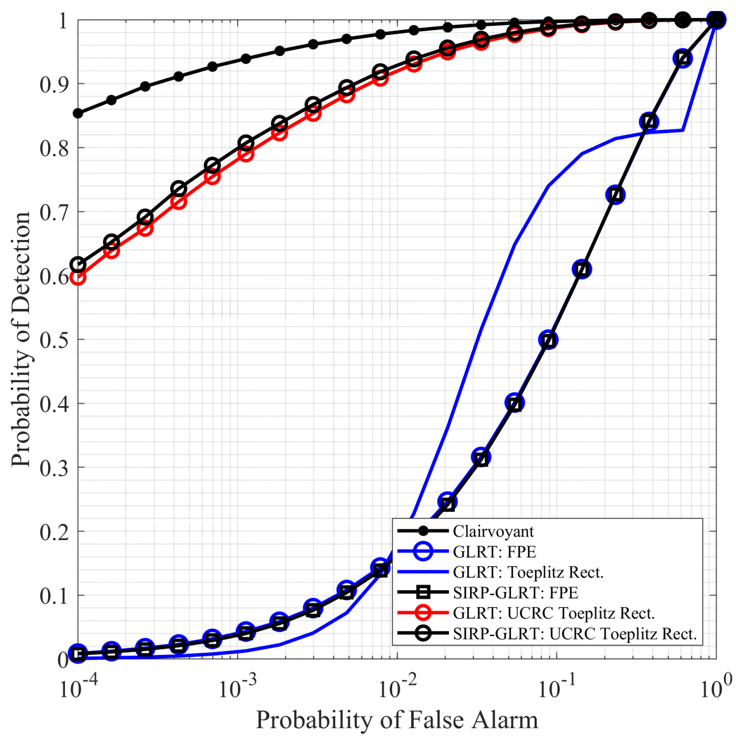

(a) ROC

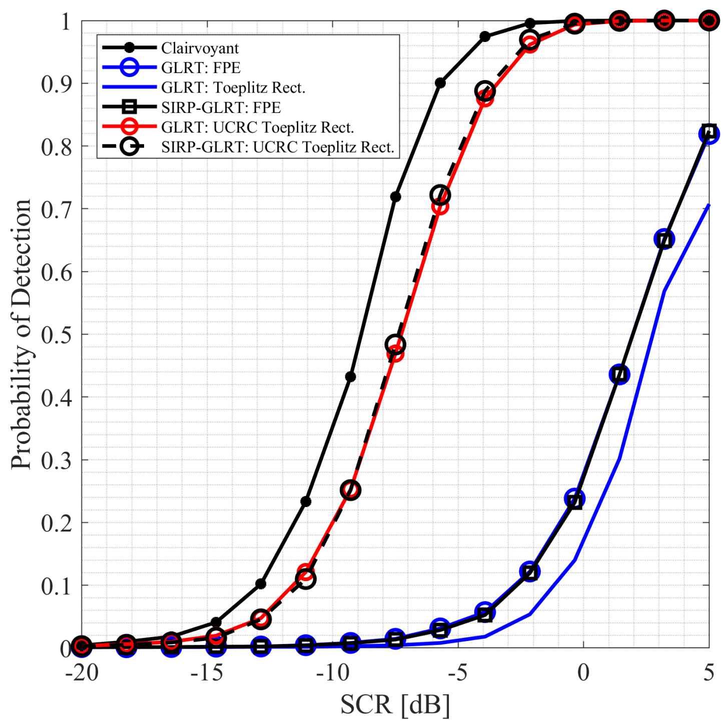

(b) P_{D} vs. SCR

Figure 7.3: Detection performance with $K_p = 12$ and $L = 13$ secondary data (a) ROC (b) P_{D} vs. SCR

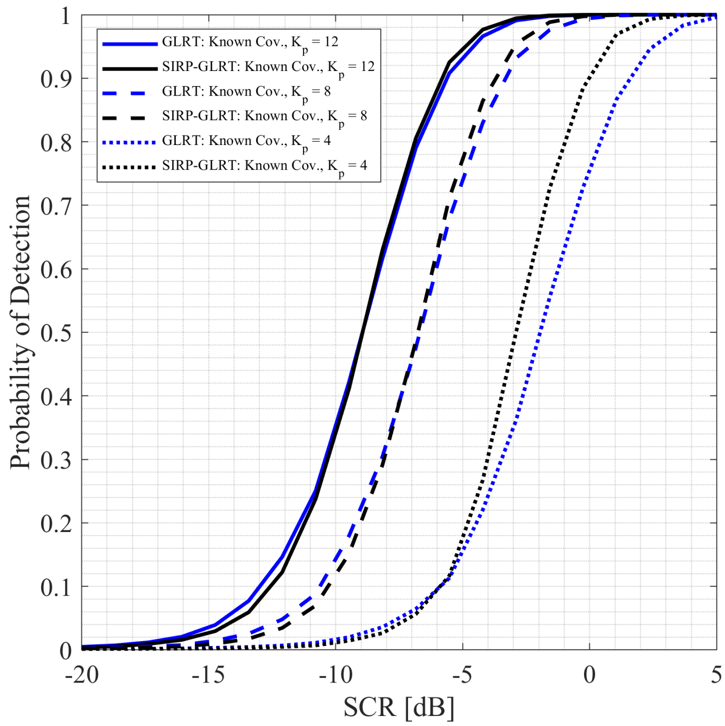

Figure 7.4: Convergence results for SIRP-GLRT and GLRT for increasing number of pulses per node.

distributed MIMO, where the GLRT convergence occurred around 16 pulses. Practically, this result demonstrates that for a distributed MIMO radar network, the performance loss of the GLRT over the SIRP-GLRT is negligible when using a smaller number of pulses per node when compared to the single-input single-output case.

7.8 Conclusion

This chapter compares the performance of the GLRT and SIRP-GLRT for moving target detection using an active MIMO radar network in compound-Gaussian clutter. The clutter were modeled as SIRP where the texture component follows an inverse-Gamma distribution. Exploiting the properties of this texture distribution within the SIRP-GLRT definition yields a closed-form expression for a detector, which explicitly accounts for the stochastic nature of the clutter power. An estimate of the clutter covariance matrix at each node was computed from a set of non-homogeneous and target-free secondary data using the fixed point estimate. The UCRC Toeplitz rectification approach described in Chapter 6 was applied using the FPE as the starting point and substituted into the corresponding GLRT and SIRP-GLRT. It was observed that the performance of both the SIRP-GLRT and GLRT in conjunction with the UCRC Toeplitz rectified estimate exceeds that of the same detectors when employing the FPE alone. Additionally, the superior performance of the detectors using the UCRC Toeplitz rectification estimate in both the SIRP-GLRT and GLRT over the same detectors utilizing the FPE in limited secondary data was also shown. Finally, the convergence in performance of the GLRT toward the SIRP-GLRT in the known covariance case was demonstrated for the case of an increasing number of pulses-per-node. The latter implies that as K_p increases beyond 8 for the case of 2x2 MIMO, the utility of prior knowledge about the texture is diminished and one may forsake the complicated SIRP-GLRT in favor of the more computationally efficient GLRT.

Conclusions and Future Work

In this dissertation, a novel Unit Circle Roots Constrained (UCRC) SASP framework was developed, which leverages polynomial symmetry to enforce unit-circle roots on sensor array polynomials that appear in beamforming using uniform linear arrays (ULA), and adaptive moving target detection using symmetrically spaced pulse trains in Gaussian and compound-Gaussian clutter in single-input single output (SISO) and multiple-input multiple output (MIMO) applications.

The new proof of the unit circle roots property for general SASP optimization with a linear constraint forms the cornerstone of the research in this dissertation. Though the same property was shown by Steinhardt et al. in 2004 [97], their proof was only specific for MVDR beamforming with uniform linear arrays, and no attempt was made to generalize to other SASP applications, such as the AMF. Our proof does generalize to the AMF, and other proportional SASP solutions, justifying the imposition of the unit circle roots constraint to a wider class of signal processing problems.

In Chapter 3, the unit circle roots constrained MVDR algorithm (UCRC-MVDR) was proposed. The UCRC-MVDR is different from the radial projection approach [102], as the unit-circle rectification is performed algorithmically; splitting the multidimensional MVDR problem into multiple one-dimensional MVDR problems. Coupling the unit circle roots constraint into the MVDR optimization problem by exploiting polynomial conjugate symmetry, the resulting root updates can be found in closed form and minimize the average output variance. It was also shown that the UCRC-MVDR has a computational complexity proportional to the sample matrix inversion (SMI) technique. Through extensive simulation examples, it is shown that the UCRC-MVDR drastically outperforms conventional techniques, including the recently proposed unit circle based MVDR approach [102].

In Chapter 4, based on the similarity between the derivation of the AMF and the MVDR, the unit circle roots constraint was applied to the AMF for radar moving target detection in homogeneous Gaussian clutter. Two versions of unit circle roots constrained AMF algorithm were presented: UCRC-AMF and M-UCRC-AMF. The former uses the conventional SCM to initialize the algorithm as well as to impose the unit circle property on each AMF root, the latter is initialized in the same manner using the SMI-based AMF roots, but the FB-SCM is used in the second stage for enforcing the unit circle property. Both UCRC-AMF and M-UCRC-AMF approaches estimate each root in closed-form by enforcing conjugate-symmetry upon the first-order polynomial factors. The UCRC-AMF is shown to outperform the SMI-based AMF, and the M-UCRC-AMF drastically outperformed the PS-AMF and UCRC-AMF for limited secondary data. The equivalence between the FB-AMF and PS-AMF was also shown, where we argued that since both detectors exploit the persymmetric structure of the clutter plus noise covariance matrix, similar performance can be expected.

In Chapter 5, radar moving target detection in low rank clutter was considered, and the unit circle approach was extended to accommodate this scenario. It was shown empirically that the roots of the PCI-based adaptive filter occur near their Clairvoyant counterparts on the unit circle. Hence, the unit circle constraint was enforced by radially projecting the roots of the PCI-based adaptive filter onto the unit circle. Using the properties of orthogonal projection matrices, the unit circle GLRT is derived by combining the primary and secondary data, and showed dramatically improved performance over the GLRT based on the eigenvectors. Additionally, it was also shown that asymptotically, the UC-GLRT provides constant false alarm rate with respect to the noise and clutter coefficients.

From the theory provided in Chapter 2 and Caratheòdory's Vandermonde decomposition, Chapter 6 proposed a Toeplitz-structured covariance matrix estimate obtained from the roots at the output of the UCRC algorithm. Unlike the approach in Chapters 3, 4, and 5, enforcing Hermitian Toeplitz structure naturally provides unit circle roots, instead of imposing them directly upon the filter design. This new covariance estimate showed improved detection performance in compound-Gaussian clutter when used in conjunction with the normalized adaptive matched filter for SISO and distributed MIMO moving target detection in Chapters 6 and 7, respectively.

8.0.1 List of Proposed Algorithms

Several algorithms have been proposed in this dissertation for temporal and spatial signal processing applications. In this section, the proposed algorithms are listed along with their intended area of application and differences between one another.

UCRC-MVDR

The UCRC-MVDR algorithm proposed in Chapter 3 pertains to spatial adaptive beamforming with uniform linear arrays. Using the UCRC algorithm, a beamformer with unit circle roots is designed by minimizing the output variance subject to a linear constraint on the look direction, and by enforcing conjugate symmetry upon the first-order array polynomial factors. The UCRC-MVDR is initialized using the roots of the SMI-based MVDR beamformer and each root is placed onto the unit circle boundary in parallel, *i.e.,* each estimated root is independent of the previously estimated root. Once all of the roots are found, mainbeam preservation is performed by moving any unit circle roots that appear within the mainbeam, *i.e.,* the area between the two CBF nulls symmetric about the signal of interest, to the nearest CBF null.

UCRC-AMF

The UCRC-AMF and M-UCRC-AMF algorithms proposed in Chapter 4 pertain to adaptive detector design in the temporal domain using symmetrically spaced pulse trains. Like the UCRC-MVDR, both M-UCRC-AMF and UCRC-AMF design the adaptive detector by maximizing the output SINR subject to a linear constraint, while imposing unit circle roots by enforcing conjugate symmetry upon the first-order filter polynomial factors. Both UCRC-AMF and M-UCRC-AMF are initialized using the roots of the SMI-based adaptive matched filter. The difference between the UCRC-AMF and the M-UCRC-AMF is that the UCRC-AMF uses the sample covariance matrix to estimate the unit circle roots and the M-UCRC-AMF uses the forward-backward sample covariance matrix to estimate the roots. Unlike the UCRC-MVDR, M-UCRC-AMF and UCRC-AMF estimate the roots sequentially

UC-GLRT

The UC-GLRT algorithm proposed in Chapter 5 radially projects the roots of the PCI-based adaptive filter onto the unit circle to improve low-rank clutter suppression. Additionally, the UC-GLRT combines the primary and secondary data to improve detection and the white noise power estimation performance. Unlike the M-UCRC/UCRC-AMF, the UC-GLRT enforces the unit circle roots constraint by radially projecting the roots instead of optimizing the output SINR. In Chapter 3, radial projection of the SMI-based roots was disregarded as suboptimal in the beamforming context. However, in Chapter 5, it was shown that while the SMI-based roots occur far from the unit circle boundary, a majority of the PCI-based roots occur near the unit circle, making radial projection a more intuitively feasible approach. Using the properties of orthogonal projection matrices, the UC-GLRT results in a closed-form filter representation which is guaranteed to have unit circle roots.

UCRC-Toeplitz Rectification

UCRC Toeplitz rectification (UCRC-TR) proposed in Chapter 6 uses the roots at the output of the UCRC algorithm to reconstruct a Toeplitz-structured covariance matrix. The resulting structured estimate can then be used to compute an adaptive filter which is guaranteed to have unit circle roots according to Theorem 1. Thus, an adaptive filter with unit circle roots can be created implicitly, instead of explicitly by using the roots to design the filter.

Though the output roots of the UCRC-AMF were used in Chapter 6, UCRC-TR is independent of spatial or temporal application, and only requires a set of unit circle roots to create a Toeplitz-structured covariance estimate. Thus, applications in either the spatial or temporal domian can be considered.

8.1 Stability Considerations of the UCRC Approach

The UCRC algorithm is the cornerstone of the research in this dissertation. Due to its fundamental importance to this research, some consideration is necessary when discussing the limitations of the UCRC approach; namely, algorithm stability when the number of roots is large.

The number of roots the UCRC algorithm must correct grows in proportion to the array size or CPI length. When the number of roots is large, initialization of the UCRC algorithm can become unstable due to rooting a high-degree SMI-based polynomial at the initialization step. Additionally, numerical instabilities when computing the final filter weights can arise after all of the roots have been estimated. Fortunately, the initial roots do not need to be limited to the SMI, and the roots of other filters can be used instead. For example, initializing the UCRC-MVDR with the roots of the conventional beamformer has shown promising preliminary results.

Finally, it is necessary to mention that the computation of the weighted covariance matrix forms a significant bottleneck in the UCRC algorithm. Therefore, more work is necessary to streamline the UCRC approach when correcting each individual root. It is hypothesized that further optimizing the UCRC algorithm may improve the aforementioned stability concerns.

8.2 Extensions and Future Work

For the remainder of this chapter, two areas of great interest for expanding the unit circle approach described in this thesis are discussed: beamforming using array geometries other than uniform linear arrays and radar space-time adaptive processing.

The foremost assumption in Chapter 3 for the UCRC-MVDR derivation was a uniform linear array. In practice, arrays with ideal spacing or geometry can be difficult and costly to design. Additionally, the MVDR is not specific to the array geometry employed, and so the UCRC-MVDR only addresses a subclass of SASP application pertinent to MVDR with ULAs. Uniform circular arrays (UCAs) have several advantages over ULAs, including uniform direction of arrival performance [7]. Since the 1990's beamspace transformations (BT) [22, 98, 64] have been developed which transform the UCA steering vectors into Vandermonde vectors. Therefore, one possible application of the UCRC approach to non-ULA beamforming is to the processing of UCA data under the application of beamspace transformations.

Since its inception over 50 years ago, space-time adaptive processing (STAP) continues to be an area of ongoing research. Integral to most modern radar systems, STAP's increased degrees of freedom allow for powerful adaptivity in the presence of both clutter and jamming. The optimal space-time filter is proportional and analogous to Eq. (2.2) [67], where the space-time covariance is of dimension $N_s K_p \times N_s K_p$, and the steering vector is of dimension $N_s K_p \times 1$ and is a function of the Doppler and spatial frequencies. However, fully-adaptive STAP is limited, due to the large amount of secondary data necessary to obtain near optimal performance [75]. Additionally, STAP is a joint domain approach and the techniques described in this dissertation can only be applied to the space or time domain separately.

One possible method to overcome this limitation is by processing the received space-time data in each domain separately. This approach is known as the extended factored algorithm (EFA) or joint domain localization (JDL) and are commonly used techniques for reduced dimension STAP [67]. Since the AMF can be utilized to perform adaptive Doppler processing, the proposed unit circle roots approach can be readily incorporated into the previously described single-domain method. Moreover, it is hypothesized that combining both spatial and temporal unit circle approaches in a prudent manner will result in improved STAP algorithm performance.

Some remarks on potential future work on specific topics have been addressed in the concluding sections of respective Chapters and are not repeated here.

Final considerations for future work pertain to the last two chapters of this dissertation. M-UCRC/UCRC-AMF were not included in Chapter 6 due to their poor performance in compound-Gaussian clutter. Improvements to these algorithms are necessary to generalize their performance to incorporate the broader class of compound-Gaussian clutter models by developing an UCRC version of the normalized Adaptive Matched filter (NAMF) [19]. Additionally, in Chapter 7, only distributed MIMO for compound-Gaussian clutter was considered. However, due to the superior performance of M-UCRC-AMF for homogeneous clutter, an extension of the M-UCRC-AMF for distributed MIMO in homogeneous Gaussian clutter should also be considered.

Bibliography

[1] D. Aalfs. Adaptive digital beamforming. In W. L. Melvin and J. Scheer, editors, *Principles of Modern Radar Vol II: Advanced Techniques*, volume 2, chapter 9, page 420. SciTech Publishing, 2013.

[2] R. Abrahamsson, A. Jakobsson, and P. Stoica. A Capon-like spatial spectrum estimator for correlated sources. In *2004 12th European Signal Processing Conference*, pages 1265–1268, 2004.

[3] Y. I. Abramovich, B. A. Johnson, and N. K. Spencer. Sample-deficient adaptive detection: Adaptive scalar thresholding versus CFAR detector performance. *IEEE Transactions on Aerospace and Electronic Systems*, 46(1):32–46, 2010.

[4] X. Anguera, C. Wooters, and J. Hernando. Acoustic beamforming for speaker diarization of meetings. *IEEE Transactions on Audio, Speech, and Language Processing*, 15(7):2011–2022, 2007.

[5] T.F. Ayoub and A.R. Haimovich. Modified glrt signal detection algorithm. *IEEE Transactions on Aerospace and Electronic Systems*, 36(3):810–818, 2000.

[6] A. Balleri, A. Nehorai, and J. Wang. Maximum likelihood estimation for compound-Gaussian clutter with inverse gamma texture. *IEEE Transactions on Aerospace and Electronic Systems*, 43(2):775–779, April 2007.

[7] F. Belloni and V. Koivunen. Beamspace transform for UCA: Error analysis and bias reduction. *IEEE Transactions on Signal Processing*, 54(8):3078–3089, 2006.

[8] O. Besson, J. Tourneret, and S. Bidon. Knowledge-aided bayesian detection in heterogeneous environments. *IEEE Signal Processing Letters*, 14(5):355–358, May 2007.

[9] D. M. Boroson. Sample size considerations for adaptive arrays. *IEEE Transactions on Aerospace and Electronic Systems*, AES-16(4):446–451, 1980.

[10] A. Breloy, G. Ginolhac, F. Pascal, and P. Forster. Robust covariance matrix estimation in heterogeneous low rank context. *IEEE Transactions on Signal Processing*, 64(22):5794–5806, 2016.

[11] Y. Bresler and A. Macovski. Exact maximum likelihood parameter estimation of superimposed exponential signals in noise. *IEEE Transactions on Acoustics, Speech, and Signal Processing*, 34(5):1081–1089, 1986.

[12] J. Cadzow. Signal enhancement using canonical projection operators. In *ICASSP '87. IEEE International Conference on Acoustics, Speech, and Signal Processing*, volume 12, pages 673–676, 1987.

[13] J. Capon. High-resolution frequency-wavenumber spectrum analysis. *Proceedings of the IEEE*, 57(8):1408–1418, 1969.

[14] C. Carathéodory and L. Fejér. über den zusammenhang der extremen von harmonischen funktionen mit ihren koeffizienten und über den picard-landau'schen satz. *Rendiconti del Circolo Matematico di Palermo (1884-1940)*, 32(1):218–239, 1911.

[15] M. Casillo, A. De Maio, S. Iommelli, and L. Landi. A persymmetric GLRT for adaptive detection in partially-homogeneous environment. *IEEE Signal Processing Letters*, 14(12):1016–1019, 2007.

[16] E. Conte and A. De Maio. Exploiting persymmetry for cfar detection in compound-Gaussian clutter. *IEEE Transactions on Aerospace and Electronic Systems*, 39(2):719–724, 2003.

[17] E. Conte, A. De Maio, and G. Ricci. Recursive estimation of the covariance matrix of a compound-Gaussian process and its application to adaptive cfar detection. *IEEE Transactions on Signal Processing*, 50(8):1908–1915, 2002.

[18] E. Conte and M. Longo. Characterisation of radar clutter as a spherically invariant random process. *IEE Proceedings F - Communications, Radar and Signal Processing*, 134(2):191–197, April 1987.

[19] E. Conte, M. Lops, and G. Ricci. Asymptotically optimum radar detection in compound-Gaussian clutter. *IEEE Transactions on Aerospace and Electronic Systems*, 31(2):617–625, 1995.

[20] H. Cox, R. Pitre, and H. Lai. Robust adaptive matched field processing. In *Conference Record of Thirty-Second Asilomar Conference on Signals, Systems and Computers*, volume 1, pages 127–131 vol.1, 1998.

[21] H. Cox, R. Zeskind, and M. Owen. Robust adaptive beamforming. *IEEE Transactions on Acoustics, Speech, and Signal Processing*, 35(10):1365–1376, 1987.

[22] J.G Davis and A.A.P Gibson. Phase mode excitation in beamforming arrays. In *2006 European Radar Conference*, pages 307–310, 2006.

[23] A. De Maio, D. Orlando, C. Hao, and G. Foglia. Adaptive detection of point-like targets in spectrally symmetric interference. *IEEE Transactions on Signal Processing*, 64(12):3207–3220, 2016.

[24] L. Dejean, D. Pastor, J. M. Quellec, M. Chabah, and N. Bon. The clutter SIRP and Gaussian models: a brief overview and a comparison. In *2008 IET Seminar on Radar Clutter Modelling*, pages 41–47, 2008.

[25] L. Du, J. Li, and P. Stoica. Fully automatic computation of diagonal loading levels for robust adaptive beamforming. *IEEE Transactions on Aerospace and Electronic Systems*, 46(1):449–458, 2010.

[26] R. Elliott. Array pattern synthesis. *IEEE Antennas and Propagation Society Newsletter*, 27(5):4–9, 1985.

[27] E. Fishler, A. Haimovich, R. S. Blum, L. J. Cimini, D. Chizhik, and R. A. Valenzuela. Spatial diversity in radars models and detection performance. *IEEE Transactions on Signal Processing*, 54(3):823–838, March 2006.

[28] P. Forster. Generalized rectification of cross spectral matrices for arrays of arbitrary geometry. *IEEE Transactions on Signal Processing*, 49(5):972–978, 2001.

[29] D. R. Fuhrmann and G. San Antonio. Transmit beamforming for MIMO radar systems using partial signal correlation. In *Conference Record of the Thirty-Eighth Asilomar Conference on Signals, Systems and Computers*, volume 1, pages 295–299, Nov 2004.

[30] D.R. Fuhrmann. Application of toeplitz covariance estimation to adaptive beamforming and detection. *IEEE Transactions on Signal Processing*, 39(10):2194–2198, 1991.

[31] A. B. Gershman. Robust adaptive beamforming: an overview of recent trends and advances in the field. In *4th International Conference on Antenna Theory and Techniques*, volume 1, pages 30–35 vol.1, 2003.

[32] A. B. Gershman, N. D. Sidiropoulos, S. Shahbazpanahi, M. Bengtsson, and B. Ottersten. Convex optimization-based beamforming. *IEEE Signal Processing Magazine*, 27(3):62–75, 2010.

[33] N. R. Goodman. Statistical analysis based on a certain multivariate complex Gaussian distribution (an introduction). *Ann. Math. Statist.*, 34(1):152–177, 03 1963.

[34] P. T. Gough. A fast spectral estimation algorithm based on the FFT. *IEEE Transactions on Signal Processing*, 42(6):1317–1322, 1994.

[35] D.A. Gray, B.D.O. Anderson, and P.K. Sim. Estimation of structured covariances with application to array beamforming. *Circuits Systems and Signal Processing*, 6:421–447, 1987.

[36] M. Greco, F. Gini, A. Farina, and J. B. Billingsley. Validation of windblown radar ground clutter spectral shape. *IEEE Transactions on Aerospace and Electronic Systems*, 37(2):538–548, 2001.

[37] Y. Gu and A. Leshem. Robust adaptive beamforming based on jointly estimating covariance matrix and steering vector. In *2011 IEEE International Conference on Acoustics, Speech and Signal Processing (ICASSP)*, pages 2640–2643, 2011.

[38] A. Haimovich. The eigencanceler: adaptive radar by eigenanalysis methods. *IEEE Transactions on Aerospace and Electronic Systems*, 32(2):532–542, 1996.

[39] A. Hassanien and B. Himed. Moving target detection for distributed MIMO radar under clutter model mismatch. In *2020 54th Asilomar Conference on Signals, Systems, and Computers*, pages 1568–1573, 2020.

[40] A. Hassanien, B. Himed, J. Metcalf, and B. D. Rigling. Moving target detection in spatially heterogeneous clutter using distributed MIMO radar. In *2018 International Conference on Radar (RADAR)*, pages 1–6, 2018.

[41] A. Hassanien, B. Himed, and B. D. Rigling. Moving target detection using fast iterative interpolated beamforming for distributed MIMO radar in non-homogeneous clutter. In *2019 53rd Asilomar Conference on Signals, Systems, and Computers*, pages 624–629, 2019.

[42] Q. He, N. H. Lehmann, R. S. Blum, and A. M. Haimovich. MIMO radar moving target detection in homogeneous clutter. *IEEE Transactions on Aerospace and Electronic Systems*, 46(3):1290–1301, 2010.

[43] J. A. Högbom. Aperture Synthesis with a Non-Regular Distribution of Interferometer Baselines. *AAPS*, 15:417, June 1974.

[44] L. A. A. Irkhis and A. K. Shaw. Compressive chirp transform for estimation of chirp parameters. In *2019 27th European Signal Processing Conference (EUSIPCO)*, pages 1–5, 2019.

[45] E. Jay, J. P. Ovarlez, D. Declercq, and P. Duvaut. Bayesian optimum radar detector in non-Gaussian noise. In *2002 IEEE International Conference on Acoustics, Speech, and Signal Processing*, volume 2, pages II–1289–II–1292, 2002.

[46] K-C. Huarng and C-C. Teh. Adaptive beamforming with conjugate symmetric weights. *IEEE Transactions on Antennas and Propagation*, 39(7):926–932, 1991.

[47] B. Kang, V. Monga, and M. Rangaswamy. Rank-constrained maximum likelihood estimation of structured covariance matrices. *IEEE Transactions on Aerospace and Electronic Systems*, 50(1):501–515, January 2014.

[48] E. J. Kelly. An adaptive detection algorithm. *IEEE Transactions on Aerospace and Electronic Systems*, AES-22(2):115–127, 1986.

[49] I. Kirsteins and D. Tufts. On the probability density of signal-to-noise ratio in an improved adaptive detector. In *ICASSP '85. IEEE International Conference on Acoustics, Speech, and Signal Processing*, volume 10, pages 572–575, 1985.

[50] I.P. Kirsteins and D.W. Tufts. Adaptive detection using low rank approximation to a data matrix. *IEEE Transactions on Aerospace and Electronic Systems*, 30(1):55–67, 1994.

[51] W. C. Knight, R. G. Pridham, and S. M. Kay. Digital signal processing for sonar. *Proceedings of the IEEE*, 69(11):1451–1506, 1981.

[52] S. Kraut and L. L. Scharf. The CFAR adaptive subspace detector is a scale-invariant GLRT. *IEEE Transactions on Signal Processing*, 47(9):2538–2541, 1999.

[53] S. Kraut, L. L. Scharf, and L. T. McWhorter. Adaptive subspace detectors. *IEEE Transactions on Signal Processing*, 49(1):1–16, 2001.

[54] R. Kumaresan, L. Scharf, and A. Shaw. An algorithm for pole-zero modeling and spectral analysis. *IEEE Transactions on Acoustics, Speech, and Signal Processing*, 34(3):637–640, 1986.

[55] R. Kumaresan and A. K. Shaw. Superresolution by structured matrix approximation. *IEEE Transactions on Antennas and Propagation*, 36(1):34–44, 1988.

[56] S. Lang and J. McClellan. Frequency estimation with maximum entropy spectral estimators. *IEEE Transactions on Acoustics, Speech, and Signal Processing*, 28(6):716–724, 1980.

[57] A. Leshem and A. D. van der Veen. Radio-astronomical imaging in the presence of strong radio interference. *IEEE Transactions on Information Theory*, 46(5):1730–1747, 2000.

[58] H. Li, Z. Wang, J. Liu, and B. Himed. Moving target detection in distributed MIMO radar on moving platforms. *IEEE Journal of Selected Topics in Signal Processing*, 9(8):1524–1535, 2015.

[59] J. Li and P. Stoica. Efficient mixed-spectrum estimation with applications to target feature extraction. *IEEE Transactions on Signal Processing*, 44(2):281–295, 1996.

[60] J. Li and P. Stoica. MIMO radar with colocated antennas. *IEEE Signal Processing Magazine*, 24(5):106–114, 2007.

[61] N. Li, G. Cui, L. Kong, T. Zhang, and Q. H. Liu. MIMO radar moving target detection in compound-Gaussian clutter. In *2014 IEEE Radar Conference*, pages 0149–0153, 2014.

[62] J. Liu, G. Cui, H. Li, and B. Himed. On the performance of a persymmetric adaptive matched filter. *IEEE Transactions on Aerospace and Electronic Systems*, 51(4):2605–2614, 2015.

[63] J. Liu, W. Liu, H. Liu, B. Chen, X-G. Xia, and F. Dai. Average sinr calculation of a persymmetric sample matrix inversion beamformer. *IEEE Transactions on Signal Processing*, 64(8):2135–2145, 2016.

[64] Y. Ma, X. Wang, and X. Cao. Coarray beamspace transformation based doa estimation for uniform circular arrays. In *2018 IEEE Radar Conference (RadarConf18)*, pages 0792–0797, 2018.

[65] M. Marden. *Geometry of Polynomials*, chapter 10, pages 194–206. Math Surveys, 1966.

[66] W. L. Melvin. A STAP overview. *IEEE Aerospace and Electronic Systems Magazine*, 19(1):19–35, 2004.

[67] W. L. Melvin. Clutter suppression using space-time adaptive processing. In W. L. Melvin and J. Scheer, editors, *Principles of Modern Radar Vol II: Advanced Techniques*, volume 2, chapter 10, pages 453–497. SciTech Publishing, 2013.

[68] X. Mestre and M. A. Lagunas. Finite sample size effect on minimum variance beamformers: optimum diagonal loading factor for large arrays. *IEEE Transactions on Signal Processing*, 54(1):69–82, 2006.

[69] G. Pailloux, P. Forster, J.-P. Ovarlez, and F. Pascal. Persymmetric adaptive radar detectors. *IEEE Transactions on Aerospace and Electronic Systems*, 47(4):2376–2390, 2011.

[70] F. Pascal, Y. Chitour, J.-P. Ovarlez, P. Forster, and P. Larzabal. Covariance structure maximum-likelihood estimates in compound Gaussian noise: Existence and algorithm analysis. *IEEE Transactions on Signal Processing*, 56(1):34–48, 2008.

[71] M. Rangaswamy. Spherically invariant random processes for modeling non-Gaussian radar clutter. In *Proceedings of 27th Asilomar Conference on Signals, Systems and Computers*, pages 1106–1110 vol.2, Nov 1993.

[72] M. Rangaswamy and F.C. Lin. Radar applications of low rank signal processing methods. In *The Thrity-Seventh Asilomar Conference on Signals, Systems Computers, 2003*, volume 1, pages 802–806 Vol.1, 2003.

[73] M. Rangaswamy, F.C. Lin, and K.R. Gerlach. Robust adaptive signal processing methods for heterogeneous radar clutter scenarios. In *Proceedings of the 2003 IEEE Radar Conference (Cat. No. 03CH37474)*, pages 265–272, 2003.

[74] I. S. Reed, J. D. Mallett, and L. E. Brennan. Rapid convergence rate in adaptive arrays. *IEEE Transactions on Aerospace and Electronic Systems*, AES-10(6):853–863, 1974.

[75] I. S. Reed, J. D. Mallett, and L. E. Brennan. Rapid convergence rate in adaptive arrays. *IEEE Transactions on Aerospace and Electronic Systems*, AES-10(6):853–863, 1974.

[76] F. C. Robey, D. R. Fuhrmann, E. J. Kelly, and R. Nitzberg. A CFAR adaptive matched filter detector. *IEEE Transactions on Aerospace and Electronic Systems*, 28(1):208–216, 1992.

[77] F. C. Robey, D. R. Fuhrmann, E. J. Kelly, and R. Nitzberg. A CFAR adaptive matched filter detector. *IEEE Transactions on Aerospace and Electronic Systems*, 28(1):208–216, Jan 1992.

[78] C. Ryan and J. R. Buck. Applying the unit circle constraint to the diagonally loaded minimum variance distortionless response beamformer. In *2017 IEEE International Conference on Acoustics, Speech and Signal Processing (ICASSP)*, pages 3366–3369, 2017.

[79] K. J. Sangston, F. Gini, and M. S. Greco. Adaptive detection of radar targets in compound-Gaussian clutter. In *2015 IEEE Radar Conference (RadarCon)*, pages 0587–0592, 2015.

[80] K.J. Sangston, F. Gini, M.V. Greco, and A. Farina. Structures for radar detection in compound Gaussian clutter. *IEEE Transactions on Aerospace and Electronic Systems*, 35(2):445–458, 1999.

[81] L. L. Scharf and B. Friedlander. Matched subspace detectors. *IEEE Transactions on Signal Processing*, 42(8):2146–2157, 1994.

[82] L.L. Scharf and L.T. McWhorter. Adaptive matched subspace detectors and adaptive coherence estimators. In *Conference Record of The Thirtieth Asilomar Conference on Signals, Systems and Computers*, pages 1114–1117 vol.2, 1996.

[83] S. A. Schelkunoff. A mathematical theory of linear arrays. *The Bell System Technical Journal*, 22(1):80–107, 1943.

[84] X. Shang and H. Song. Radar detection based on compound-Gaussian model with inverse gamma texture. *IET Radar, Sonar Navigation*, 5(3):315–321, March 2011.

[85] A. Shaw, J. Smith, and A. Hassanien. MVDR beamformer design by imposing unit circle roots constraints for uniform linear arrays. *IEEE Transactions on Signal Processing*, 69:6116–6130, 2021.

[86] A. Shaw, J. Smith, and A. Hassanien. Unit circle roots constrained MVDR beamformer. In *2021 55th Asilomar Conference on Signals, Systems, and Computers*, pages 192–198, 2021.

[87] A. K. Shaw. *Structured Matrix Approximation Problems in Signal Processing*. PhD thesis, University of Rhode Island, 1987.

[88] A. K. Shaw. A novel cyclic algorithm for maximum likelihood frequency estimation. In *IEEE 1991 International Conference on Systems Engineering*, pages 412–415, 1991.

[89] A. K. Shaw. Maximum likelihood estimation of multiple frequencies with constraints to guarantee unit circle roots. *IEEE Transactions on Signal Processing*, 43(3):796–799, 1995.

[90] A.K. Shaw, S. Pokala, and R. Kumaresan. Toeplitz and hankel matrix approximation using structured approach. In *Proceedings of the 1998 IEEE International Conference on Acoustics, Speech and Signal Processing, ICASSP '98 (Cat. No.98CH36181)*, volume 4, pages 2349–2352 vol.4, 1998.

[91] A. P. Shikhaliev, L. C. Potter, and Y. Chi. Low-rank structured covariance matrix estimation. *IEEE Signal Processing Letters*, 26(5):700–704, May 2019.

[92] J. Smith and A. Shaw. Improved moving target detection by modified unit circle roots constrained adaptive matched filter. *2022 IEEE Radar Conference*, New York City, NY, Mar., 2022.

[93] J. Smith and A. Shaw. Unit circle roots property for sensor array signal processing. In *NAECON 2021 - IEEE National Aerospace and Electronics Conference*, pages 210–216, 2021.

[94] J. Smith, A. Shaw, and A. Hassanien. A new approach to moving target detection using unit circle roots constrained adaptive matched filter. In *2021 55th Asilomar Conference on Signals, Systems, and Computers*, pages 1091–1097, 2021.

[95] J. P. Smith and A. Shaw. Moving target detection using distributed MIMO radar in non-homogeneous clutter with limited training data. In *2020 54th Asilomar Conference on Signals, Systems, and Computers*, pages 617–622, 2020.

[96] I. S. D. Solomon and A. J. Knight. Spatial processing of signals received by platform mounted sonar. *IEEE Journal of Oceanic Engineering*, 27(1):57–65, 2002.

[97] A. Steinhardt and J. Guerci. STAP for RADAR: what works, what doesn't, and what's in store. In *Proceedings of the 2004 IEEE Radar Conference*, pages 469–473, 2004.

[98] A.H. Tewfik and W. Hong. On the application of uniform linear array bearing estimation techniques to uniform circular arrays. *IEEE Transactions on Signal Processing*, 40(4):1008–1011, 1992.

[99] J. Theiler, B. R. Foy, and A. M. Fraser. Beyond the adaptive matched filter: nonlinear detectors for weak signals in high-dimensional clutter. In S. S. Shen and P. E. Lewis, editors, *Algorithms and Technologies for Multispectral, Hyperspectral, and Ultraspectral Imagery XIII*, volume 6565, pages 26–37. International Society for Optics and Photonics, SPIE, 2007.

[100] D. W. Tufts, I. Kirsteins, and R. Kumaresan. Data-adaptive detection of a weak signal. *IEEE Transactions on Aerospace and Electronic Systems*, AES-19(2):313–316, 1983.

[101] S. R. Tuladhar and J. R. Buck. Unit circle MVDR beamformer. In *2015 IEEE International Conference on Acoustics, Speech and Signal Processing (ICASSP)*, pages 2484–2488, 2015.

[102] S. R. Tuladhar and J. R. Buck. Unit circle rectification of the minimum variance distortionless response beamformer. *IEEE Journal of Oceanic Engineering*, 45(2):500–510, 2020.

[103] T. J. Ulrych and R. W. Clayton. Time series modelling and maximum entropy. *Physics of the Earth and Planetary Interiors*, 12(2):188–200, 1976.

[104] P. Vallet and P. Loubaton. On the performance of music with toeplitz rectification in the context of large arrays. *IEEE Transactions on Signal Processing*, 65(22):5848–5859, 2017.

[105] S. A. Vorobyov. Principles of minimum variance robust adaptive beamforming design. *Signal Processing*, 93(12):3264–3277, 2013. Special Issue on Advances in Sensor Array Processing in Memory of Alex B. Gershman.

[106] P. Wang, H. Li, and B. Himed. Moving target detection using distributed MIMO radar in clutter with nonhomogeneous power. *IEEE Transactions on Signal Processing*, 59(10):4809 – 4820, 2011.

[107] P. Wang, H. Li, and B. Himed. Moving target detection using distributed MIMO radar in clutter with nonhomogeneous power. *IEEE Transactions on Signal Processing*, 59(10):4809–4820, Oct 2011.

[108] J. Ward. Space-time adaptive processing for airborne radar. In *1995 International Conference on Acoustics, Speech, and Signal Processing*, volume 5, pages 2809–2812 vol.5, 1995.

[109] D. Xu, R. He, and F. Shen. Robust beamforming with magnitude response constraints and conjugate symmetric constraint. *IEEE Communications Letters*, 17(3):561–564, 2013.

[110] Kung Y. A representation theorem and its applications to spherically-invariant random processes. *IEEE Transactions on Information Theory*, 19(5):600–608, 1973.

[111] Zai Y. and Lihua X. Frequency-selective vandermonde decomposition of toeplitz matrices with applications. *Signal Processing*, 142:157–167, 2018.

[112] Z. Yang, L. Xie, and P. Stoica. Vandermonde decomposition of multilevel toeplitz matrices with application to multidimensional super-resolution. *IEEE Transactions on Information Theory*, 62(6):3685–3701, 2016.

[113] Y. Yoon, M. G. Amin, and F. Ahmad. MVDR beamforming for through-the-wall radar imaging. *IEEE Transactions on Aerospace and Electronic Systems*, 47(1):347–366, 2011.

[114] A. Zaimbashi. Invariant subspace detector in distributed multiple-input multiple output radar: Geometry gain helps improving moving target detection. *IET Radar, Sonar & Navigation*, 10, 09 2015.

[115] L. Zhang, W. Liu, and L. Yu. Performance analysis for finite sample MVDR beamformer with forward backward processing. *IEEE Transactions on Signal Processing*, 59(5):2427–2431, 2011.

[116] J. Zhuang and A. Manikas. Interference cancellation beamforming robust to pointing errors. *IET Signal Processing*, 7(2):120–127, 2013.

[117] I. Ziskind and M. Wax. Maximum likelihood localization of multiple sources by alternating projection. *IEEE Transactions on Acoustics, Speech, and Signal Processing*, 36(10):1553–1560, 1988.